Spring 1990

Control and Mechanism Interaction for Ground-Based Testing of Space Structures

Li-Farn Yang
Old Dominion University

CONTROL AND MECHANISM INTERACTION FOR GROUND-BASED TESTING OF SPACE STRUCTURES

by

Li-Farn Yang

B.S. June 1983, National Cheng-Kung University,

Taiwan, R. O. C.

M.S. May 1988, Old Dominion University,

Department of Mechanical Engineering and Mechanics

Norfolk, Virginia 23529

A Dissertation Submitted to the Faculty of

Old Dominion University in Partial Fulfillment

of the Requirements for the Degree of

DOCTOR OF PHILOSOPHY

ENGINEERING MECHANICS

OLD DOMINION UNIVERSITY

May, 1990

Approved by:

Meng-Sang Chew (Director)

Jen-Kuang Huang (Co-director)

Chuh Mei

Jer-Nan Juang

Kenny Elliott

ACKNOWLEDGMENTS

I am delighted to acknowledge that the research demonstrated herein was sponsored by the Department of Mechanical Engineering and Mechanics, Old Dominion University and NASA Langley Research Center under Grant NAG-1-830. I would also wish to appreciate my advisor Dr. Mason Chew and co-advisor Jen-Kuang Huang for their instruction and their aid, and to Dr. Jer-Nan Juang for his suggestions and topics in this research.

Above all, I greatly thank my mother for her encouragement in my academic learning.

TABLE OF CONTENTS

LIST OF TABLES

LIST OF FIGURES

LIST OF SYMBOLS

§Chapter 3§

A : one parameter of disk coordinates

b : y-intercept of a general straight line

C : cable

D : noncircular disk

EI : flexural rigidity

$\bar{f}$: nonlinear force vector

f_1 : element of force vector f

f_2 : element of force vector f

g : gravitational constant

I_c : moment inertia of noncircular disk

$\bar{K}$: stiffness matrix

k_s : torsional spring stiffness

k_1 : spring stiffness of a soft spring suspension system

k_2 : spring stiffness of a linear spring

L : Lagrangian

$\bar{L}$: length of the beam

$\bar{M}$: inertia matrix

m : slope of a general straight string

m_1, m_2 : two masses associated with two rigid bodies

n : number of vibrational modes

O : rotational center

$\bar{q}(t)$: generalized coordinate vector

R : smooth ring

r_a : distance between rotational center and ring

r_b : original length of a swinging string

r_1, r_2 : moment arms of noncircular disk

S : torsional spring

T : kinetic energy

T_{s1}, T_{s2} : loading torques due to test structures

V : potential energy

V_0 : initial velocity

W : weight of test structure

x,y : coordinates of disk profile

x_1 : x-coordinate of the local coordinate

$y_1(x_1, t)$: y-coordinate of the local coordinate

$\bar{x}_1, \bar{y}_1$: vectors tangent to $x_1 - y_1$ coordinates

ϕ : rotational displacement of the string $\overline{PT}$

ϕ_0 : initial orientation of the string $\overline{PT}$

$\bar{\psi}(x_1)$: vector of mode shapes

$\bar{\ell}_1$: vector along the displacement ℓ_1

ℓ_{s1} : initial elongation of a linear spring

ℓ_1, ℓ_2 : positions of two masses

$\dot{\ell}_1, \dot{\ell}_2$: velocities of two masses

θ : angular displacement of disk

θ_{s0} : initially preloaded disk angle

θ_0 : preloaded angle of torsional spring

$\dot{\theta}$: angular velocity of disk

$\bar{\xi}$: state vector

$\bar{\omega}$: modal frequency vector

§Chapter 5§

$\tilde{A}$: system matrix of the first-order state equation

a : tracking arc length of gear O_1

B : control input matrix

b : tracking arc length of gear O_2

$\tilde{B}$: input matrix of the first-order state equation

$\bar{C}$: center-to-center distance of two gears

C_f : output measurement matrix

c_v : gear train viscous drag coefficient

c_p : conversion factor between the output shaft angle and e_p

c_s : conversion factor between the strain and e_0

c_t : conversion factor between the output angular velocity and e_t

c_i : parameters of hyperbolic gear ratios

c_{iopt} : optimal parameters of hyperbolic gear ratios in optimization problem

$c\theta_i$: $\cos(\theta_i)$

$\bar{D}$: damping matrix of dynamic equations with the motor's back-EMF

da : tracking arc length of gear O_1

db : tracking arc length of gear O_2

$d\theta_1$: small angle of gear O_1

$d\theta_2$: small angle of gear O_2

E_a : voltage input vector

EI : bending rigidity of the flexible beam

e : offset distance of gear center

$\hat{e}$: output measurement vector

e_a : applied voltage for the armature

e_0 : strain output voltage

e_p : potentiometer output voltage

e_t : tachometer output voltage

$F(\bar{x})$: cost function of optimization problem

$F(\bar{x}^0)$: starting value of cost function in optimization problem

$\tilde{f}$: the nonlinear force vector of the first-order state equation

$\tilde{f}(\theta_1)$: function of angle θ_1

G : output feedback gain matrix of the first-order state equation

G_{opt} : optimal control gain of optimization problem

$\tilde{g}(\theta_1)$: function of angle θ_1

$\tilde{h}(\theta_1)$: function of angle θ_1

$f\left(\xi, \dot{\xi}\right)$: nonlinear force vector in the dynamic equations

h : half-thickness of flexible beams

I_m : motor inertia

I_1, I_2 : moments of inertia for the first beam and the second beam

$\hat{I}_1$: $n_1 \times n_1$ identity matrix

$\hat{I}_2$: $n_2 \times n_2$ identity matrix

J : control performance index

K : stiffness matrix of the dynamic equations

K_b : back-EMF (Electro-Motive-Force) constant

K_t : motor torque constant

K_{1ij}, K_{2ij} : stiffness constants for two articulated flexible beams

L : length of flexible beam

L_a : armature inductance

M : inertia matrix of the dynamic equations without motor's inertia

$\bar{M}$: inertia matrix of the dynamic equations with motor's inertia

N_{g1}, N_{g2} : variant gear ratios of noncircular gears

$\dot{N}_{g1}, \dot{N}_{g2}$: time rates of noncircular gear ratios

N_{p1}, N_{p2} : idler gear ratios

n : number of mode shapes for flexible one-beam structure

n_1, n_2 : numbers of mode shapes for the flexible two-beam structure

O_1	: rotational center of gear O_1
O_2	: rotational center of gear O_2
$\overline{O_1O_2}$	: center line between two gears
$\tilde{p}(\theta_2)$	: function of angle θ_2
Q	: state weighting matrix
$\tilde{Q}$	: weighting coefficient of cost function
Q_i	: external forces of Lagrange's equations of motion
q_1, q_2, q_3	: generalized coordinates for the flexible beam-like structure
R	: input weighting matrix
R_a	: armature resistance
r_1, r_2	: operating pitch radii of noncircular gears
$s\theta_i$	: $\sin(\theta_i)$
t	: time
u(k)	: the control input of the first-order state equation at the sequence k
$\omega, \omega_1, \omega_2$	: weighting coefficients of cost function
$\bar{x}$	: the vector of design variables in optimization problem
$\bar{x}^0$	: starting point of design variables in optimization problem
$\bar{x}_{max}$	: upper-bound vector of design variables
$\bar{x}_{min}$	: lower-bound vector of design variables
x, y	: fixed inertial coordinates
x_a, x_b, x_c	: positions of strain gages along a flexible beam
x_1, y_1	: moving relative coordinates for the first flexible beam
x_2, y_2	: moving relative coordinates for the flexible fore-beam
ϕ	: pressure angle
ϕ_i	: the inequality functions of optimization problem
$\dot{\psi}_1(x_1)$	: mode shapes diagonal matrix for discretization of bending deflection of the flexible beams
ψ_1, ψ_2	: mode shapes diagonal matrices for the articulated manipulator
ψ_i	: the equality functions of optimization problem

κ_{ij} : elements of the stiffness matrix K

ω_i : frequencies associated with shape functions ψ_i

ρ : mass density (per unit length) of flexible beams

θ : angular displacement of inverted pendulum

θ_1, θ_2 : angular displacements of noncircular gears

$\dot{\theta}_1, \dot{\theta}_2$: angular velocities of noncircular gears

$\ddot{\theta}_1, \ddot{\theta}_2$: angular accelerations of noncircular gears

θ_1 : root angle and output motor shaft angle for the first flexible beam

θ_2 : root angle and output motor shaft angle for the fore-beam

θ_m : motor shaft angular position

τ_1, τ_2 : input/output torques in gear transmission

τ_a : available torque from the motor shaft

τ_i : control forces of the dynamic equations of motion

τ_m : motor torque

$\bar{\xi}$: state variable vector for second-order dynamic equations

$\bar{\xi}(k)$: state variable vector of first-order state equations at the sequence k

$\bar{\xi}(k+1)$: state variable vector of first-order state equations at the sequence k+1

$\times$: vector cross product

$\dot{(\ )}$: $\frac{d(\ )}{dt}$

$(\ )^T$: transpose of the matrix

$(\ )_{,xx}$: $\frac{\partial^2(\ )}{\partial x^2}$

$\triangle$: triangle

§Chapter 6§

A : system matrix composed of stiffness and damping matrices

$\tilde{A}$: matrix formed by A+E

a : constant parameter $\left[= \frac{3m_p g}{(4m_c+m_p)}\right]$

B : constant input matrix in Lagrange's equation of motion

$\bar{B}$: constant input matrix composed of matrix B

b : constant parameter $\left[= \frac{6(m_c+m_p)g}{L(4m_c+m_p)}\right]$

c : weighting vector of Lyapunov-based control input

D : constant damping matrix in Lagrange's equation of motion

E : matrix consisting of inertia submatrix in first-order state equations

f : nonlinear force vector in Lagrange's equation of motion

$\tilde{f}$: nonlinear force vector composed of vector f

f_3, f_4 : elements of nonlinear force vector

g : gravitational constant

I : identity matrix with appropriate dimensions associated with state equation

I_p : moment inertia of pendulum

M : inertia matrix of Lagrange's equation of motion

m_c : trolley mass of inverted pendulum

m_p : pendulum mass of inverted pendulum

n : number of states

P : weighting matrix of Lyapunov's function

p : number of inputs

Q : weighting matrix of Riccati equation

q : state vector of first-order state equations

q_e : equilibrium state

q_0 : original state

R : input weighting matrix of performance index

$r(t_0)$: real constant number depending on initial time

$T(\nu, q_0, t_0)$: time depending on ν, x_0, t_0

t : time

t_0 : initial time

u : control input vector

u_0 : optimal control law

u_1 : nonlinear control input

V(q,t) : Lyapunov function

$\dot{V}(q,t)$: time rate of Lyapunov function

x : displacement of dynamic equations

$\dot{x}$: velocity of dynamic equations

$\ddot{x}$: acceleration of dynamic equations

$\frac{d(\ )}{dt}$: differentiation of a variable with respect to time

ε : real positive number

ν : real number

δ : real positive number

$\| \bullet \|$: norm

$(\ )^{\dagger}$: pseudoinverse

$(\ )^{-1}$: matrix inversion

$(\ )^{T}$: matrix transpose

§Appendices A, B, C, D and E§

A : system matrix in the state equation

B : control input matrix

C_f : output measurement matrix

c : one parameter in envelope of a family of curves

c_v : gear train viscous drag coefficient

c_p : conversion factor between the output shaft angle and e_p

c_s : conversion factor between the strain and e_0

c_t : conversion factor between the output angular velocity and e_t

c_0 : a point of c

$c\theta_i$: $\cos(\theta_i)$

$\bar{D}$: damping matrix of dynamic equations with the motor's back-EMF

E_a : voltage input vector

EI : bending rigidity of the flexible beam

$\hat{e}$: output measurement vector

e_a : applied voltage for the armature

e_0 : strain output voltage

e_p : potentiometer output voltage

e_t : tachometer output voltage

f(q) : nonlinear function of state vector

f(q,t) : nonlinear function of state vector and time

$f\left(\xi, \dot{\xi}\right)$: nonlinear force vector in the dynamic equations

F : a continuous function of envelope theory

$g(q)$: nonlinear function of state vector

grad ( ) : gradient with respect to state vector

h : half-thickness of flexible beams

I_m : motor inertia

I_1, I_2 : moments of inertia for the first beam and the fore-beam

$\hat{I}_1$: $n_1 \times n_1$ identity matrix

$\hat{I}_2$: $n_2 \times n_2$ identity matrix

K : stiffness matrix of the dynamic equations

K_b : back-EMF (Electro-Motive-Force) constant

K_t : motor torque constant

K_{1ij}, K_{2ij} : stiffness constants for two articulated flexible beams

L : length of flexible beam

L_a : armature inductance

M : inertia matrix of the dynamic equations without motor's inertia

$\tilde{M}$: inertia matrix of the dynamic equations with motor's inertia

m : total mass of the trolley and the beam driver

N_g : overall gear ratio

n : number of mode shapes for the flexible one-beam structure

n_1, n_2 : numbers of mode shapes for the flexible two-beam structure

P : symmetric and positive-definite matrix

Q : symmetric and positive-definite matrix

Q_i : external forces of Lagrange's equations of motion

q : state vector

q_e : equilibrium state vector

q_1 : generalized coordinate vector for the flexible one-beam structure

q_1, q_2 : generalized coordinate vectors for the flexible two-beam structure

R : symmetric positive-definite matrix

R_a : armature resistance

R_N : weighting matrix of Lyapunov-based control input

r : transmission pulley radius

S : skew-symmetric matrix

$S\{\gamma_c\}$: a family of smooth curves on a surface

$s\theta_i$: $\sin(\theta_i)$

T : kinetic energy of the system

t : time

V : potential energy of the system

V(q,t) : scalar positive-definite function of state vector and time

V(q) : scalar positive-definite function of state vector

x, y : fixed inertial coordinates

x_a, x_b : positions of strain gages along a flexible beam

x_1, y_1 : moving relative coordinates for the first flexible beam

x_2, y_2 : moving relative coordinates for the flexible fore-beam

y : translational displacement of the trolley

y_1, y_2 : bending deflection in the horizontal plane

α, β : nondecreasing scalar functions

$\psi_1(x_1)$: mode shapes diagonal matrix for discretization of bending deflection of the flexible beams

ψ_1, ψ_2 : mode shapes diagonal matrices for the articulated manipulator

κ_{ij} : elements of the stiffness matrix K

ω_i : frequencies associated with shape functions ω_i

ρ : mass density (per unit length) of flexible beams

τ : continuous scalar function

θ : angular displacement of inverted pendulum

θ_1 : root angle and output motor shaft angle for the first flexible beam

θ_2 : root angle and output motor shaft angle for the second beam

θ_m : motor shaft angular position

σ : scalar number

τ_a : available torque from the motor shaft

τ_i : control forces of the dynamic equations of motion

τ_m : motor torque

ξ : state variables vector for second-order dynamic equations

$\times$	: vector cross product
$\frac{d(\ )}{dt}$	: differentiation of a variable with respect to time
$\dot{(\ )}$	: $\frac{d(\ )}{dt}$
$(\ )^T$	: transpose of the matrix
$\|\bullet\|$	: norm
$(\ )_{,xx)}$	: $\frac{\partial^2(\ )}{\partial x^2}$
$\frac{\partial(\ )}{\partial t}$	: partial derivative with respect to time
∞	: infinite
$(\ )^{-1}$	: matrix inversion

ABSTRACT

CONTROL AND MECHANISM INTERACTION FOR GROUND-BASED TESTING OF SPACE STRUCTURES

Li-Farn Yang

Old Dominion University, 1990

Director: Dr. Meng-Sang Chew

Co-director: Dr. Jen-Kuang Huang

Rapid maneuvering and ground-based testing of large flexible space structures can be improved by using ingenious mechanisms. An integrated analysis is thus conducted to establish a link between the control and the mechanism to achieve the same desired structural performance. In the ground-based validation testing, the adverse effect of terrestrial conditions such as a gravitational force interferes with the dynamic behavior of space structures. A suspension system is developed to assess the structural characteristics in a simulated zero-gravity environment. Using a mechanisms approach, the synthesis of a noncircular disk with a torsional spring at its rotational axis is designed to counteract the gravitational force of test structures during the testing. A discrete and a continuous parameter models of test articles are employed for suspension simulations.

The multibody dynamics of a flexible steel beam carried on a rigid trolley has been investigated. The system is constructed in such a way that the rapid and large-angle slewing maneuver is performed by means of hybrid rotational/translational motions. The intention is to develop a new maneuvering

testing which extends the work space of the space structure through a translational trolley. The strategy of the control is to use a terminal position control that simultaneously suppresses structural vibration. The comparable simulations are used to verify the experimental performances.

The inclination of noncircular gears to the joints of the space structures necessitates an integrated approach to the investigation of control synthesis and mechanisms design in the slewing maneuvers of flexible space structures. A flexible one-beam structure and a flexible two-beam structure with such noncircular gears will be investigated. Such a noncircular-gear device consists of two specially shaped cams, which are wrapped in a proper mesh by two pairs of thin metal bands. The rolling contact between two noncircular gears is always ensured during relative rotation without friction, slipping, lag or backlash. The varying gear ratio of noncircular gears is specified to produce varying output speeds so as to tune the rapid slewing maneuver while suppressing structural vibration. One optimization technique based on the Generalized Reduced Gradient Method is employed to determine the optimal design of the controllers as well as the noncircular gears for vibrational suppression during the rapid slewing maneuvers. The numerical simulations are implemented to evaluate the effectiveness of the integrated design of control and mechanism for the slewing maneuvers of flexible space structures.

In the slewing maneuver of flexible space structures an increasing need for nonlinear controllers for the compensation of kinematic nonlinearities has been observed. Based on Lyapunov's stability criterion, the stability analysis of space structures leads to the design of a Lyapunov-based controller that yields a stable closed-loop system. Such a controller is developed by combining a linear part and a nonlinear part for the rotational/translational maneuver. The simulations of three kinds of nonlinear dynamic systems are performed to verify the usefulness of Lyapunov-based nonlinear feedback control. Two types of beam-like flexible space structures, i.e. the flexible one-beam structure on a trolley and the

flexible articulated two-beam structure on a trolley, are simulated to implement maneuvering tasks of position control while suppressing the structural vibration simultaneously. An inverted pendulum is stabilized through its Lyapunov-based nonlinear controller to confirm the feasibility of such a nonlinear controller for unstable systems.

Chapter 1

INTRODUCTION

§ 1.1 General

Satellites have successfully been placed and deployed into the earth's orbit for over three decades. Existing satellites have ranged in size from only a few inches, such as the Explorer, to over 100 feet, like Space Shuttle Orbiter and Probes. Without any loss of generality, they could be treated dynamically as rigid bodies during their mission operations. However, interest in orbiting very large space structures has established a need to maneuver and control flexible structures. This need creates a demand for the state of the art dynamic analysis and experimental verification of large flexible space structures in a zero-gravity environment. Several large flexible space structures that have been under investigation include the Mobile Satellite, the Large Deployable Reflector, the permanent Freedom Space Station and SDI weapon systems. These flexible space structures provide the basis for current investigation into the weightless environment of orbital flight as well as various forms of preflight testing and analysis.

§ 1.2 A space structure suspension system

Dynamics and control of flexible space structures have been a subject of intense activity at NASA. For validation, much of the simulations have to be continuously verified using ground-based testing. In general, the performance of missions for the flexible space structures relies mainly on their accurate ground-based validation testing. Hence, a zero-gravity environment must be prepared on ground

for the dynamic testing of low-frequency flexible space structures. Several suspension devices [1-7] have been utilized to satisfy such a demand towards the accomplishment of the ground-based testing for decades. Figure 1.1 shows a novel suspension system [71] which is designed from a mechanisms perspective to simulate the weightless environment. The development of this invention is based first on the study of static equilibrium for the test structures. Then, an analytical method is derived to determine a disk profile which plays a crucial role in this suspension system. Using the envelope theory [8], in conjunction with the kinematic inversion technique, the polar coordinates of such a disk profile can then be determined. Such a suspension device will be applied to ground-based testing of a lumped-parameter model and a flexible beam under initial displacement and initial impulse conditions.

§ 1.3 Slewing maneuvers of flexible space structures

In the investigation of slewing maneuvers of flexible space structures, these structures may be modeled as a multi-body dynamic system which is composed of a rigid member connected to a flexible or compliant member. The coupled interaction between the rigid and the flexible members in conjunction with the dynamic nonlinearities causes immense difficulties in vibrational control during rapid maneuvers or large motions. Since the dynamics of the space structures is characterized by their huge size and flexibility, the resulting vibrations of the flexible member is likely to influence the system dynamic behavior and therefore degrades the effectiveness of the feedback control. Therefore, the control performance of flexible structures must be improved to some extent to counteract the effects of flexibility. An experimental setup [72,73] (see Fig. 1.2) consisting of a flexible steel beam carried on a translational trolley is developed to carry out the position control mission. Flexibility feedback from the strain gages can be applied to both the beam motor and the trolley motor. The beam slewing maneuver with the translational motion of trolley is then performed through numerical

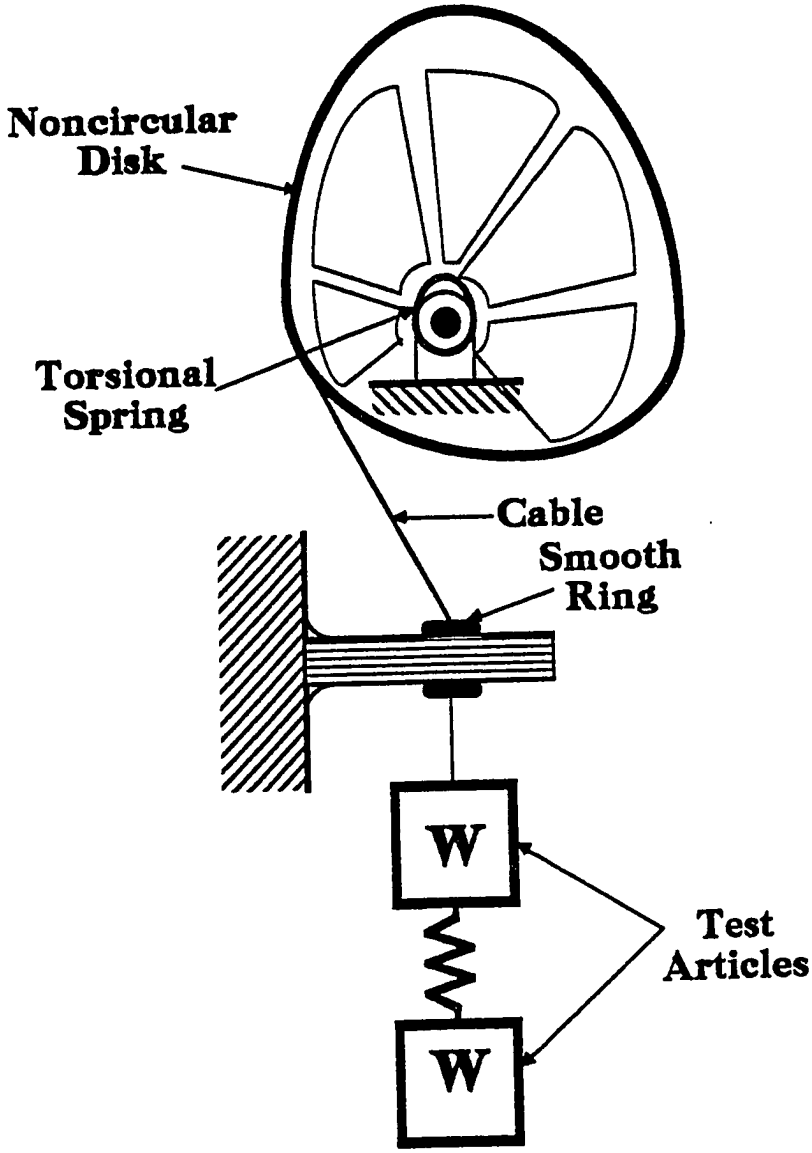

Figure 1.1: Disk suspension system

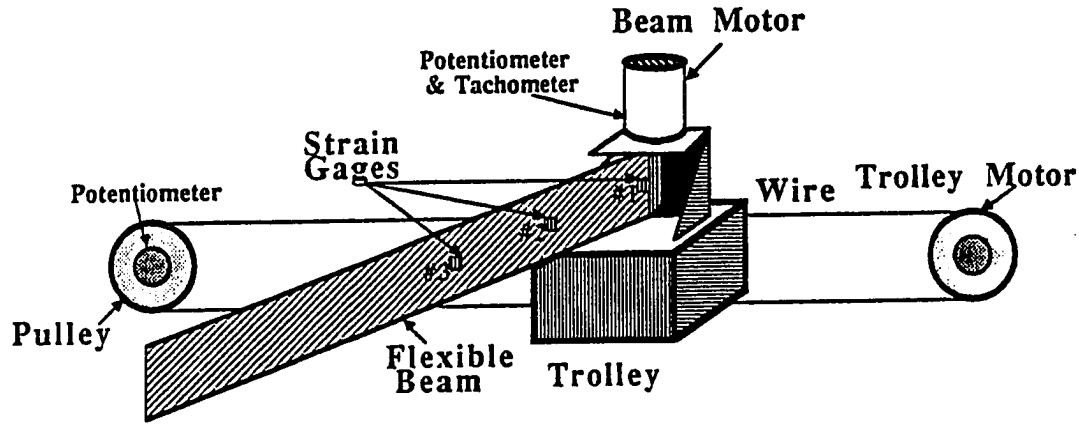

Figure 1.2: One flexible steel beam on a trolley

simulation as well as experimental setup according to the strain-gage feedback control. The simulation and experimental results demonstrate the effectiveness of the strain-gage feedback for suppressing flexural vibrations of the beam.

§ 1.4 Non-circular gearing for vibrational suppression

A noncircular gear system (see Fig. 1.3) consisting of two convex cylinder-type cams is investigated to modify the slewing characteristics of the large flexible space structures. The two specially shaped gears that are implemented as convex cams in Fig. 1.3 are properly meshed and well balanced through the use of two pairs of thin metal bands, that wrap the two noncircular cams in opposite directions, and are then tightly clamped by two holders at the two ends. In a rotation of one beam relative to another, such noncircular gears rolling on each other would minimize friction, slipping, lag and jam. The noncircular cams, synthesized through the use of appropriate hyperbolic gear ratio, are installed in the junctions of motors and structures in two kinds of flexible space structures. The hyperbolic gear ratio, specified as a two-parameter function of output angle, produces varying and cyclical output speeds to transfer the initial rapid slewing characteristic, thereby suppressing structural vibration. Two 90-degree slewing tasks of a single-beam flexible structure and a double-beam flexible structure are implemented by using output feedback controllers in conjunction with these noncircular gears at their rotational joints. Optimal designs of the noncircular gears associated with the gear ratio are also conducted to improve the suppression of the vibrational motion during rapid slewing maneuvers. For the design optimization of noncircular gear ratio, the Generalized Reduced Gradient Method (GRG) [9-12], which is derived from a finite difference approach, utilizes the line search technique to minimize a quadratic cost function. This cost function has been specified as the sum of the square of the vibrational-mode magnitudes. Furthermore, the output feedback gains of both flexible beam-like structures can be included into the optimization of the noncircular gear designs within the same cost function. In this way, an

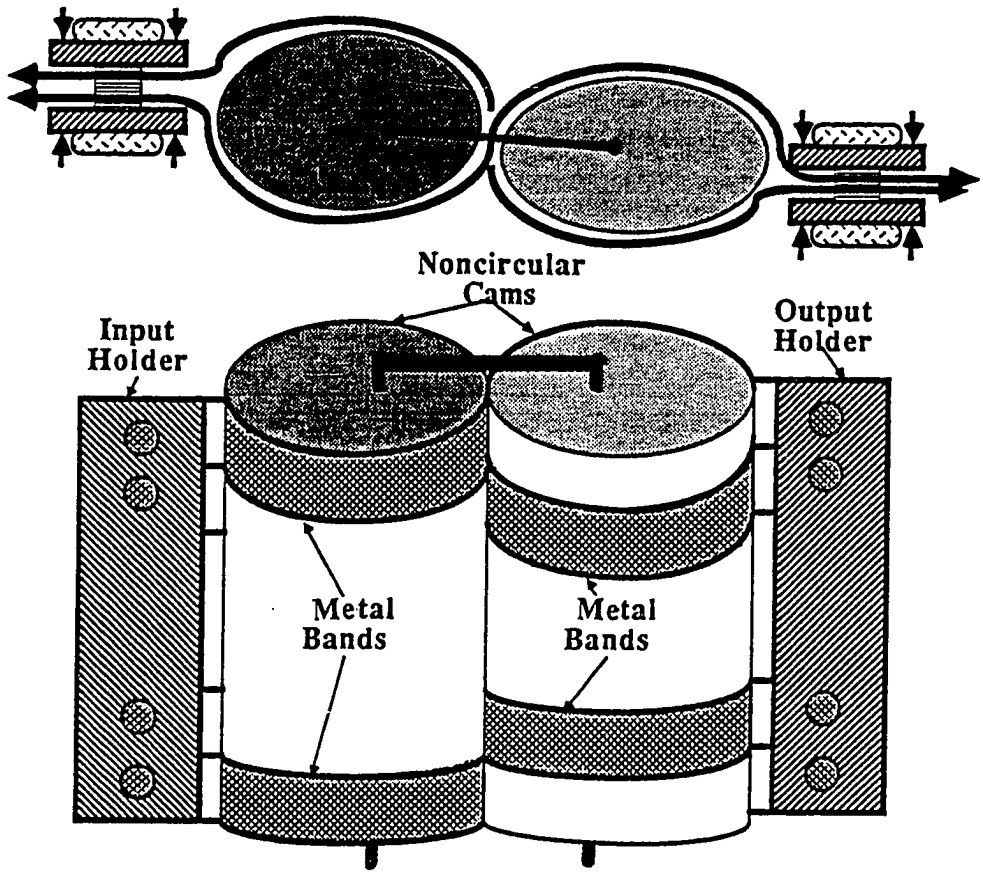

Figure 1.3: A pair of noncircular gears wrapped via the thin bands

integrated approach to controller design and mechanism design is realized using an optimization technique. Improvements in maneuvering performances with less vibration are achieved for rapid and large-scale slewing maneuvers.

§ 1.5 Lyapunov feedback controller

From the results of the rotational/translational maneuvering experiments of a flexible steel beam, the significant kinematic nonlinearities are encountered during the rapid and large angle slewing of the beam, thereby complicating the controller design. Under such rapid and complicated maneuvers of the flexible beam, the requirement for a nonlinear controller to provide for the good control performance of the space flexible structures is essential. An approach based on a Lyapunov stability criterion is developed for a feedback controller to provide a stable closed-loop system [74,75]. This Lyapunov-based design strategy consists of two parts. A feedback control law is first generated for the linear portion of the system equation by using linear control theory. Then, a feedback controller is designed for the nonlinear portion of the system equation by making the time derivative of a positive definite Lyapunov function, to be negative. The combination of these two parts thus provides a stable feedback control design for nonlinear systems in a Lyapunov sense.

Therefore, in this dissertation four mutually related topics are included to deal with the control analysis and testing of flexible space structures. They are

(1) **A space structure suspension system**
(2) **Maneuvering experiments and simulations of flexible structures**
(3) **Noncircular gear design for vibrational reduction in flexible structures**
(4) **Lyapunov-based nonlinear controller designs for flexible space structures**

In topic (1), the design of a suspension system is developed and the suspension simulations are performed to verify its feasibility. In topic (2), the investigation is conducted to implement the numerical simulations and control experiments for the rapid maneuver of a multi-body structure. In topic (3), the slewing maneuvers of a flexible one-beam structure and a flexible articulated two-beam structure are simulated to verify the integrated design of noncircular gears and feedback gain. In topic (4), the analytical derivations of Lyapunov-based nonlinear controls are applied to three different dynamic systems to perform the nonlinear control simulations.

Chapter 2

OBJECTIVES

§ 2.1 Objective, motivation and scope of a space structure suspension system

The objective of this suspension system (see Fig. 1.1) is to simulate the space environment and suspend low-frequency structures for ground-based validation testing. Flexible space structures, in general, experience free-free boundary conditions that are not readily replicable on the ground. Yet, to conduct the testing of such space structures, special devices must be introduced to support the weight of the structure without introducing any constraint forces which in turn impose boundary conditions that do not simulate the desired free-free boundary conditions in space. Several existing approaches and devices [1-7] have been used or proposed for suspending space structures for dynamic testing. Some of these are illustrated below:

(1) **Long Cables** :

The structure is suspended from a high ceiling through several long cables. Testing of the dynamic of the structure is conducted on the horizontal plane so as to reduce the gravitation contribution on the dynamic of the structure. The overhead suspension system of Langley Lunar Landing Research Facility is a typical long-cables system to support five-sixths of the weight of the Apollo Lunar Lander Training Module.

(2) **Air Pads** :

Various designs based on the principle of reducing or eliminating friction on the horizontal plane have been proposed. The most common is the use of air pads that act as hydrostatic air bearings on which the structure is suspended. Again, in such a design, the dynamic testing of the structure is conducted on a horizontal plane.

(3) **Pneumatic/Electric Device** :

An external air tank under pressure drives a piston which is suspended on the test structure. Since the pneumatic system incurs a positive spring stiffness, a linear DC motor is incorporated to introduce a negative spring stiffness to the pneumatic system so that from the perspective of the test article, the system has very low stiffness. However, such an approach necessitates a very complex control system to insure the proper operation of the suspension device. This device has been developed under the NASA/LaRC Pathfinder Dynamic Scale Technology Program [2].

(4) **Springs** :

Different combinations of springs in different configurations have been proposed to introduce a near- zero stiffness of the suspension system. However, all such configurations always result in a very small domain of operation (stroke) under which the test structure could move and yet see no constraining force.

In Chapter 3, a novel band mechanism [71] (see Fig. 1.1) is designed to provide a simulated zero-gravity environment [3] for ground-based dynamic testing of the space structures. The dynamic interaction between this system and the test article

forms the basis of investigation that is reported in Chapter 3. The system features a noncircular disk, around which a cable winds and unwinds as the disk rotates. The envelope theory and kinematic inversion [8] are employed to derive coordinate equations of disk profile. This disk has a special profile designed in conjunction with the load it is to suspend, as well as the spring stiffness of the torsional spring. The torsional spring loads the disk as the latter rotates so that the torque exerted by the spring about the disk axis of rotation is exactly counterbalanced by the force exerted by the weight of the test article on the cable that winds around the disk. In this way, the suspension system is capable of keeping the test structure in static equilibrium at any vertical location so that, on a static basis, the weightless effect of a test structure in space can be simulated on earth through this suspension system. The cable which connects the disk and test structure is always in tension during dynamic testing. The noncircular disk within the suspension system can be configured to remain unchanged for test articles with the different weights as long as the torsional spring is replaced to maintain the originally designed frequency ratio of $\frac{W}{k_s}$. A constraint on the system is that the profile of the disk must be convex to allow the cable to wind around its edge.

The comparsion between the above-mentioned suspension systems illustrates the advantages of this noncircular disk suspension system over the four prior approaches. The experimental performances of the prior four suspension systems have revealed some inadequacies in their usage. In the case of long cables, the testing is constrained within the horizontal plane while the gravitational effect of the structure is compensated through several long cables. Thus, the entire suspension system must occupy a large space with tall ceilings. Nevertheless, the test model of this invention may be reducible to an appropriate scale within the work region. In the case of air pads, friction on the horizontal plane may influence the performance of the testing. The inertia of air pads may also change the system dynamics particularly when a large number of air pads are used for the large space structure. Moreover, the planar design of air pads constrains the feasibility

of testing in the vertical direction. In the case of pneumatic/electric device [2], a complicated control system is employed to produce a negative spring stiffness. A piston with an external air tank is a cumbersome way when compared to the single cable in this proposed suspension. Furthermore, the controller design must be involved with a linear DC motor to provide the appropriate feedback for the negative stiffness rate. No matter how accurately the output is measured for feedback, the influence of noise upon the dynamic performance cannot be ignored. In the case of springs, the working domain of operation with zero stiffness rate, is strictly limited so that the test structure can move only within a small stroke.

Two test articles have been selected for the investigation of this disk suspension device. The first test article, which consists of two masses and one linear connecting spring, is suspended from an equilibrium position. Such a lumped-parameter system is thus treated as a simple two-degree-of-freedom discrete system whose flexibility is characterized by the connecting spring. Another test article is a flexible steel beam which is hung at its two ends in equilibrium through two identical band drive suspension mechanisms. Simulation of the suspension system with the test articles originally at rest are carried out with excitations such as an initial displacement and an initial velocity (impulse) on the masses. The characteristics of the flexible space structures are then analyzed in conjunction with this band drive suspension system.

In Chapter 3, the concept of the suspension system is deduced by investigating the static equilibrium of the test structure at two different positions in section 3.1. In section 3.2, the envelope theory, in conjunction with the kinematic inversion technique, is applied to determine the rectangular coordinates of the noncircular disk. The disk profile is developed by tracing the tangent points on a family of string trajectories observed from a viewer fixed at the rotational center. Section 3.3.1 displays dynamic equations for testing space structures which are modeled as the spring-mass elements (lumped-parameter model) hung by this disk suspension

device. Section 3.3.2 is conducted to derive dynamic equations of a testing flexible steel beam hung by two disk suspension systems at its two ends. The simulation results of the lumped-parameter model are shown in section 3.4.1. Section 3.4.2 demonstrates the simulation results of the flexible steel beam. Both simulation results in sections 3.4.1 and 3.4.2 involve the dynamic responses for the excitations of the initial displacement and the initial impulse. Finally, a brief summary is made in section 3.5.

§ 2.2 Objective, motivation and scope of maneuvering experiments and simulations of flexible structures

Research and experiments on the control of large flexible structures have gained much attention in the past decade. For several years, NASA has conducted research in the area of control and structure interaction and reviews of progress have been presented in references [13-21]. Future space manipulators may need translational base motion to expand the access region of a manipulator. The objective of this maneuvering experiment is to present experimental results for the slewing of a flexible structure with coupled rotational and translational axes while simultaneously suppressing vibrational motion during the maneuver. In Chapter 4, a flexible steel beam, carried by a translational trolley, is maneuvered by an active controller to perform position control tasks [72,73]. The experimental setup consists of a rigid translational trolley with one flexible steel beam attached to a motor at the root end. One translational motion and one rotational motion for this system are thus introduced. The difference between this experiment and many others [22] lies in the translational motion which couples with the flexible-body motion in such a nonlinear fashion that the mathematical model is more complicated and the controller design more difficult. However, simple output feedback control methods are applied in this chapter to the position control of the flexible steel beam with translational and rotational motions.

In Chapter 4, the dynamic system of a flexible steel beam carried on a rigid and translational trolley is described in section 4.1. The experimental setup in section 4.2 includes several tables of equipment which have been employed to perform four different cases of rotational/translational maneuvering experiments. An output feedback control loop is constructed by using EAI-2000 Analog Computer as a controller in section 4.3. Four cases of simulation and experimental results are shown in section 4.4 to illustrate the influence of the structural flexibility of the steel beam to the active feedback controller. On the other hand, both simulation and experimental results fairly resemble each other in the four cases so that the validation of such maneuvering experiments can be verified through the analytical simulations developed herein. The discussion concerning system nonlinearity and the damping effect is demonstrated in section 4.5, which forms the motivation for the investigation that will be reported in thenext two chapters.

§ 2.3 Objective, motivation and scope of noncircular gear design for vibrational reduction in flexible structures

The experimental results in Chapter 4 have shown the significant importance of measurement feedback due to strain gages upon the rotational/translational maneuvers of a flexible steel beam on a trolley. Apparently, the suppression of the structural vibration has been enhanced through the active feedback controllers, including the flexibility feedback. It has been noted that rapid and large angle slewing may excite the huge amplitudes of vibrational modes during control process. Herein, a noncircular gear mechanism will be investigated to tune the kinematic characteristics of the slewing maneuvers so that the structural vibration can be suppressed more effectively than through the conventional feedback control approach. To further suppress these vibrations, an integrated application of control feedback and noncircular gears is introduced in conjunction with an optimization technique to simultaneously determine the optimal noncircular gear profiles as well as the output feedback gains.

This particular choice for noncircular gears over the linkages, cams and band mechanisms, is primarily due to the compactness in size, well-balanced construction and high- speed operation. The profiles of the noncircular gears have been seen in many special shapes, such as logarithmic spiral gears, elliptical gears and square gears [23-27]. These specially shaped gears can always be constructed as long as their center distance remains constant during the rotation. Reference [24] demonstrates several industrial applications of noncircular gears such as the variable frequency oscillator for space vehicles, quick-return drives, intermittent mechanisms, automated-feed machines, etc. This study also validates the feasibility of several noncircular gears which are designed to roll with special racks. Moreover, an eccentric circular gear can be shown to be in proper mesh with four different kinds of mating gears, including elliptical-shaped gears, as well as an internal gear. Reference [24] displays several combinations of basic and high-order elliptical gears which can produce several speed cycles per revolution. More detailed analysis of elliptical gears has been implemented by S. Rappaport [28] to provide cyclic output speed variations. A cigaret machine is shown to demonstrate the usefulness of elliptical gears in that same article. A single pair of twin eccentric gears have been investigated by S.V Miano [29] to meet the prescribed variable output speeds. This paper provides the analytical derivation to evaluate the nonlinearities, i.e. backlash, lag, jam and critical contact ratio, due to the eccentricity. Based on the design equations shown in reference [24], the parameters of twin eccentric gears must be carefully specified to avoid much of such difficulties.

Figure 1.3 illustrates a pair of noncircular gears composed of two convex cylinder-type cams which are wrapped by using two pairs of thin metal bands to maintain a proper mesh. Rolling contact is always guaranteed in the rotation of the noncircular gears in addition to reduced friction levels, slipping, lag, jam, and backlash. Two such noncircular cams, running on a collinear center-to-center line, will produce the varying and cyclical output speeds needed to tune the rapid

slewing of the beam in a way that will suppress vibrations. Their gear ratio, which is determined by equating the reverse pitch radii of input/output gears, has initially been specified as a hyperbolic function of the slewing angle. Instead of using an established pitch profile for the gears or cams, the two pitch profiles of the noncircular gears will be synthesized by employing some mechanism synthesis techniques. The noncircular gears are installed with an idler gear box in junction with an actuator and a flexible beam. A simulation of the 90-degree slewing maneuvers of two kinds of flexible space structures, i.e. a flexible one-beam structure and a flexible articulated two-beam structure, will be conducted with the noncircular gears present at the joints of the articulated structures. The regulator-type output feedback control gains are first solved using optimal control theory as a means for understanding the dynamic characteristics of this highly nonlinear system. Subsequently, an optimization technique based on Generalized Reduced Gradient Method [9-12] is then employed to determine the optimal parameters of such noncircular gears as well as the feedback gains so as to minimize the vibrational amplitudes present in the flexible beams. This integration of the design of the control and mechanism parameters represents a powerful and systematic approach to the design for rapid slewing maneuvers of flexible space structures.

In Chapter 5, the general concept of noncircular gears is addressed to illustrate their widespread applications in section 5.1. In section 5.2, three common design equations based on the given gearing relationships [24] offer three different approaches to obtain pitch curves of noncircular gears. The formulation in case 1 will be the approach employed for designing the desired noncircular gears. In section 5.3, the desired noncircular gears for slewing maneuvers of space structures are characterized by having an appropriate hyperbolic gear ratio which is specified as a function of the slewing angle. The construction of such noncircular gears is also illustrated. The advantages of this new device over the conventional ones [23-29] are also discussed. Some simulation results illustrate the output characteristics of these noncircular gears. In section 5.4, the actuator dynamics which

generates the available torque due to the applied voltage, is developed. Instead of a conventional actuator, this actuator with the desired noncircular gears introduces varying gear ratios and varying torque outputs. The dynamic equations of a flexible one-beam structure and a flexible articulated two-beam structure in the presence of actuator dynamics are derived using Lagrange's functions. These are shown in Appendix B in sections 5.5.1 and 5.5.2. Section 5.6 discusses the numerical simulations that verify the feasibility of noncircular gears for two kinds of slewing maneuvers of flexible structures. To further suppress structural vibration of the beams, a Generalized Reduced Gradient Method is employed in section 5.6 to determine the optimal designs of noncircular gears. Simulations in section 5.7 demonstrate the lower vibrational amplitudes for the previous two kinds of slewing maneuvers while the optimal designs of noncircular gears are applied. As an even further step, the integrated optimization of both control feedback gains and mechanism parameters are performed in section 5.8. Both feedback gains and parameters of noncircular gears are optimized in this section to minimize vibrational amplitudes at the beam. In section 5.9, the simulations associated with the integrated optimal design of control and mechanism are implemented. Finally, the discussion of this chapter is concluded in section 5.10.

§ 2.4 Objective, motivation and scope of Lyapunov-based nonlinear controller design for flexible space structures

In the area of control of flexible structures, there are many existing methods available today for designing feedback controllers for the nonlinear systems [30-51]. For example, the feedback linearization method is developed in reference [35], and modified and extended in references [37] and [38] for active control of flexible structures. This method is applied in reference [38] to actively control an articulated flexible manipulator carried on a translational cart. The nonlinear dynamic equations for the manipulator are derived. The time-variant inertia matrix is linearized without approximation by using the feedback linearization approach.

Linear feedback control theory is then employed to design a controller to move the manipulator in an attainable workspace while suppressing the bending vibration of the flexible arms simultaneously.

On the other hand, the Lyapunov stability criterion is often used for the development of nonlinear control methods. For example, the deployment and retrieval of a subsatellite is studied in Ref. [47] using a mission function (Lyapunov function). The required mission function must be selected corresponding to system nonlinearity. With the special mission function, a freely assignable part of control is adjusted to make the time derivative of the mission function negative during the control process. This would ensure the system stability in the Lyapunov sense.

In Chapter 6, a Lyapunov-based control system [74,75] for rapid large angle maneuvers of a flexible-link structure is proposed in a way different from the mission function control. Basically, the equations of motion for a typical kinematically nonlinear system consist of two parts, namely, the linear or linearized part and the nonlinear part. The linear control law can easily be designed for the linear part. Feedback control obtained for the linear part may actually satisfy the stability criteria for the original nonlinear dynamic equation as long as the nonlinear part is insignificant. However, for rapid large angle maneuvers in which the system nonlinearity becomes significant, there is no guarantee for system stability through the use of the linear control law. In such cases, an additional feedback control input is required to compensate for any nonlinear dynamic behavior. Consequently, the Lyapunov-based control law derived herein consists of a linear control and a nonlinear control to provide a stable closed-loop control design for nonlinear systems. The nonlinear control of Lyapunov-based control law is based on the sufficient requirements of the Lyapunov's second method for system asymptotical stability [52-64]. To generate a standard performance index of system energy, a quadratic form of Lyapunov function is chosen with a weighting matrix derived from the Riccati equation associated with the optimal control

design for the linearized system equation. The nonlinear control law based on the weighting matrix is thus derived making the time derivative of the Lyapunov function negative. The nonlinear control law thus derived is directly related to the states and the nonlinear portion of the system dynamic equation. The entire closed-loop feedback control is accomplished by combining the nonlinear control with the linear control law.

Several types of stability are discussed in section 6.1. The concept of asymptotical stability is employed herein to find the Lyapunov-based nonlinear control design. The general derivation of Lyapunov-based nonlinear control design is demonstrated in section 6.2. Three nonlinear dynamic models, namely a flexible one-arm structure, a flexible two-arm structure [38] and an inverted rigid pendulum, are selected to illustrate the Lyapunov-based design concept. In section 6.3, these three kinds of dynamic equations are derived based on the information as shown in appendices B, C and E. Numerical simulations are given in sections 6.3.1-6.3.3 for comparing the system responses with and without the nonlinear control law.

Chapter 3

A SPACE STRUCTURE SUSPENSION SYSTEM

The suspension system is a practical research tool for assessing characteristics of flexible space structures proposed for operation in zero-gravity environments. The ground-based validation testing of the flexible space structures has been implemented for decades by using the existing suspension devices, such as long cable, air pads, pneumatic/electric device, spings, etc. Instead of the conventional approaches to the design existing suspension devices, a mechanisms approach is employed to construct a novel suspension. The dynamics of low-frequency space structures can thus be tested in simulated weightless surroundings which are provided by this suspension device. This novel suspension system is characterized by a noncircular disk as shown in Fig. 1.1. This disk has a special profile designed in conjunction with a frequency ratio of $\frac{W}{k_s}$, which indicates the suspended load over the spring stiffness of the torsional spring. This torsional spring loads the disk as the latter rotates so that the torque exerted by the spring about the disk axis of rotation is exactly counterbalanced by the force exerted by the weight of the test article on the cable that winds around the disk. In such a way, this suspension system, associated with a specially profiled disk, is capable of keeping the test structure in static equilibrium at any vertical location. Based on the equilibrium at any vertical position, a special profile of the noncircular disk is synthesized by using the envelope theory in conjunction with the kinematic inversion technique [8]. The profile of the disk must be convex so as to allow the cable winding and unwinding around its edge. The concept of this novel suspension system indicates that the weightless phenomenon in space can be simulated for the structural

testing on earth. The state of the art design of this suspension system allows no change of the disk profile for the test articles with different weights. Two test articles are selected for the suspension simulations, including a lumped- parameter model and a flexible steel beam, in conjunction with the suspension system. The first test article is composed of two masses connected by one connecting spring so that it can be treated as a simple two-degree-of-freedom discrete system whose flexibility is characterized by a connecting spring. Another test article is a flexible steel beam which is hung at its two ends through two identical suspension systems. The simulations of the ground-based dynamic testing are performed by providing the test articles, originally at rest, with the proper excitations, such as the initial displacement and the initial velocity (impulse). The characteristics of the flexible space structures are thus investigated by using this band drive suspension system.

§ 3.1 Concept of the band drive suspension system

The problem of simulating space environments on earth inspires the development of many suspension systems that can counteract the gravitational effect on test structures in the vertical direction. The attention of this investigation is focused primarily on the vertical direction of the suspension problem. The weightless effect during the ground-based testing of structures provides the concept of a mechanical device to act as a suspension system. This concept has been designed to produce a torque in a torsional spring at any instant considered to counteract the loading torque due to the weight of the test structure moving in the gravitational direction. The loading torque is generated by multiplying the weight of the test structure and a moment arm about the rotational axis of the noncircular disk. The torsional spring, which is located at the rotational axis of the noncircular disk, is preloaded according to the initial position of the test article. In this way, the weight of the test structure is thus counterbalanced during the entire period of the ground-based dynamic testing.

To begin, in the design of the suspension device, the statics of a suspension

system must be analyzed to determine the force equilibrium of the ground-based test article at any vertical location. Figures 3.1(a) and (b) show two arbitrary positions of a test article in static equilibrium suspended under this suspension device. The consequential two locations shown in Fig. 3.1(a) and (b) are displaced by a distance ℓ_1. The suspension device consists of:

(1) **a noncircular and specially profiled disk (D),**

(2) **a torsional spring (S),**

(3) **a thin cable (C),**

(4) **a smooth ring (R),**

(5) **a test article (W).**

Assume that a test article is originally suspended and kept in static equilibrium at the position shown in Fig. 3.1(a) with the thin cable C wrapped around the edge of the noncircular disk D. This cable passes through the smooth ring R, and extends downward to suspend the test article W. This smooth ring R may be assumed frictionless. To prevent the cable from driving the disk D and hence unwinding, a torsional spring S is attached to the axis of rotation of the disk D such that the torque exerted on the disk D, due to the load imposed by the test article W, is balanced by the torque T_{s1} in the torsional spring S, i.e.,

$$Wr_1 = T_{s1} \tag{3.1}$$

where r_1 is the moment arm which is the perpendicular distance from the disk rotational center to the cable. Assume that θ_1 denotes the corresponding rotation of the noncircular disk D and k_s, the torsional spring stiffness in Fig. 3.1 (a). Then the equilibrium equation of Eq. (3.1) can be further written as

$$k_s(\theta_{s0} + \theta_1) = Wr_1 \tag{3.2}$$

where θ_{s0} is the angle of preload in the torsional spring S. Note that this equation provides an explicit relationship between the angle of rotation θ_1, of noncircular disk D, and the moment arm r_1. Suppose the test article W is displaced downward

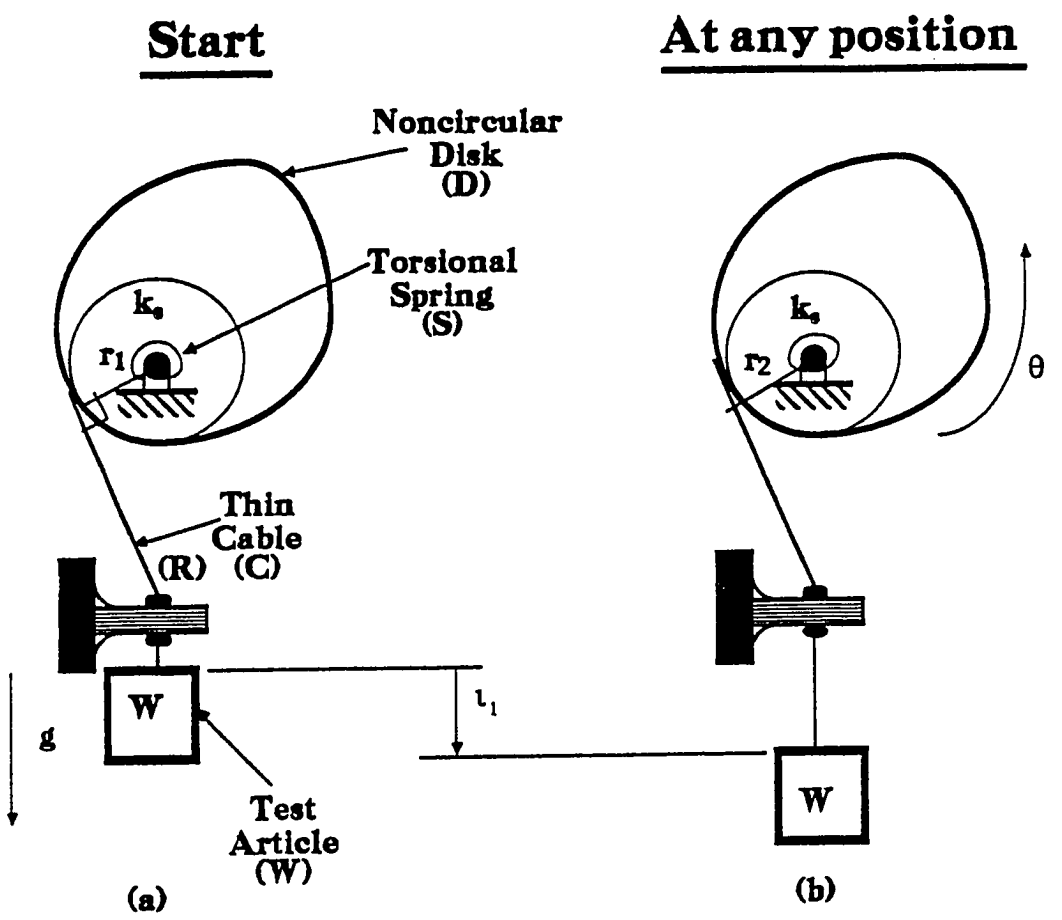

Figure 3.1: Static equilibrium of a test article at two different positions under disk suspension system

a distance of ℓ_1 from its original equilibrium position, as shown in Fig. 3.1(a). To enable the test article W to remain in equilibrium at this new position, illustrated in Fig. 3.1(b), the moment arm r_2 subtended at the axis of rotation of the disk D has to be larger than r_1. This is because to balance the increased torsional spring torque, while the cable is at the same tension W, an increase in the moment arm on the noncircular disk is needed, so that:

$$Wr_2 = T_{s2} \tag{3.3}$$

In this new equilibrium position:

$$k_s(\theta_{s0} + \theta_2) = Wr_2 \tag{3.4}$$

where θ_{s2} is new rotational displacement of disk D, as illustrated in Fig. 3.1(b). Note that the moment arms r_1, r_2 are not the radial distances to the points of tangency of the cable at the disk profile, but are the perpendicular distances from the disk rotational axis to the cable. Since the moment arm r_2 is different from r_1, it is then possible to determine the profile of the noncircular disk D such that a continuous change in the moment arm is obtained for any given position of the test article W, in such a way that when displaced from one position of static equilibrium to other position, the test article will remain in static equilibrium in its new position. That causes a weightless situation which simulates that in a space environment. This device will also simulate the behavior of the test article subjected to an impulse. The body will accordingly translate at a constant velocity. This is what is observed in the test article W. When the latter is imposed with an initial velocity v_0, such as a short-period impulse, the test article will continue to travel at that same velocity v_0 over a considerable range of travel. This is because the tension in the cable is constant and is exactly equal to the weight of the test article, so that there is no net driving force on the article during its entire range of motion. With that observation, it therefore leads to a constant velocity of the test article and in so doing, exactly simulates the motion of an object in

space. Likewise, the impulse response of a flexible structure is performed in this suspension device. The entire test structure will travel at a constant velocity as a rigid-body motion, while the traveling beam is oscilating due to its flexible modes within the moving coordinates.

The static characteristic of the suspension system is thus governed by equations (3.1)-(3.4). Compared with prior suspension systems discussed in the section 2.1, where complicated electrical devices or the huge facilities are needed, this band drive suspension system is a rather simple mechanical system. Obviously, the noncircular disk plays a very crucial role in such a suspension system. The profile coordinates of the noncircular disk will be derived by using envelope theory [8] in conjunction with the equilibrium equations given by Eqs. (3.1)-(3.4). This will be the subject of discussion in the following section.

§ 3.2 Design of the disk profile

The envelope theory will be applied to generate the coordinates of the disk profile given in Fig. 3.2. Using kinematic inversion, an observer fixed to the disk would view the sequential positions of the cable, which tracks a sequence of straight trajectories $\overline{P_0T_0}$, $\overline{P_1T_1}$, $\overline{P_2T_2}, \cdots, \overline{P_nT_n}$ as shown in Fig. 3.2, as the disk rotates. The swinging point $P_i\ (i = 1, 2, \cdots, n)$ is observed to lie on a circular path with a radius r_a, which is the distance from the rotational center O to the ring R. These straight trajectories, together when taken infinitesimally apart, give the envelope which forms the disk profile. In Fig. 3.1, the normal distance from the rotational center of the disk to the cable provides the moment arms of r_1 and r_2 in equations (3.1)-(3.4), such that the loading torques of T_{s1} and T_{s2} are counteracted to maintain the equilibrium of the test article no matter where the test article is located. Instead of the circular disk, the contact point where the cable is tangent to the noncircular disk does not have to coincide with the end point of moment arm except for the starting point P_0 in Fig. 3.2. Since the

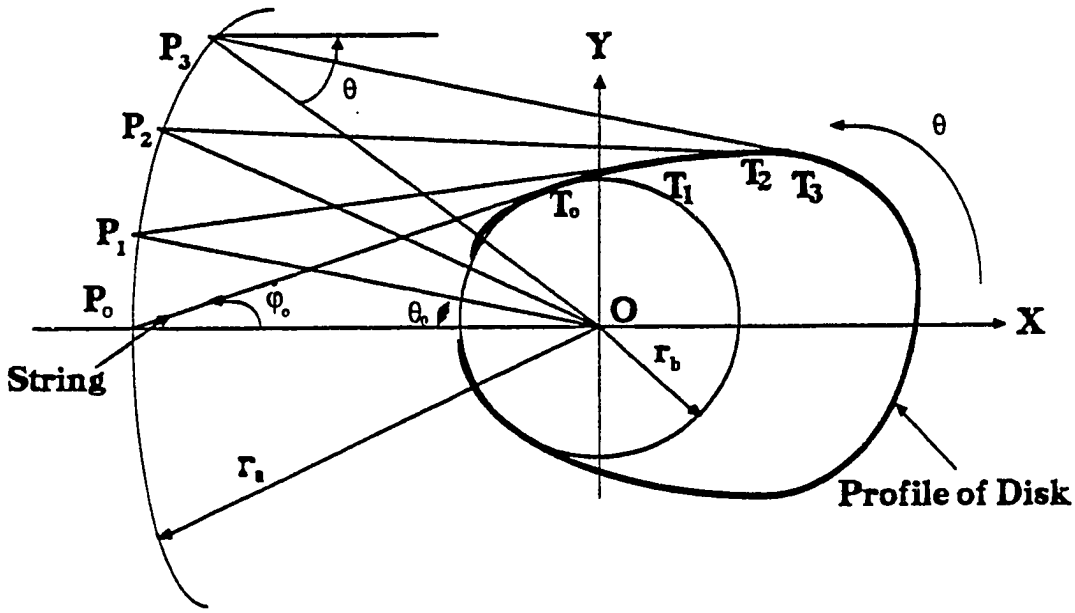

Figure 3.2: Development of noncircular disk profile

change of the disk angle in Eqs. (3.2) and (3.4) is continuous, the circumference of the disk must be continuously smooth. Due to the increasing moment arm of $r_2 > r_1$ in section 3.1, the disk will be inclined toward a convex profile which meets the convexity for the thin cable C in Fig. 3.1 winding around the noncircular disk.

The process to determine the disk profile coordinates is demonstrated in Fig. 3.2. A family $S\{\nu_c\}$ (see Appendix A) in the envelope theory is composed of the trajectories of a swinging straight string. And the corresponding envelope ν is associated with the desired disk profile. To derive equations for disk profile coordinates, the relative geometry of the disk and the swinging string must be described at both the lowest string position and at some displaced string position consistent with the rotational direction of the disk. A base circle is specified and located at a center O with a radius r_b. The point O indicates the rotational center of the noncircular disk. In fact, the radius r_b indicates the initial moment arm of the test article at the starting position, which means that the tangent point of the cable coincides with the vertex of the moment arm. The kinematic inversion method is applied to assume an observer fixed with the disk at its center. From the observer, the centric swinging string tracks the envelope of a family of sequential straight trajectories $\overline{P_0T_0}$, $\overline{P_1T_1}$, $\overline{P_2T_2}, \cdots,$ $\overline{P_nT_n}$ while the disk rotates. The swinging point P_i $(i = 1, 2, \cdots, n)$ is observed to lie on a circular path with a radius of r_a, which indicates the distance between the rotational center O and the ring R. The points T_i $(i = 1, 2, \cdots, n)$, at which the string is tangent to the disk, track the envelope of a family of swinging strings $\overline{P_iT_i}$. Assuming that the initial swinging point P_0 is tangent to both the base circle O and the disk profile, the angle ϕ_0, which denotes the starting rotational position of the string, is given by:

$$\phi_0 = \sin^{-1}\left(\frac{r_b}{r_a}\right) \tag{3.5}$$

Suppose that the string is viewed by the observer at center O, while the disk rotates through an angle θ. Then the thin cable will subtend an angle of $\phi_0 + \phi$ with the vertical at the ring. The increment angle ϕ is the rotational displacement

of the string trajectory $\overline{PT}$ from its initial orientation. There therefore exists a relationship between disk rotation θ and the string angular displacement ϕ. This relationship will be derived using the equilibrium equations (3.2) and (3.4). From theorem A.1 in Appendix A, a general equation of the family of lines forming the envelope is governed by a straight line which is:

$$y = mx + b \tag{3.6}$$

where the slope of the swinging string at the disk angular position θ is given by

$$m = \tan(\phi + \phi_0 - \theta) \tag{3.7}$$

and y-intercept of the string $\overline{PT}$, based on the Cartesian system in Fig. 3, is

$$b = r_a \cos\theta \, \tan(\phi + \phi_0 - \theta) + r_a \sin\theta \tag{3.8}$$

This general equation of the cable $\overline{PT}$ in Eq. (3.7) gives a one-parameter family of strings as a function of the disk angle of rotation θ. From the theory of envelope, an envelope of the family of the straight lines is governed by an equation:

$$\begin{aligned} F(x,y,\theta) &= y - mx - b \\ &= y - \tan(\phi + \phi_0 - \theta)\,[x + r_a \cos\theta\,] - r_a \sin\theta = 0 \end{aligned} \tag{3.9}$$

Equation (3.9) is continuous and is a continuously differentiable function in the coordinates x and y as well as in the variable θ. Differentiating the equation (3.9) with respect to the disk angle θ provides:

$$\begin{aligned} \frac{\partial F}{\partial \theta} &= \tan\beta \; (r_a \sin\theta\,) - [x + r_a \cos\theta\,] \sec^2\beta \left(\frac{\partial \phi}{\partial \theta} - 1\right) \\ &\quad - r_a \cos\theta = 0 \end{aligned} \tag{3.10}$$

where β equals to $\phi + \phi_0 - \theta$. The rate of $\frac{\partial \phi}{\partial \theta}$ can be determined, while the static equilibrium equations such as Eqs. (3.2) and (3.4) are claimed as the functions of

θ and ϕ. According to [8], the coordinates of disk profile at a given angle θ may be obtained by solving equations (3.9) and (3.10), i.e.:

$$x = -r_a [A \sin\beta + \cos\theta] \tag{3.11}$$

where

$$A = \frac{\cos(\theta+\beta)}{\frac{\partial\phi}{\partial\theta} - 1} \tag{3.12}$$

Substituting Eq. (3.11) into Eq. (3.9) provides

$$y = r_a [-A \sin\beta + \sin\theta] \tag{3.13}$$

The disk profile coordinates are thus obtained by evaluating Eqs. (3.11) and (3.13) in terms of the angular parameters θ and ϕ. Initially, the angles θ and ϕ equal zero so that the starting coordinate of the noncircular disk becomes:

$$x = -2r_a \sin\left(\frac{\phi_0}{2}\right), \tag{3.14}$$

$$y = \frac{\sin 2\phi_0}{2} \tag{3.15}$$

which coincides with the point at which the starting string $\overline{P_0T_0}$ is tangent to the base circle in Fig. 3.

The rate of change as a function of disk rotation $\frac{\partial\phi}{\partial\theta}$ in orientation of the string can be determined by investigating the relationship between the angles θ and ϕ. Based on Eq. (3.2) and illustrated in Fig. 3.1, the equation of the initial equilibrium is governed by:

$$Wr_a \sin\phi_0 = k_s\theta_0 \tag{3.16}$$

For the incremental angles of θ and ϕ, from the initial orientation angles θ_0 and ϕ_0, the new equilibrium state becomes:

$$Wr_a \sin(\phi_0+\phi) = k_s(\theta_0+\theta) \tag{3.17}$$

Subtracting Eq. (3.16) from Eq. (3.17) provides:

$$Wr_a\left[\sin(\phi_0+\phi) - \sin\phi_0\right] = k_s\theta \tag{3.18}$$

which can be rewritten as

$$\phi = \sin^{-1}\left[\frac{k_s\theta}{Wr_a} + \sin\phi_0\right] - \phi_0 \tag{3.19}$$

Differentiating Eq. (3.19) with respect to the angle θ yields

$$\frac{\partial\phi}{\partial\theta} = \frac{k_s}{Wr_a\cos(\phi_0+\phi)} \tag{3.20}$$

Then, the profile of the noncircular disk is determined by substituting ϕ and $\frac{\partial\phi}{\partial\theta}$ in Eqs. (3.19) and (3.20) into the equations for the disk coordinates given by equations (3.11) and (3.13). Note that the profile of the disk must be convex.

Several parameters are needed to generate the profile of the noncircular disk, and they include r_a, r_b, k_s, and W. It can readily be shown that each disk profile can be specified according a parameter which is the ratio of the weight of the test article to the stiffness of the torsional spring, i.e. $\frac{W}{k_s}$. This means that if testing is to be conducted for another test article twice its original, the torsional spring stiffness must be increased by the same factor so that the same disk can again be used. Such a design, therefore, permits tremendous flexibility since different loads can be used on this device, without the need to fabricate a new disk every time a new test article with a different mass is used.

With the disk profile design, the dynamics of the test articles can then be suspended on this band mechanism. The dynamics of these test articles in the presence of a suspension mechanism will be presented in the next section.

§ 3.3 Dynamics of test articles and suspension system

In simulating the test experiments of flexible space structures, the test article may be modeled as a discrete or a continuous system. Two models of test articles will be considered: a lumped-parameter model and a continuous parameter flexible steel beam. In the lumped-parameter model, the test article will be modelled as two masses and a connecting linear spring suspended in equilibrium as shown in Fig. 3.3(b). Such a lumped-parameter system is thus treated as a simple two-degree-of-freedom discrete system whose flexibility is characterized by the connecting spring. In the continuous parameter model, a flexible steel beam is hung at its two ends and is suspended through two identical disk suspension systems, as shown in Fig. 3.4. The profile of the noncircular disk in each case is developed through Eqs. (3.11) and (3.13) to maintain the static equilibrium of the test article at any vertical position. Simulation of the ground-based validation testing will be implemented by providing the test article, originally in equilibrium, with the excitations such as an initial displacement or an initial velocity (impulse). The characteristics of flexible space structures are then analyzed together with the band mechanism suspension system.

§§ 3.3.1 A lumped-parameter model of a test article

The flexible space structures can be discretized into a series of lumped-parameter elements. The first test structure in Fig. 3.3(b) illustrates a discrete lumped-parameter system which approximates a flexible structure through the use of two masses and one connecting spring. Table 3.1 shows the model parameters of such a lumped-parameter system. The band drive suspension system is connected to one of the masses, mass ♯1. Notice that the mass in Eqs. (3.16)-(3.20) stands for the sum of the two masses, so that care is needed while developing the profile of the noncircular disk for this test article. Since this band drive mechanism contains a very nonlinear function within Eqs. (3.11) and (3.13), the total system will be a nonlinear two degree-of-freedom dynamic system, even though the test article

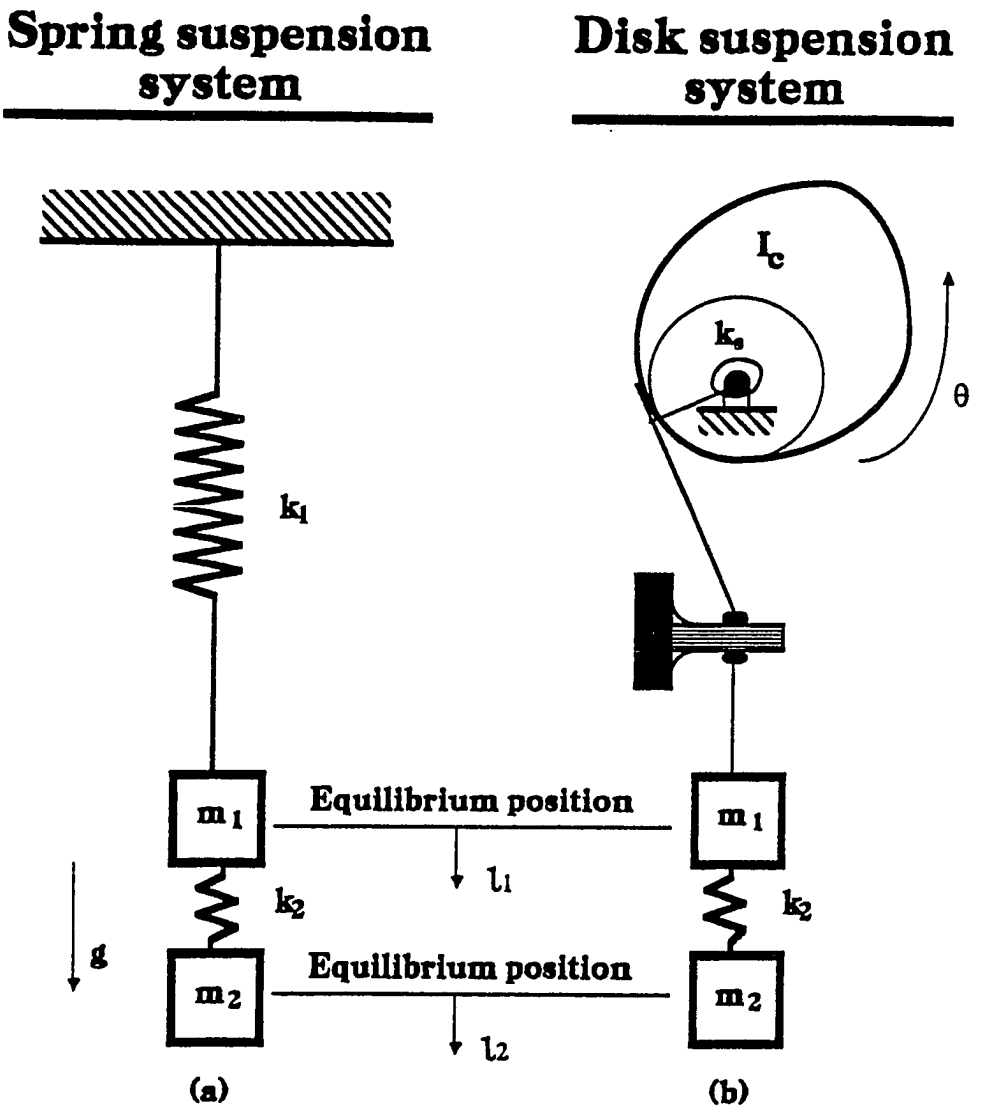

Figure 3.3: A lumped-parameter model for two kinds of suspension systems

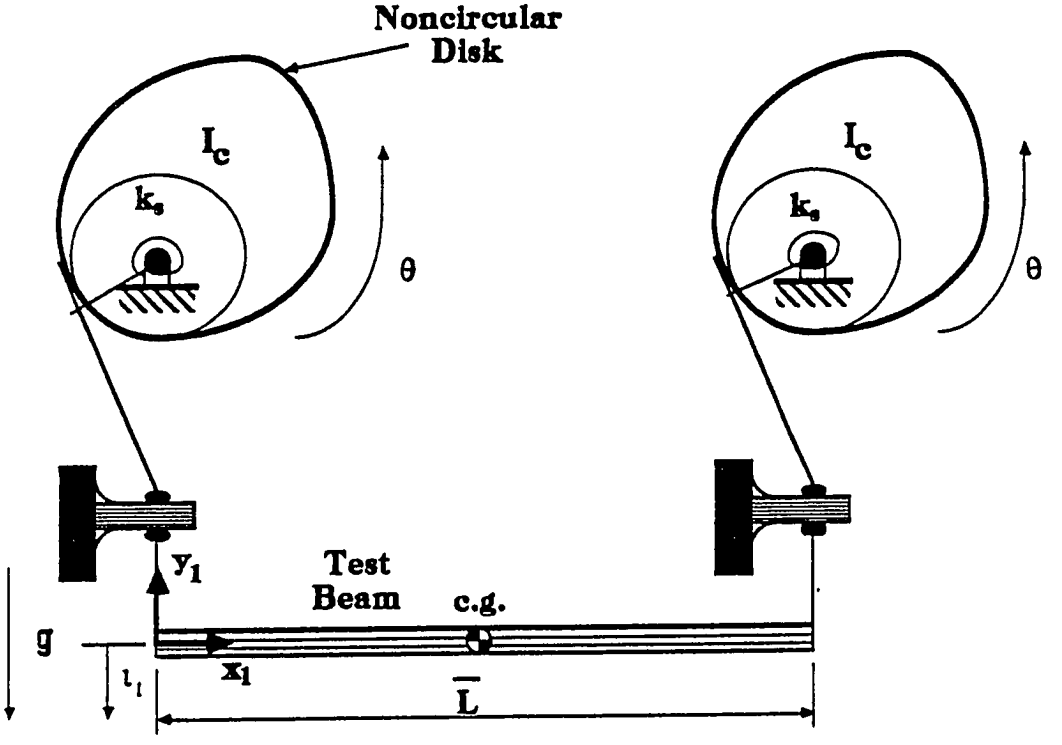

Figure 3.4: A flexible steel beam with disk suspension system

may be a linear system. A derivation of the dynamic equations will be discussed below.

Assume that m_1 and m_2 are the masses of the two rigid bodies, k_2 the spring stiffness between the two bodies, I_c the moment inertia of the disk, k_s the torsional spring rate and, r_a the distance between rotational center O and the ring R. Furthermore, the displacements of the two masses are denoted by ℓ_1 and ℓ_2 respectively, while θ and $\dot{\theta}$ denote the angular displacement and angular velocity of the noncircular disk, and ϕ is the displacement angle of the cable. Then from Fig. 3.3(b), the static equilibrium of the test article at any position is governed by

$$\begin{aligned} W &= (m_1 + m_2)g \\ &= \frac{k_s(\theta + \theta_0)}{r_a \sin(\phi + \phi_0)} \\ &= \frac{k_s\theta_0}{r_a \sin\phi_0} \end{aligned} \tag{3.21}$$

and

$$m_2 g = k_2 \ell_{s1} \tag{3.22}$$

where ℓ_{s1} indicates the static elongation of the spring, θ_0 is the preloaded angle of torsional spring, and ϕ_0 denotes the initial angular position of the cable. Note that the linear displacement ℓ_1 of mass m_1 must be consistent with disk angle θ since the suspension cable is directly connected to mass m_1. Due to the convexity of disk profile, the displacement ℓ_1, in Fig. 3.3(b), can be equated by integrating along the curvilinear path of the disk profile through the rotation θ so that:

$$\begin{aligned} \ell_1 &= \int_0^{\theta} r_a \sin(\phi + \phi_0)\, d\theta \\ &= \frac{k_s\left[\frac{\theta^2}{2} + \theta_0\theta\right]}{W} \end{aligned} \tag{3.23}$$

Note that the position ℓ_1 of mass m_1 is a parabolic function of the disk angle θ. In fact, equation (3.23) shows a function generator which generates a parabolic

curve of the displacement ℓ_1 in terms of θ. Moreover, differentiating Eq. (3.23) with respect to time yields

$$\dot{\ell}_1 = \left[\frac{k_s(\theta + \theta_0)}{W}\right]\dot{\theta} \tag{3.24}$$

which indicates the velocity relation between $\dot{\ell}_1$ and $\dot{\theta}$. Therefore, the position and velocity of mass m_1 can be replaced by the disk angle and angular velocity through Eqs. (3.23) and (3.24).

Applying Lagrange's equation of motion [69], the Lagrangian function for this system is given by

$$L = T - V \tag{3.25}$$

where the kinetic energy T and the potential energy V are:

$$T = \frac{1}{2}\{I_c\dot{\theta}^2 + m_1\left[\frac{k_s(\theta + \theta_0)}{W}\right]^2\dot{\theta}^2 + m_2\dot{\ell}_2^2\}, \tag{3.26}$$

$$V = \frac{k_s(\theta + \theta_0)^2}{2} + \frac{k_2}{2}\left[\frac{k_s\left(\frac{\theta^2}{2} + \theta_0\theta\right)}{W} - \ell_2 - \ell_{s2}\right]$$

$$- \frac{m_1 g k_s\left(\frac{\theta^2}{2} + \theta_0\theta\right)}{W} - m_2 g\ell_2 \tag{3.27}$$

Based on the Lagrangian from Eq. (3.25), the dynamic equation of motion in matrix form may be written in the following form:

$$\bar{M}\ddot{\xi} + \bar{K}\xi = \bar{f} \tag{3.28}$$

where ξ denotes the state vector $[\theta \ \ell_2]^T$. The inertia, stiffness matrices, and nonlinear force vector become

$$\bar{M} = \begin{pmatrix} I_c + m_1\left[\frac{k_s(\theta + \theta_0)}{W}\right]^2 & 0 \\ 0 & m_2 \end{pmatrix}, \tag{3.29}$$

$$\bar{K} = \begin{pmatrix} k_s + \frac{k_s k_2}{W}\left(\frac{k_s \theta_0^2}{W} - \ell_{s1}\right) & -\frac{k_s k_2 \theta_0}{W} \\ -\frac{k_s k_2 \theta_0}{W} & k_2 \end{pmatrix} \tag{3.30}$$

$$\bar{f} = [\, f_1 \quad f_2]^T, \tag{3.31}$$

where

$$f_1 = \frac{m_1 g k_s (\theta + \theta_0)}{W} - k_s \theta_0 + k_s k_2 \{\theta \ell_2 + \ell_{s1}\theta_0 - \frac{k_s \theta^3}{2W}$$

$$- \frac{3k_s \theta_0 \theta^2}{2W} - m_1 (\theta + \theta_0)\left(\frac{k_s}{W}\right)^2 \dot{\theta}^2\}$$

and

$$f_2 = \frac{k_s k_2 \theta^2}{2W}$$

Note that the nonlinearities occur in both the inertia matrix $\bar{M}$ and the nonlinear forcing function vector $\bar{f}$, due to the kinematic nonlinearity arising from the noncircular disk profile. The displacement and velocity of mass #1 may be determined from Eqs. (3.23) and (3.24) during the simulation process, even though they do not appear explicitly in Eq. (3.28).

The characteristics of such a lumped-parameter model may then be observed with different initial conditions placed on the lumped masses. For comparison purposes, the dynamic responses of the same test article will be re-simulated using the soft spring suspension system shown in Fig. 3.3(a). The stiffness of the soft spring has been chosen to be equivalent to the torsional spring rate in the disk suspension system, i.e. $k_1 = \frac{k_t}{r_b^2}$. The governing linear dynamic equation for the suspension system in Fig. 3.3(a) can be found in [65,67] and will not be included in this chapter. A second model of the test article is based on a continuous parameter system. The second model will be the subject of investigation in the section below.

§§ 3.3.2 A flexible steel beams of a test article

The band mechanism suspension system may be applied for the dynamic testing of continuous parameter models of flexible structures as well. Figure 3.4 demonstrates a uniform rectangular cross-section steel beam hung on two identical disk suspension systems at its two ends. Testing of such a flexible beam is aimed at flexural vibrational behavior. The model parameters of the flexible steel beam are given in Table 3.2. Assume that the total weight of the flexible beam in static equilibrium is evenly suspended by two identical disk suspension systems. Then, the profile of the noncircular disk is developed using half the weight of the flexible beam when Eqs. (3.18) and (3.20) are applied.

Assume that the rigidity of the flexible beam is given by EI product, its density p, the length L, and the displacement of the beam at the left end is denoted by P. The local coordinates $x_1 - y_1$ are located at the left end of the flexible beam for determining the local deflection of the beam. The technique of the modal analysis [65,66,67] will be applied to discretize the beam deflection into a series of flexural modes. The flexible beam deflects during bending vibration about its deformed static equilibrium shape, which is caused by gravity. As will be seen in the simulation of the beam behavior, only odd modes will be excited so that the flexural deflection of this floating hinged-hinged beam in the coordinates $x_1 - y_1$ is symmetrical about its center of this floating gravity. A setup of such a system is shown in Fig. 3.4.

The flexible beam can be maintained in static equilibrium as long as equations (3.16) and (3.17) are satisfied for half the weight of the flexible beam. The displacements and velocities of the flexible beam at two ends can be substituted by the disk angle r and angular velocity r in Eqs. (3.23) and (3.24) derived in the lumped-parameter system. For the flexible beam, as shown in Fig. 3.4, the kinetic energy T and the potential energy V can be expressed as:

$$2T = 2I_c\dot{\theta}^2 + \int_0^{\bar{L}} \rho\left[\dot{\bar{\ell}}_1 - \dot{\bar{y}}_1\right] \bullet \left[\dot{\bar{\ell}}_1 - \dot{\bar{y}}_1\right] dx_1, \tag{3.32}$$

$$2V = 2k_s[\theta + \theta_0]^2 + \int_0^{L} EI\{\frac{\partial^2 y_1}{\partial x_1 \partial x_1}\}^2 dx_1 \tag{3.33}$$

where $\bar{x}_1$ is a vector at the root end, and is tangent to the longitudinal x_1 axis of the flexible beam. Moreover, the distributed coordinates are expanded in an orthogonal basis of assumed mode shapes so that:

$$\bar{y}_1(x_1,t) = \bar{\psi}^T(x_1)\ \bar{q}(t),$$

$$\bar{\psi}^T = [\psi_1,\cdots,\psi_n] \qquad and\ \ \bar{q}^T = [q_1,\cdots,q_n] \tag{3.34}$$

where $\bar{\psi}(x_1)$ is a vector of assumed mode shapes relative to a spatial coordinates derived from the hinged- hinged boundary condition problem, $\bar{q}(t)$ is a generalized coordinate vector [65,66,67], and n is the number of assumed modes.

Inserting Eq. (3.34) into Eqs. (3.32) and (3.33) yields

$$2T = 2I_c\dot{\theta}^2 + \rho\bar{L}\dot{\ell}_1^2 + \sum_{i=1}^{n}\sum_{j=1}^{n} m_{ij}\dot{q}_i\dot{q}_j - 2\sum_{i=1}^{n} h_i\dot{q}_i\dot{\ell}_1, \tag{3.35}$$

$$2V = 2k_s[\theta + \theta_0]^2 + \sum_{i=1}^{n}\sum_{j=1}^{n} \kappa_{ij}q_iq_j \tag{3.36}$$

where

$$m_{ij} = \int_0^{\bar{L}} \rho\psi_i(x_1)\,\psi_j(x_1)\ dx_1,$$

$$h_i = \int_0^{\bar{L}} \rho\psi_i(x_1)\ dx_1,$$

$$\kappa_{ij} = \int_0^{\bar{L}} EI\frac{\partial^2\psi_i}{\partial x_1\partial x_1}\frac{\partial^2\psi_j}{\partial x_1\partial x_1}\,dx_1 \qquad for\ \ i,j = 1,2,\cdots,n$$

Therefore, the Lagrangian for the system, as given by Eq. (3.25), can then be obtained. From Eqs. (3.35) and (3.36), the displacement and velocity at the beam

ends are converted into the angular displacement and angular velocity of the disk. To simplify the state variables in the above equations, denote $\xi_0 = 0$, $\xi_i = q_i$, for $i = 1, 2, \cdots, n$. Using the Lagrange's equations of motion [9], the equation of motion of the system may be written as:

$$\bar{M}\ddot{\xi} + \bar{K}\xi = \bar{f} \tag{3.37}$$

where the state vector $\bar{\xi}^T = [\theta, q_1, q_2, , q_n]$. The inertia matrix $\bar{M}$, the stiffness matrix $\bar{K}$, and the nonlinear force vector $\bar{f}$ are given by:

$$\bar{M} = \begin{pmatrix} 2I_c + 4\rho\bar{L}\left(\frac{k_s}{W}\right)^2[\theta + \theta_0]^2 & -\frac{2k_s[\theta+\theta_0]\bar{h}^T}{W} \\ \textbf{symmetric} & \rho\bar{L}\hat{I} \end{pmatrix} \tag{3.38}$$

$$\bar{K} = Diag\,[\,0,\ \rho\bar{L}\bar{\omega}^2\,]\ ; \quad \bar{\omega} = Diag\,[\,\omega_1, \cdots, \omega_n\,], \tag{3.39}$$

$$\bar{f} = \begin{pmatrix} -4\rho\bar{L}\left(\frac{k_s}{W}\right)^2[\theta + \theta_0]\dot{\theta}^2 \\ 2k_s\dot{\theta}^2\bar{h} \end{pmatrix} \tag{3.40}$$

where $\hat{I}$ is an n×n identity matrix and $\omega_i\ (i = 1, \cdots, n)$ is the modal frequencies associated with the hinged-hinged shape functions $\bar{\psi}_i(x_1)$ used in discretizing the deflection of the flexible beam. The nonlinearities of the system all reside within the inertia matrix and the nonlinear force vector. The displacement and velocity at the ends of the beam can be computed directly from Eqs. (3.23) and (3.24) during the simulation. In this way, symmetric motions of the flexible beam may then be tested using two identical disk suspension systems.

§ 3.4 Simulation results

The dynamics of test articles have been derived in the previous section, and they include a lumped-parameter system as well as a continuous-parameter system. One disk suspension system is required for the lumped-parameter system, while two identical disk suspension systems are needed to suspend the flexible beam at its two ends. For each test article, two different excitations to the system will be implemented. The first is with an initial displacement and the second with an initial velocity, with a total of four simulations to verify the feasibility of this disk suspension system. A soft spring will be employed as a suspension system (see Fig. 3.3(a)) for the lumped-parameter system, and its simulations are then compared to those on the disk suspension system.

The parameters of the disk suspension system, which will be used for simulations, are shown in Tables 3.1 and 3.2. A convex profile of the noncircular disk is then drawn by evaluating Eqs. (3.11) and (3.13). Figure 3.5 shows the resulting profile of the noncircular disk, with several spokes which can eliminate its moment of inertia. The disk radius varies from 3 inches to 9.5 inches. In the middle of the disk thickness, a curvilinear groove is cut along the edge of the disk for the winding cable. The range along the disk edge allows the disk to rotate about 200 degrees. Such a noncircular disk, as shown in Fig. 3.5, will be used to implement the following dynamic simulations.

§§ 3.4.1 Simulation results of a lumped- parameter model

Table 3.1 summarizes the model parameters of a lumped-parameter system. Two kinds of suspension systems, a band mechanism and spring suspension system, will be used. In both types of suspension systems, the test article is hung in static equilibrium by connecting mass ♯1 to the suspension system through a thin cable. In the first simulation, -0.2 inch and 0.2 inch of initial displacements are specified to masses ♯1 and ♯2 respectively, but with no initial velocity. Figures 3.6-3.11

Table 3.1: Parameters of a lumped-parameter model with disk suspension system

(a) Disk suspension system:

r_a	= 12 in	r_b	= 6 in
k_s	= 0.5 lb/rad	I_c	= 0.01 $lb-in^2$

(b) Test article: (A lumped-parameter model)

m_1	= 12 lb	m_2	= 12 lb
k_2	= 1 lb/in		

Table 3.2: Parameters of a flexible steel beam with disk suspension systems

(a) Disk suspension systems:

r_a	= 12 in	r_b	= 6 in
k_s	= 0.5 lb/rad	I_c	= 0.01 $lb-in^2$

(b) Test article: (A flexible steel beam)

$\bar{L}$	= 6.562	ft
EI	= 74.8953	$lb-ft^2$
ρ	= 0.30480	lb/in
h	= 1.614×10^{-2}	in

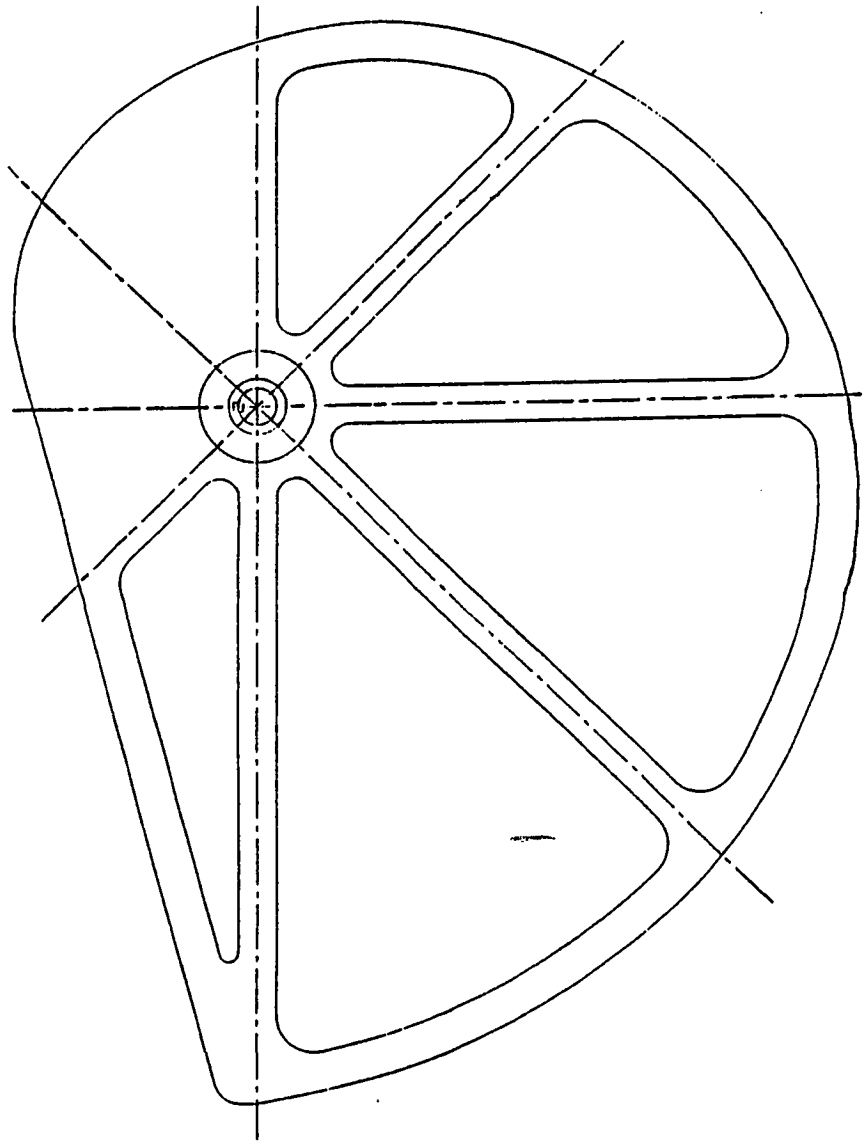

Figure 3.5: Profile of noncircular disk

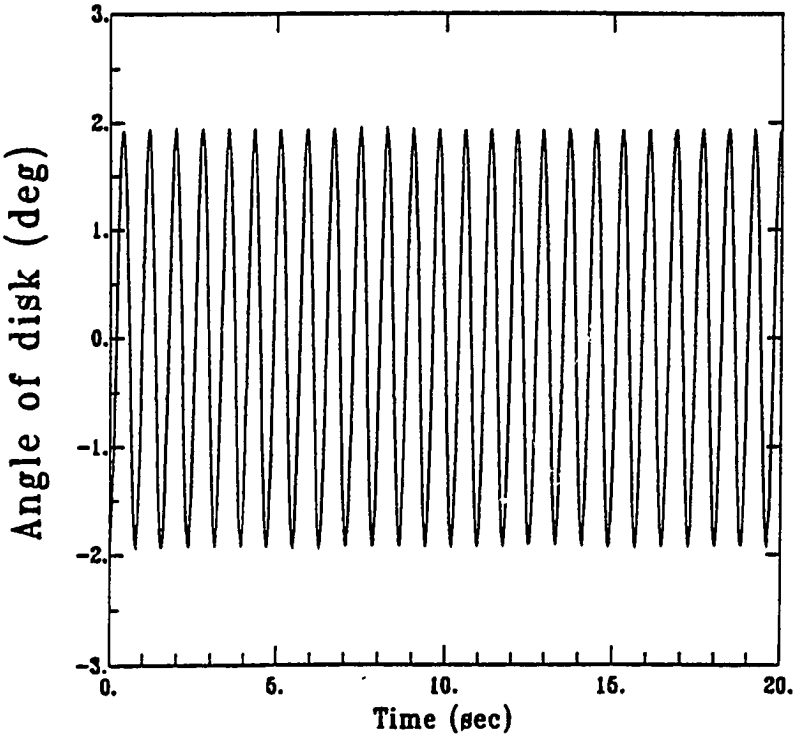

Figure 3.6: Disk angle of a lumped-parameter model for the initial displacement

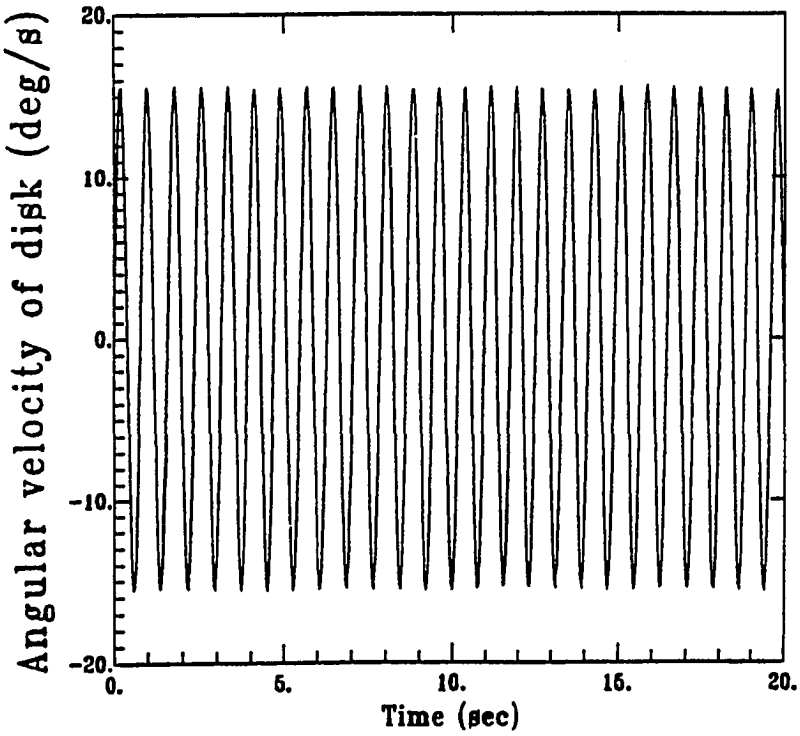

Figure 3.7: Disk angular velocity of a lumped-parameter model for the initial displacement

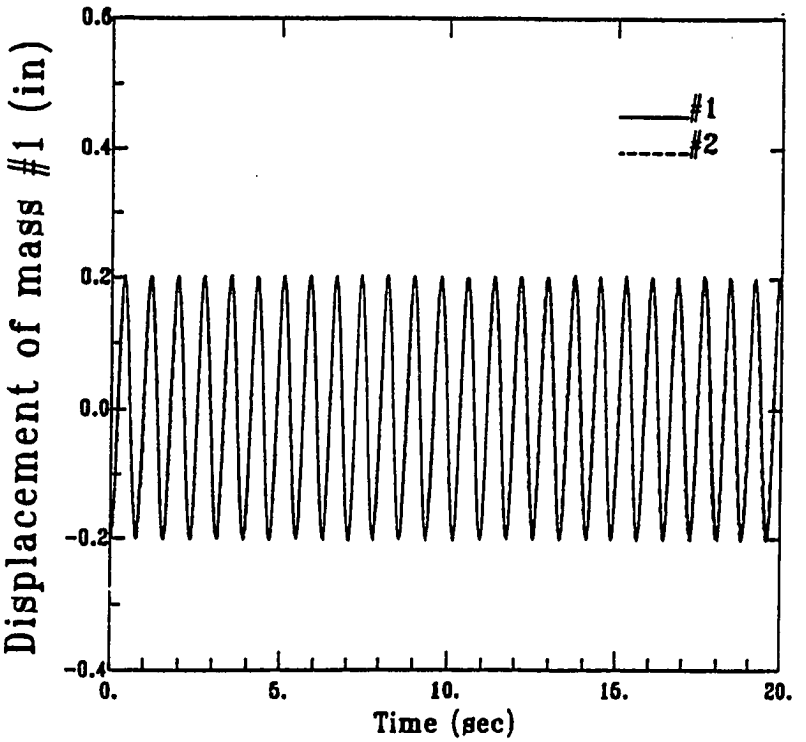

Figure 3.8: Mass #1 displacement of a lumped-parameter model for the initial displacement

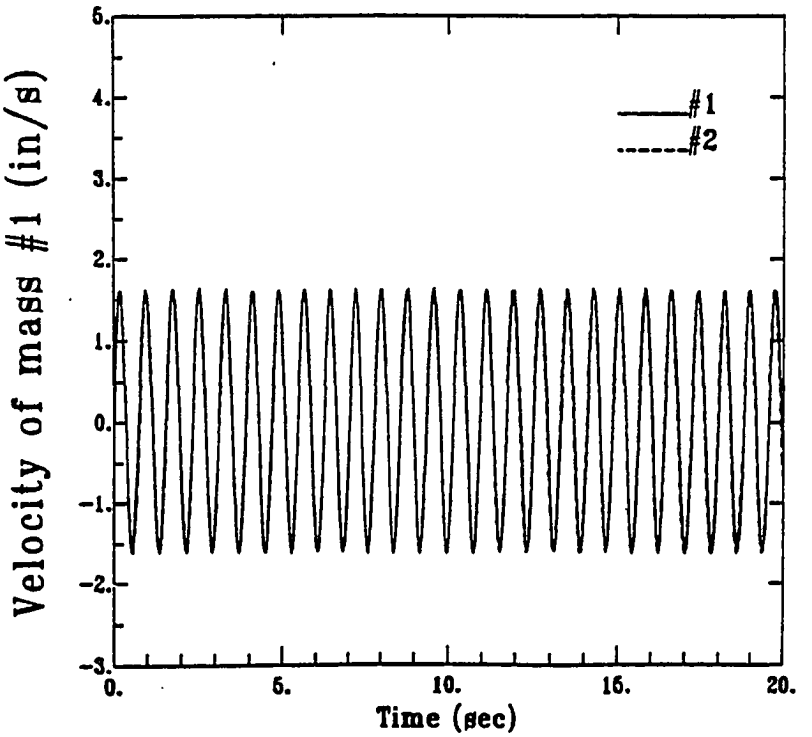

Figure 3.9: Mass #1 velocity of a lumped-parameter model for the initial displacement

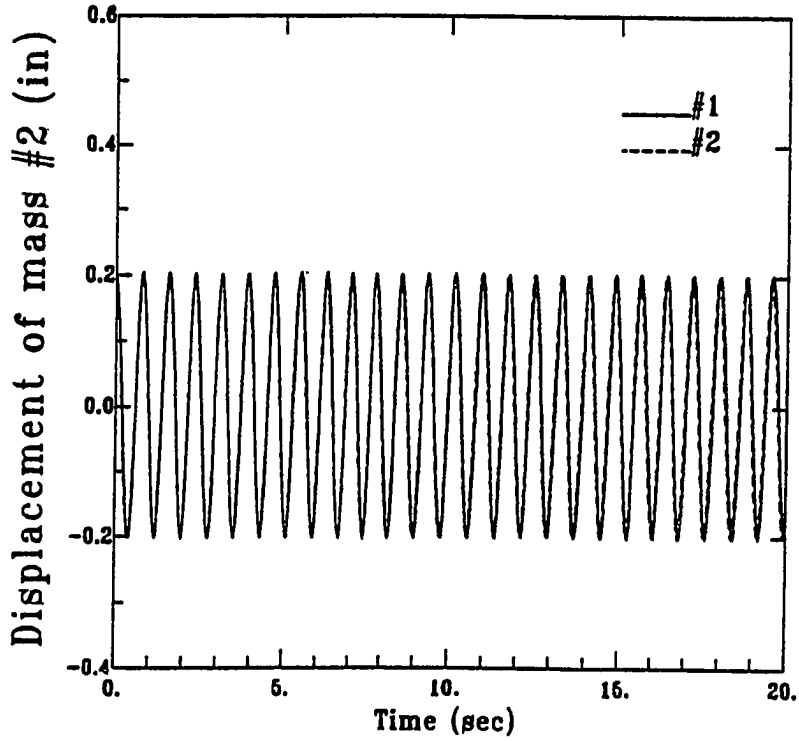

Figure 3.10: Mass #2 displacement of a lumped-parameter model for the initial displacement

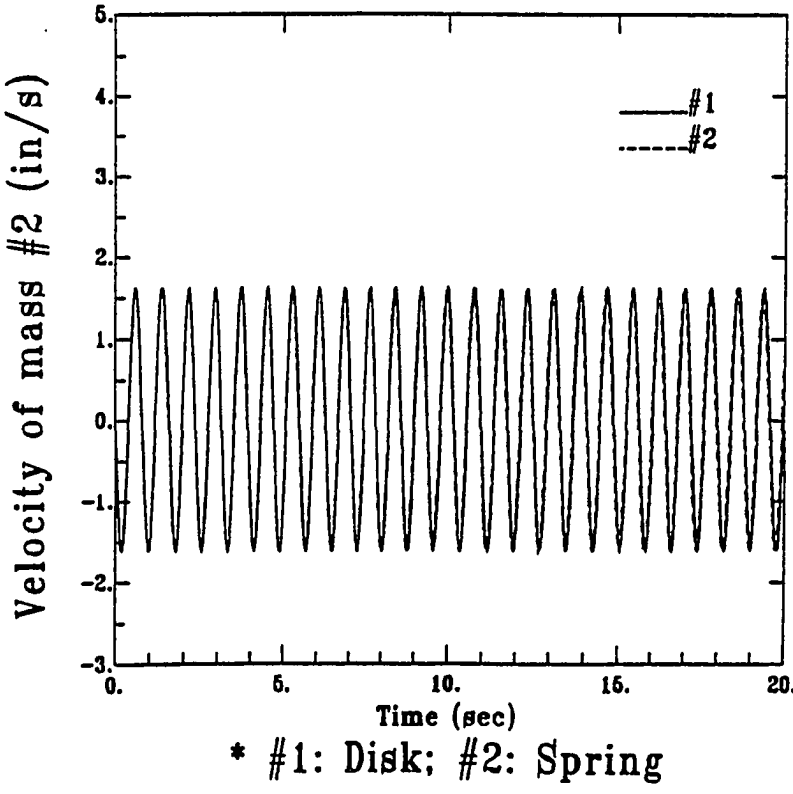

Figure 3.11: Mass #2 velocity of a lumped-parameter model for the initial displacement

are the simulation results of the two suspension systems. The results associated with the disk suspension system are indicated by a solid line, while those of the spring suspension system are indicated by a dotted line. Figures 3.6 and 3.7 show the angular displacement and angular velocity of the disk respectively of the disk suspension system. Both angular displacement and angular velocity oscillate with the natural frequency of the test article. The displacement and velocity of mass ♯1 are respectively shown in Figs. 3.8 and 3.9, while the displacement and velocity of mass ♯2 are given in Figs. 3.10 and 3.11 respectively. All the trajectories of masses ♯1 and ♯2 represent pure oscillatory motions about their equilibrium positions. The cable which connects the test article and the disk is found always in tension. It can be seen that there is no difference between disk suspension system and the simple spring system under specifications of initial displacements. The spring in the spring system may be too soft due to the equivalent relationship, $k_1 = \frac{k_t}{r_b^2}$, so that it may not be able to suspend heavy test articles. The spring stiffness for this spring suspension system cannot be arbitrarily increased because that will distort the natural frequency of the test article. The initial-displacement results provide an insight in verifying the validity of disk suspension system when compared to the conventional spring suspension system. It also shows that the results correspond to the anticipated vibrational characteristics of mass ♯1 and ♯2 in space.

The second simulation of a lumped-parameter system deals with the dynamic response subjected to initial velocity specification. An initial velocity of 2 inches per second acts on mass ♯2 to excite the whole system to move as if under an impulse. Figure 3.12 shows the dynamic history of the disk angle. It has an oscillatory motion superimposed on the dropping angular displacement trajectory. Figure 3.13 illustrates this oscillatory motion of the disk but with an average angular velocity, 9.5 deg/sec, superimposed upon that oscillation. The displacements and velocities of masses ♯1 and ♯2 are shown in Figs. 3.14-3.15. In Figs. 3.16 and 3.17, the solid lines associated with disk suspension system show that the entire

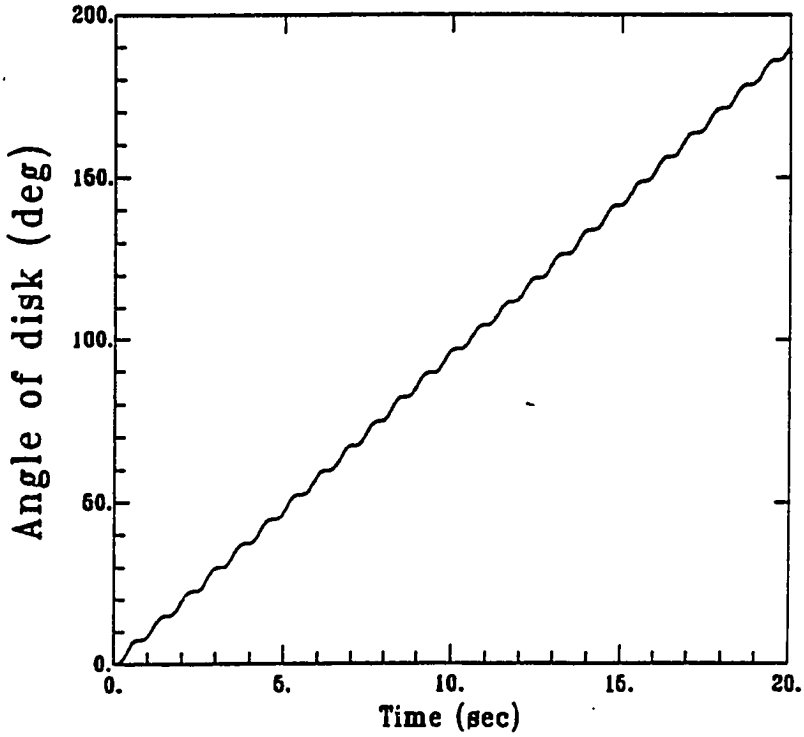

Figure 3.12: Disk angle of a lumped-parameter model for the initial velocity

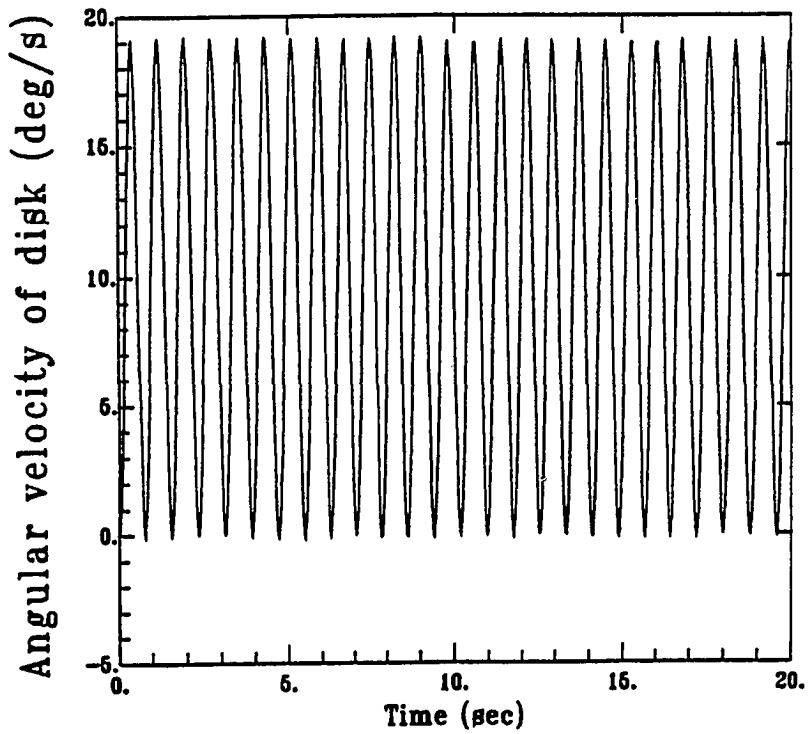

Figure 3.13: Disk angular velocity of a lumped-parameter model for the initial velocity

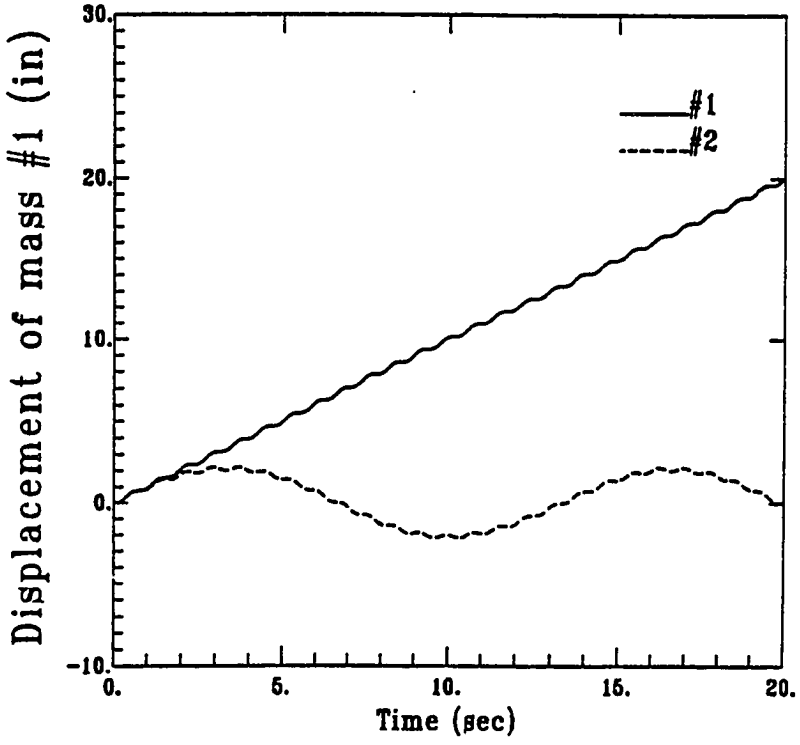

Figure 3.14: Mass #1 displacement of a lumped-parameter model for the initial velocity

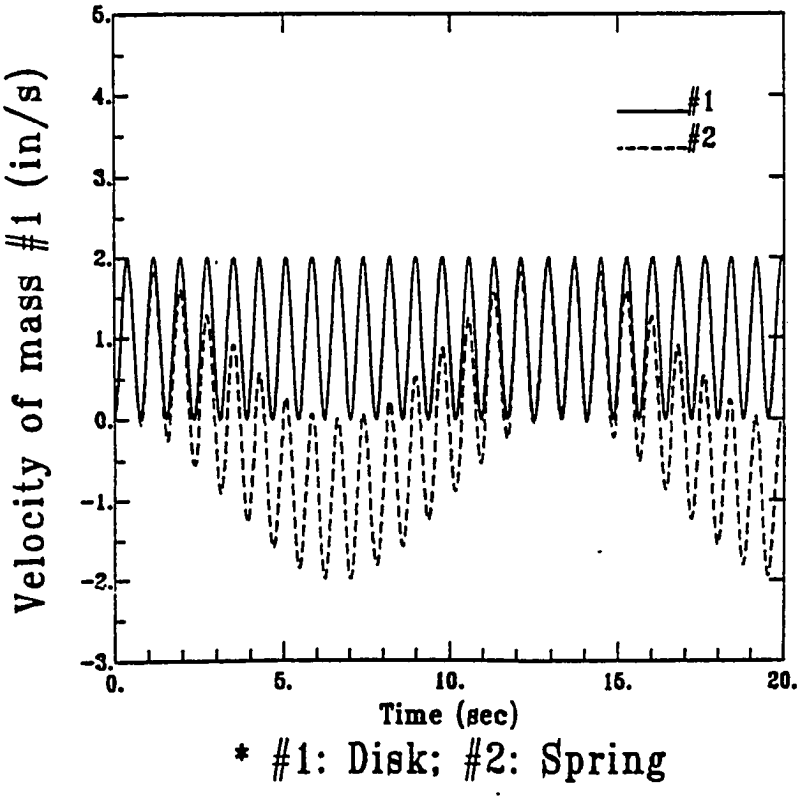

Figure 3.15: Mass #1 velocity of a lumped-parameter model for the initial velocity

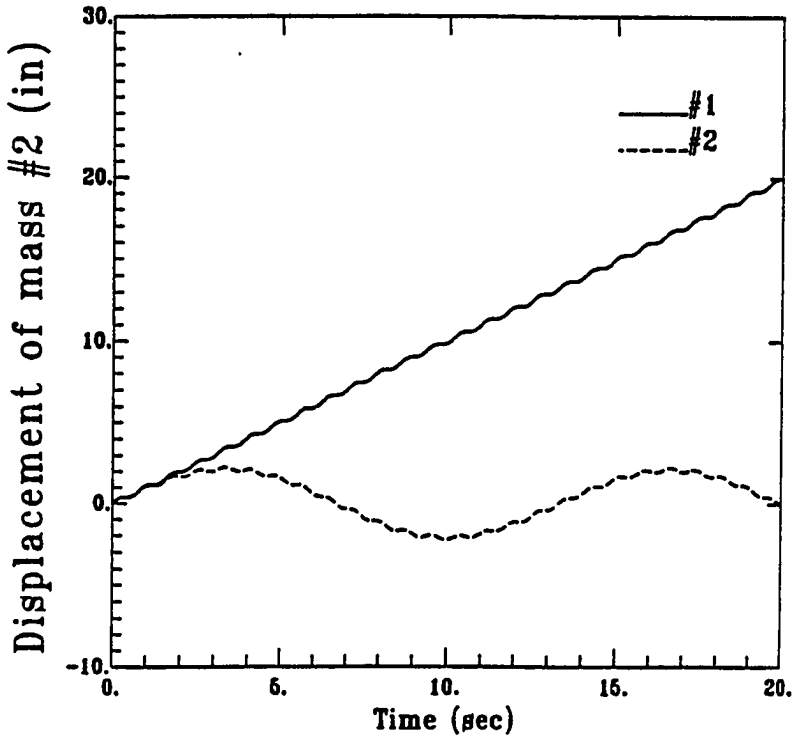

Figure 3.16: Mass #2 displacement of a lumped-parameter model for the initial velocity

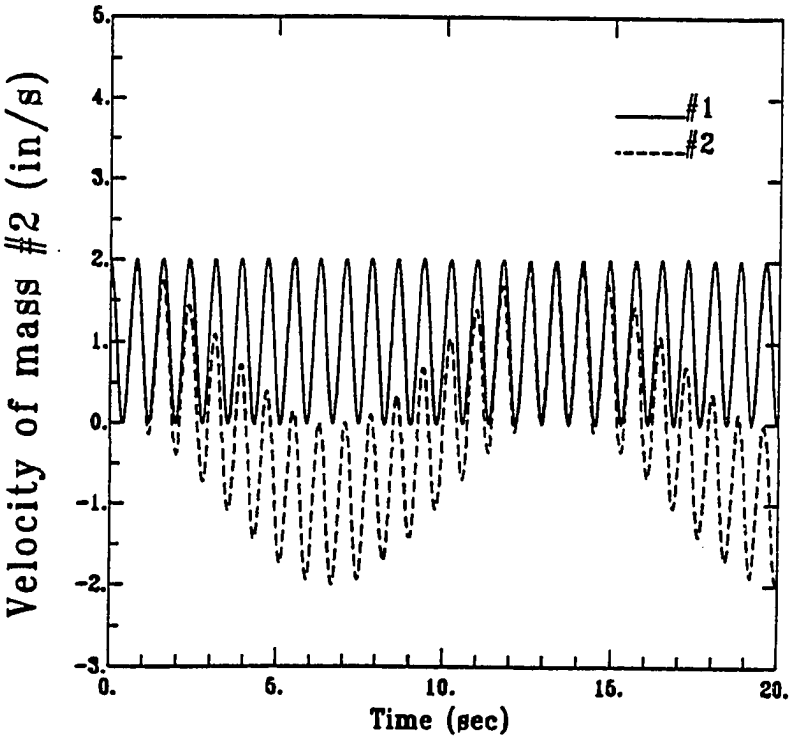

* #1: Disk; #2: Spring

Figure 3.17: Mass #2 velocity of a lumped-parameter model for the initial velocity

test article is dropping at a constant velocity, while masses ♯1 and ♯2, which model the test article are oscillating during this downward motion. This shows that with the use of this disk suspension system the impulse response indeed corresponds to that in a zero-gravity condition. On the other hand, figures 3.14 and 3.16 also show that the spring suspension system does not satisfy this anticipated motion trajectory of the test article (masses). The velocities of masses shown in Fig. 3.15 and 3.17, confirm that the masses in the disk suspension system, on the average, do not accelerate. The pure oscillations of both the mass velocities indicate an average constant velocity of 1 in/sec rather than zero, implying that the constant velocities are indeed due to the impulse response. This implication shows that the entire test article beneath the disk suspension system is not accelerated due to the initial impulse. Such a phenomenon is consistent with the behavior deduced from mass displacements in Fig. 3.14 and 3.16. Note that the masses oscillate at 180 degrees out of phase with each other. These figures also show that the simple spring suspension system does not result in a correct motion for the masses in response to an initial impulse.

Figures 3.12-3.17 thus ensure that this disk suspension system is capable of simulating the dynamic behavior of the test article subjected to an impulse. The test body, accordingly, translates at a constant velocity. When the mass is imposed with an initial velocity v_0, (equivalent to an impulse) the test article will continue to travel at that same velocity, v_0, over a considerable range of travel. This is because the tension in the cable is constant and is exactly equal to the weight of the test article, so that there is no net driving force on the article during its entire range of motion. With that observation, it therefore leads to a constant velocity of the test article, and in so doing, exactly simulates the motion of an object in space.

§§ 3.4.2 Simulation results of a flexible steel beam

In this simulation experiment, two identical disk suspension systems are employed to suspend a flexible beam that has the same weight as in the lumped-parameter model of the previous section. The model parameters of a flexible steel beam are listed in Table 3.2. Three hinged-hinged flexible modes will be assumed for the flexible steel beam. On the other hand, a free-free flexible beam in space is simulated under the initial excitations for comparison. In this simulation, the first and third modes will be specified with initial values. This means that the flexible beam is originally bent into a symmetric deformed configuration about its static equilibrium configuration, and then released from rest. Hence, the first and third modes are excited by this initial deformation. The simulation results are given in Figs. 3.18-3.23. Solid line denotes the results under the disk suspension system, and dashed line indicates the results for a free-free flexible beam in space. Figures 3.18 and 3.19 show the angular displacement and angular velocity of the disk, while figures 3.20 and 3.21 show the deflection and velocity of the beam at its center of gravity. Figures 3.22 and 3.23, on the other hand, show the deflection and velocity of the beam at one-fourth length of the beam. The odd modes, as anticipated, are very active, as can be seen from results of displacement and velocity in the figures. This is due to the symmetry of the deflection about a plane through the center of gravity of the beam. In Fig. 3.20, the displacement at the beam's c.g. implies that the beam oscillates about its original static equilibrium configuration during the process. Obviously, two kinds of initial displacement responses superimpose together. This implies that the disk suspension system can simulate the initial displacement response of the free-free steel beam in space. Hence, the multi-mode vibration of a flexible beam can be implemented under the disk suspension system.

Finally, a fourth simulation has been conducted with the flexible beam subjected to an initial impulse. Similarly, the free-free flexible beam is simulated under the initial impulse response, which is denoted by the dashed line. Simulation

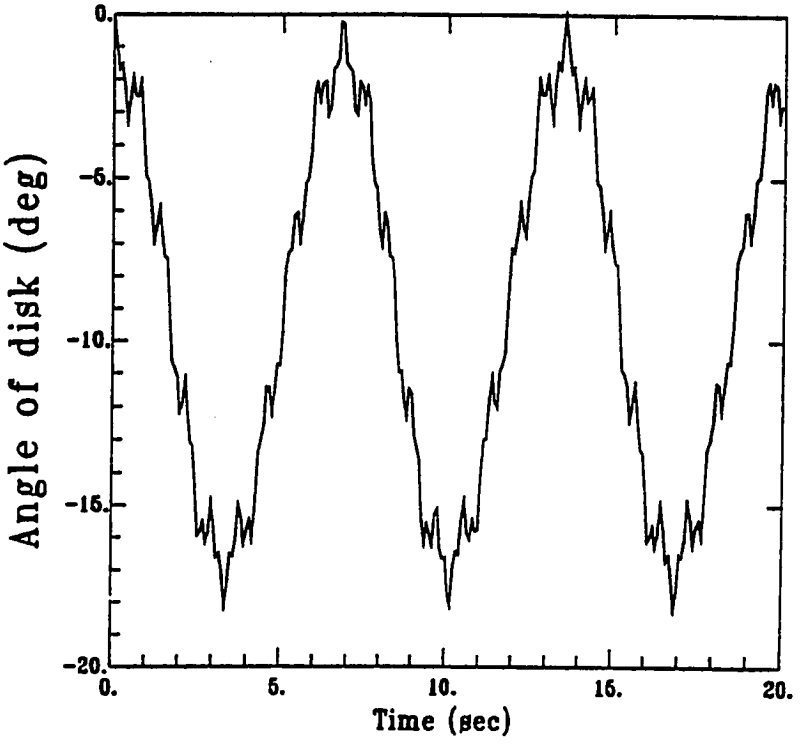

Figure 3.18: Disk angle of a flexible steel beam for the initial displacement

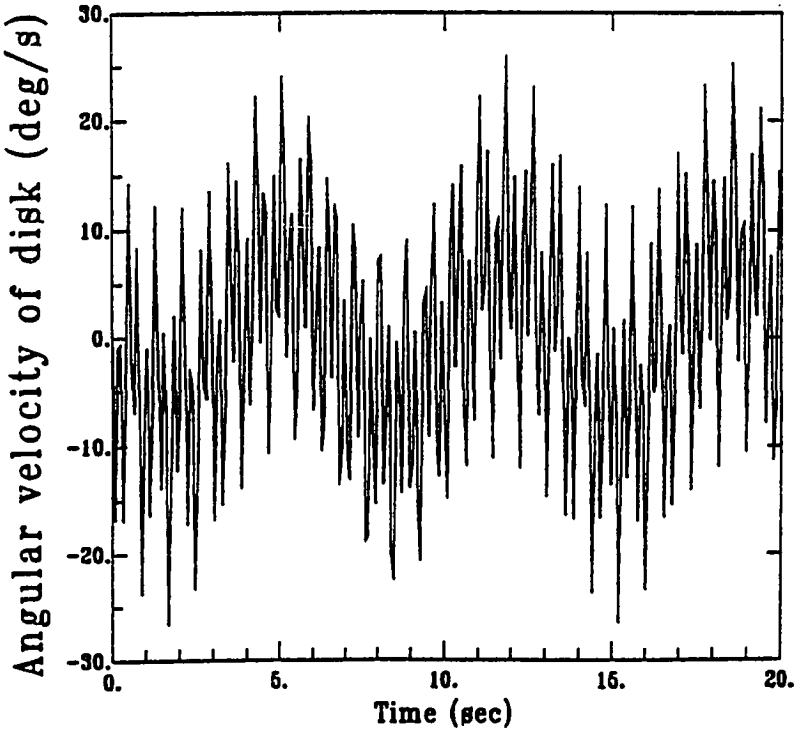

Figure 3.19: Disk angular velocity of a flexible steel beam for the initial displacement

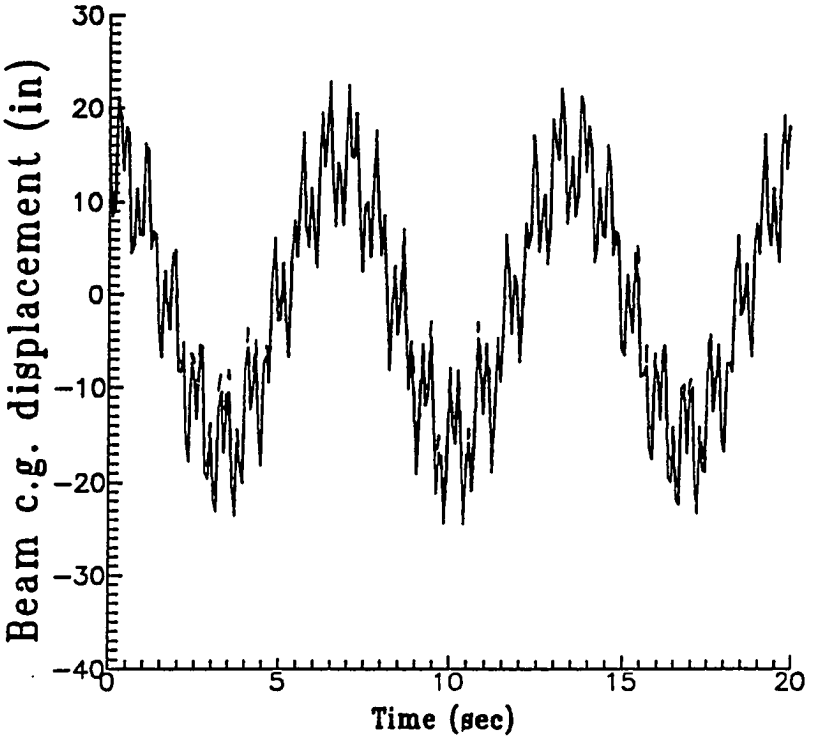

Figure 3.20: Beam c.g. displacement of a flexible steel beam for the initial displacement

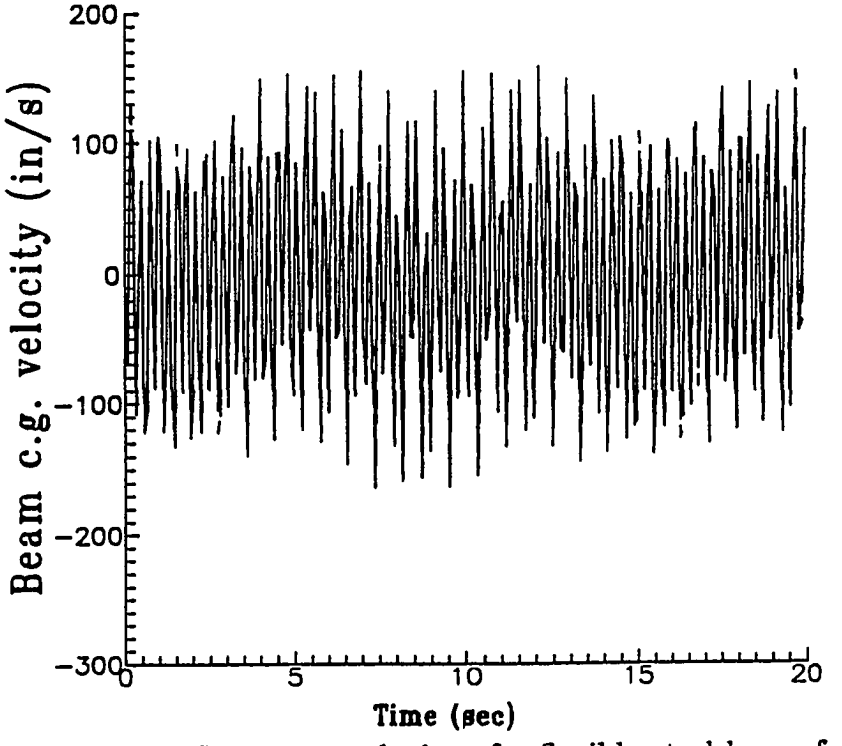

Figure 3.21: Beam c.g. velocity of a flexible steel beam for the initial displacement

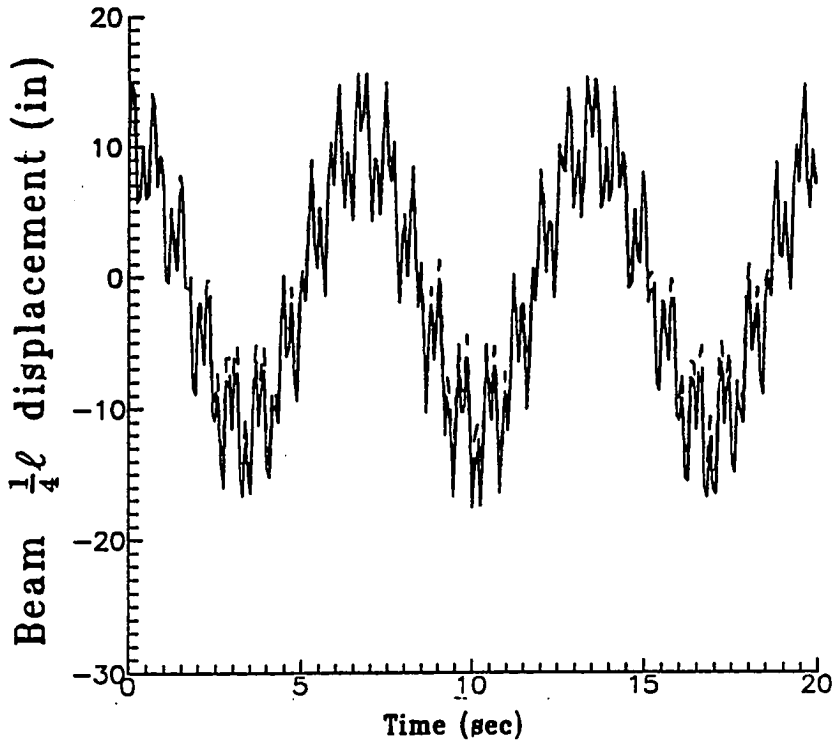

Figure 3.22: Beam $\frac{1}{4}$-length displacement of a flexible steel beam for the initial displacement

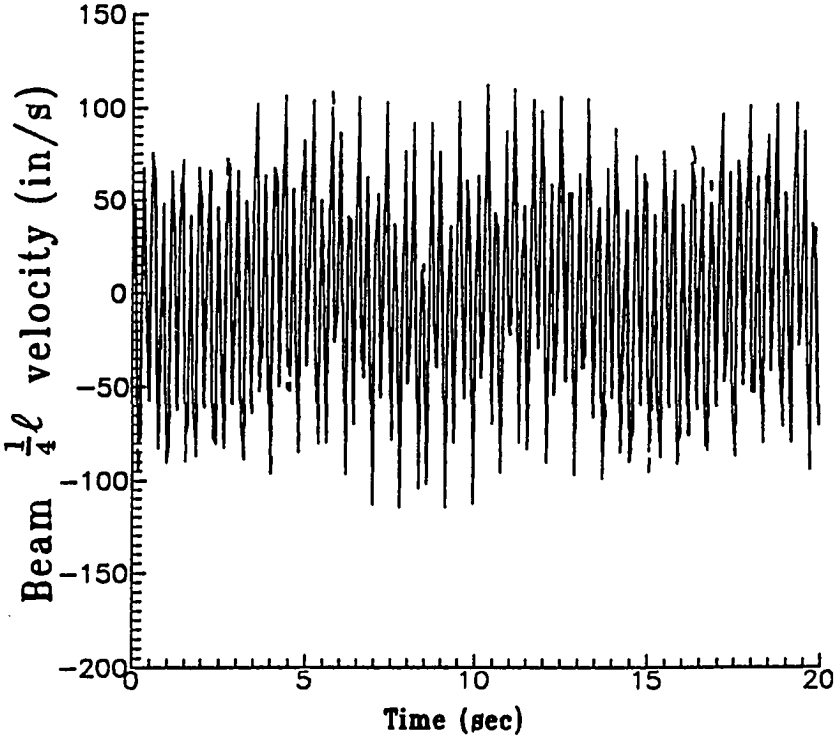

Figure 3.23: Beam $\frac{1}{4}$-length velocity of a flexible steel beam for the initial displacement

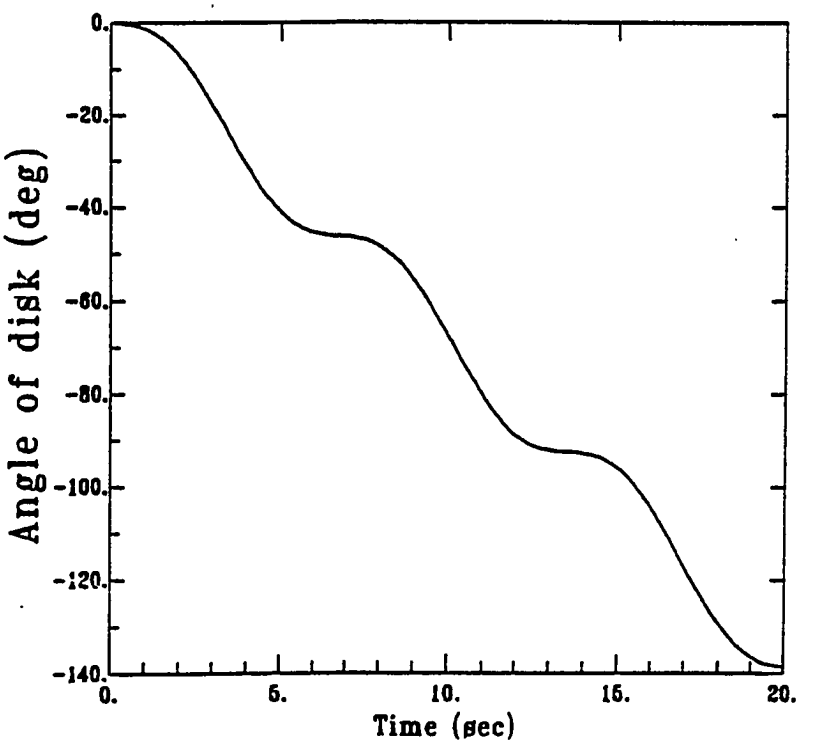

Figure 3.24: Disk angle of a flexible steel beam for the initial velocity

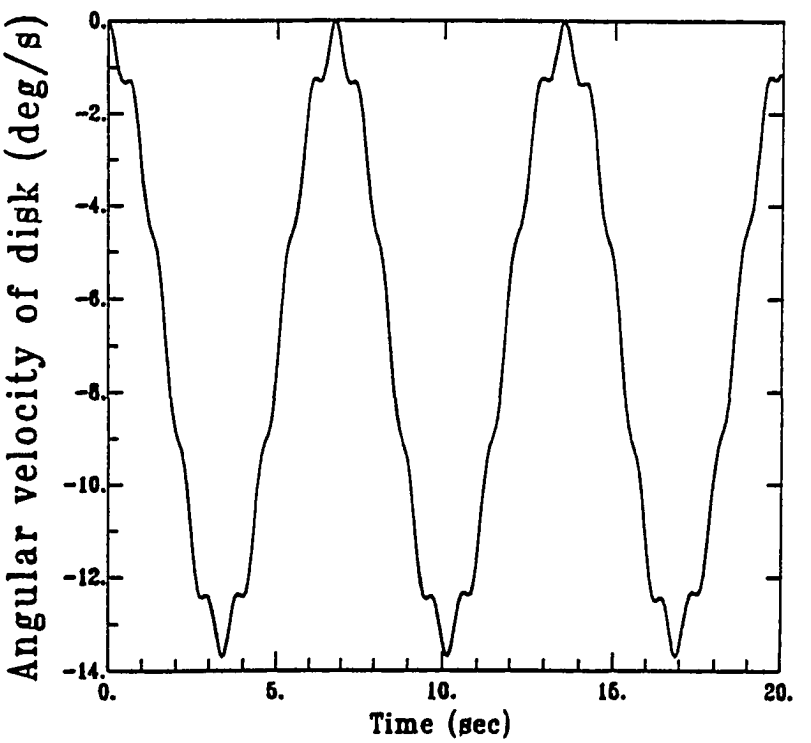

Figure 3.25: Disk angular velocity of a flexible steel beam for the initial velocity

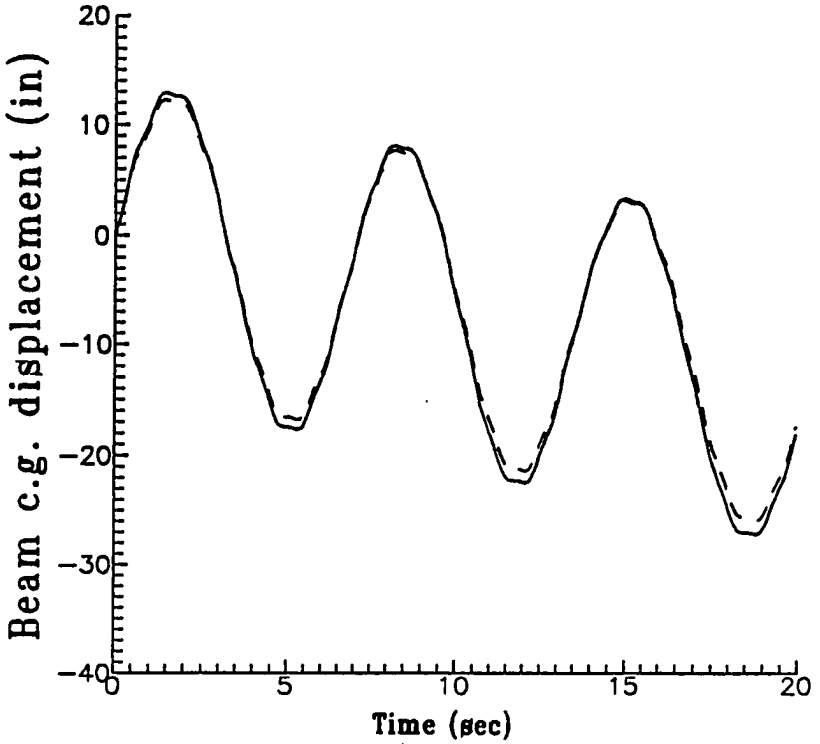

Figure 3.26: Beam c.g. displacement of a flexible steel beam for the initial velocity

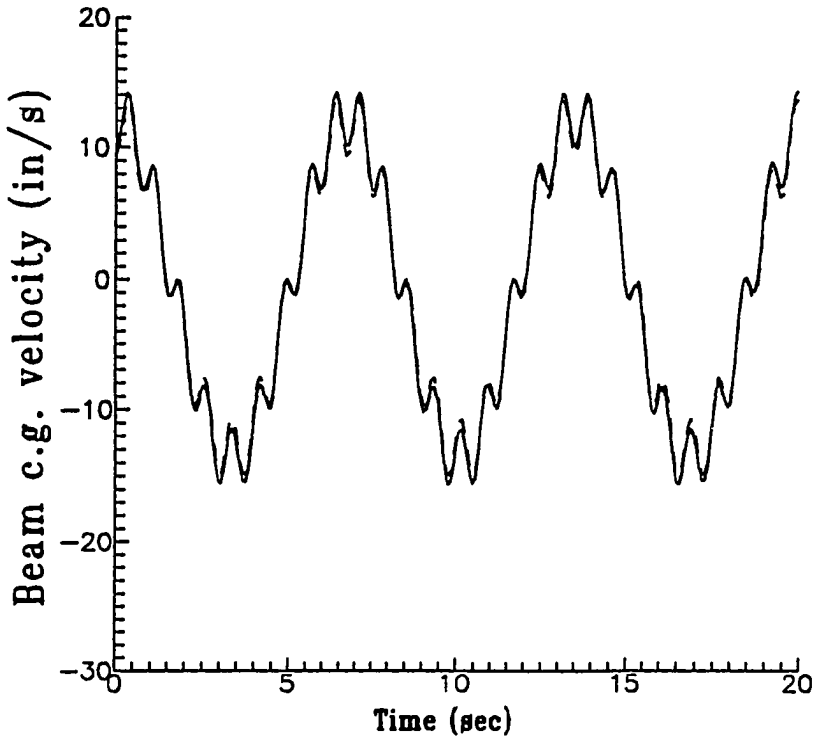

Figure 3.27: Beam c.g. velocity of a flexible steel beam for the initial velocity

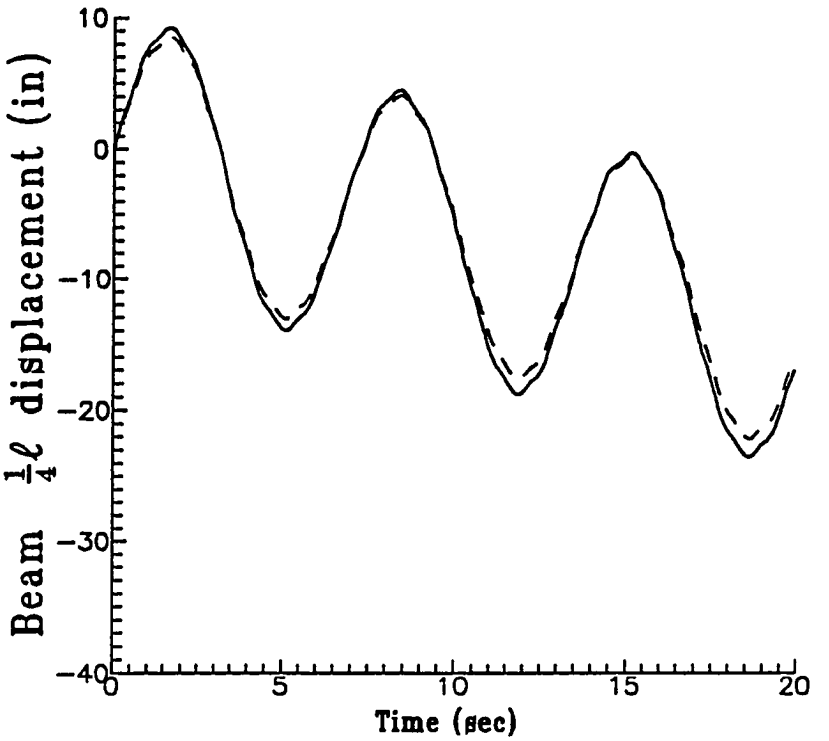

Figure 3.28: Beam $\frac{1}{4}$-length displacement of a flexible steel beam for the initial velocity

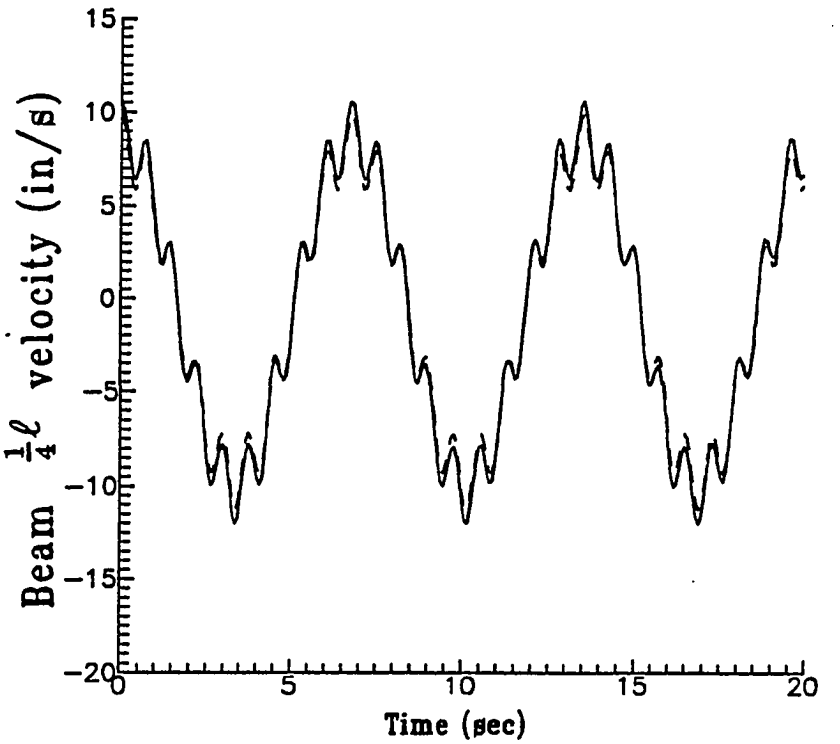

Figure 3.29: Beam $\frac{1}{4}$-length velocity of a flexible steel beam the for the initial velocity

results are shown in Figs. 3.24-3.29, including the disk angle, angular velocity of disk, beam's c.g. displacement and velocity, and beam's one-fourth-length displacement and velocity. The third mode is more pronounced in the velocity plots, and the amplitude of the beam's deflection at the center of gravity is larger than those at one-fourth length of the beam. The linear slope in the oscillatory behavior, in Figs. 3.26 and 3.28, indicates a constant-speed motion associated with a rigid-body mode. The flexible beam is moving upward at a constant speed while simultaneously vibrating with respect to the local coordinates $x_1 - y_1$. The constant speed is approximately 0.7 in/sec. In fact, these impulse results of a beam implies a compound motion of the flexible space structure that includes a constant-speed rigid-body motion with a flexible-body vibration superimposed on it. Apparently, the results of a free-free beam are similar with the ones under the disk suspension system. The small difference between two kinds of results is caused by the inertia of noncircular disk.

The impulse response of a flexible structure has shown to be consistent in the use of this disk suspension device. The entire test structure will travel at a constant velocity with a rigid-body motion, while the traveling beam oscillates, with its flexible modes, about the moving local coordinate system. The similarities of the second and fourth simulation results validate the applicability of this disk suspension system for both discrete and continuous models.

§ 3.5 Discussion and summary

This chapter has presented a band mechanism that is to be used as a ground-based suspension system to assess the characteristics of flexible space structures that operate in a weightless environment. This mechanism is characterized by a noncircular disk with a convex profile constrained into rotational motion by a torsional spring. The suspension system is constructed to counteract the weight of the test article by using a specially shaped disk in conjunction with an appropriate

torsional spring. The basic principle behind this suspension system is to maintain static equilibrium of the test article at any given vertical position. The convex profile of the disk is determined using the envelope theory. It has also been shown that this suspension system is applicable for test articles with the different weights without the need to change the disk profile; the torsional spring rate has to be adjusted to maintain the static equilibrium condition of the new test article.

This mechanism has shown, under numerical simulation, to be applicable and suitable for ground-based dynamic testing of test articles, be they discrete or continuous models. Two kinds of test articles have been chosen for the simulation, a lumped-parameter system and a flexible steel beam. The lumped-parameter element is composed of two masses and a connecting spring which provides a single-mode vibration. Simulation results indicate that the characteristics of the flexible space structures can be precisely tested under this disk suspension system. It has also shown to be capable of permitting a constant-speed motion superimposed with flexural vibration in an impulse response. Furthermore, the free-free flexible steel beam in space can be simulated on the ground by suspending the flexible beam at its two ends through the use of the disk suspension system. These simulation results provide very useful insights in building up the experimental equipment at NASA-Langley.

Chapter 4

MANEUVERING EXPERIMENTS AND SIMULATIONS OF FLEXIBLE STRUCTURES

The dynamic equation of a flexible steel beam carried on a rigid and translational trolley has been derived in reference [38]. The detailed functions and characteristics of the laboratory equipments are listed into several tables in section 4.2. By using the pole-placement technique [42], the output feedback gains are achieved for four performances of position controls in order to investigate the influence of the flexibility feedback. The first case demonstrates position control with no strain feedback. The second case studies position control with the strain feedbacks only to the beam motor. The third case involves position control with the strain feedbacks simultaneously to the trolley motor. The fourth case shows the position control with the strain feedbacks simultaneously to the trolley and the beam motors. For each case, the corresponding simulation and experiment are carried out in conjunction with the designated maneuver mission. In four cases, the measurements from three strain gages will demonstrate suppression of vibration due to the translational motion of the trolley.

§ 4.1 System dynamics

In this chapter, the dynamic system represents a typical multibody system with a flexible steel beam carried on the rigid and translational trolley. Lagrange's equation of motion, in conjunction with the the modal expansion to discretize the deflection of the flexible steel beam, is applied to derive the dynamic equation of

motion [65,66,67] which is illustrated in Appendix A. For the orientation of the system, an absolute coordinate is selected at a reference position along the track. And a moving relative coordinate, which translates with the trolley, is referred at the root end of the beam to indicate the slewing root angle of the beam. The histories of trolley motion and beam slewing are thus adequately described through two independent variables, namely, the trolley displacement and beam root angle. The flexible steel beam is modeled as a cantilever beam [65,66,67] with the fixed end at the motor and the free end at the tip. The first three modes of the cantilever beam are assigned to discretize the flexural vibration of the flexible steel beam. The first mode dominates the magnitude of the vibrational motion, and the third mode produces high frequency oscillation. Only the bending vibration is allowed during the motion of the arm. Therefore, ten states of the system are required for the first-order state equation in the analytical simulation.

Dynamics of actuators and characteristics of sensors are involved in the closed-loop model of the system for simulation [37,38]. In the second-order dynamic equation, kinematic nonlinearities take place in the inertia matrix and the nonlinear forcing term. By performing a rapid and large angle maneuver, the kinematic nonlinearities of this system are excited to behave significantly. And the interaction of rigid-body motion and flexible-body vibration can be evaluated by looking at the coupling effect due to the nonlinearities. Without loss of generality, the viscous damping of air drag and the friction on the trolley wheels are ignored in the simulation. The damping effect absorbs the system energy because of the back-EMF of the motor. The system flexibility is associated with the stiffness of the flexible steel beam in the maneuvers. Two external forces provide the trolley and beam with active control inputs based on the feedback of output measurements. The control force to the translational trolley is generated by the trolley motor through the transmission system of pulley and wire. The output feedback gain, shown in Fig. 4.1, is based on pole-placement technique [42]. The measurements are measured by the sensors including trolley potentiometer, beam potentiometer,

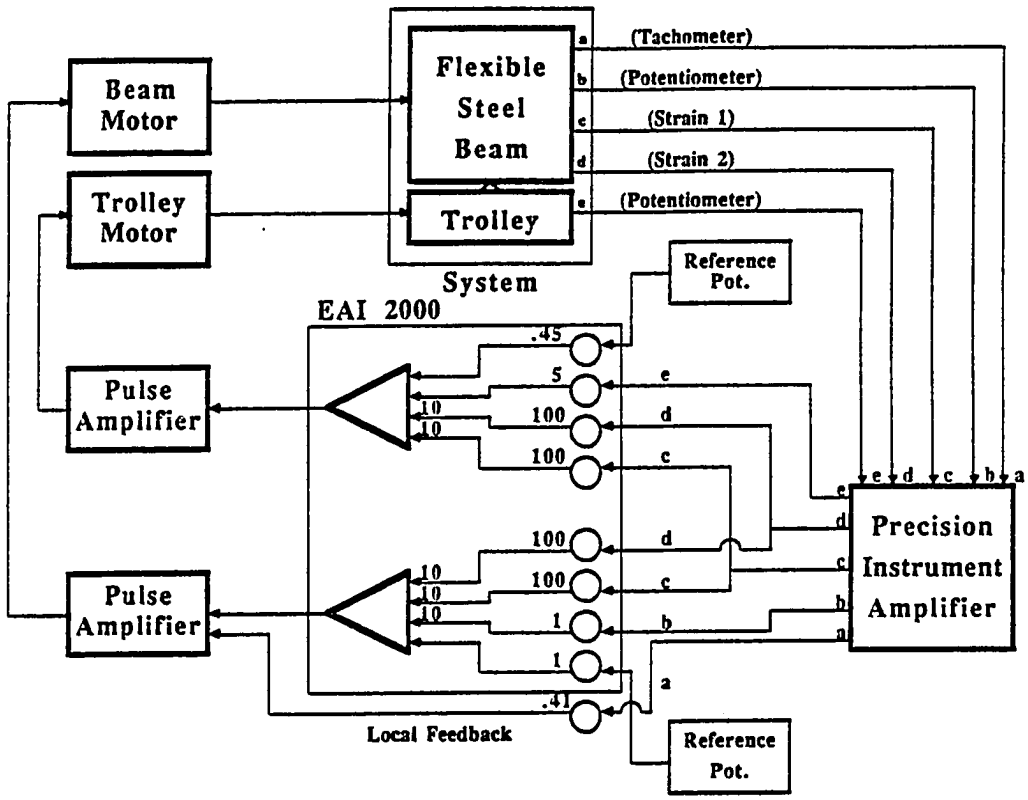

Figure 4.1: Global and local output feedback control loop

beam tachometer, and three strain gages. To be consistent with the units of experimental results, all of the physical output measurements are converted into corresponding voltages through the conversion factors shown in section 4.2.

§ 4.2 Experimental setup

A brief description of the laboratory apparatus is given in this section. A trolley (see Fig. 1.2) is mounted on a 2.5-m-long horizontal aluminum I-beam track with a cross section of 7.6 cm by 6.4 cm. The trolley is driven by a dc PMI motor (Table 4.1) through a 7.6 cm diameter driver pulley and a cable transmission system. The cable used to drive the trolley is a steel wire cable with nylon coating and is 0.1 cm in diameter with a 534 N breaking strength. A 7.6 cm idler pulley is located at the free end of the track with a ten-turn potentiometer (Table 4.2) attached to it to measure the location of the trolley. The trolley consists of eight railroad-type wheels connected with leaf spring suspension systems. A 1.1-m-long flexible steel beam with a cross section of 7.6 cm by 0.081 cm (Table 4.3) is clamped on the axial shaft of a dc gear motor (Table 4.4). The beam motor is mounted on the top of the trolley. The beam is cantilevered in a vertical plane and rotated in the horizontal plane by the beam motor so that only the bending vibration is allowed. A dummy mass is mounted on the other side of the trolley to balance the beam so that the trolley is not tilted. Three full-bridge strain gages (Table 4.5) are used to measure bending moments induced by bending deformation of the steel beam. An angular potentiometer and a tachometer in the beam motor (Table 4.4) are used to measure the angle and speed of rotation, respectively, at the beam root. The strain gages are located at the root, at 22% of the beam length from the root, and at the mid-span. Signals from all six sensors (3 strain gages, 2 potentiometer, and 1 tachometer) are amplified (Table 4.6) and then monitored by an analog data acquisition system. An analog computer closes the control loop and generates two voltage signals for the trolley motor and the beam motor through two pulse width modulation servo amplifiers (Table 4.7). A limit

switch to stop translational motion is placed at each end of the track to avoid system damages. All the input and output signals are stored in a data analyzer for data analysis. Power supply information is presented in Table 4.8.

§ 4.3 Output feedback control loop

The dynamic system of this experiment consists of a translational motion of the trolley and a rotational maneuver of the flexible steel beam. The trolley and the beam are moved to a desired location while simultaneously suppressing the flexural vibration of the beam. In this experiment, both dynamics of the trolley and the beam are coupled through the inertia reaction. The flexural steel beam is excited to vibrate due to the rotation of the beam and the translation of the trolley. Significant kinematic nonlinearities, coupled with vibrational motion, occur especially when the flexible beam is rapidly maneuvered through large angles. These nonlinearities must be taken into account in the feedback control design. As shown in references [20,21,22], the controller should be kept as simple as possible for easy real time implementation and as insensitive as possible to the kinematic nonlinearities.

Figure 4.1 shows a simple output feedback controller design, which includes both a local and a global feedback. The output measurements include the trolley position, the beam root angle and its angular velocity, and three strains of the flexible beam. The trolley position is locally fed back to the trolley motor. Similarly, the beam angular displacement and velocity are locally fed back to the beam motor. The beam motor has a tachometer to measure the angular velocity of the motor input shaft. In order to effectively suppress the flexural vibration of the beam, two of the three strain gages are sufficient for the active controller for feedback to the trolley motor and the beam motor. As a result, the system has two motors as inputs, two strain gages, two potentiometers, and one tachometer as outputs. All output signals are multiplied by proper control gains (see EAI

block In Fig. 4.1) in an analog computer and combined into feedback control signals for the trolley motor and the beam motor. The flowchart implemented in the EAI-2000 Analog Computer is also shown in Fig. 4.1. Several simulations are given in reference [38] to illustrate the feasibility and effectiveness of the active position control schemes in performing the translational and slewing tasks while suppressing flexural vibrations of the flexible beam.

Four different control cases are studied in both the experiment and the simulation. For each case, the trolley translates a certain displacement while the flexible beam slews an assigned angle. Basically, the control performances show the typical position controls while suppressing vibrational motion of the flexible beam. In the first case, the position control is demonstrated with no strain feedback. In the second case, the position control is studied by using the first two strain feedbacks only to the beam motor. In the third case, the position control involves position control with the first two strain feedbacks simultaneously to the trolley motor. In the fourth case, the position control is shown by applying the first two strain feedbacks simultaneously to the trolley and the beam motors. The corresponding output feedback gains for four control cases are illustrated in Table 4.9.

Table 4.1: Trolley motor (PMI type U9M2)

Function:

- Drive trolley via cable

Characteristic:

- 12 V-DC, 3600 RPM, 0.16 N-m continuous torque
- $3.2 \times 10\ kg\ m^2$ total inertia
- 2.35 N m pulse torque (5 ms @ 1% dutycycle)
- 7.1 Amp rated current
- Torque constant 0.0235 N m/Amp
- Back EMF constant 0.0232 V s/rad
- Armature resistance 0.175 Ohm
- Armature inertia $3.9 \times 10^{-2}\ kg\ m^2$

Measured characteristics:

- Input for measurement 1Volt SQ-wave @ 1Hz
- Resistance 0.42 Ohm @ 1 kHz
- Inductance 25 νh @ 1 kHz
- Capacitance 80 νf @ 1 kHz
- Impedence 7.15 Amp
- Voltage at motor 22.6 Volt
- Pulse repetition rate 22.6 kHz

Table 4.2: Potentiometer (Bourns 3500s-42-103)

Function:

- Measure angular displacement
- Null potentiometer is in parallel with potentiometer to set zero signal output

Characteristic:

- 10k Ohm+3%, 10 turns, linearity 0.1%
- Regulated +5 V-DC applied

Table 4.3: Beam and trolley characteristics

Steel beam:

- Length 1.1 m
- Rigidity 0.71 N m
- Mass/length 0.47916 kg/m
- Thickness 0.082×10^{-2} m

Rigid trolley:

- Mass 3.201 kg

Trolley track:

- Length 2.5 m

Conversion factors:

Beam pot. (angle)	72.70	deg./V
Trolley pot. (position)	0.096	m/V
Strain	2.64	V/in/in

Table 4.4: Beam motor (DC MICROMO MOTORS) (series 3540-006C)

Function:

- Drive for beam

Characteristics:

- 6 V-DC, 6000 RPM, 210 mA no load current
- Permanent magnet type
- Gear box 210:1 reduction
- 6.82 oz-in stall torque
- Integral tachometer (14 Volt+10%/1000 RPM)
- Torque constant 0.0092 V s/rad
- Armature resistance 1.1 Ohm
- Armature inertia $2.3 \times 10^{-5}\ kg\ m^2$

Measured characteristics:

- Input for measurement 300 mV SQ-wave @ 1 Hz
- Resistance 0.40 Ohm @ 1 kHz
- Inductance 110 mh @ 1 kHz
- Capacitance 2.5 mf @ 1 kHz
- Impedence 12.8 Ohm
- Current 1.63 Amp
- Voltage at motor 20.5 Volt
- Pulse repetition rate 22.6 kHz

Tachometer of beam motor: (Built-in MicroMo T9)

- Maximum speed 5000 RPM
- Armature resistance 23 Ohm
- Moment of inertia $1.06 \times 10^{-5}\ kg\ m^2$

Table 4.5: Strain gages (MICRO-MEASUREMENTS INC.) (type CEA-06-187VW-350)

Function:
– Measure longitudal bending moment of beam
Characteristics:
– 350 Ohm nominal resistance
– 2.075 nominal gage factor
– Full bridge, mounted for bending moment only

Table 4.6: Precision instrument amplifier (NASA model-83: 7 channels)

Function:
– Amplify and condition strain gage and feedback potentiometer signals
Characteristics:
– Reg. +5 V-DC voltage supplied to gage
– Panel mounted balance control (10 turn), RUN/ZERO switch, calibration switch
– Internal regulated power suppliers $\pm$ 15 V, $\pm$ 5 V
– Panel mounted gain control: 1, 2, 5, 10, 20, 50, 100 (switchable)
– IC complement: 1 $_{EA}$ AD524BD, 2 $_{EA}$ OP-7 per channel

Table 4.7: Pulse amplifier (LOPLEY CONTROLS CORP.) (model 241)

Amplifier:

Type:

- High power, high frequency, switching amplifier with bridge type output

Function:

- Width-modulated current pulses to drive motors *Characteristics:*
- Inputs: Differential signal input, auxiliary input, tachometer input
- Output: 22 kHz variable width current pulses, current monitor 0.1 V/Amp
- Failsate circuits: Overload, current limit, temperature, travel limits
- Peak power output 150 Volt (at 60 Amp, 9 kW)
- Current limit 3 to 60 Amp
- Power requirement 30 to 155 Volt (at 60 Amp)

Front – end controller for amplifier:

Type:

- Special design and fabrication by NASA

Function:

- Control interface to servo-amplifiers

Characteristics:

- 2 channel control-indicator inputs: BNC connectors for reference input, auxiliary input and tachometer input terminal boards for limit switches
- Controls: Enable/Disable, over-current reset
- Indicators: Enable, over-current, +limit, -limit

Table 4.8: Power supply (HP 6032A)

Function:

- Supply high 15 Amp current, low 24 V-DC voltage to servo-amplifiers

Characteristics: (type CV/CC)

- Output: 0-60 Volt @ 0-50 Amp
- Regulation: Voltage -0.01 %+5 mV

  Current -0.01 %+10 mA
- Accuracy: Voltage -0.035 %+40 mV

  Current -0.02 %+85 mA

Table 4.9: Output feedback gains on EAI flowchart

(1) **Case1**:

$$K = -\begin{pmatrix} 5 & 0 & 0 & 0 & 0 & 0 & 0 & 0 & 0 & 0 \\ 0 & 10 & 0 & 0 & 0 & 0 & 0.41 & 0 & 0 & 0 \end{pmatrix}$$

(2) **Case2**:

$$K = -\begin{pmatrix} 5 & 0 & 0 & 0 & 0 & 0 & 0 & 0 & 0 & 0 \\ 0 & 10 & 1000 & 1000 & 0 & 0 & 0.41 & 0 & 0 & 0 \end{pmatrix}$$

(3) **Case3**:

$$K = -\begin{pmatrix} 5 & 0 & 1000 & 1000 & 0 & 0 & 0 & 0 & 0 & 0 \\ 0 & 10 & 0 & 0 & 0 & 0 & 0.41 & 0 & 0 & 0 \end{pmatrix}$$

(4) **Case4**:

$$K = -\begin{pmatrix} 5 & 0 & 1000 & 1000 & 0 & 0 & 0 & 0 & 0 & 0 \\ 0 & 10 & 1000 & 1000 & 0 & 0 & 0.41 & 0 & 0 & 0 \end{pmatrix}$$

§ 4.4 Experimental and simulation results

In this setup, the maneuvering experiment and a simulation of the experiment are performed using local and output feedback controls. The architecture of the system is shown in Fig. 4.1. The simulation is carried out with an aid of DE nonlinear integration subroutine [70] in FORTRAN language. In the experiment, two feedback control inputs are provided for the motors of the trolley and beam. The output measurements involve: (1) Trolley displacement: measured by a potentiometer which is connected with the shaft of the trolley pulley at one end of the track. (2) Beam root angle and angular velocity: measured respectively by the built-in potentiometer and tachometer. (3) Three strains of arm: sensed through three strain gages located in the root, 22% and 50% of the beam length respectively. During the control process, signals of output measurements and two inputs are processed to the Real Time Gen-Rad Analyzer for data storage. For the sake of comparison, each experimental result and the corresponding simulation result are drawn together and denoted by the solid line and dash line respectively in the same plot. Note that the simulation results are converted into voltages according to the conversion factors in Table 4.3.

In order to investigate the influence of the flexibility feedback, four different control cases are studied in both the experiment and the simulation. For each case, the trolley translates approximately 0.45 m, while the flexible beam slews about 25 deg. Figure 4.2 demonstrates this mission of position control. The first case demonstrates position control with no strain feedback. The second case studies position control with the first two strain feedbacks only to the beam motor. The third case involves position control with the first two strain feedbacks simultaneously to the trolley motor. The fourth case shows the position control with the first two strain feedbacks simultaneously to the trolley and the beam motors.

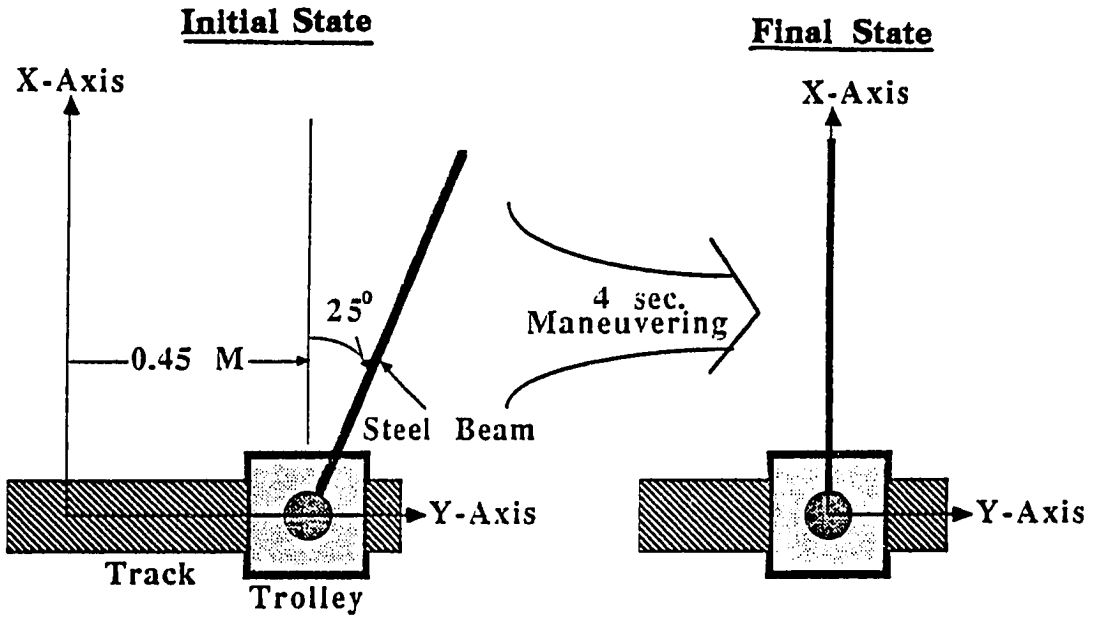

Figure 4.2: Maneuvering mission of one flexible steel beam on a trolley

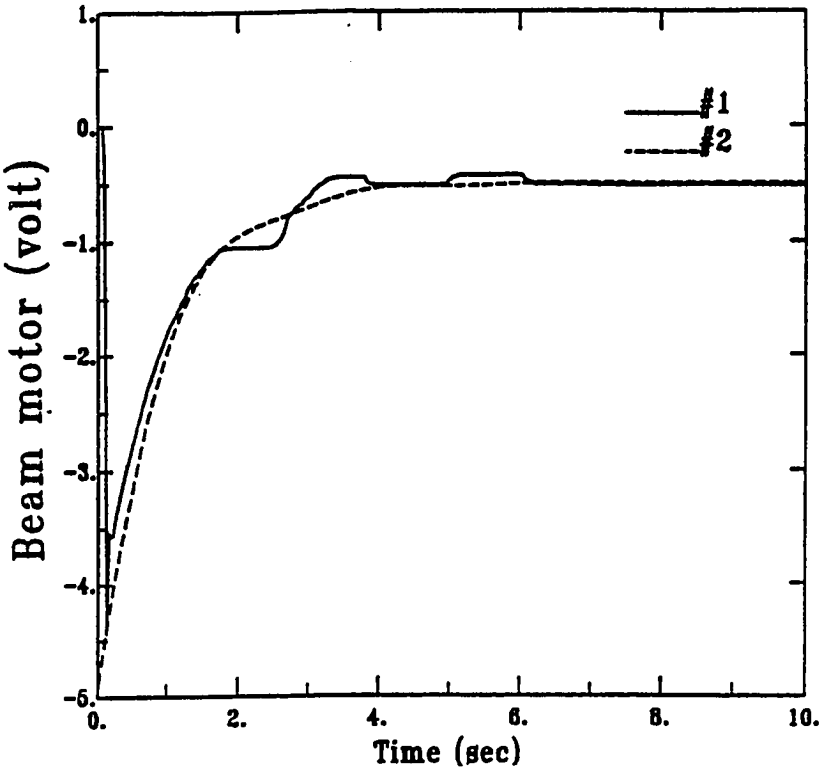

Figure 4.3: Beam motor of slewing maneuver without strain feedback

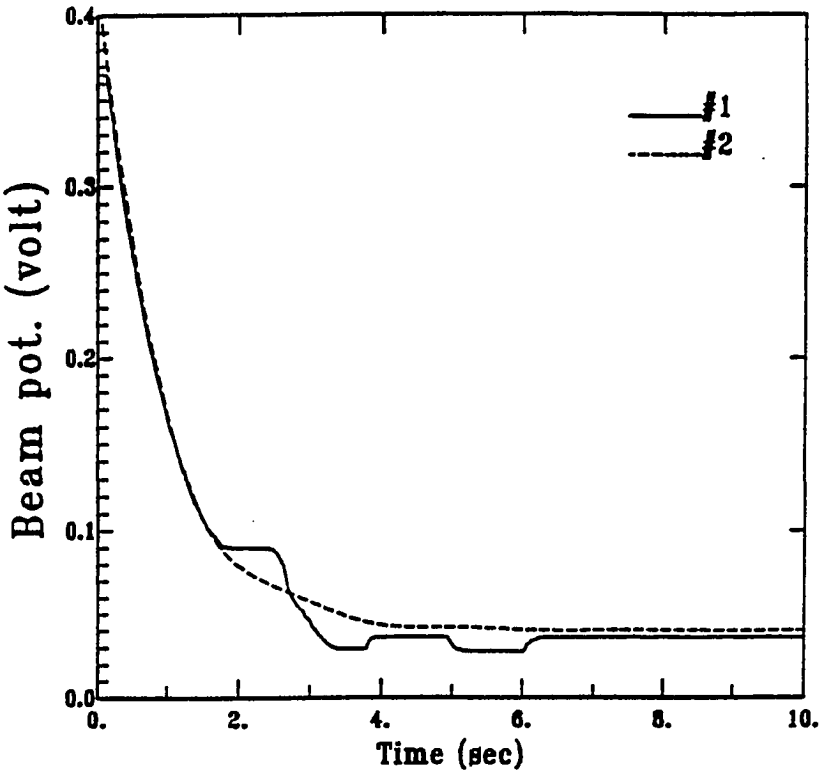

* #1: Experiment; #2: Simulation

Figure 4.4: Beam potentiometer of slewing maneuver without strain feedback

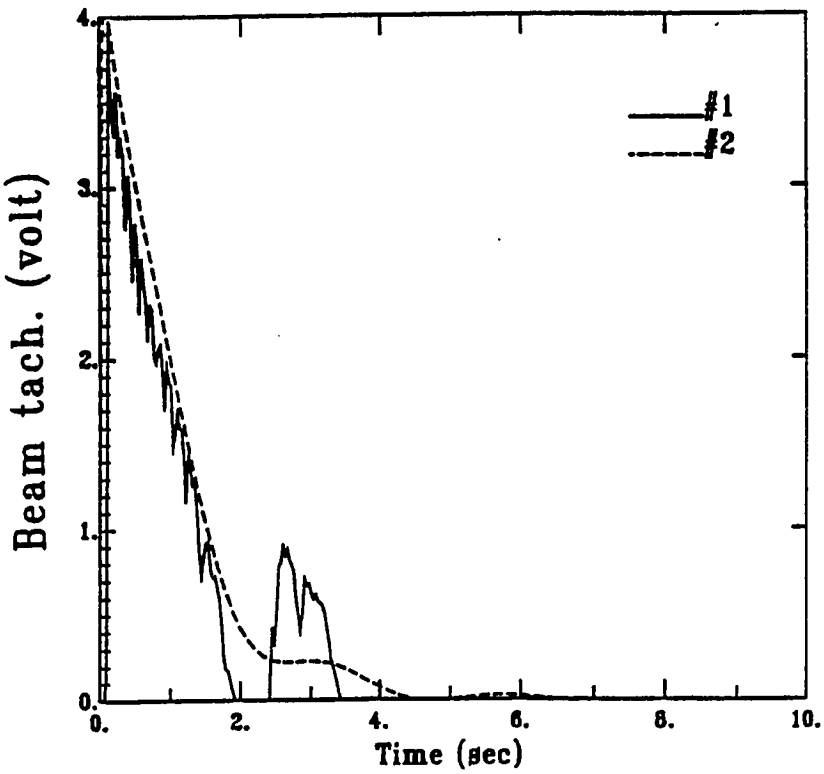

Figure 4.5: Beam tachometer of slewing maneuver without strain feedback

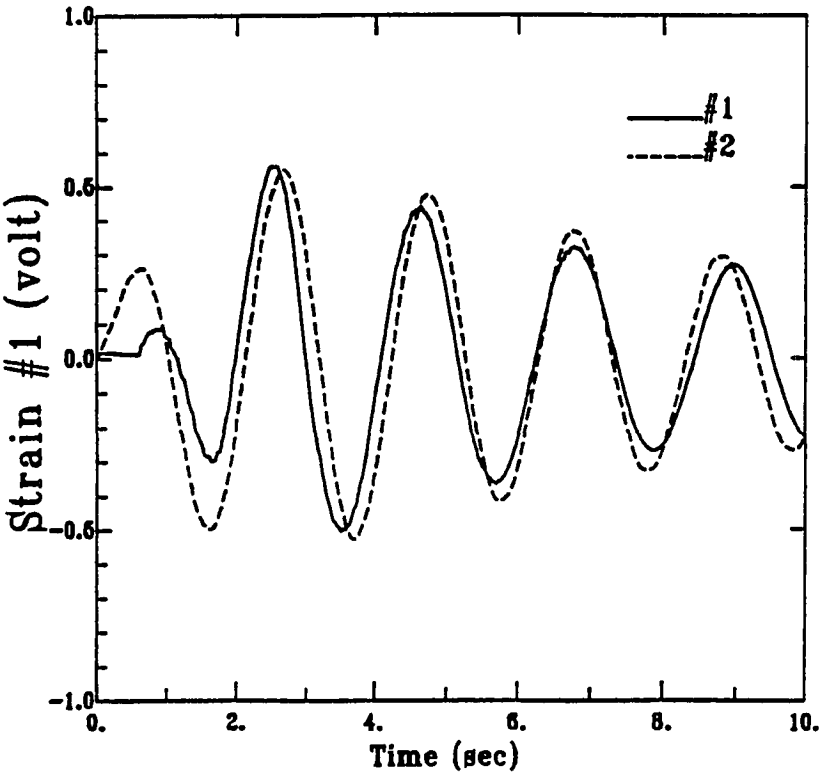

* #1: Experiment; #2: Simulation

Figure 4.6: Strain #1 of slewing maneuver without strain feedback

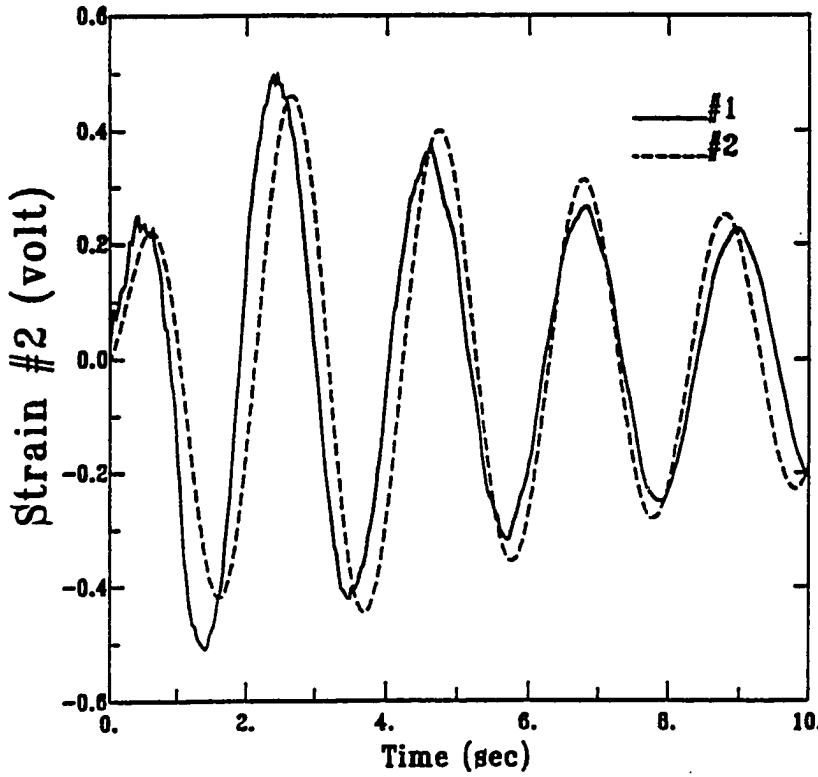

Figure 4.7: Strain #2 of slewing maneuver without strain feedback

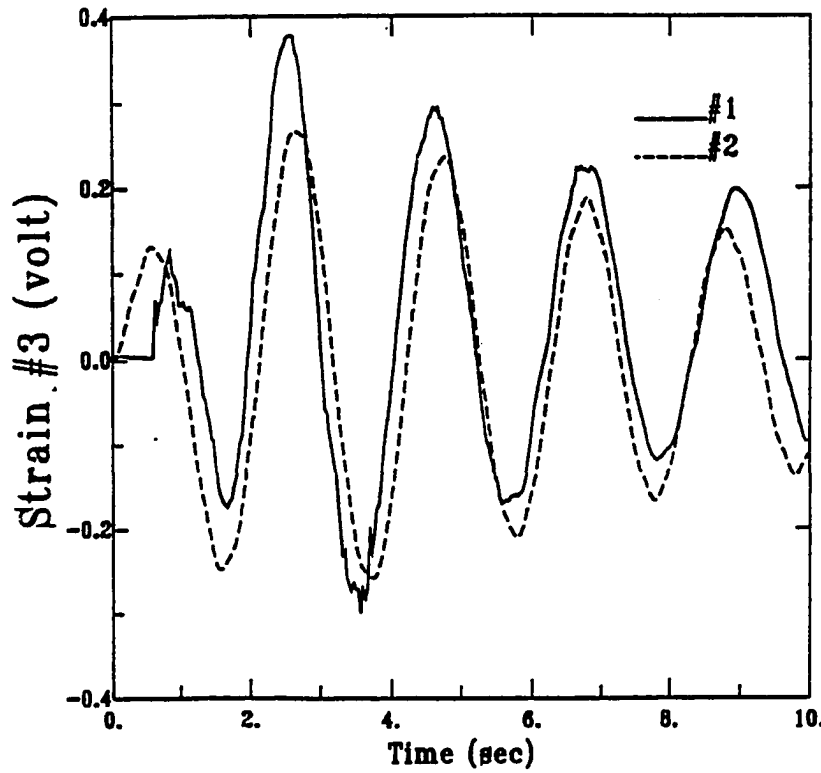

* #1: Experiment; #2: Simulation

Figure 4.8: Strain #3 of slewing maneuver without strain feedback

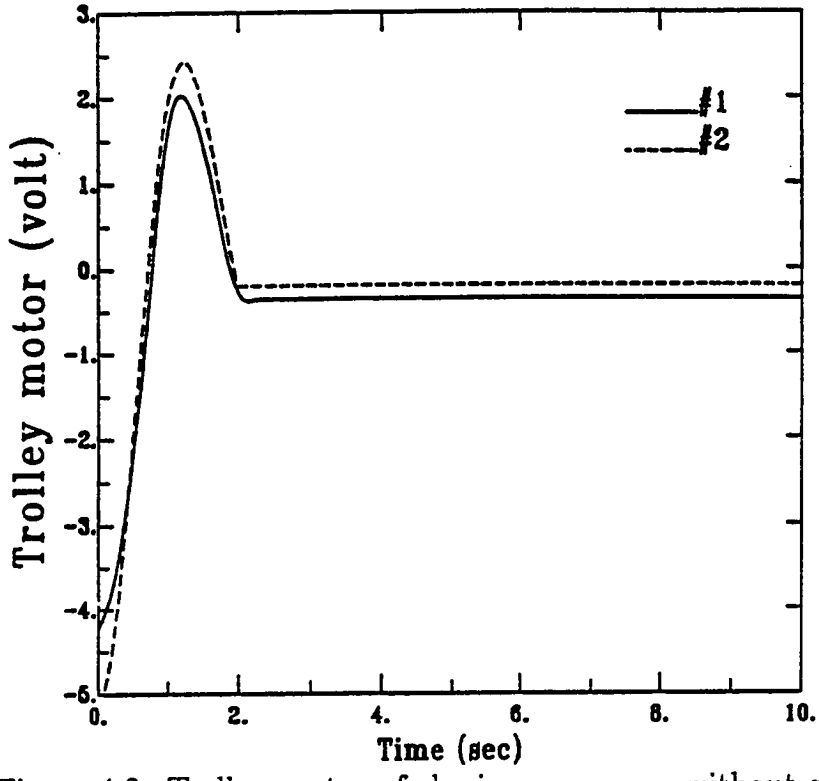

Figure 4.9: Trolley motor of slewing maneuver without strain feedback

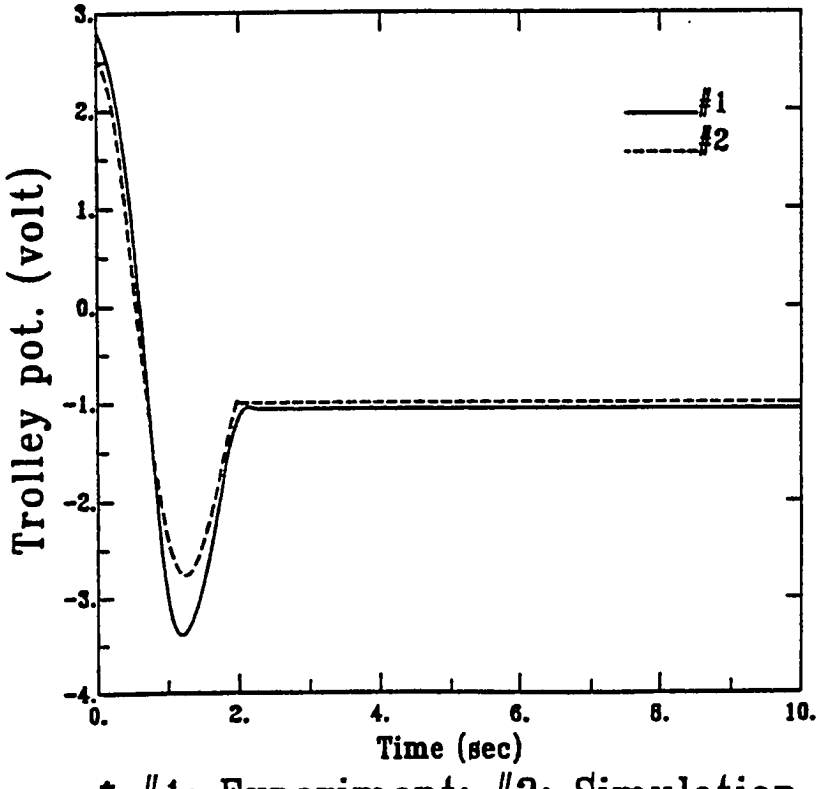

* #1: Experiment; #2: Simulation

Figure 4.10: Trolley potentiometer of slewing maneuver without strain feedback

The first case, shown in Figs. 4.3-4.10, has no strain feedback. In other words, only the translational motion of the trolley and the slewing of the beam are manipulated while neglecting beam flexural vibration. Each plot shows sensor and simulation voltages versus time. The good fitness between the experimental and simulation results is demonstrated in Figs. 4.3-4.10. Noise occurs fairly significantly in the experimental tachometer of Fig. 4.5. The beam control input starts initially at -3.8 V and reduces to -0.5 V in 6.9 sec. The angle and angular velocity of the the beam damp out at 6.8 sec and 3.6 sec respectively. The trolley control input starts initially at -4.4V, increases to a peak value of 2 V in 1.2 sec, and then decreases to a constant value of -0.4 V within 2.3 sec. The trolley position has a large overshoot and ends at 2.1 sec. The damping of the trolley translational motion basically comes from the back-EMF of the trolley motor and the friction between the trolley and the track. With no strain feedback, figures 4.6-4.8 show three almost undamped strain measurements with the first mode frequency at 0.44 Hz. The beam vibration is mainly excited by the angular motion of the beam and the translational motion of the trolley. In both the experiment and simulation, the vibration is clearly dominated by the first mode. It is a good example of why the strain information must be applied to control inputs for the active control of flexural vibration.

The second case adds strain feedback to the beam motor (Figs. 4.11-4.18). The control input to the beam motor includes the feedbacks of the beam angle and its angular velocity, and the first two strains. During this experimental maneuver, the beam motor excites the higher order modes, which are not expected in the simulation, such that the experimental results are a little bit different from the simulation results. Figure 4.12 shows that the desired beam angle is reached within 3.8 sec, which is shorter than the first case. The response of the beam angular velocity (Fig. 4.13) demonstrates a significant difference due to the flexibility (strain) feedbacks. It is very interesting to see how the beam motor reacts with the flexural vibration. The beam motor rotates the beam to the desired angle

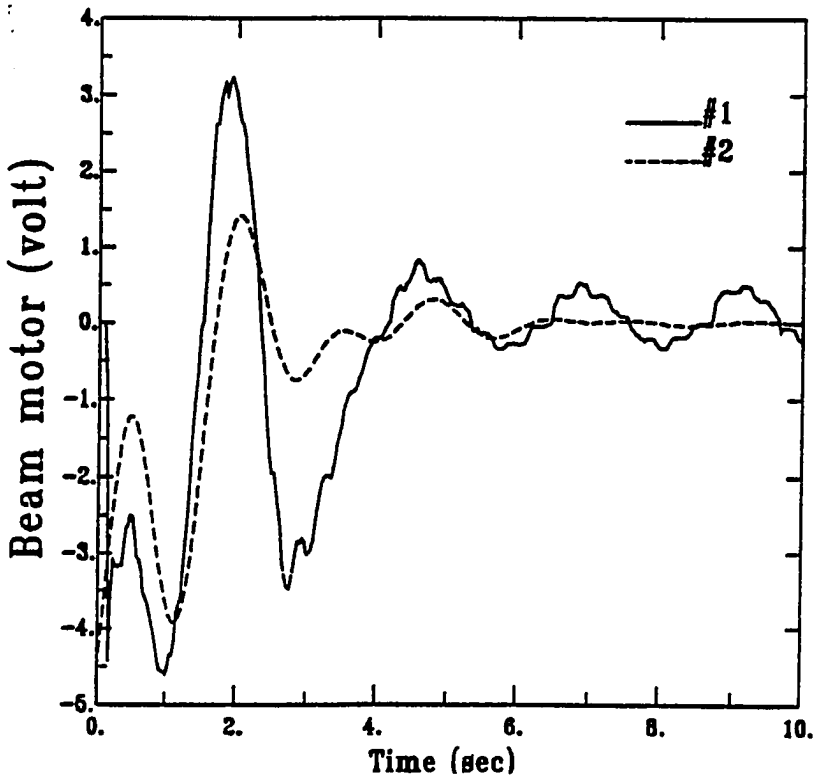

Figure 4.11: Beam motor of slewing maneuver with strain feedback to beam motor

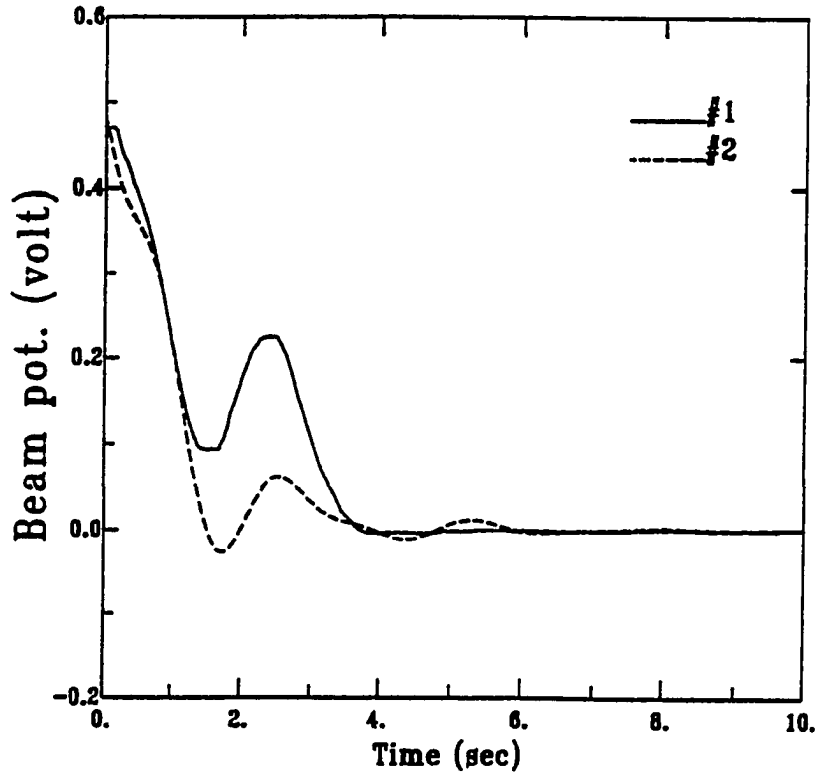

* #1: Experiment; #2: Simulation

Figure 4.12: Beam potentiometer of slewing maneuver with strain feedback to beam motor

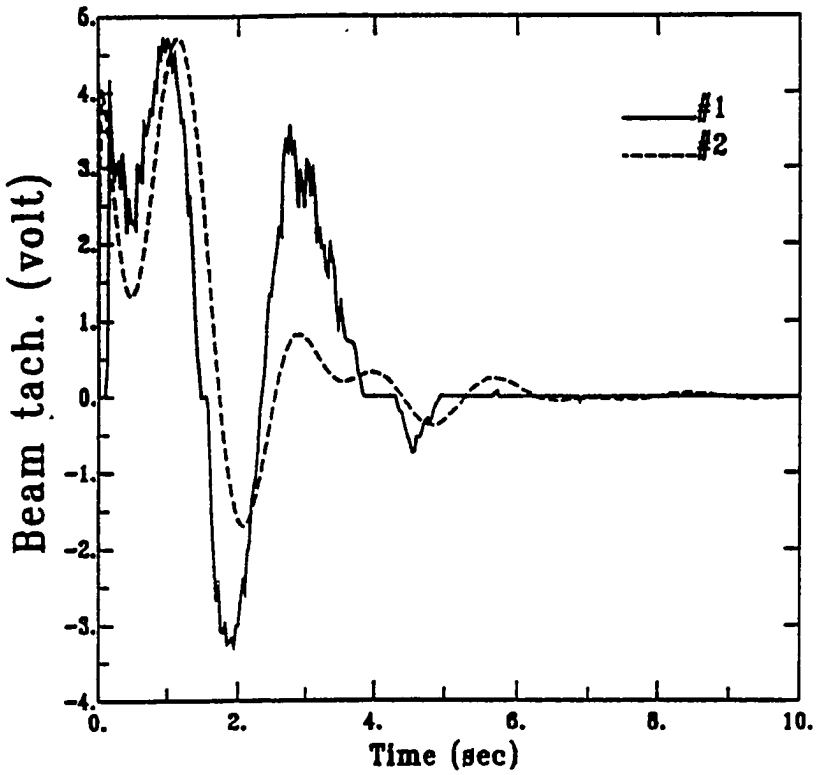

Figure 4.13: Beam tachometer of slewing maneuver with strain feedback to beam motor

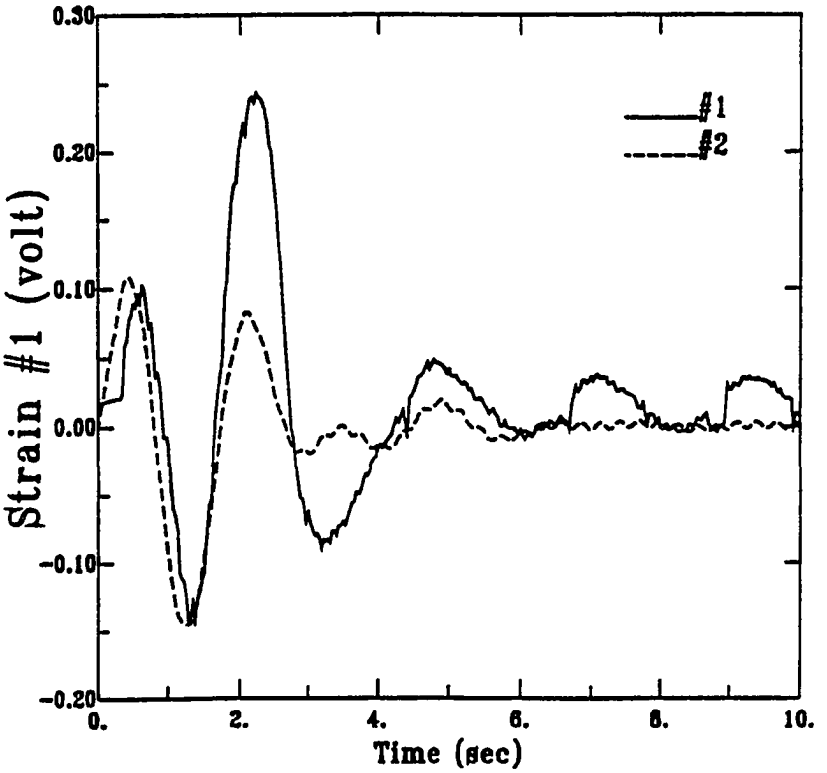

* #1: Experiment; #2: Simulation

Figure 4.14: Strain #1 of slewing maneuver with strain feedback to beam motor

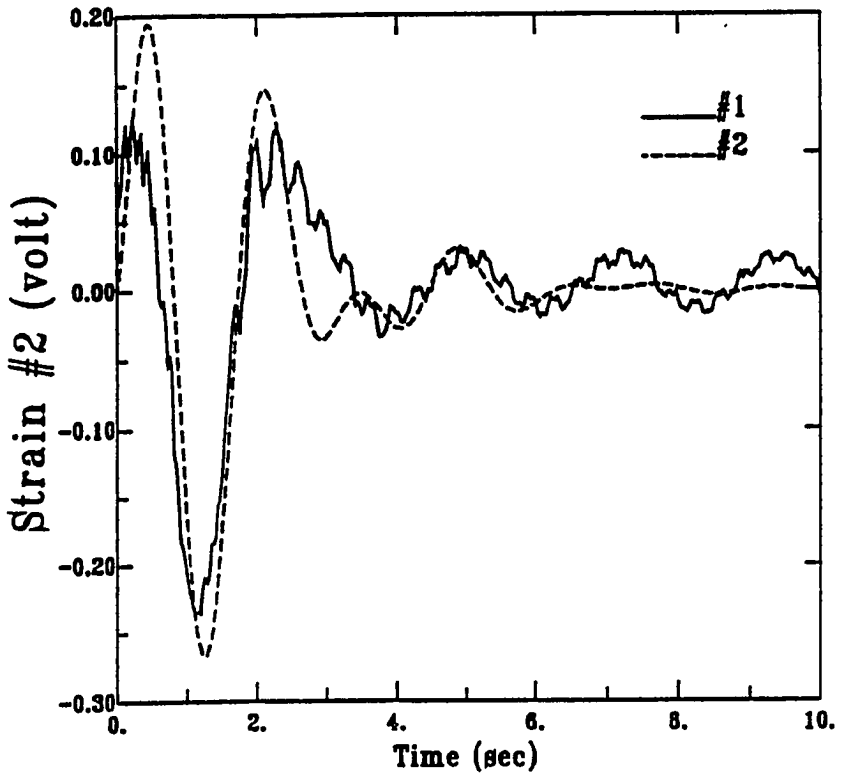

Figure 4.15: Strain #2 of slewing maneuver with strain feedback to beam motor

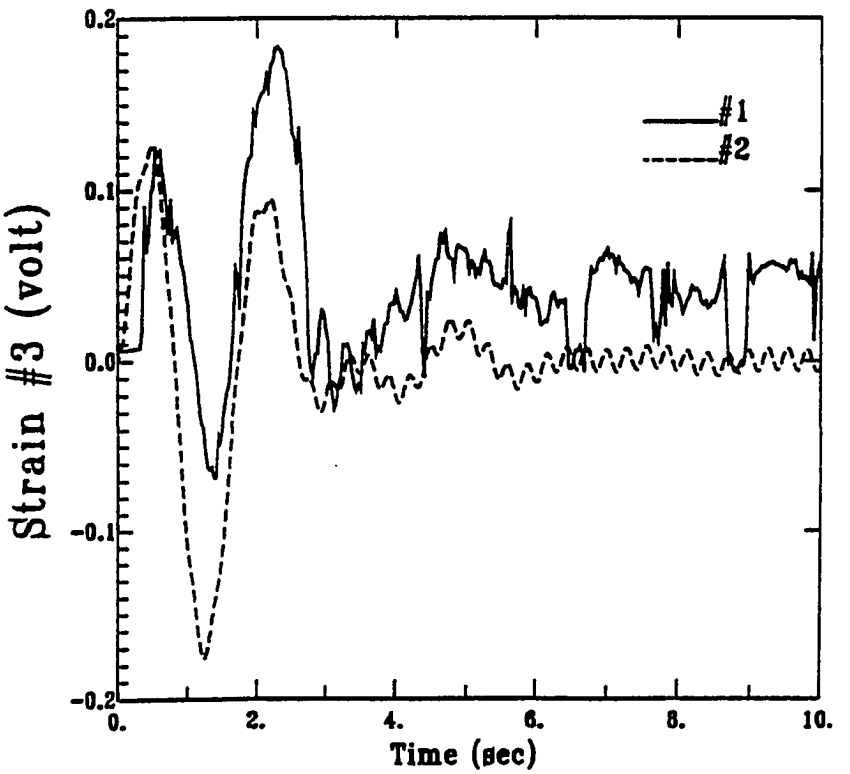

* #1: Experiment; #2: Simulation

Figure 4.16: Strain #3 of slewing maneuver with strain feedback to beam motor

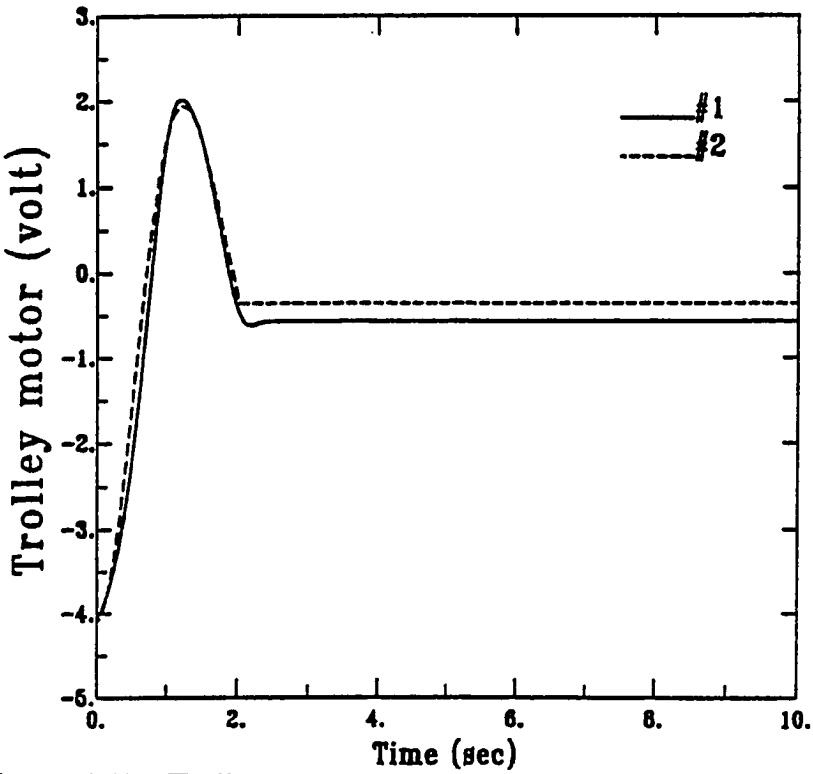

Figure 4.17: Trolley motor of slewing maneuver with strain feedback to beam motor

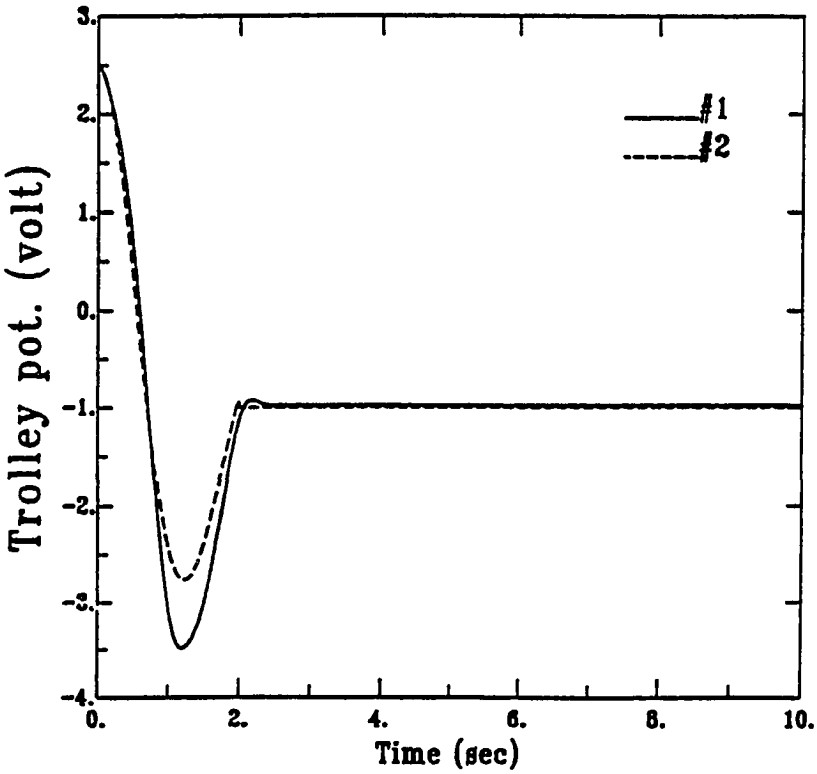

* #1: Experiment; #2: Simulation

Figure 4.18: Trolley potentiometer of slewing maneuver with strain feedback to beam motor

while simultaneously suppressing the beam vibration based on the information of two strain measurements. With two strain feedbacks to the beam motor, the peak amplitudes of the three measured strains, in Figs. 4.14-4.16, are decreased by about 45% as compared to the previous ones in Figs. 4.6-4.8. The high frequency modes are more active in the third measured strain (Fig. 4.16) because strain #3 is located further away from the root end of the beam. Obviously, the flexural vibration of the beam diminishes more rapidly than the first case. Note that residual vibrations from high frequency modes are visible in the root strain (strain #1). The trolley motor still has local feedback from the trolley position only. Figure 4.17 shows that the trolley control input begins with a -4.2 V and reduces to -0.5 V within 2.1 sec. It takes the trolley about 2 sec to reach the terminal position as shown in Fig. 4.17. Basically, the trolley input and the trolley position histories are similar to the ones in the first case because of the absence of strain feedbacks to the trolley motor in both cases. And all experimental results associated with the trolley match the corresponding simulation results in Figs. 4.17 and 4.18.

The third case studies the position control with the strain feedback to the trolley motor only. The results in this case are comparable to those in the second case, which has flexibility feedback to the beam motor only. The beam control input, shown in Fig. 4.19, has a smoother critical damping behavior than those shown in Figs. 4.3 and 4.11. Similarly, the beam angle also shows a smooth critical damping response and reaches its desired angle within 2.5 sec. No overshoot appears in the beam angular velocity in this case. Apparently, the previous three experimental results of the beam are fitted by the simulation results. The control input, shown in Fig. 4.25, for the trolley motor is more irregular than that in the two previous cases. The trolley motor in this case takes full responsibility for the flexural vibration of the beam. The unexpected high modes which are fed back into the trolley motor input perhaps cause the difference of the experimental results from simulation results in Figs. 4.25-4.26. The trolley takes approximately 6 sec to reach the desired position. It is obvious that the beam flexibility does

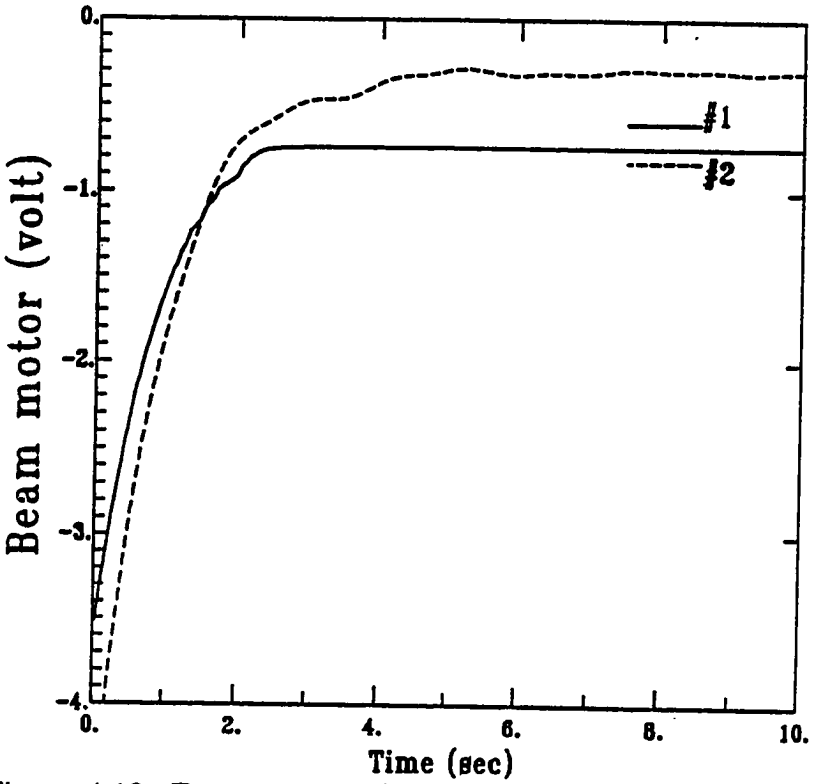

Figure 4.19: Beam motor of slewing maneuver with strain feedback to trolley motor

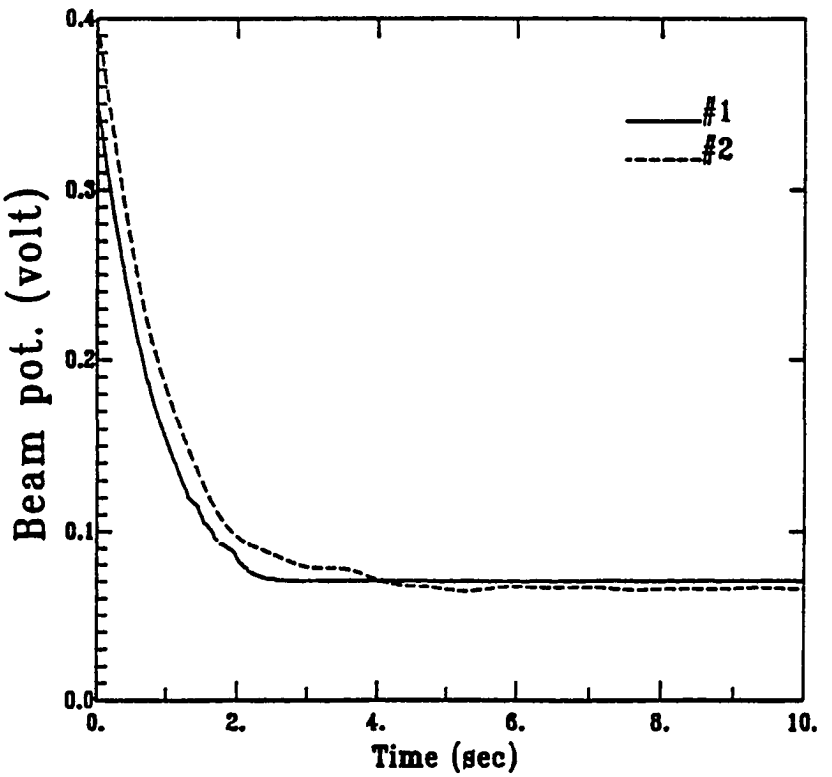

* #1: Experiment; #2: Simulation

Figure 4.20: Beam potentiometer of slewing maneuver with strain feedback to trolley motor

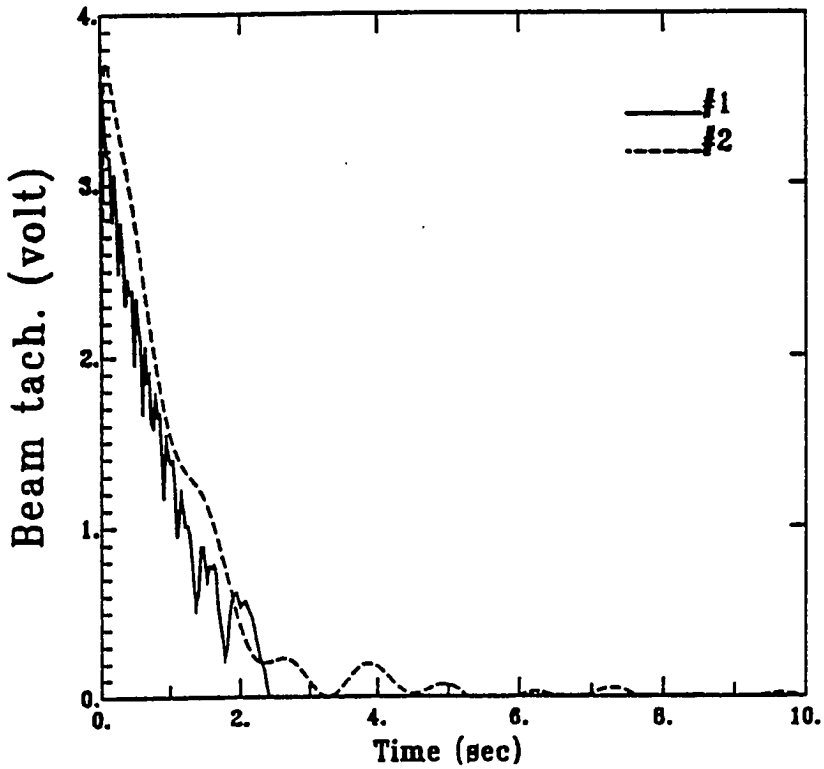

Figure 4.21: Beam tachometer of slewing maneuver with strain feedback to trolley motor

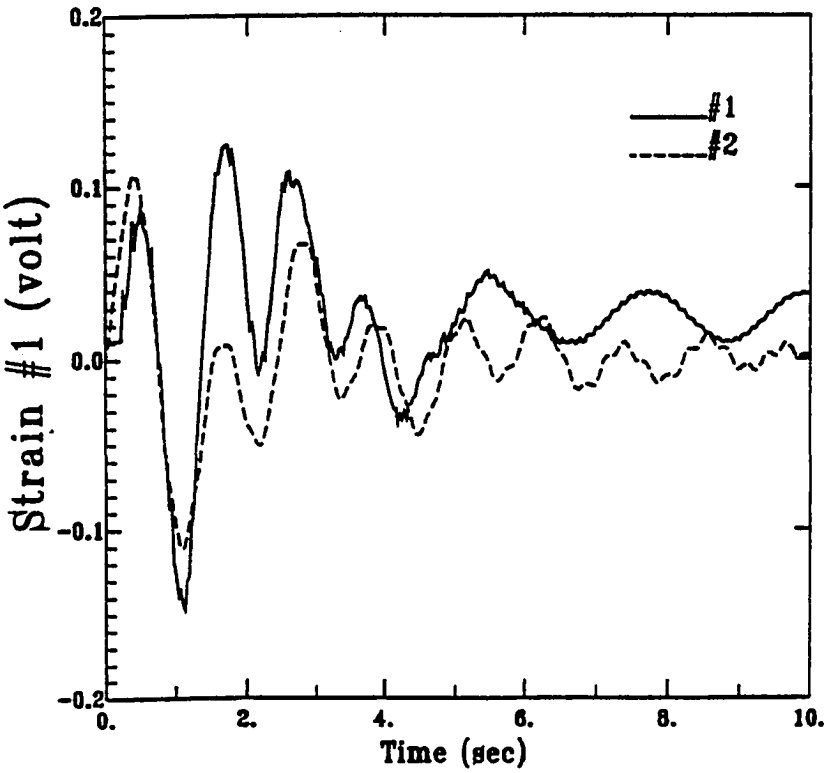

* #1: Experiment; #2: Simulation

Figure 4.22: Strain #1 of slewing maneuver with strain feedback to trolley motor

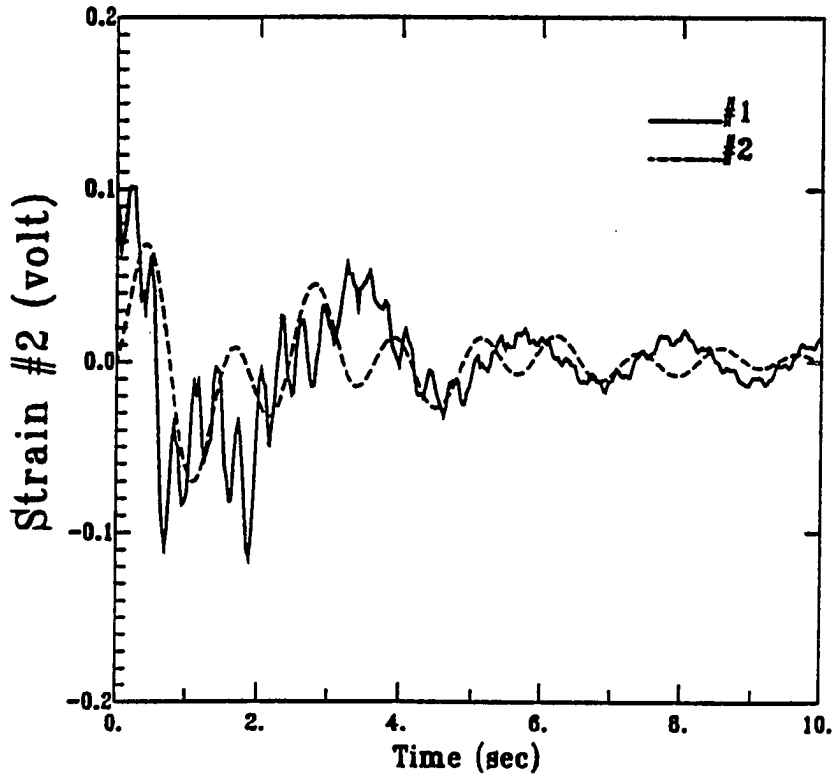

Figure 4.23: Strain #2 of slewing maneuver with strain feedback to trolley motor

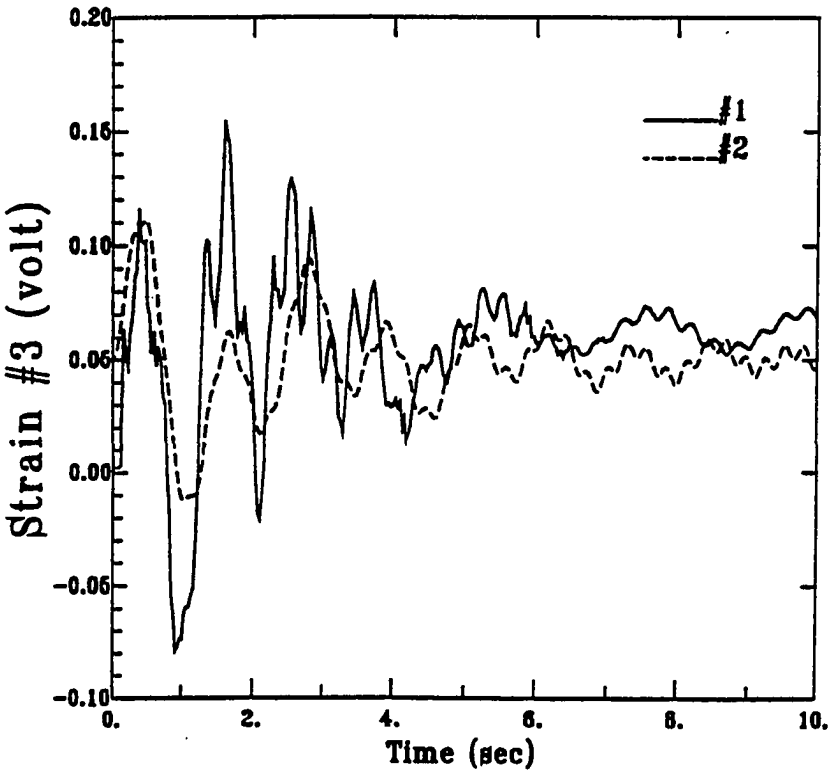

* #1: Experiment; #2: Simulation

Figure 4.24: Strain #3 of slewing maneuver with strain feedback to trolley motor

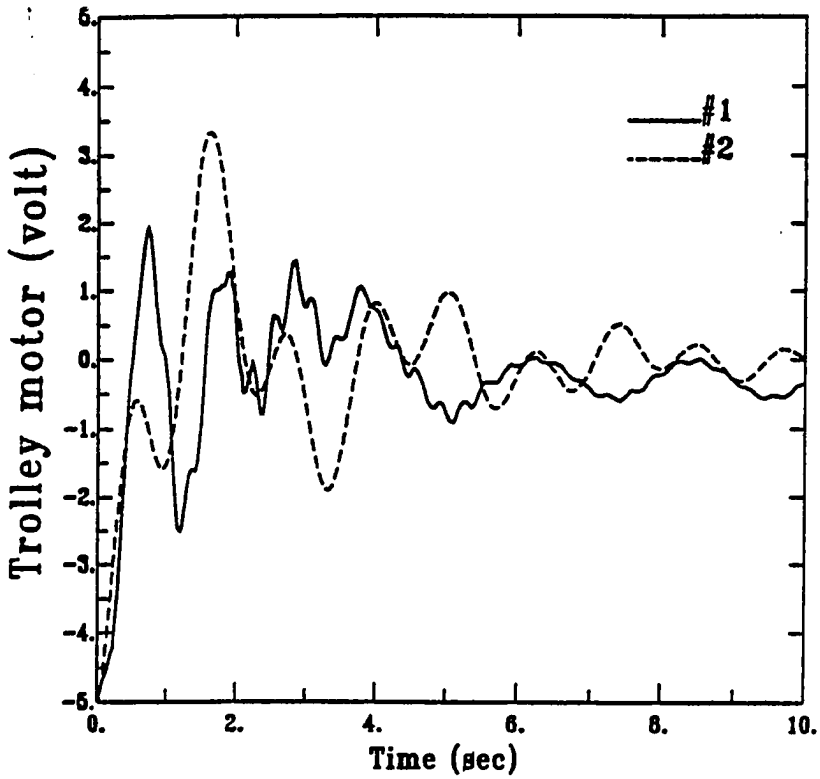

Figure 4.25: Trolley motor of slewing maneuver with strain feedback to trolley motor

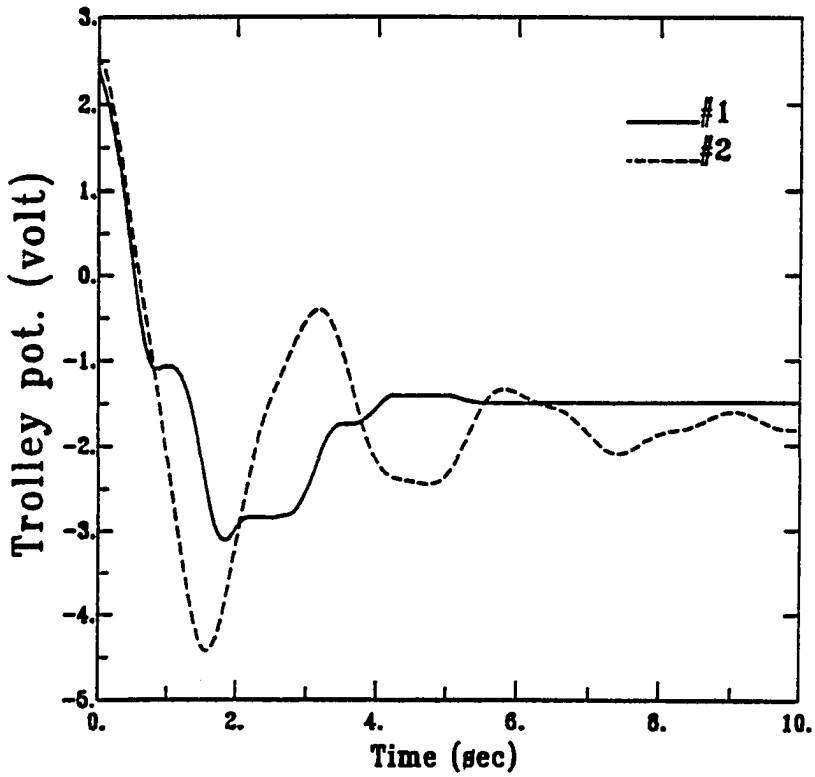

* #1: Experiment; #2: Simulation

Figure 4.26: Trolley potentiometer of slewing maneuver with strain feedback to trolley motor

influence the response of the trolley position. The peak magnitudes of the three measured strains are reduced by 21% to 26% as compared to the first case. The time history of the root strain (strain ♯1) is somewhat smoother than that for the second case in both experiment and simulation. This is because the higher modes are more difficult to excite indirectly by the trolley motor than by the beam motor. The significant behaviors of high frequency modes are observed through the measured strains gages ♯2 and ♯3 in Figs. 4.23 and 4.24. Both the second and third cases provide some insight into the system responses to different controller designs.

The fourth case studies the position control with both the beam motor and the trolley motor using strain feedback to suppress the beam vibration with the same gains as the ones in the second and third cases. The trolley motor not only moves the trolley along the track to the desired location but also provides the damping to the flexible beam. Similarly, the beam motor rotates the beam while suppressing the flexural vibration of the beam by using the strain feedback. Hence, the dynamics of the trolley and the beam are related by the coupled inertia and nonlinear forces, as well as the control input due to strain feedback. The responsibility of the beam control input for suppressing vibration is reduced, as shown in Fig. 4.27. The overshoots which took place before the end of beam rotation in the second case drop significantly due to the flexibility control from the trolley motor. The beam angle takes 5 sec to reach the desired angle without an overshoot. The beam angular velocity takes about the same time to settle down with a very slight overshoot and its peak magnitude is reduced as compared to that in the second case. The trolley moves to the terminal position in 4.3 sec, as shown in Fig. 4.34. The strain feedback shows a significant influence on both the trolley control input and the beam control input, which in turn suppresses the flexural vibration. The peak magnitudes of the three measured strains are decreased by 60% to 80% of the amounts in the first case, compared to a reduction at only 45% when strain feedback was supplied to the beam motor only. The

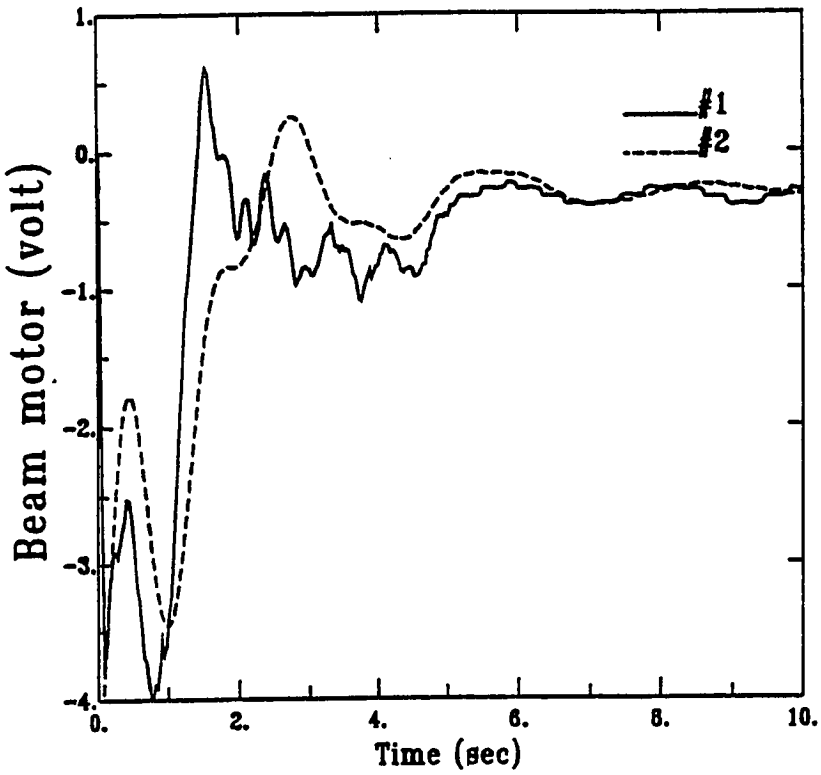

Figure 4.27: Beam motor of slewing maneuver with strain feedback to beam and trolley motors

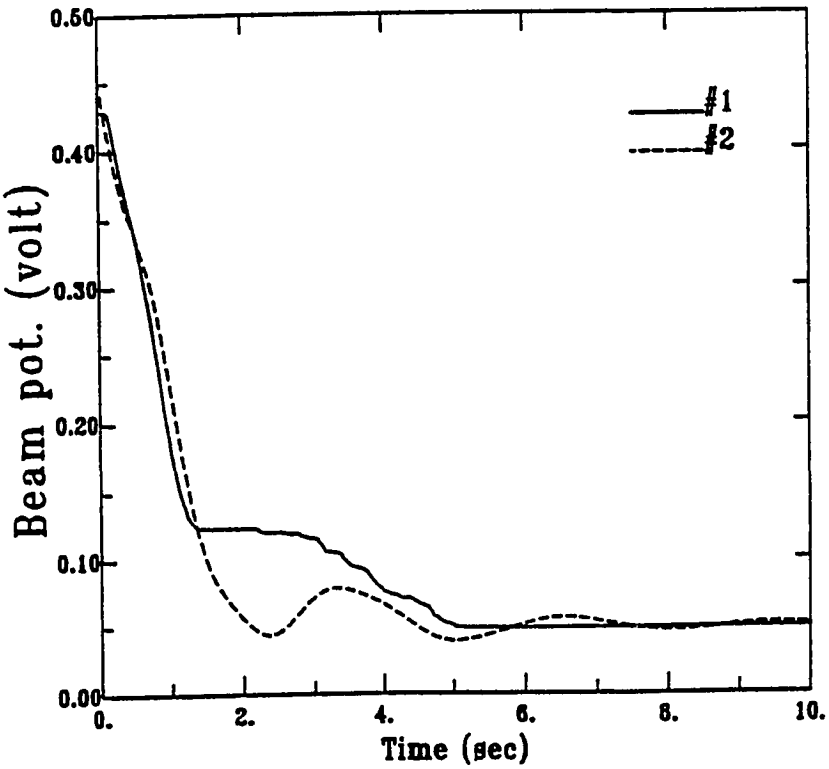

* #1: Experiment; #2: Simulation

Figure 4.28: Beam potentiometer of slewing maneuver with strain feedback to beam and trolley motors

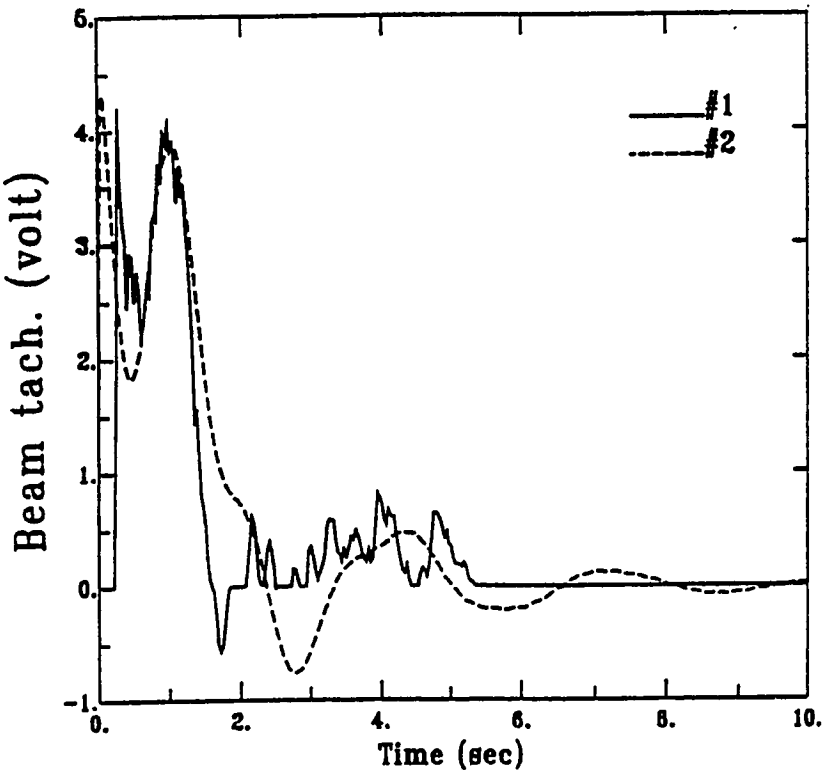

Figure 4.29: Beam tachometer of slewing maneuver with strain feedback to beam and trolley motors

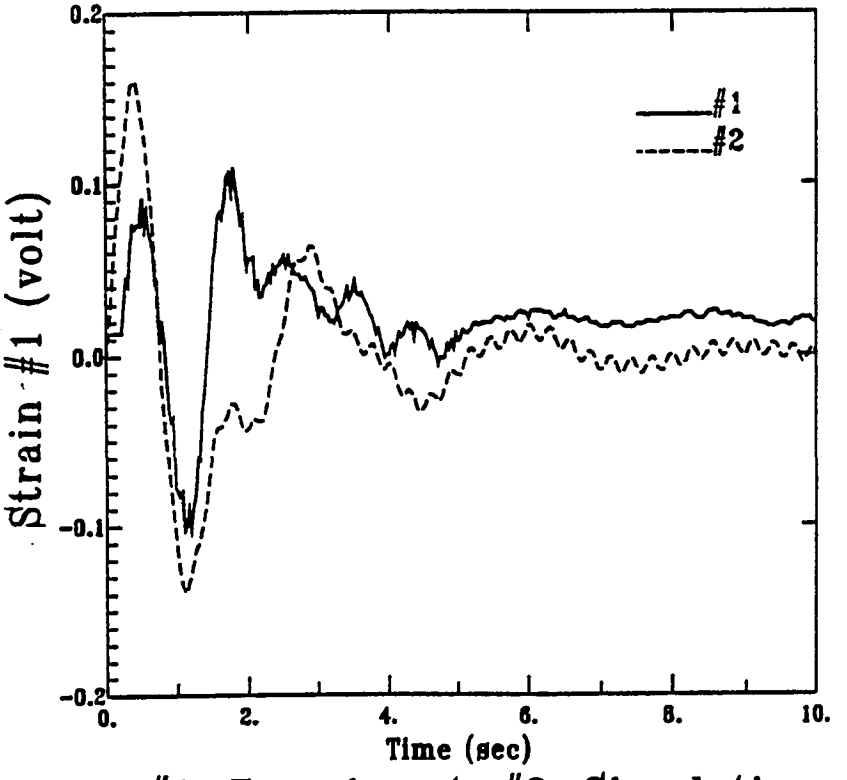

* #1: Experiment; #2: Simulation

Figure 4.30: Strain #1 of slewing maneuver with strain feedback to beam and trolley motors

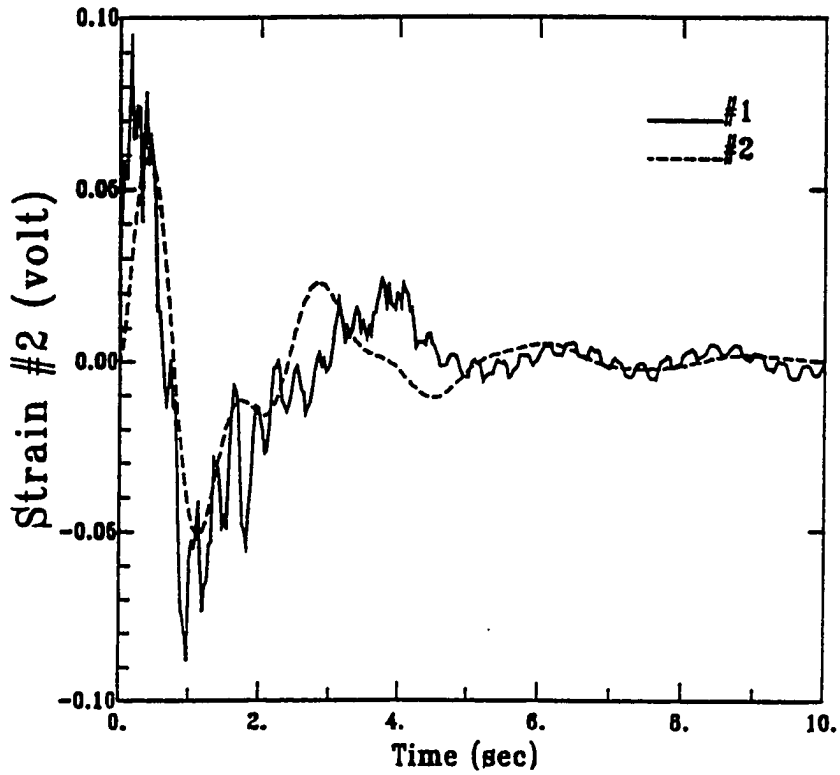

Figure 4.31: Strain #2 of slewing maneuver with strain feedback to beam and trolley motors

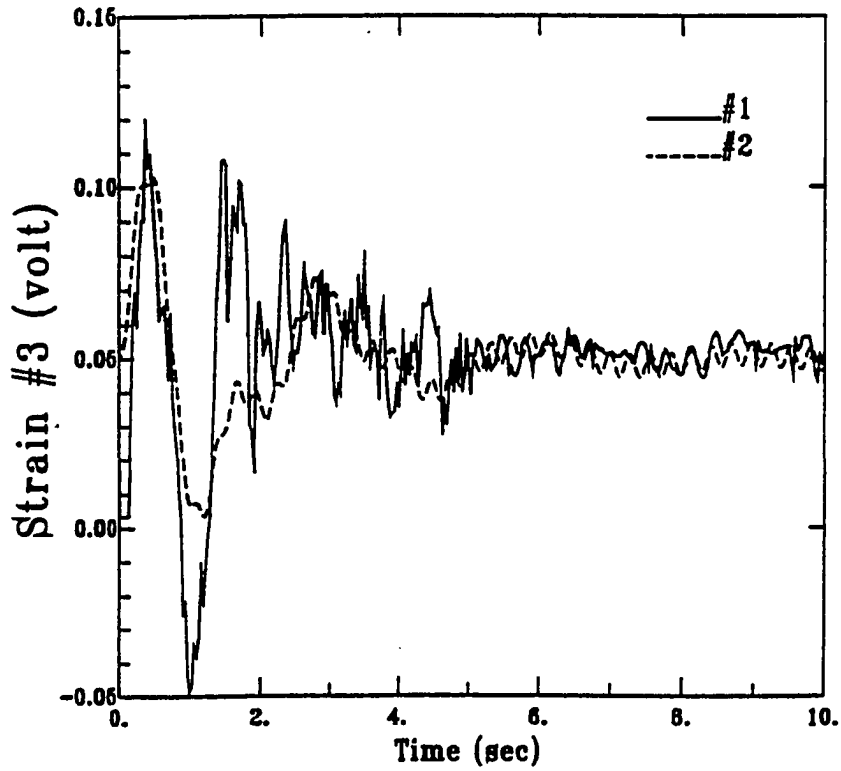

* #1: Experiment; #2: Simulation

Figure 4.32: Strain #3 of slewing maneuver with strain feedback to beam and trolley motors

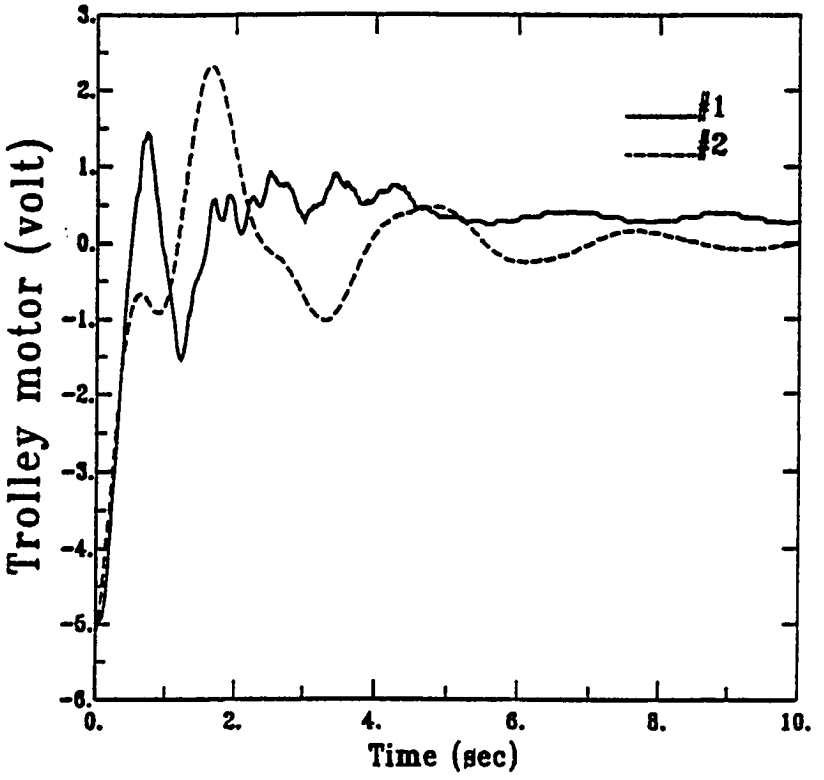

Figure 4.33: Trolley motor of slewing maneuver with strain feedback to beam and trolley motor

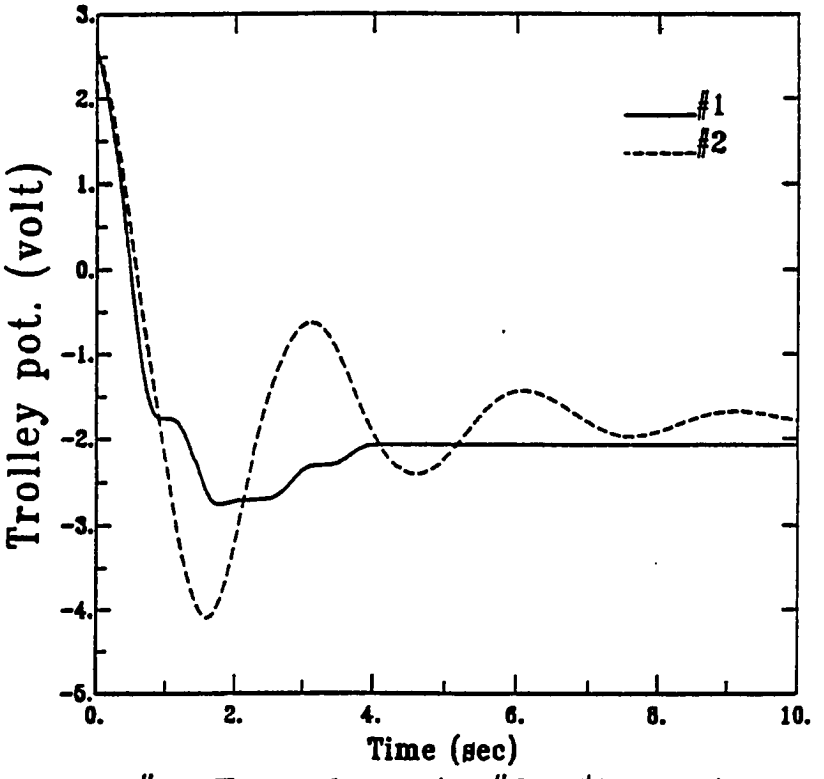

* #1: Experiment; #2: Simulation

Figure 4.34: Trolley potentiometer of slewing maneuver with strain feedback to beam and trolley motors

vibrational modes which are observed in Fig. 4.32, obtain higher frequencies than the previous three cases. The residual vibration is considerably reduced. Hence, the experimental and simulation results imply that the best performance of rapid position control is achieved by having strain feedback to both the trolley motor and the beam motor.

§ 4.5 Discussion and summary

In this chapter, simulation and experimental transient responses for slewing maneuvers of a flexible beam in multiple translational/rotational axes are presented. Four cases are studied, varying the strain feedback to the beam motor and trolley motor. Some decrease in flexural amplitude is achieved by adding feedback to only one motor. Further substantial decrease is achieved by adding strain feedback to both motors. The consequential results of four simulations and four experiments highlight the importance of the control feedback associated with strain gages for the space flexible structures.

For each case, the simulation is implemented to confirm the performance of the corresponding experiment for the assigned output feedback control. In the simulation, the flexible beam is modeled as a cantilever, and the deflection of the beam is characterized by the first three modes. Therefore, the simulation results can closely match the experimental results as long as the the higher modes of the beam are not excited. With the feedback of the flexibility, the behavior of higher modes has been easily observed through the measured strains ♯2 and ♯3 from case 2 to case 4. Without loss of generality, the simulation results still show their fitness toward the experimental results even though the higher modes are discarded in those simulations. On the other hand, the simulation herein ignores some negligible nonlinear effects such as the viscous air drag, the backlash of the gear box, the friction on the trolley wheels, and the wire slippery on pulleys. Such factors may cause the bias of the experimental results compared with the simulation results.

Several important issues related to slewing experiments with flexible structures include system nonlinearities, calibration of actuators and sensors. Nonlinear effects due to kinematic nonlinearities and large bending deflections during the large angle maneuver did not cause significant problems in this experiment. Special attention should be given to evaluating the back-EMF (Electro-Motive-Force) in an electrical motor which may provide significant passive damping for active control designs. In the simulation and experiment, there is no angular velocity feedback to the trolley motor. Significant damping because the trolley comes from the motor back-EMF and the friction between the trolley and the track. Appropriate use of the back-EMF may yield highly robust controller designs and reduce dependence on active suppression of the vibrational motion of flexible structures. Accurate measurements of the back-EMF may require significant efforts since it is usually a nonlinear variable. On the other hand, back-EMF induces damping for the beam motor basically comes from the angular velocity feedback. Experience has also shown that extension of many instruments will lead to accuracy problems in this type of laboratory experiment.

Obviously, the nonlinearities of this system behave significantly in the transient responses of three strains for each case since the rapid maneuvers excite the significant kinematic nonlinearities which affect the vibrational motion of the beam. In particular, the figures 4.27 and 4.33 show the influence of system nonlinearity upon the trolley and beam motors while the strain feedback is applied to both motors. To deal with such quick and nonlinear maneuvers, the analytical investigation of the nonlinear control design is required in Chapter 6 to compensate for the behavior of the system nonlinearities in the space flexible structures. And the stability of the nonlinear feedback control will be investigated in the Lyapunov's sense by evaluating the time derivative of Lyapunov function.

Chapter 5

NONCIRCULAR GEAR DESIGN FOR VIBRATIONAL REDUCTION IN FLEXIBLE STRUCTURES

The experiments of a flexible structure on a trolley in Chapter 4 have illustrated the slewing maneuvers performed through the feedback control methods. Herein, a noncircular gear mechanism (see Fig. 1.3) in conjunction with a control technique are integrated to enhance the maneuvering performance of large flexible space structures. Two convex cylinder-type cams, meshed by the wrapping of two pairs of thin metal bands, produce varying output speeds to input speeds. This speed variation tunes the kinematic characteristics of the flexible space structures during rapid slewing maneuvers while controlled by a regulator-type feedback controller. Pure rolling contact, hence, low friction between the noncircular cams, reduces stiction nonlinearities into the system. The instantaneous gear the ratio, which is defined as ratio of driven to driving angular velocities, can be determined by equating the pitch radii of the input to output cams at that moment. Based on a given desired maneuvering behavior, the gear ratio of the noncircular gears is specified as a hyperbolic function of the slewing angle. A mechanism synthesis method is employed to derive the design equations for the convex pitch profiles of two noncircular gears. The slewing maneuvers of two kinds of flexible space structures, i.e. a one-beam flexible structure and an articulated two-beam flexible structure, are investigated by using the designed noncircular gears to perform both positioning control tasks. The noncircular gears are installed at the junction of the motor and the flexible structure. Their regulator-type control problems are first solved using optimal control theory. Then, the resulting regulator feedback

gains are applied to the system. Furthermore, an optimization technique based on the Generalized Reduced Gradient Method [9-12] is employed to determine the optimal hyperbolic gear ratios as well as the optimal control gains to further suppress vibrational motions of the flexible beams. The simulation results associated with such optimal designs and parameters are then compared to the original noncircular gears.

§ 5.1 Concept of the noncircular gearing

The noncircular gears have gained much attention in their application of mechanical devices because they offer distinct advantages over linkages, band mechanisms, and cams. Generally, the noncircular gears are employed based on the following reasons [24]:

(1) **Cyclically varying angular velocity of the driven gear is demanded:** quick-return drives, intermittent mechanisms as in printing presses, planers, shears, winding machines, automatic-feed machines.

(2) **Precise nonlinear functions must be generated:** computing machines for extracting roots of numbers and raising numbers to any power, barometric instruments for reading pressure as a function of altitude, potentiometers and synchros to vary the output as a function of angular displacement, output shafts of limited-travel gear trains to compensate for the accumulated eccentricities of the intermediate gears and producing trigonometric, hyperbolic and logarithmic functions.

(3) **Jointed integration of mechanism and control techniques is conducted:** suppressing vibration during the rapid and large-scale slewing maneuvers of large flexible space structures.

Normally, the cyclically varying output speed can also be achieved by means

of cams, four-bar linkages and band mechanisms. Compared to four-bar linkages, noncircular gears are more compact, accurate, and easier to balance in operation. Also, noncircular gears considerably surpass the cams and band systems while operating in high-speed mechanisms or non-reciprocating motions. Noncircular gears have previously cost more than competitive devices such as linkages, cams, and band mechanisms. Yet the cost of manufacture is reduced for noncircular gears via modern production methods.

For the noncircular gears to be properly in mesh, so that their centers of rotation are a fixed distance apart, the varying torque and speed are transmitted without slipping from driving gear to driven gear. That shear force, normally taken by the gear teeth, is taken by the bands. Noncircular pitch curves are designed to generate the variant gear ratio. Rolling contact, without slipping between driving to driven gears, must always hold in the rotation. Figure 5.1 shows two noncircular gears centered at O_1 and O_2 with the pitch radii r_1 and r_2 respectively. Their angular displacements are indicated by θ_1 and θ_2, angular velocities $\dot{\theta}_1$ and $\dot{\theta}_2$, and angular acceleration $\dot{\theta}_1$ and $\dot{\theta}_2$ respectively. The center distance $\overline{O_1O_2}$ is denoted by C and the pressure angle by ϕ. The necessary conditions for rolling contact between two gears O_1 and O_2 as shown in Fig. 5.1 are

(1) Contact point is aligned along their center-to-center line $\overline{O_1O_2}$,

(2) The equivalent tracking arc length must satisfy

$$r_1 \, d\theta_1 = r_2 \, d\theta_2 \tag{5.1}$$

where $d\theta_1$ and $d\theta_2$ the small angles of gears O_1 and O_2 respectively.

To ensure the contact point aligned between the centers of two gears, the sum of two pitch radii of gears at the contact point must always equal to the center distance C, as shown in Fig. 5.1. Moreover, dividing Eq. (5.1) by dt yields the

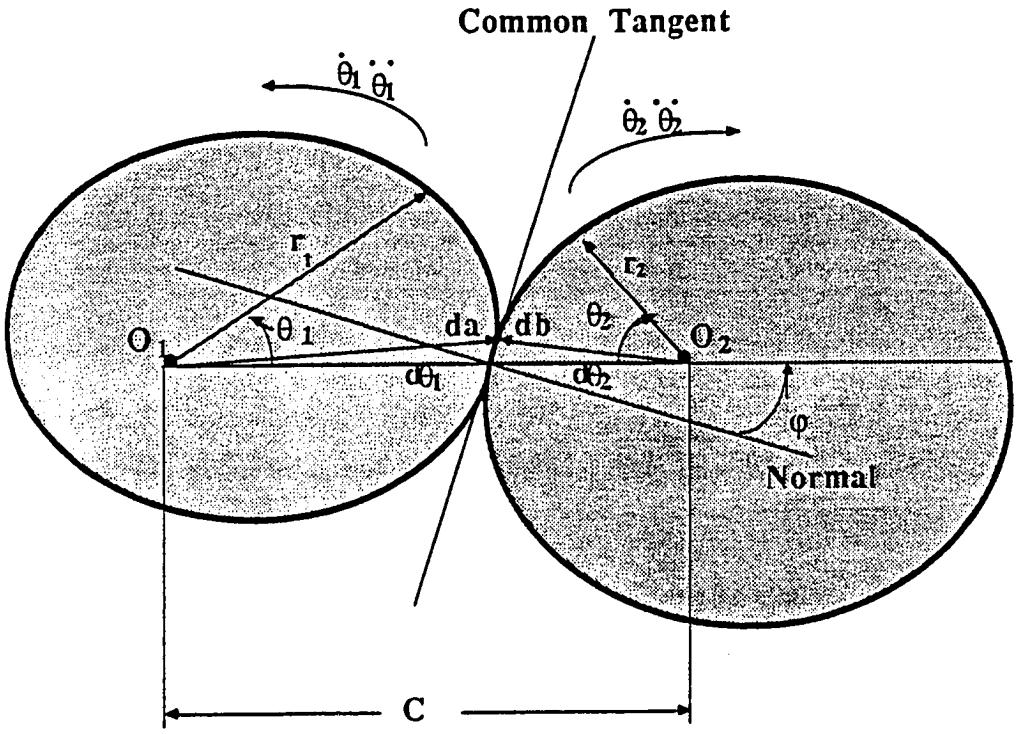

Figure 5.1: Configuration of noncircular gears

velocity equation between gears O_1 and O_2 such as

$$\frac{\dot{\theta}_2}{\dot{\theta}_1} = \frac{r_1}{r_2} \tag{5.2}$$

which implies that the instantaneous velocity ratio equals to the inverse ratio of instantaneous radii. In fact, equation (5.2) indicates the gear ratio defined as

$$N_g = \frac{\dot{\theta}_2}{\dot{\theta}_1} = \frac{r_1}{r_2} \tag{5.3}$$

by assuming the driving gear O_1 and the driven gear O_2. Note that the gear ratio defined in Eq. (5.3) varies according to the reverse ratio of the pitch radii of the driving to driven gears. Also, the input torque τ_1 is related to the output torque τ_2 by

$$\tau_2 = N_g \tau_1 \tag{5.4}$$

through the noncircular gears as shown in Fig. 5.1. Rewriting Eq. (5.3) provides that

$$\dot{\theta}_1 = \frac{\dot{\theta}_2}{N_g} \tag{5.5}$$

The angular acceleration equation can be achieved by differentiating Eq. (5.5) with respect to time. Rewriting Eq. (5.5) and the angular acceleration equation in matrix form yields

$$\begin{pmatrix} \dot{\theta}_1 \\ \ddot{\theta}_1 \end{pmatrix} = \begin{pmatrix} \frac{1}{N_g} & 0 \\ -\frac{\dot{N}_g}{N_g^2} & \frac{1}{N_g} \end{pmatrix} \begin{pmatrix} \dot{\theta}_2 \\ \ddot{\theta}_2 \end{pmatrix} \tag{5.6}$$

Equation (5.6) implies a transformation matrix to transmit the driving states $\begin{bmatrix} \dot{\theta}_1 & \ddot{\theta}_1 \end{bmatrix}^T$ to driven states $\begin{bmatrix} \dot{\theta}_2 & \ddot{\theta}_2 \end{bmatrix}^T$. Such a transformation of Eq. (5.6) will be employed to derive a closed-loop system consisting of the noncircular gears with variant gear ratio N_g in section 5.4.

The specially shaped gears are thus able to be designed to roll and mesh properly during gear operation. Table 5.1 demonstrates five types of existing noncircular gearing systems [24]. They are

Tabel 5.1: Characteristics of five noncircular gear systems [24]

Type	Comments	Basic equations	Velocity equations ω_1 = constant
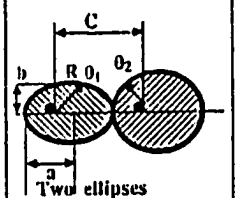 Two ellipses rotating about foci	Gears are identical. Compuratively easy to manufacture. Used for quick-return mechanisms, printing presses, automatic machinery.	$R = \frac{b^2}{a(1+\epsilon\cos\theta)}$ ϵ = eccentricity $= \sqrt{1-\left(\frac{b}{a}\right)^2}$ $a = \frac{1}{2}$ major axis $b = \frac{1}{2}$ minor axis	$\omega_2 = \omega_1\left[\frac{r^2+1+(r^2-1)\cos\theta_2}{2r}\right]$ where $r = \frac{R_{max}}{R_{min}}$ 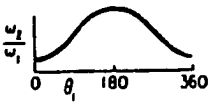
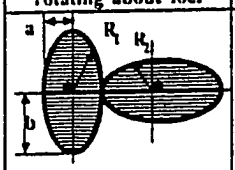 2nd order elliptical gears rotating about their geometric centers	Gears are identical. Geometric properties well known. Better balanced than true elliptical gears. Used where two complete speed cycles are required for one resolution.	$R = \frac{2ab}{(a+b)-(a-b)\cos 2\theta}$ $C = a+b$ a = maximum radius b = minimum radius	$\omega_2 = \omega_1\left[\frac{r+1+(r^2-1)\cos 2\theta_2}{2r}\right]$ where $r = \frac{a}{b}$ 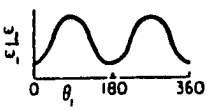
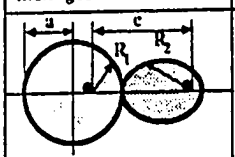 Eccentric circular gear rotating with its conjugate	Standard spur gear can be employed as the eccentric. Mating gear has special shape.	$R_1 = e\cos\theta_1 + \sqrt{a^2 - e^2\sin^2\theta}$ $\theta_2 = -\theta_1 + C\int \frac{e\,d\theta}{C - e\cos\theta_1 \cdot \sqrt{a^2 - e^2\sin^2\theta_1}}$ $R_2 = C - R_1$	$\frac{\omega_2}{\omega_1} = -\frac{R_1}{R_2}$ 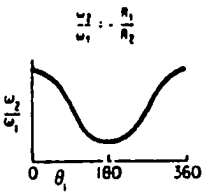
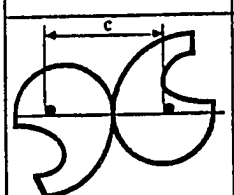 Logarithmic spiral gears	Gears can be identical although can be used in combinations to give variety of functions. Must be open gears.	$R_1 = Ae^{k\theta_1}$ $R_2 = C - R_1 = Ae^{k\theta_2}$ $\theta_2 = \frac{1}{k}\log(C - Ae)^{k\theta_1}$ e = natural log base	$\frac{\omega_2}{\omega_1} = \frac{Ae^{k\theta_1}}{C - Ae^{k\theta_1}}$ 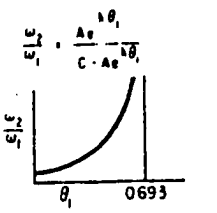
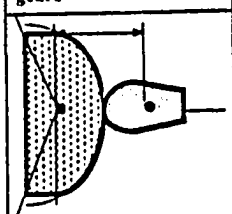 Sine-function gears	For producing angular displacement proportional to sine of input angle. Must be open gears.	$\theta_2 = \sin^{-1}(k\theta_1)$ $R_2 = \frac{C}{1+k\cos\theta_1}$ $R_1 = C - R_2 = \frac{Ck\cos\theta_1}{1+k\cos\theta_1}$	$\frac{\omega_2}{\omega_1} = k\cos\theta_1$ 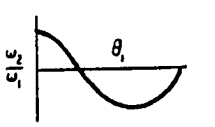

(1) Two ellipses pivoted at foci,

(2) Second-order ellipses rotated about their geometric centers,

(3) Eccentric circular gear meshing with its conjugate,

(4) Logarithmic spirals and

(5) Sine-function gears.

Except for the standard circular spur gear in type (3), the pitch curves of gears are noncircular. To ensure rolling contact, the point of rolling contact must always be located along the center- to-center line and the center distance has to remain a constant in rotation. For type (1), true elliptical gears can only be allowed to roll and mesh properly if they are twins, and if they are rotated about their focal centers [29]. For type (3), an eccentric spur gear, rotating about point A, can roll properly only with specially developed pitch curves, as shown in Fig. 5.2 [24]. One of pitch curves, however, resembles an ellipse which has twice as many gear teeth as that standard spur gear. With the given radius r and eccentricity e, the major semi-axis of the elliptically profiled gear becomes 2r+e and the minor 2r-e. Furthermore, an internal noncircular gear is permissible to roll well with an assigned eccentric spur gear. In each type, the pitch radii of driving to driven gears indicate the design parameters, i.e. the gear ratio, to determine the velocity equation. The velocity equations shown in Table 5.1 are based on the design equations of noncircular gears in the next section.

§ 5.2 Design equations for the noncircular gearing

To begin with the design of the noncircular gears, equations (5.1), (5.2) and (5.4) must always hold no matter what type of noncircular gears are constructed. Three common design requirements are studied to illustrate three different approaches to the design of pitch curves for the noncircular gears. Generally, they are valid for any noncircular gear pair.

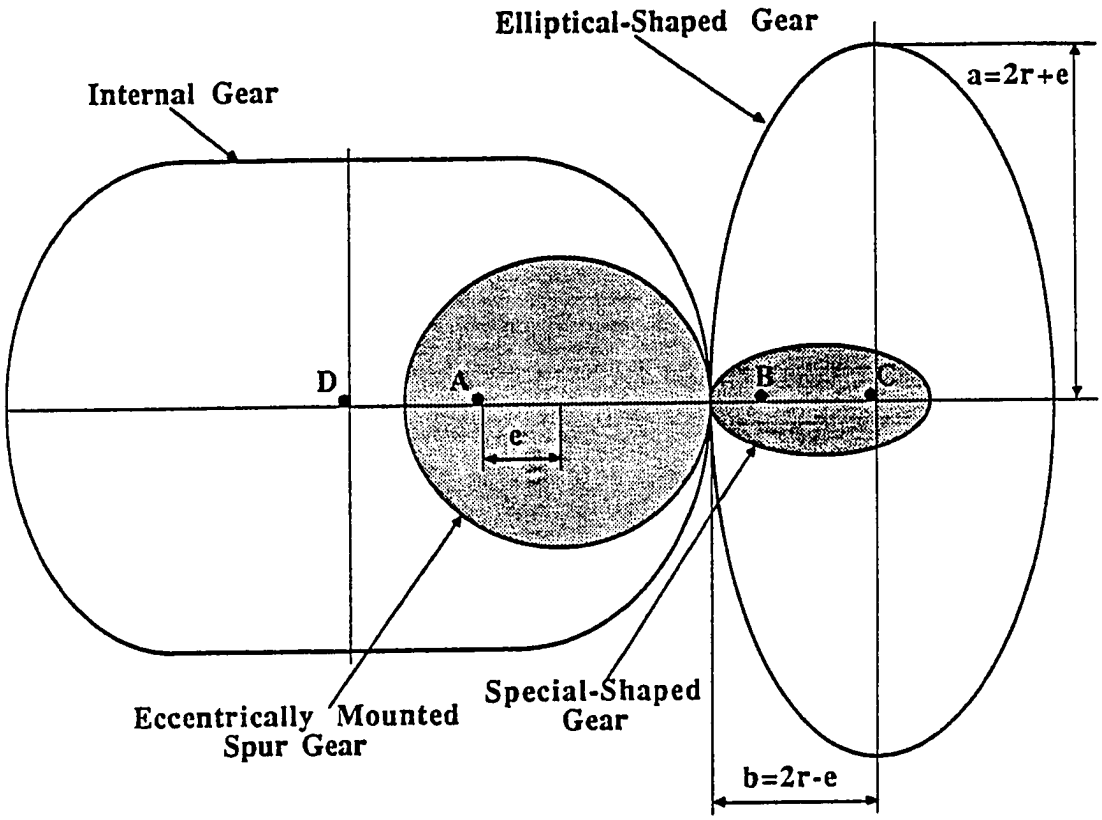

Figure 5.2: One standard spur gear and four kinds of mating conjugate gears

Case1: Suppose that the noncircular pitch profile of gear O_1 in Fig. 5.1 is a polar equation of angle θ_1 which is specified by

$$r_1(\theta_1) = f(\theta_1) \tag{5.7}$$

with the center distance $\bar{C}$. For proper mesh between gears O_1 and O_2, equation (5.1) must be satisfied such as

$$d\theta_2 = \left[\frac{r_1(\theta_1)}{r_2(\theta_2)}\right] d\theta_1, \tag{5.8}$$

$$r_2(\theta_2) = \bar{C} - \tilde{f}(\theta_1) \tag{5.9}$$

where $r(\theta_2)$ stands for the noncircular pitch profile of mating gear O_2. Rewriting Eq. (5.8) provides that

$$d\theta_2 = \left[\frac{\bar{C}}{\bar{C} - \tilde{f}(\theta_1)}\right] d\theta_1 - d\theta_1 \tag{5.10}$$

Equation (5.10) implies that a differential output angle $d\theta_2$ can be determined for a small angle $d\theta_1$ at any instant input angle θ_1 as long as the function $\tilde{f}(\theta_1)$ is specified beforehand. To determine the output angle θ_2, equation (5.10) is integrated from 0 to θ_1 as follows.

$$\theta_2 = -\theta_1 + \bar{C}\int_0^{\theta_1} \frac{d\theta_1}{\left[\bar{C} - \tilde{f}(\theta_1)\right]} \tag{5.11}$$

Equations (5.9) and (5.11) thus provide the parametric functions of θ_2 and $r_2(\theta_2)$ in terms of input angle θ_1. The variant gear ratio can be evaluated by Eq. (5.3) while the $r_1(\theta_1)$ and $r_2(\theta_2)$ are determined numerically. Types 1-4 in Table 5.1. are the examples of this case. The pitch radius of each type is catalogued in the column of basic equations based on Eq. (5.7). And the corresponding velocity equation in Table 5.1 can be derived by using Eq. (5.2). The approach of case 1 will be employed to conduct the analytical derivation of two kinds of noncircular gears, namely, a pair of eccentric gears and Tandem eccentric gears in the next section.

Case2: If the input to output relationship is governed by a differentiable function such as

$$\theta_2 = \tilde{g}(\theta_1) \tag{5.12}$$

with their center distance $\bar{C}$. The following equations must be satisfied for the noncircular gears in Fig. 5.1.

$$r_1 + r_2 = \bar{C} \tag{5.13}$$

$$\tilde{g}(\theta_1) = \frac{d\theta_2}{d\theta_1} = \frac{r_1}{r_2} \tag{5.14}$$

Substitution of Eq. (5.14) into Eq. (5.12) yields

$$r_1 = \frac{\bar{C}\tilde{g}(\theta_1)}{[1 + \tilde{g}(\theta_1)]}, \tag{5.15}$$

$$r_2 = \frac{\bar{C}}{[1 + \tilde{g}(\theta_1)]} \tag{5.16}$$

Compared to case 1, this case displays a straight-forward approach without numerical integration, such as the function in Eq. (5.10), to solve the output angle θ_2. Namely, the parameters θ_2, r_1, and r_2 can be found to be analytical functions of the input angle θ_1. Since input to output pitch radii are obtained from Eqs. (5.15) and (5.16), the gear ratio at any instant can be computed by using Eq. (5.3). Type 5 in Table 5.1, i.e. the sine-function gears, is an example of the case where the output angle is specified as a sine function of the input angle. Based on Eq. (5.2), the velocity equation of $\frac{\dot{\theta}_2}{\dot{\theta}_1} = k\cos(\theta_1)$ in Table 5.1 can thus be determined.

Case3: Assume that the angular velocity ratio is specified by

$$\frac{\dot{\theta}_2}{\dot{\theta}_1} = \tilde{h}(\theta_1) \tag{5.17}$$

in conjunction with the center distance $\bar{C}$. From Eq. (5.2) we obtain

$$\frac{\dot{\theta}_2}{\dot{\theta}_1} = \frac{r_1}{r_2} = \tilde{h}(\theta_1) \tag{5.18}$$

Also, equation (5.13) must hold for the contact point in Fig. 5.1, always lying along center-to-center line $\overline{O_1O_2}$. The following equations are thus achieved for the pitch radii of two gears.

$$r_1 = \frac{\bar{C}\tilde{h}(\theta_1)}{\left[1 + \tilde{h}(\theta_1)\right]}, \tag{5.19}$$

$$r_2 = \frac{\bar{C}}{\left[1 + \tilde{h}(\theta_1)\right]} \tag{5.20}$$

And the output angle θ_2 can be numerically determined by integrating Eq. (5.17) as follows.

$$\theta_2 = \int_0^{\theta_1} \tilde{h}(\theta_1)\, d\theta_1 \tag{5.21}$$

In fact, this case unveils a useful technique for dealing with the design equations of noncircular gears, while the varying gear ratio is specified by Eq. (5.18).

Case4: Similarly, the angular velocity ratio is given as a function of the output angle θ_2 such as

$$\frac{\dot{\theta}_2}{\dot{\theta}_1} = \tilde{p}(\theta_2) \tag{5.22}$$

Then, the pitch radii of two noncircular gears are derived to be

$$r_1 = \frac{\bar{C}\tilde{p}(\theta_2)}{[1 + \tilde{p}(\theta_2)]}, \tag{5.23}$$

$$r_2 = \frac{\bar{C}}{[1 + \tilde{p}(\theta_2)]} \tag{5.24}$$

And the input angle θ_1 of the driving gear can be computed by integrating Eq. (5.22) as follows.

$$\theta_1 = \int_0^{\theta_2} \left[\frac{1}{\tilde{p}(\theta_2)}\right] d\theta_2 \tag{5.25}$$

The pitch curves of two noncircular gears in this case can thus be determined through Eqs. (5.23)-(5.25).

Besides the criteria expressed in Eq. (5.1), the arc lengths tracked by input to output pitch profiles must equal each other for the construction of noncircular

gears. From Fig. 5.1, the cumulative arc lengths da and db due to small angular displacements $d\theta_1$ and θ_2 provide

$$da = \sqrt{\left[r_1^2 + \left(\frac{dr_1}{d\theta_1}\right)^2\right]}\, d\theta_1, \tag{5.26}$$

$$db = \sqrt{\left[r_2^2 + \left(\frac{dr_2}{d\theta_2}\right)^2\right]}\, d\theta_2, \tag{5.27}$$

The tracking arc lengths a and b shown in Fig. 5.1 are thus numerically calculated by integrating Eqs. (5.26) and (5.27) as follows.

$$\mathbf{a} = \int_0^{\theta_1} \sqrt{\left[r_1^2 + \left(\frac{dr_1}{d\theta_1}\right)^2\right]}\, d\theta_1, \tag{5.28}$$

$$\mathbf{b} = \int_0^{\theta_2} \sqrt{\left[r_2^2 + \left(\frac{dr_2}{d\theta_2}\right)^2\right]}\, d\theta_2, \tag{5.29}$$

Therefore, no matter what case of gearing derivation is used, the arc lengths tracked by input to output gears must satisfy a=b, derived in Eqs. (5.28) and (5.29). Namely, both tracking arc lengths are equivalent at any instant of operation. Numerical method can calculate the tracking arc lengths in Eqs. (5.28) and (5.29) to verify the feasibility of the designed noncircular gears based on the derivations herein.

§ 5.3 Mechanism synthesis of the noncircular gears

The advantages of noncircular gears over the other competitive mechanisms, such as four-bar linkages and cams, have been discussed in section 5.1. Nevertheless, conventional noncircular gears still can not overcome some nonlinear problems such as backlash and slipping, as expressed in section 5.1. A new design of a set of noncircular gears is developed such that pure rolling contact between the driving and driven gears is always present. As shown in Fig. 1.3, such a device of noncircular gears consists of

(1) Two cylinder-type and specially shaped cams,

(2) Two pairs of thin metal bands and

(3) Two holders.

The noncircular gears are constructed by a single pair of convex cylinder-type cams which are wrapped in a mesh arrangement by two pairs of thin metal bands. These thin metal bands are clamped together by two holders at the two ends of bands where the holders are then attached to either the shaft of the motor or the end of the structure for the torque transmission. This device has several attributes when compared to conventional gears. They are

(1) No backlash,

(2) No friction,

(3) No slipping,

(4) No teeth,

(5) No need of lubrication and

(6) Low cost of manufacture.

The output characteristics of the noncircular gears are governed by Eq. (5.6) derived in section 5.2. Pitch curves of two noncircular gears can be determined through four cases in section 5.2 as long as the various gear ratio is properly specified. Based on Case 4 in section 5.2, a hyperbolic gear ratio defined as a function of the driven output angle is used such that

$$N_g = \frac{\dot{\theta}_2}{\dot{\theta}_1} = \frac{c_2}{[c_1 + \theta_2]} \tag{5.30}$$

In Eq. (5.30), c_1 and c_2 indicate two parameters which can be determined by giving two points along the hyperbolic curve. During the slewing control process, the noncircular gears characterized by a hyperbolic gear ratio shown in Eq. (5.30) can transform the output angular displacement and velocity to behave more smoothly while simultaneously suppressing the flexural vibration. Figure 5.3 shows a hyperbolic gear ratio as a function of the output angle θ_2 from 0 deg to 90 deg for the

parameters $c_1 = \frac{\pi}{10}$, $c_2 = \frac{\pi}{5}$ and $\bar{C} = 10$. The pitch radii of two noncircular gears can be found by Eqs. (5.23) and (5.24) as follows.

$$r_1 = \frac{\bar{C}N_g}{[1 + N_g]}, \tag{5.31}$$

$$r_2 = \frac{\bar{C}}{[1 + N_g]} \tag{5.32}$$

where $\bar{C}$ is the center distance of two noncircular gears. From Eq. (5.25), the input angle θ_1 of the driving gear can be computed by integrating Eq. (5.22) as follows.

$$\theta_1 = \frac{\left[c_1\theta_2 + \frac{\theta_2^2}{2}\right]}{c_2} \tag{5.33}$$

The plots of $r_1(\theta_1)$ and $r_2(\theta_2)$ in polar coordinates would directly confirm whether the requirements of convexity are adhered to. Based on the hyperbolic gear ratio as shown in Fig. 5.3 and Eqs. (5.31)-(5.33), the pitch curves of the two noncircular gears are given in Fig. 5.4. The convexity of two profiles ensures the feasibility of the hyperbolic gear ratio for this design of noncircular gears.

§ 5.4 Actuator dynamics with noncircular gears

The noncircular gears developed in section 5.3 are characterized by several advantages over those of the conventional gears such as the ones shown in Table 5.1. In this section, the dynamics of the actuator in the presence of noncircular gears are investigated. For the slewing control of flexible space structures, the noncircular gears are installed at the rotating joints to transform the available torque from the actuator to the flexible beam through a varying mechanical advantage given by Eq. (5.4). A pair of cylindrically shaped cams (to be used as gears), shown in Fig. 1.3, are wrapped together such that the noncircular gears can roll on each other without slipping and friction. In this way, the pitch profiles of noncircular gears must be convex. A constant step- down gear box is built into the motor so that the constant gear ratio should also be considered in the actuator dynamics. The output shaft of the step-down gear box is axially connected to the holder of

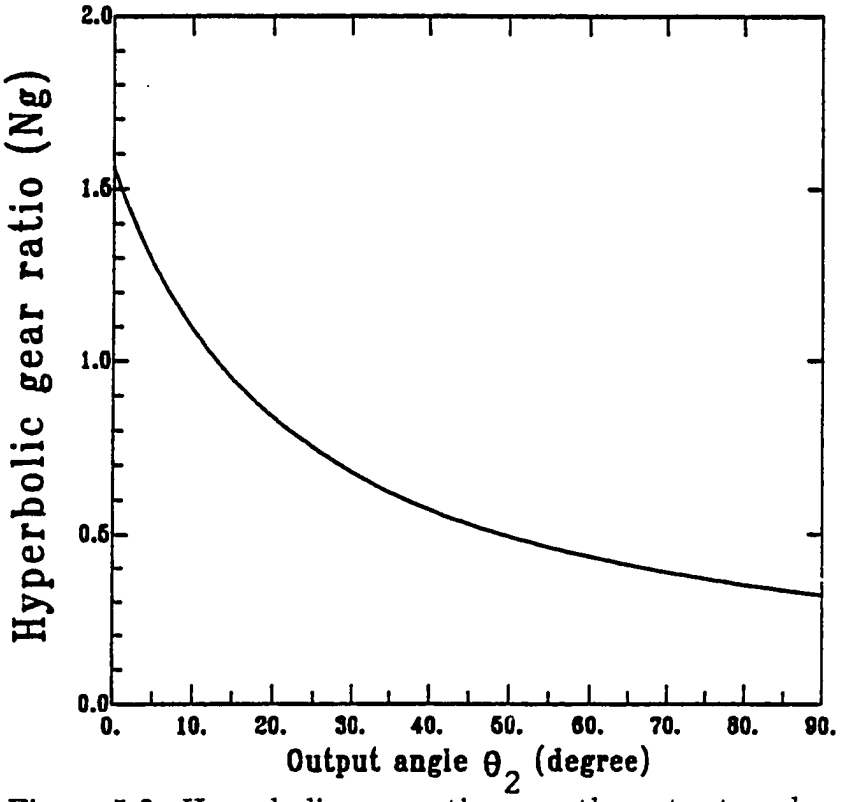

Figure 5.3: Hyperbolic gear ratio verse the output angle of the driven gear

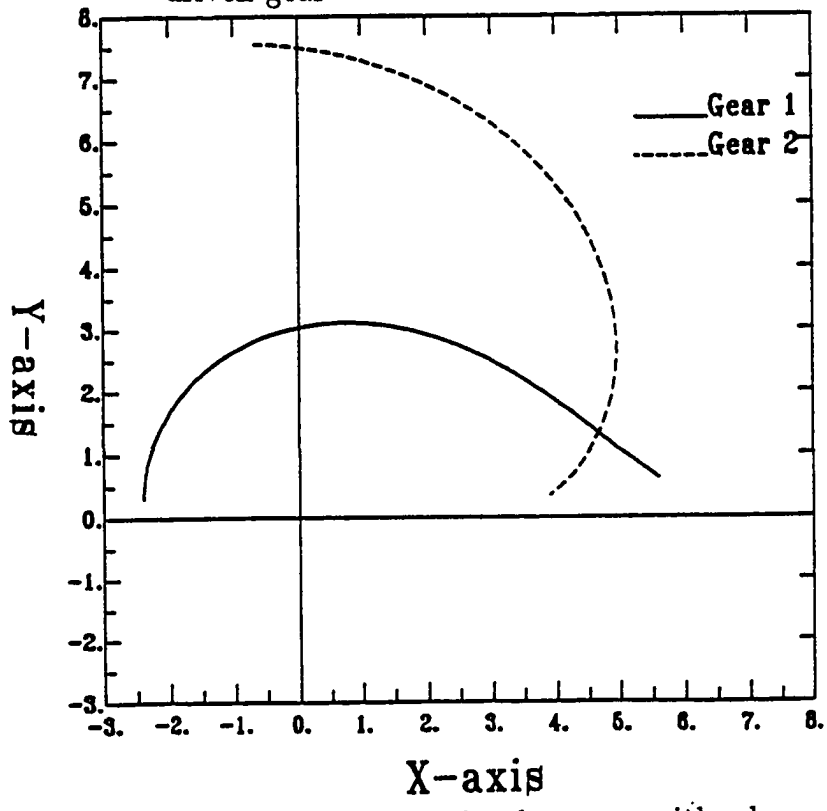

Figure 5.4: Pitch curves of noncircular gears with a hyperbolic gear ratio

a noncircular gear, while the end of the flexible beam is attached to the other gear holder (see Fig. 5.5). The motor can be regarded as a standard armature circuit. Denote the armature resistance by R_a, the back-EMF (Electro-Motive-Force) constant by K_b, the motor torque constant by K_t, the gear train viscous drag coefficient by C_v, the motor inertia by I_m, the available motor torque by τ_a, and the applied voltage into the armature by e_a. Then, the motor dynamics is governed by

$$I_m\ddot{\theta}_m + \left(C_v + \frac{K_t K_b}{R_a}\right)\dot{\theta}_m + \tau_a = \frac{K_t e_a}{R_a} \tag{5.34}$$

where θ_m denotes the output shaft angle of the motor. Figure 5.5 shows a motor and a gear train of a gear box and the noncircular gears. The output shaft of the gear box is attached to the input holder of noncircular gears. Assume one end of a flexible structure is attached to the output holder of noncircular gears. Denote the varying (non-constant) gear ratio of noncircular gears by N_g and constant gear ratio of step- down gear box by N_p. Based on Eq. (5.4), the transmission from available torque τ_a to the torque τ_s associated with structure input is thus provided by

$$\tau_a = N_g N_p \tau_s \tag{5.35}$$

Based on Eq. (5.6), the angular velocity and acceleration of motor can be written by

$$\begin{pmatrix} \ddot{\theta}_m \\ \dot{\theta}_m \end{pmatrix} = \begin{pmatrix} \frac{1}{N_g(\theta_s)} & 0 \\ -\frac{\dot{N}_g(\theta_s)}{N_g^2(\theta_s)} & \frac{1}{N_g(\theta_s)} \end{pmatrix} \begin{pmatrix} \ddot{\theta}_s \\ \dot{\theta}_s \end{pmatrix} \tag{5.36}$$

where θ_s denotes the angular displacement of the structural root end. For the sake of convenience, the gear ratio N_g in Eqs. (5.35) and (5.36) is specified as a function of θ_s, i.e. $N_g(\theta_s)$, because motor characteristics in Eq. (5.34) will be combined into structrual dynamics to perform a closed-loop system in the next section. Due to the dynamic criteria of structural maneuvers, the investigation of the entire closed-loop system must be conducted to find the appropriate gear ratio N_g. Substitution of Eqs. (5.35) and (5.36) into Eq. (5.34) provides the structural

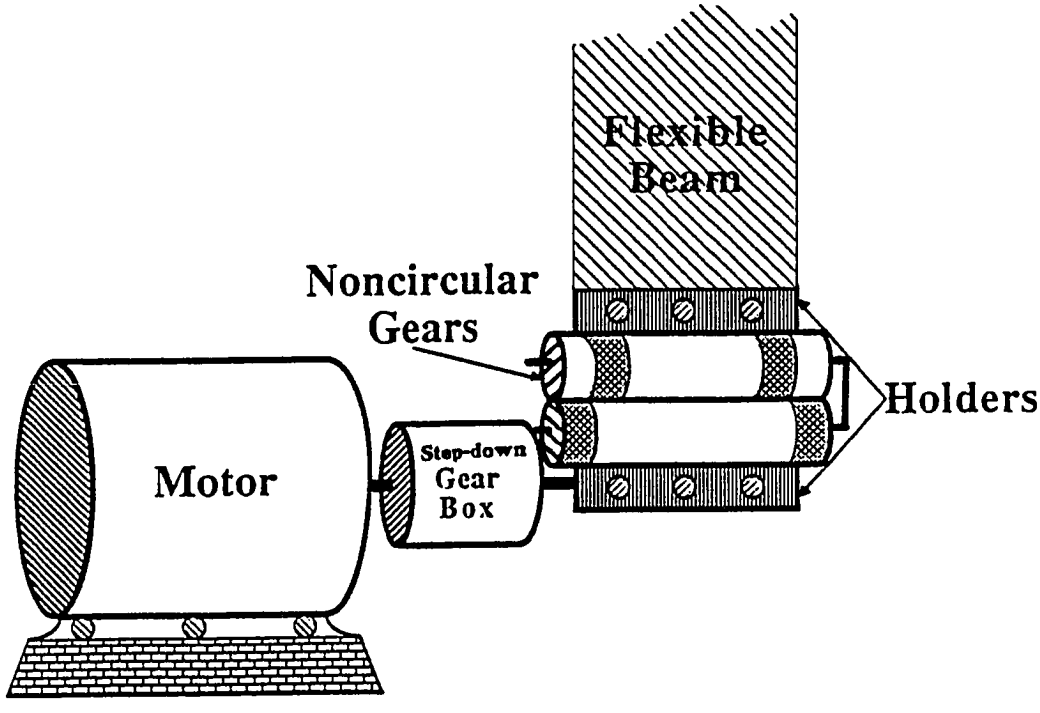

Figure 5.5: Motor with a gear box and a pair of noncircular gears

torque τ_s which is expressed by

$$\tau_s = \frac{K_t e_a}{(R_a N_g N_p)} - \frac{\left(C_v + \frac{K_t K_b}{R_a}\right)\dot{\theta}_s}{(N_g N_p)^2} + \frac{I_m\left(N_g N_p \dot{\theta}_s - N_p \dot{N}_g \dot{\theta}_s\right)}{(N_g N_p)^3} \tag{5.37}$$

Since the gear ratio of noncircular gears is defined as a function of beam angle θ_b in Eq. (5.35), the time rate of change of the gear ratio $\dot{N}_g$ in Eq. (5.37) can be computed by

$$\dot{N}_g = \left[\frac{dN_g}{d\theta_b}\right]\dot{\theta}_b \tag{5.38}$$

which means the time-rate gear ratio is equivalent to the multiplication of the slope of the gear ratio verse the structural root angle and the angular velocity of the structure. The noncircular gear ratio N_g, defined in Eq. (5.35), is associated with the fourth case in section 5.2. From Eqs. (5.23) and (5.24), the pitch radii of the two gears shown in Fig. 5.1 are then determined by

$$r_1(\theta_m) = \frac{\bar{C} N_g}{(1 + N_g)}, \tag{5.39}$$

$$r_2(\theta_s) = \frac{\bar{C}}{(1 + N_g)} \tag{5.40}$$

where $\bar{C}$ is the center distance defined in Eq. (5.13). Hence, the profiles of two noncircular pitch curves can be found by solving Eqs. (5.39) and (5.40) as long as the varying gear ratio N_g is specified based on the criterion for the maneuvering performance. Notice the gear ratio N_g must be selected to ensure two convex profiles of pitch curves. Yet the motor angle θ_m in Eq. (5.39) must be solved to determine the pitch curve r_1. From Eq. (5.36), the motor angle θ_m can be computed by

$$\theta_m = \int_0^{\theta_s} \frac{d\theta_s}{N_g} \tag{5.41}$$

for any given structural root angle θ_s. The plots of $r_1(\theta_m)$ and $r_2(\theta_s)$ can thus be drawn in polar coordinates. The convexity of Eqs.(5.39) and (5.40) has to hold for the construction of these noncircular gears.

§ 5.5 Dynamic equations of flexible space structures with noncircular gears

In this section, the investigation is conducted to display the dynamic equations of two kinds of flexible space structures, i.e. the one-beam and the articulated two-beam structures, in conjunction with the current noncircular gear design. The cylinder-type noncircular gears are set up to link the actuator and one end of flexible beam through two holders. Equations (5.36) and (5.37) are employed to link the actuator characteristics and structural dynamics together in order to implement the closed-loop control systems. Such two models of flexible structures will be used for numerical simulations in the next section.

§§ 5.5.1 Dynamic equation of a flexible one-beam structure

The input to output relationship of the motor with noncircular gears is derived in Eq. (5.37). On the other hand, the detailed structural dynamics has yet to be presented. In this section, attention will be focused on the derivation of the structural dynamics of a flexible one-beam structure along with a single pair of noncircular gears. Figure 5.6 shows a planar flexible beam clamped on a device consisting of a motor and its gear train. The flexible beam is modeled as a cantilever beam with the fixed end at the motor and the free end at the tip $x_1 = L$ (see Fig. 5.6(a)). Only the bending vibration is allowed during the motion of the arm. In Fig. 5.6(b), the x-y axes are the fixed inertial coordinate, whereas the $x_1 - y_1$ axes represent the moving relative coordinate. Lagrange's equations of motion [69], in conjuction with the modal expansion to discretize the deflection of the flexible-link manipulator, are then applied to derive the dynamic equations of motion. Let the state vector be defined by

$$\xi = [\, \theta_s,\, q^T \,]^T \quad ; \quad q^T = [\, q_1,\, q_2, \cdots,\, q_n \,] \tag{5.42}$$

where θ_s indicates the root angle of the flexible beam and q_i (i=1,....,n) the general coordinates corresponding to the shape functions ψ_i (i=1,.....,n) for

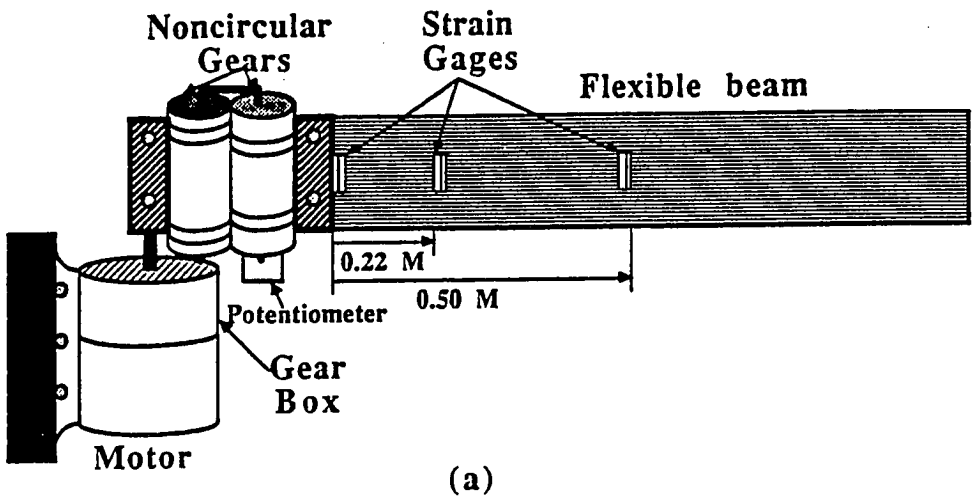

(a)

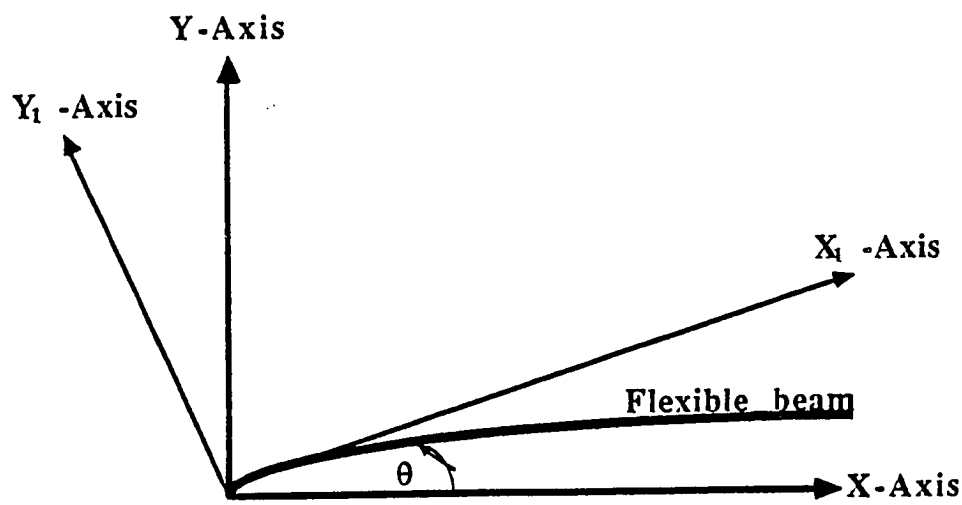

(b)

Figure 5.6: Configuration and coordinates of one flexible steel beam

discretization of the bending deflection of the flexible beam. The kinetic and potential energies of one flexible beam are given by Eqs. (B.11) and (B.12) which result in Lagrange's function. The control torque needed to perform desired slewing maneuvers can be expressed by the vector

$$\tau = [\ \tau_b,\ 0, \cdots,\ 0\ ]^T \tag{5.43}$$

where τ_b represents the applied torque for the slewing of the flexible beam. Note that τ_b in Eq. (5.43) is identical to τ_s derived in Eq. (5.36).

Assume that the damping of the flexible beam is negligible. The Lagrange's equations of motion for one-beam structure can thus be governed by

$$M\ddot{\xi} + K\xi = \tau \tag{5.44}$$

where M indicates the inertia matrix, and K the stiffness matrix. Apparently, equation (5.44) demonstrates linear structural dynamics. Denote ρ the mass density of the arm per unit length, L the length of the flexible beam, and I the total moment of inertia. Hence, the inertia matrix in Eq. (5.44) is expressed by

$$M = \begin{pmatrix} I & \textbf{symmetric} \\ -\tilde{p} & \rho L\hat{I} \end{pmatrix} \tag{5.45}$$

where $\hat{I}$ is an $n \times n$ identity matrix. The constant vector $\tilde{p}$ is defined in references [37] and [38]. Furthermore, the constant stiffness matrix in Eq. (5.44) is specified by

$$K = Diag[\ 0,\ \rho L\omega^2\ ] \quad ;\ \omega = Diag[\ \omega_1, \cdots,\ \omega_n\ ] \tag{5.46}$$

where ω_i (i=1,...,n) is the modal frequencies associated with the cantilevered shape functions $\psi_i(x_1)$, which are used to discretize the deflection of the flexible beam. The nonlinear forcing terms such as Coriolis and centrifugal forces do not exist in the Eq. (5.44).

The actuator dynamics and sensor characteristics must be involved into Eq. (5.44) to construct a closed-loop system. The actuator for the feedback control is the dc electric motor. One idler gear box and a pair of noncircular gears are set up in the same way as in the previous section. Since the relationship including actuator characteristics and noncircular gearing mechanisms has been established in Eq. (5.37), the applied beam torque τ_b in Eq. (5.43) can be replaced by Eq. (5.37) such that

$$\tau_b = \frac{K_t e_a}{(R_a N_g N_p)} - \frac{\left(C_v + \frac{K_t K_b}{R_a}\right)\dot{\theta}_b}{(N_g N_p)^2} + \frac{I_m\left(N_g N_p \dot{\theta}_b - N_p \dot{N}_g \dot{\theta}_b\right)}{(N_g N_p)} \qquad (5.47)$$

Obviously, equation (5.47) produces the appropriate torque for beam slewing due to the applied voltage e_a, which is determined through output feedback control. The motor characteristics, such as back-EMF as well as moment inertia, are included in Eq. (5.47), which is represented in terms of beam variables. Instead of the conventional motor's back-EMF with a constant gear ratio, the back-EMF in Eq. (5.47) can be tuned through the varying gear ratio N_{g1}. The angular velocity and acceleration of the motor's shaft can then be obtained by using Eq. (5.36).

The output measurement equation is derived to relate the physical measurements, such as angular displacement and velocity, and the output voltages of the sensors. Referring to the sensors, the rotational angle is measured by the 10-turn rotary potentiometer, whereas the angular velocity is calibrated by a tachometer. Strain gages, used to sense the bending moments along the flexible beam are, deduced. Denote c_p as the conversion factor between the beam root angle θ_b and the output voltage e_p of the potentiometer; c_t as the conversion factor between the beam angular velocity and the output voltage e_t; c_s as the conversion factor between the strain and the strain output voltage e_0. Suppose three strain gages are placed along the flexible beam respectively at x_a, x_b, and x_c. An output measurement equation can be written in the following matrix form

$$\hat{e} = [\, e_t,\ e_p,\ e_0(x_a),\ e_0(x_b),\ e_0(x_c)\,]^T = C_f \left[\, \dot{\theta}_s,\ \xi^T \,\right]^T$$

$$= Diag[\, c_t,\ c_p,\ C_e \,] \left[\, \dot{\theta}_s,\ \theta_s,\ q^T \,\right]^T \tag{5.48}$$

where each element of the matrix C_e is a product of the conversion factor c_s, the half thickness of the flexible beam, and the second derivative of the corresponding mode shape to a generalized coordinate evaluated at the corresponding sensor location. All the observed measurements in Eq. (5.48) contribute to the output feedback control input, namely, e_a in Eq. (5.47). Apparently, the matrix C_f in Eq. (5.48) is composed of the conversion factors of the sensors. More detailed information about the output measurements is provided in references [20,21,38]. Equation (5.48) thus relates the output voltage $\hat{e}$ to the state variables θ_s and ξ through the coefficients of the matrix C_f.

Substituting Eq. (5.47) into Eq. (5.44) provides

$$\bar{M}\ddot{\xi} + \bar{C}\dot{\xi} + K\xi = BE_a(t) \tag{5.49}$$

in which,

$$\bar{M} = M + Diag\left[\, \frac{I_m}{(N_g N_p)^2},\ 0,\ 0,\ 0 \,\right],$$

$$\bar{C} = Diag\left[\, \frac{\left(\frac{K_t K_b}{R_a} + C_v - \frac{I_m \dot{N}_g}{N_g}\right)}{(N_g N_p)^2},\ 0,\ 0,\ 0 \,\right],$$

$$B = Diag\left[\, \frac{K_t}{(R_a N_g N)},\ 0,\ 0,\ 0 \,\right],$$

and $E_a(t) = [\, e_a \,]^T$ with e_{a1} being the applied voltage for the motor of the flexible beam. Moreover, the signals of output voltages $\hat{e}$ will be fed back to the motor through the desired feedback gain matrix so that

$$E_a = G\hat{e} = GC_f\xi \tag{5.50}$$

where G denotes output feedback gain matrix which will be determined for the slewing maneuvers of the flexible beam. Equation (5.49) thus demonstrates a

closed-loop system of a flexible one-beam structure in conjunction with a pair of noncircular gears. Recall that the time rate of change of the gear ratio in damping matrix $\bar{C}$ of Eq. (5.49) can be found by using Eq. (5.38).

§§ 5.5.2 Dynamic equation of an articulated flexible two-beam structure

The noncircular gears can be incorporated into multibody flexible structures. An articulated two-beam structure is designed to study the feasibility of two pairs of noncircular gears for two flexible beams. One flexible beam is articulated on the tip of the previous beam to result in an articulated flexible two-beam structure as shown in Fig. 5.7(a). Such an additional beam is also treated as a cantilevered beam. An extra actuator is required, which is concatenated axially with that for the first beam as shown in Fig. 5.7(a). The fore-beam is manipulated by this additional motor through a wire or tendon configuration. In Fig. 5.7(b), denote θ_1 as the root angle of the first flexible beam and θ_2 as the root angle of the second beam, measured relative to the previous local coordinates, i.e., $x_1 - y_1$ axes. The state vector similar to Eq. (5.42) becomes

$$\xi = [\, \theta_1,\, \theta_2,\, q_1^T,\, q_2^T \,]^T;$$

$$q_1^T = [\, q_{11}, \cdots, q_{1n_1} \,] \quad \textit{and} \quad q_2^T = [\, q_{21}, \cdots, q_{2n_2} \,] \tag{5.51}$$

where q_{1i} (i=1,$\cdots$, n_1) are the general coordinates corresponding to the shape functions ψ_{1i} (i=1,$\cdots$, n_1) for discretization of the bending deflection of the first flexible beam. The quantities q_{2i} and ψ_{2i} are defined similarly for the fore-beam. The input vector for the articulated flexible beams is

$$\tau = [\, \tau_{b1},\, \tau_{b2},\, 0, \cdots,\, 0 \,]^T \tag{5.52}$$

where τ_{b1} and τ_{b2} represent the applied torques for the two flexible beams repectively.

The kinetic and potential energies of an articulated flexible two-beam structure are specified in Eqs. (A.17) and (A.18). Application of Lagrange's equations

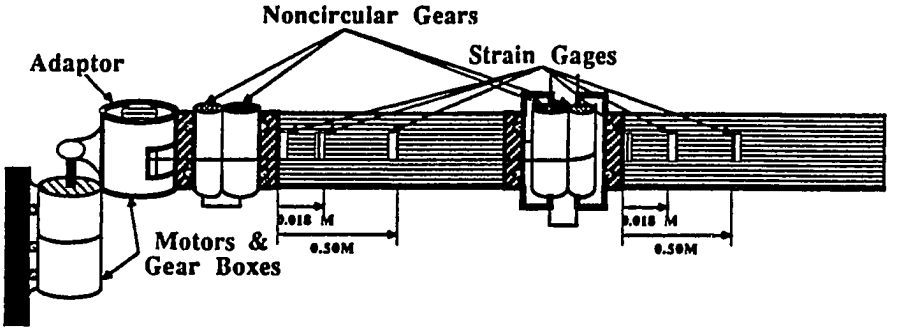

(a)

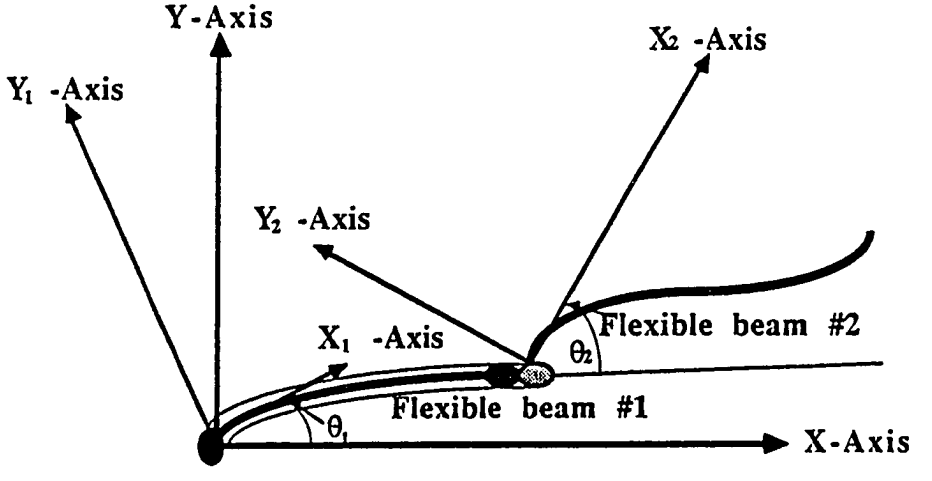

(b)

Figure 5.7: Configuration and coordinates of two articulated flexible steel beams

of motion in terms of state variables yields a set of equations in matrix form as follows.

$$M\ddot{\xi} + K\xi = \tau + f\left(\xi, \dot{\xi}\right) \tag{5.53}$$

where M, K and τ are defined similarly to Eq. (5.44), and $f\left(\xi, \dot{\xi}\right)$ represents a nonlinear force vector. In Eq. (5.53), there exists the nonlinear terms, such as cosine functions of the beam angles, due to the interaction of the dynamics of the two flexible beams. The inertia matrix M in Eq. (5.53) represents a constant matrix. The symmetry inertia matrix M in Eq. (5.53) becomes

$$M = \begin{pmatrix} 4I_1 & \frac{\rho L^3 c\theta_2}{2} & -\rho L^2 \psi_1^T(L) - P_1^T & -L h_2^T c\theta_2 \\ \frac{\rho L^3 c\theta_2}{2} & I_2 & \frac{-\rho L^2 \psi_1^T(L) c\theta_2}{2} & -P_2^T \\ -\rho L^2 \psi_1(L) - P_1 & \frac{-\rho L^2 \psi_1(L) c\theta_2}{2} & \rho \psi_1(L)\psi_1^T(L) + \rho L \hat{I}_1 & h_2 \psi_1^T(L) c\theta_2 \\ -L h_2 c\theta_2 & -P_2 & h_2 \psi_1(L) c\theta_2 & \rho L \hat{I}_2 \end{pmatrix} \tag{5.54}$$

where $c\theta_1 = \cos(\theta_1)$, $c\theta_2 = \cos(\theta_2)$ and $c(\theta_1 + \theta_2) = \cos(\theta_1 + \theta_2)$. Here $\hat{I}_1$ and $\hat{I}_2$ are $n_1 \times n_1$ and $n_2 \times n_2$ identity matrices respectively with n_1 and n_2 being the numbers of the mode shapes respectively for discretization of bending deflections of the two beam-like flexible beams. Moreover, the stiffness matrix becomes

$$K = Diag\left[\, 0,\ 0,\ \rho L \omega_1^2,\ \rho L \omega_2^2 \,\right] ;$$

$$\omega_1 = Diag[\, \omega_{11}, \cdots, \omega_{1n_1} \,] \quad and \quad \omega_2 = Diag[\, \omega_{21}, \cdots, \omega_{2n_2} \,] \tag{5.55}$$

and the nonlinear force vector yields

$$f\left(\xi, \dot{\xi}\right) = [\, f_1,\ f_2,\ f_3,\ f_4 \,]^T \tag{5.56}$$

where

$$f_1 = \frac{\rho L^3}{2} s\theta_2 \dot{\theta}_2^2 - L s\theta_2 \left(h_2^T \dot{q}_2\right) \dot{\theta}_2$$

$$f_2 = -s\theta_2 \left(\psi_1^T(l)\dot{q}_1\right)\left(h_2^T \dot{q}_2\right) + L s\theta_2 \left(h_2^T \dot{q}_2\right) \dot{\theta}_1$$

$$f_3 = -\frac{\rho L^2}{2} \psi_1(L) s\theta_2 \dot{\theta}_2^2 + s\theta_2 \psi_1(L) \left(h_2^T \dot{q}_2\right) \dot{\theta}_2$$

$$f_4 \;=\; -Ls\theta_2 h_2 \dot{\theta}_1 \dot{\theta} \;+\; h_2 s\theta_2 \left(\psi_1^T(L)\dot{q}_1\right)\dot{\theta}_2$$

where $s\theta_1 \;=\; \sin(\theta_1)$, $s\theta_2 \;=\; \sin(\theta_2)$, and $s\left(\theta_1+\theta_2\right) \;=\; \sin(\theta_1+\theta_2)$.

There are two motors which produce the torques for the independent slewings of the two beams. The applied beam torque τ_{b1} for the first beam in Eq. (5.52) is identical to the one shown in Eq. (5.47). One idler gear box (constant gear ratio N_{p2}) and a pair of noncircular gears (variant gear ratio N_{g2}) are set up for the torque transmission of the second beam. Therefore, the applied beam torque τ_{b2} is generated by

$$\tau_{b2} \;=\; \frac{K_{t2}e_{a2}}{(R_{a2}N_{g2}N_{p2})} \;-\; \frac{\left(C_{v2} \;+\; \frac{K_{t2}K_{b2}}{R_{a2}}\right)}{(N_{g2}N_{p2})^2}\dot{\theta}_{b2} + \; I_{m2}\frac{\left(N_{g2}N_{p2}\dot{\theta}_{b2} \;-\; N_{p2}\dot{N}_{g2}\dot{\theta}_{b2}\right)}{(N_{g2}N_{p2})^3} \tag{5.57}$$

where the motor parameters for fore-beam are defined in the same way as Eq. (5.47). Equation (5.57) generates the torque τ_{b2} for the second beam, slewing through the applied voltage e_{a2}.

Then, the output measurement equation is

$$\begin{aligned}\hat{e} &= \left[e_{t1}, e_{t2}, e_{p0}, e_{p1}, e_{p2}, e_{o1}\left(x_a\right), e_{01}\left(x_b\right), e_{01}\left(x_c\right), e_{02}\left(x_a\right), e_{02}\left(x_b\right), e_{02}\left(x_c\right)\right]^T \\ &= C_f\;\left[\;\dot{\theta}_1,\;\dot{\theta}_2,\;q^T\;\right]^T \end{aligned} \tag{5.58}$$

where

$$C_f \;=\; Diag[\;c_{t1},\;c_{t1},\;c_{p'},c_{p1},\;C_{e1},\;C_{e2}\;],$$

$$C_{ei} \;=\; c_s h\begin{pmatrix} \frac{\partial^2\psi_{i1}}{\partial x_1\partial x_1}\left(x_1\right),\cdots,\frac{\partial^2\psi_{in_1}}{\partial x_1\partial x_1}\left(x_1\right) \\ \frac{\partial^2\psi_{i1}}{\partial x_2\partial x_2}\left(x_2\right),\cdots,\frac{\partial^2\psi_{in_2}}{\partial x_2\partial x_2}\left(x_2\right)\end{pmatrix} \quad for\; i \;=\; 1,2.$$

The dynamic equations can thus be developed which yields

$$\bar{M}\ddot{\xi} \;+\; \bar{C}\dot{\xi} \;+\; K\xi \;=\; BE_a(t) \;+\; f\left(\xi,\dot{\xi}\right) \tag{5.59}$$

in which,

$$\bar{M} = M + Diag\left[\frac{I_{m1}}{(N_{g1}N_{p1})^2}, \frac{I_{m2}}{(N_{g2}N_{p2})^2}, 0, 0, 0, 0, 0, 0\right],$$

$$\bar{C} = Diag\left[\frac{\left(\frac{K_{t1}K_{b1}}{R_{a1}} + C_{v1} - \frac{I_{m1}\dot{N}_{g1}}{N_{g1}}\right)}{(N_{g1}N_{p1})^2}, \frac{\left(\frac{K_{t2}K_{b2}}{R_{a2}} + C_{v2} - \frac{I_{m2}\dot{N}_{g2}}{N_{g2}}\right)}{(N_{g2}N_{p2})^2}, 0, 0, 0, 0, 0, 0\right],$$

$$B = \begin{pmatrix} \frac{K_{t1}}{(R_{a1}N_{g1}N_{p1})} & 0 \\ 0 & \frac{K_{t2}}{(R_{a2}N_{g2}N_{p2})} \\ 0 & 0 \\ 0 & 0 \\ 0 & 0 \\ 0 & 0 \\ 0 & 0 \\ 0 & 0 \end{pmatrix}$$

and $E_a(t) = [\, e_{a1},\, e_{a2}\,]^T$ which can be obtained by using the output feedback control technique as shown in Eq. (5.50).

§ 5.6 Simulations of slewing controls with noncircular gears

Two dynamic models, namely a flexible one-beam structure and an articulated flexible two-beam structure, have been developed in the previous section. The noncircular gears associated with the hyperbolic gear ratio are installed into two such flexible space structures to perform controlled slewing experiments. For each beam-like structure, 90-degree slewing maneuvers are simulated to compare two cases of slewing performances, i.e. with and without noncircular gears.

§§ 5.6.1 Simulation of a flexible one-beam structure

Three cantilevered modes are assigned for the flexible steel beam. Table 5.2 summarizes the model parameters of a flexible one-beam structure. Using the

optimal control techniques [68], the slewing control of this flexible structure is investigated to determine an optimal control law so as to minimize the quadratic performance index such as

$$J = \int_0^\infty \left[q^T Q q + u^T R u\right] dt \tag{5.60}$$

where q^T indicates the state vector $\left[\xi, \dot{\xi}\right]^T$ and u^T the input vector. The positive-definite matrices Q and R in Eq. (5.60) stand for the state and input weighting matrices respectively shown in Table 5.3. A Riccati equation [68] based on Eq. (5.60) will be solved to obtain the output feedback gain matrix as shown in Table 5.3. The varying gear ratio for noncircular gears is specified as shown in section 5.2. The parameters of hyperbolic gear ratio are listed in Table 5.2. Figure 5.8 demonstrates the task of a 90-degree slewing control for this flexible one-beam structure. Two cases of slewing simulations are performed: one with the regular circular gears and the other with noncircular gears. The results associated with noncircular gears are indicated by a solid line (♯1) and the results for circular gears by the dashed line (♯2) respectively.

The performance results for such a slewing maneuver are thus summarized in Figs. 5.9-5.14. The flexible steel beam slews 90 degrees in 6 sec as shown in Fig. 5.9. Apparently, the noncircular gears slow down the slewing maneuver during the first 7-degrees of slew, thereby providing a smoother actuation to the desired final angle than that in the presence of the circular gears. In Fig. 5.10, both results of the beam angular velocities damp out in 6 seconds. The higher modes are clearly observed in the result for circular gears while nearly absent in the results for noncircular gears. That indicates the efficient suppression of structural vibration in the presence of noncircular gears. The slewing angular velocity of noncircular gears illustrates a smoother trajectory after 0.8 sec which implies that the beam slewing and vibrational motion have been tuned through the noncircular gears. Moreover, the peak angular velocity magnitude is also significantly reduced. Two control torques which resemble each other start with 1 N-M and dwindle to zero

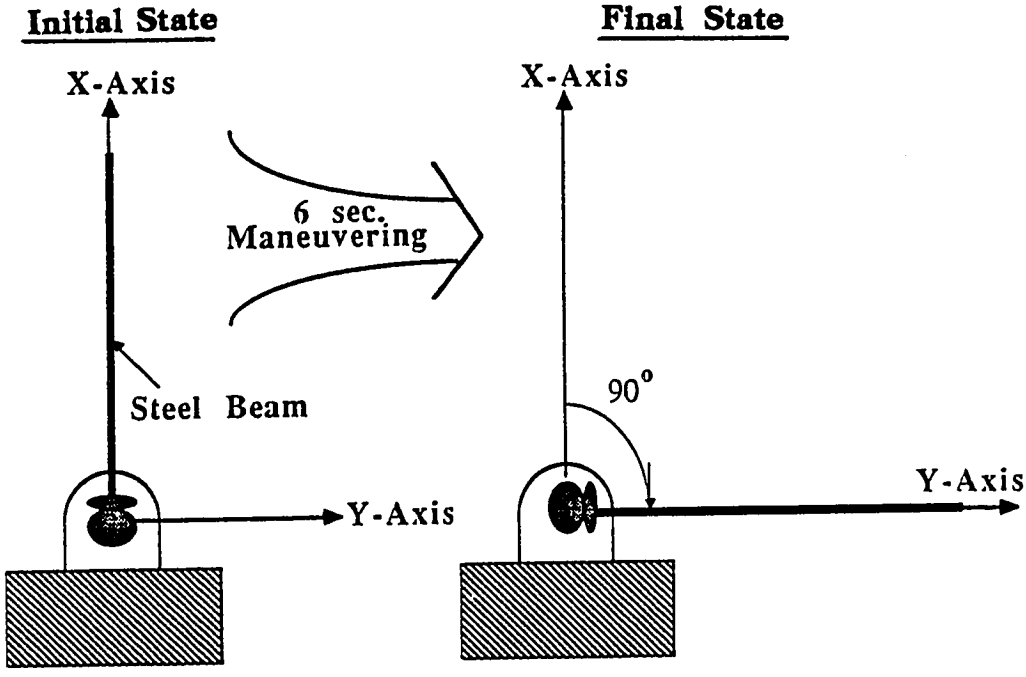

Figure 5.8: 90-degree slewing mission of a flexible one-beam structure

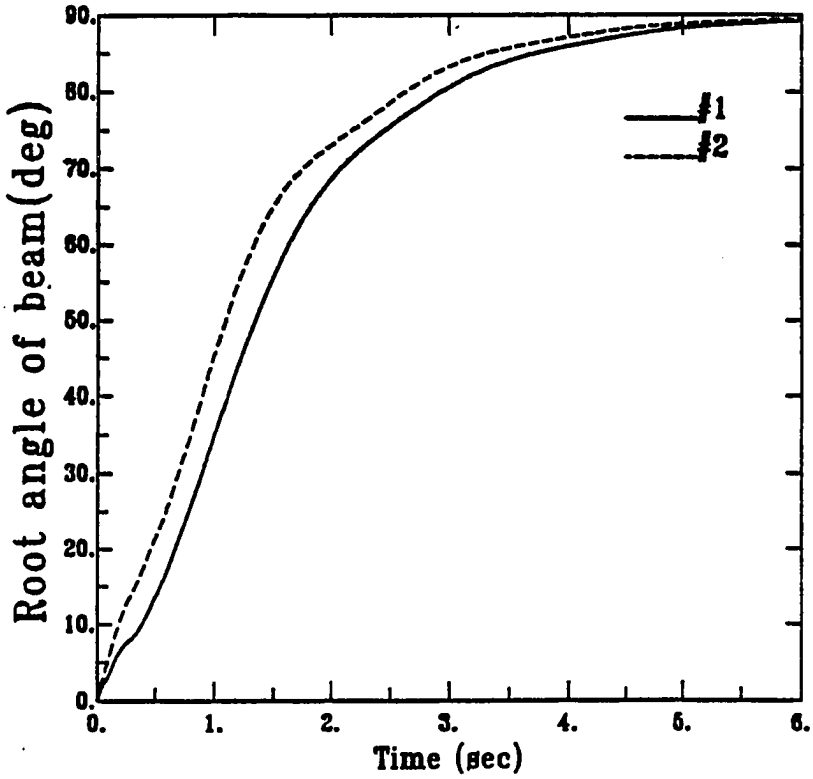

Figure 5.9: Beam angular displacement of a flexible one-beam structure

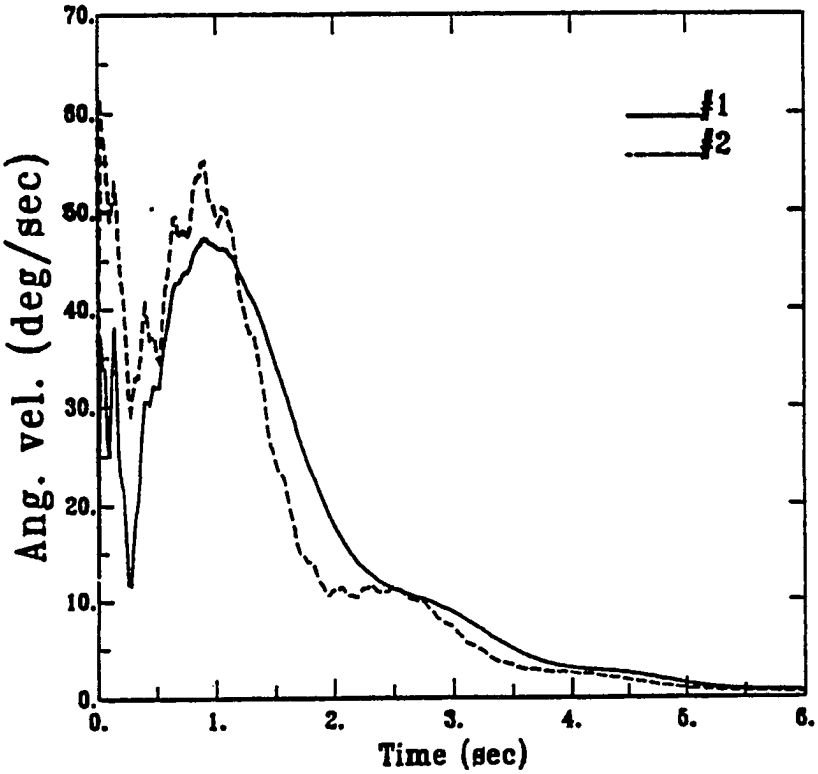

* #1: Noncircular ; #2: Circular

Figure 5.10: Beam angular velocity of a flexible one-beam structure

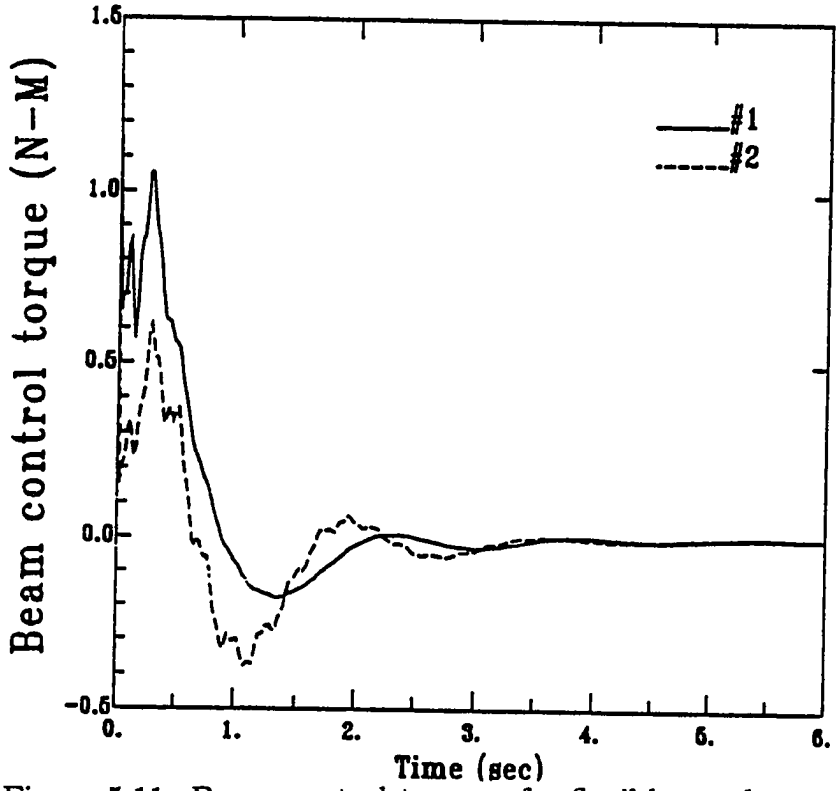

Figure 5.11: Beam control torque of a flexible one-beam structure

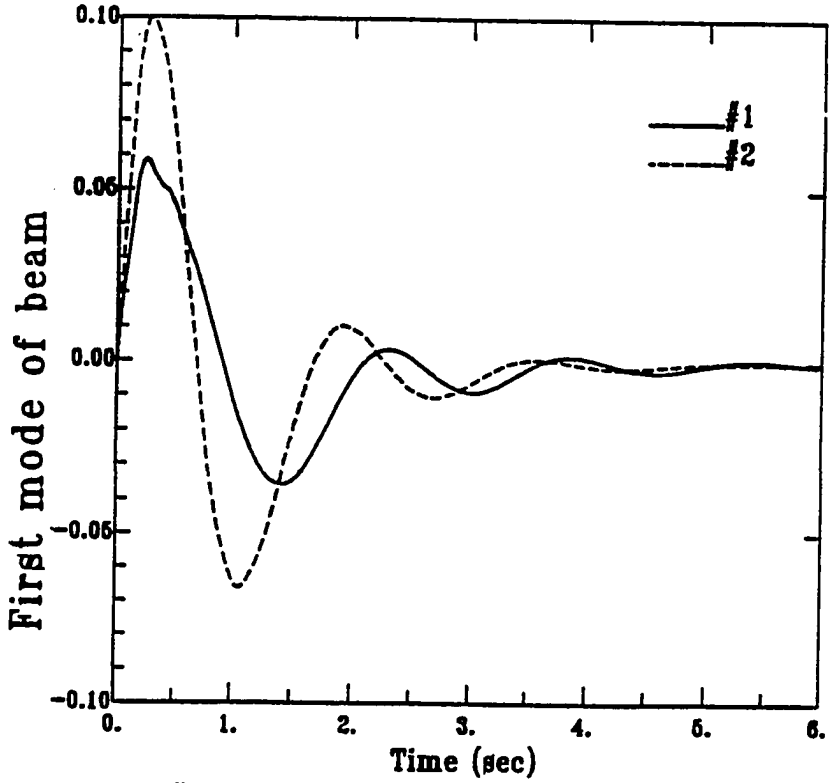

* #1: Noncircular ; #2: Circular

Figure 5.12: First mode of a flexible one-beam structure

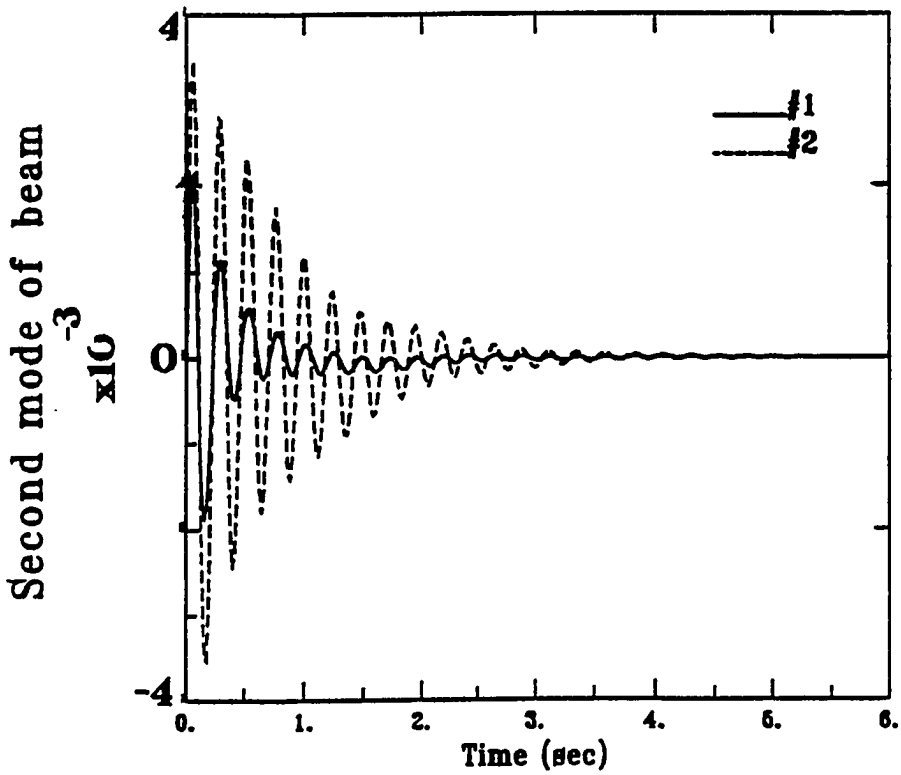

Figure 5.13: Second mode of a flexible one-beam structure

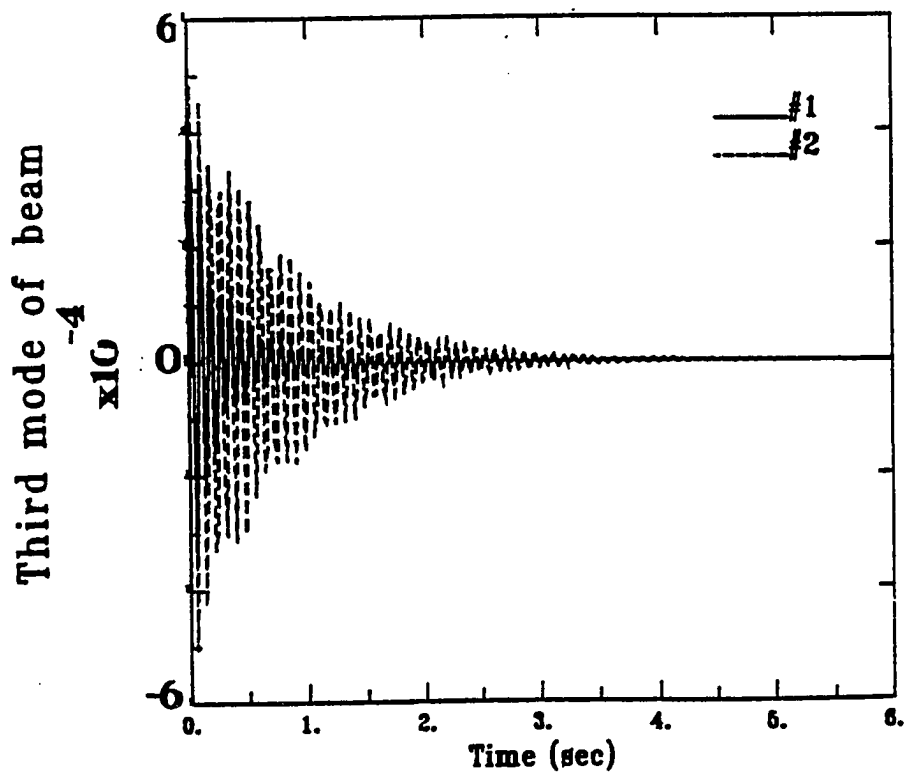

* #1: Noncircular ; #2: Circular

Figure 5.14: Third mode of a flexible one-beam structure

N-M as shown in Fig. 5.11. Apparently, the control torque in the presence of noncircular gears damps out faster than that for circular gears. Also, the vibrational modes behave significantly lower as shown in Fig. 5.11. The behaviors of the three modes are demonstrated in Figs. 5.12-5.14. The vibrational modes can be suppressed by output feedback control in the case of circular gears and are further suppressed through noncircular gears in conjunction with the feedback control. As can be seen in Fig. 5.12, the noncircular gears suppress the first mode more than circular gears do. At 0.3 sec, the first mode with circular gears produces a peak amplitude of 0.1 units compared to 0.06 units with noncircular gears. Figure 5.13 shows two case histories of the second mode. The peak amplitude of each mode is considerably reduced, with noncircular gears contributing to vibrational suppression of the second mode even more than with circular gears. A similar situation happens in the behavior of the third mode. Figure 5.14 shows that smaller amplitude of the third mode is achieved by noncircular gears. The simulation results in Figs. 5.9-5.14 thus provide some insights into the slewing maneuvers of flexible one-beam structure to the mechanism of the noncircular gears.

Moreover, the hyperbolic gear ratio of noncircular gears can be optimized to improve the suppression of vibrational motion of the flexible beam. The optimal parameters of noncircular gears, i.e. c_1 and c_2 in Table 5.2, can be determined in section 5.7 by employing a optimalization technique. The control gain can also be taken into account when dealing with such an optimization problem. The simulations associated with the optimal design of noncircular gears and gain are comparable to the results obtained in this section.

Table 5.2: Model parameters of one flexible beam

a. Beam motor:

$K_{t1} = 9.3 \times 10^{-3}$	$N \bullet m/Amp$	$K_{b1} = 9.2 \times 10^{-3}$	$N \bullet m/Amp$
$R_{a1} = 1.1$	Ohm	$I_{m1} = 2.3 \times 10^{-6}$	$kg - m^2$

b. Steel beam:

Length	$\bar{L} = 1.0$	m
Rigidity	EI = 0.71	$N - m^2$
Density	$\rho = 0.47916$	kg/m
Thickness	h $= 0.041 \times 10^{-2}$	m

c. Parameters of noncircular gear ratio:

$c_1 = \frac{\pi}{10}$

$c_2 = \frac{3\pi}{5}$

Table 5.3: Weighting and feedback gain matrices of one flexible beam

a. Weighting matrices:

State weighting matrix:

$$Q = Diag[\ 80\ 0.001\ 0.001\ 0.001\ 100\ 0.001\ 0.001\ 0.001\ ];$$

Input weighting matrix:

$$R = [\ 100\ ];$$

b. Output feedback gain matrix:

$$G = [\ -0.8944\ 0.0933\ 0.0153\ 0.0054\ -1.1315\ 0.2245\ 0.0365\ 0.0130\ ].$$

§§ 5.6.2 Simulation of a flexible two-beam structure

A flexible beam is articulated on the tip of another steel beam to create an articulated flexible structure, as shown in Fig. 5.7. The entire system becomes a 2-body dynamics composed of two identical flexible steel beams. Two cantilevered modes are assigned to discretize the flexural vibration of each flexible beam. The model parameters of the flexible two-beam structure are listed in Table 5.4. To solve the optimal control law, two positive-definite weighting matrices, defined in Eq. (5.60), are specified and these are shown in Table 5.6. By solving the matrix Riccati equation, a constant output feedback gain matrix as shown in Table 5.6 is determined for slewing maneuvers of these two articulated flexible beams. The parameters of two hyperbolic gear ratios are demonstrated for two flexible steel beams in Table 5.6. Figure 5.15 shows a 90-degree slewing control mission for this articulated two-beam structure. The 90-degree slewing simulations are performed through the regular circular gears and the noncircular gears respectively. Two kinds of simulation results are indicated herein, as is indicated in the previous section.

The simulation results of this slewing maneuver are demonstrated in Figs. 5.16-5.25. Figure 4.16 shows the angular displacement of the flexible beam ♯1. The noncircular gears prevent an overshoot in Fig. 5.16 which takes place in the result with the circular gears. A similar situation happens for the angular displacement of the flexible beam ♯2 in Fig. 5.17. The peak magnitudes of the angular velocities in Figs. 5.18 and 5.19 are considerably reduced using the noncircular gears. In Fig. 5.18, an approximately constant angular velocity of 24 deg/sec is maintained for beam ♯1, slewing from 1.5 sec to 3.0 sec. Apparently, the higher modes behave significantly negatively in the results for the circular gears. With the noncircular gears, the smooth trajectory histories of angular velocities in Figs. 5.18 and 5.19 imply that the structural vibrations of two flexible beams are

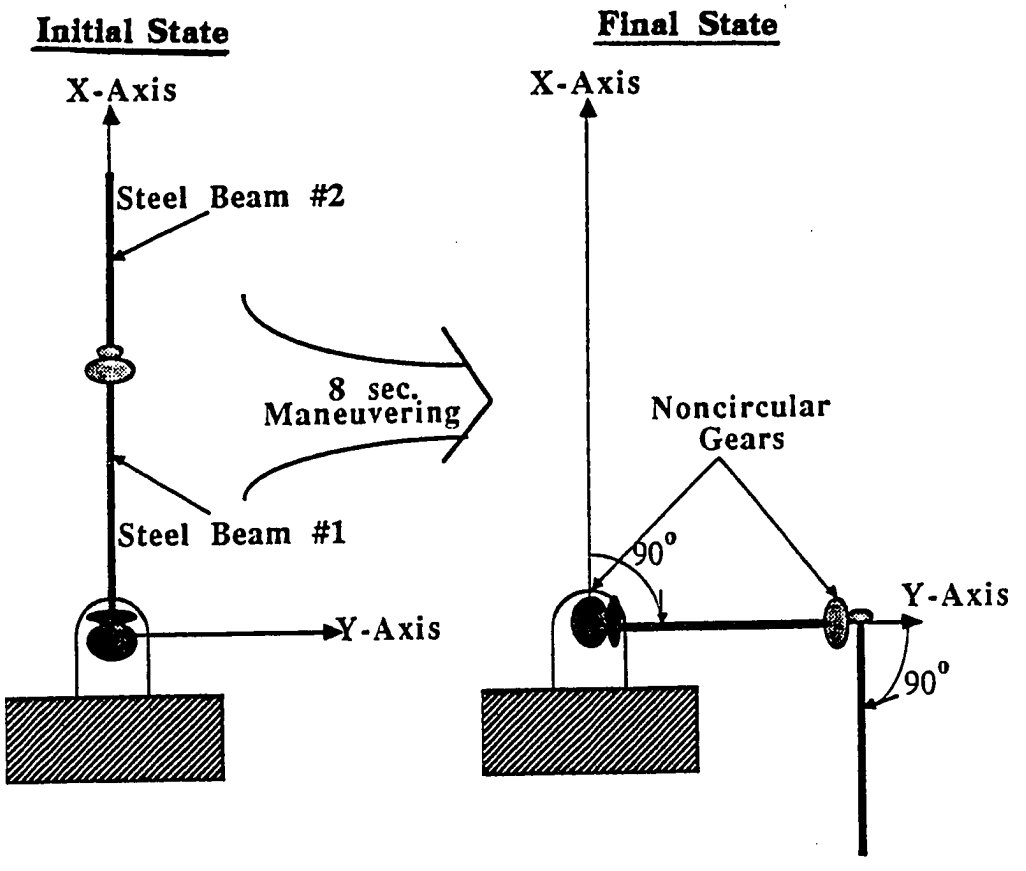

Figure 5.15: 90-degree slewing mission of a flexible two-beam structure

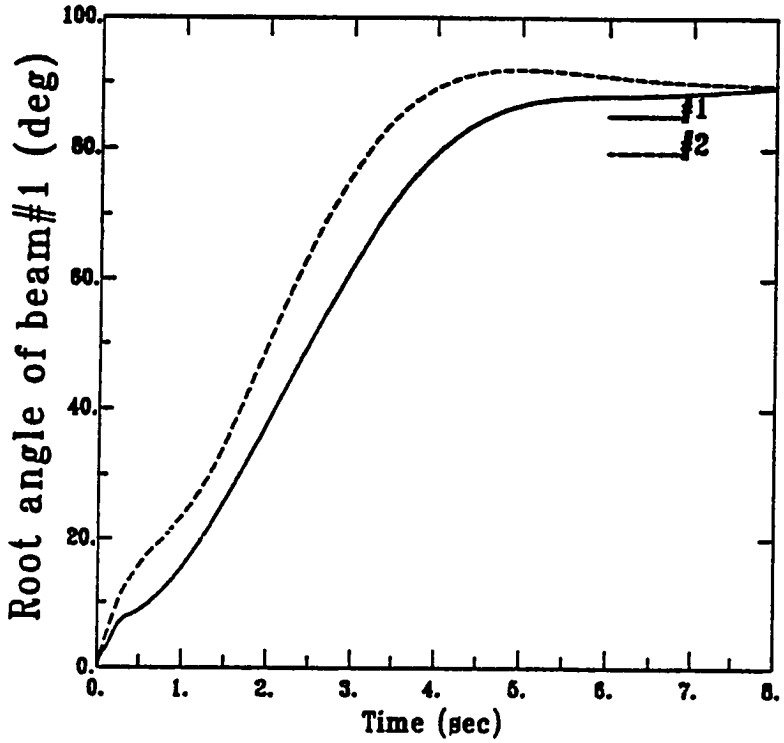

Figure 5.16: Beam #1 angular displacement of a flexible two-beam structure

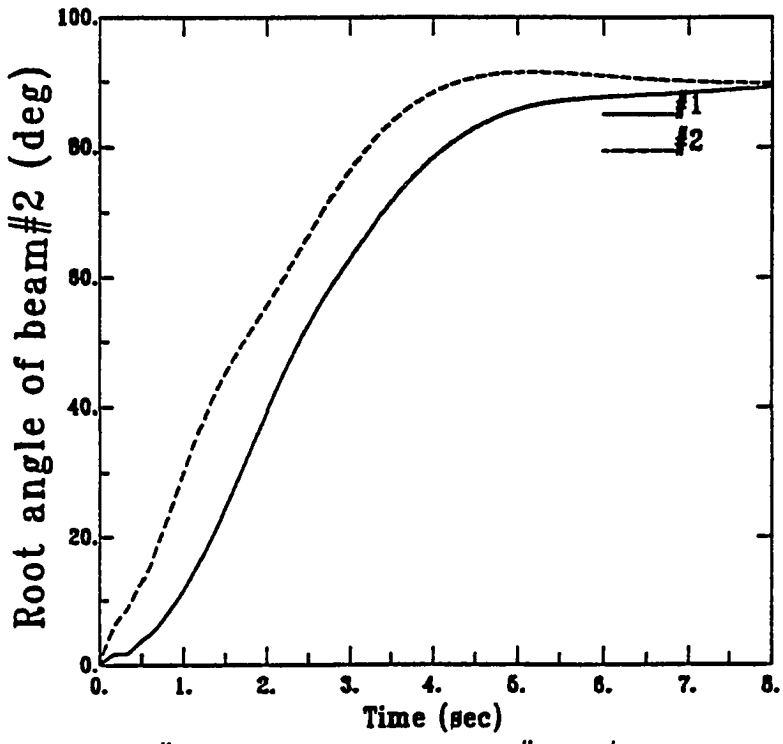

* #1: Noncircular ; #2: Circular

Figure 5.17: Beam #2 angular displacement of a flexible two-beam structure

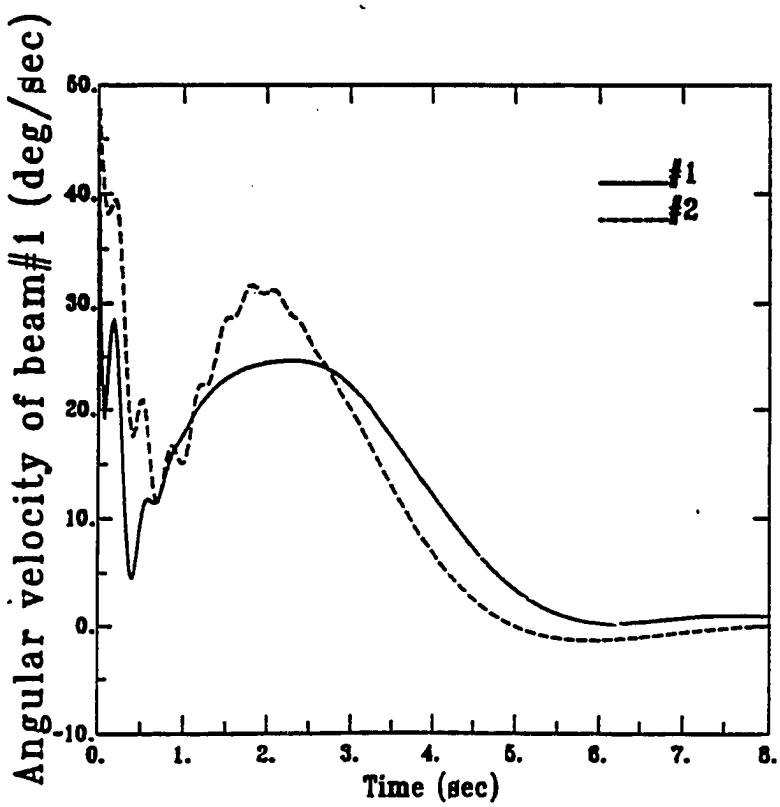

Figure 5.18: Beam #1 angular velocity of a flexible two-beam structure

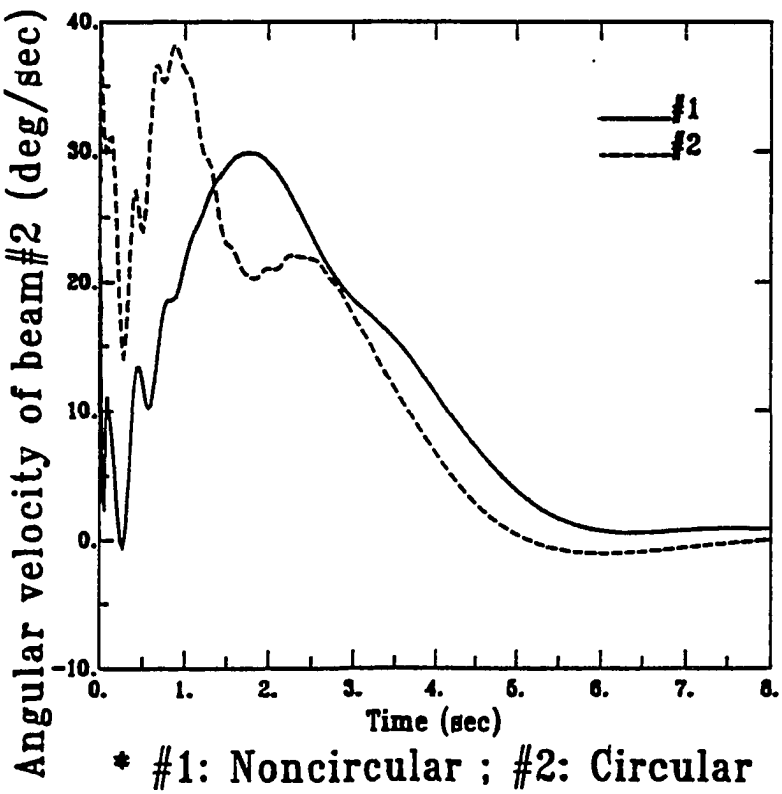

* #1: Noncircular ; #2: Circular

Figure 5.19: Beam #2 angular velocity of a flexible two-beam structure

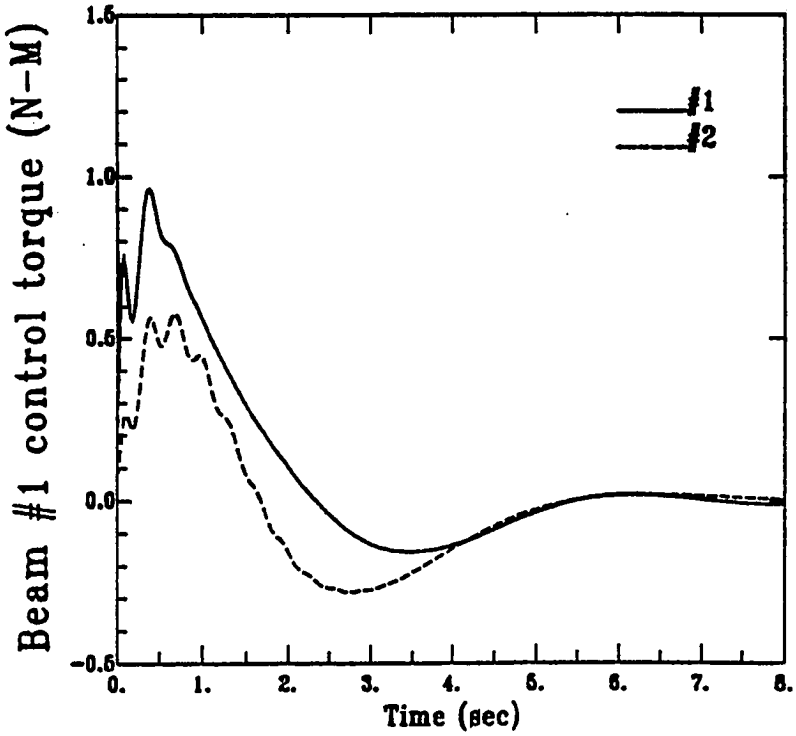

Figure 5.20: Beam #1 control torque of a flexible two-beam structure

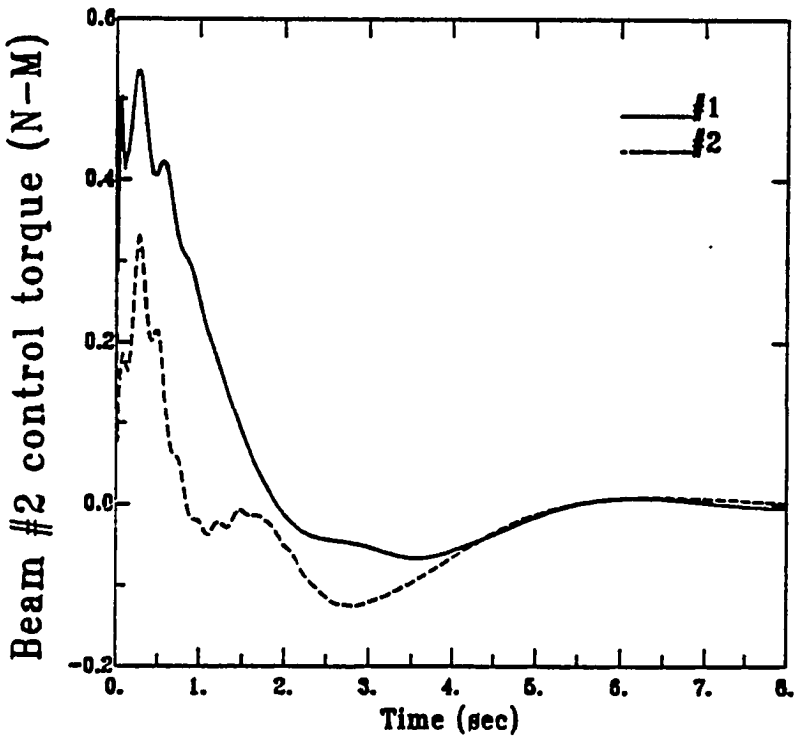

* #1: Noncircular ; #2: Circular

Figure 5.21: Beam #2 control torque of a flexible two-beam structure

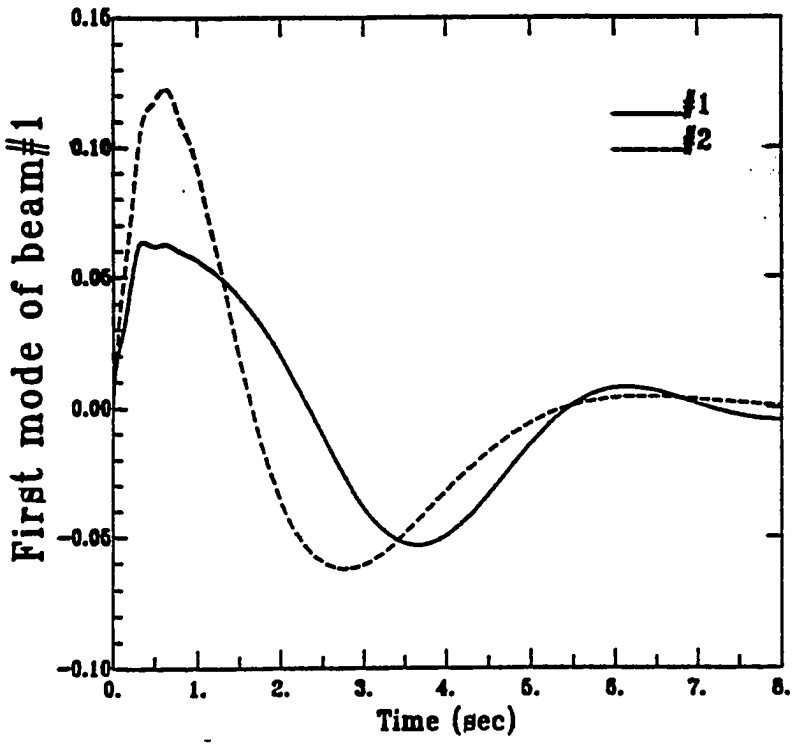

Figure 5.22: First mode of beam #1 for a flexible two-beam structure

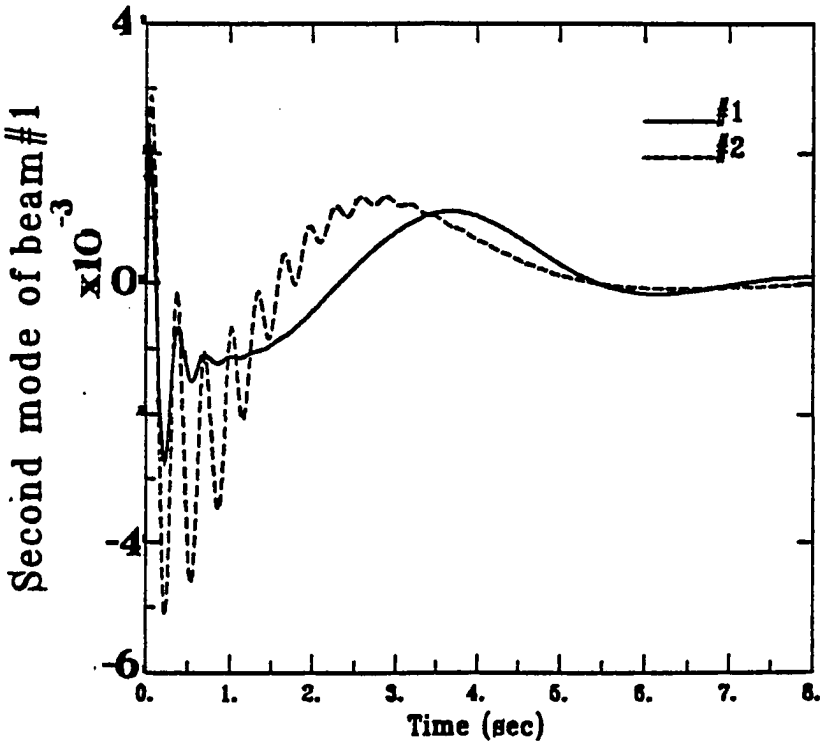

* #1: Noncircular ; #2: Circular

Figure 5.23: Second mode of beam #1 for a flexible two-beam structure

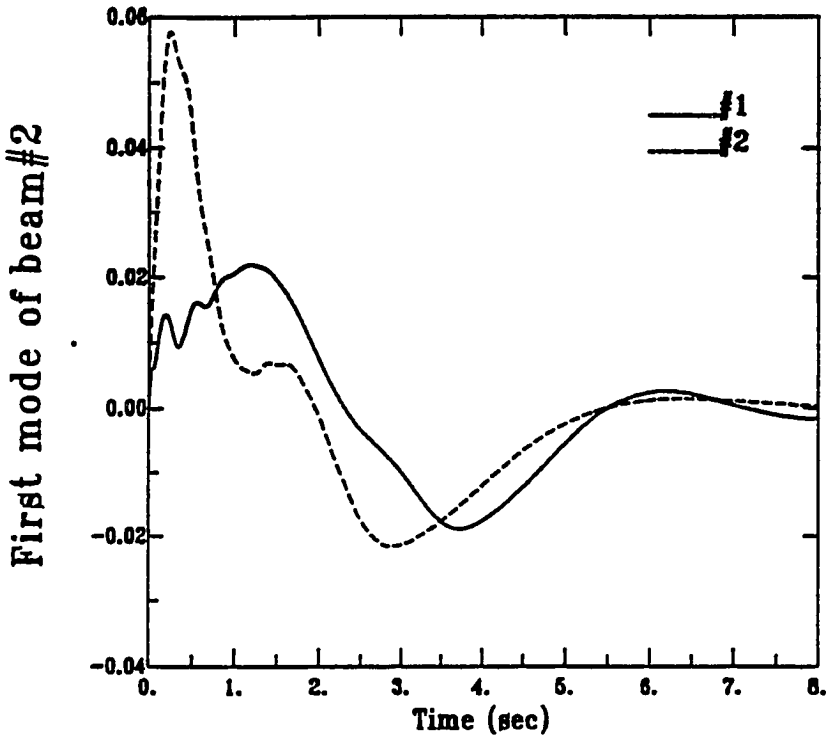

Figure 5.24: First mode of beam #2 for a flexible two-beam structure

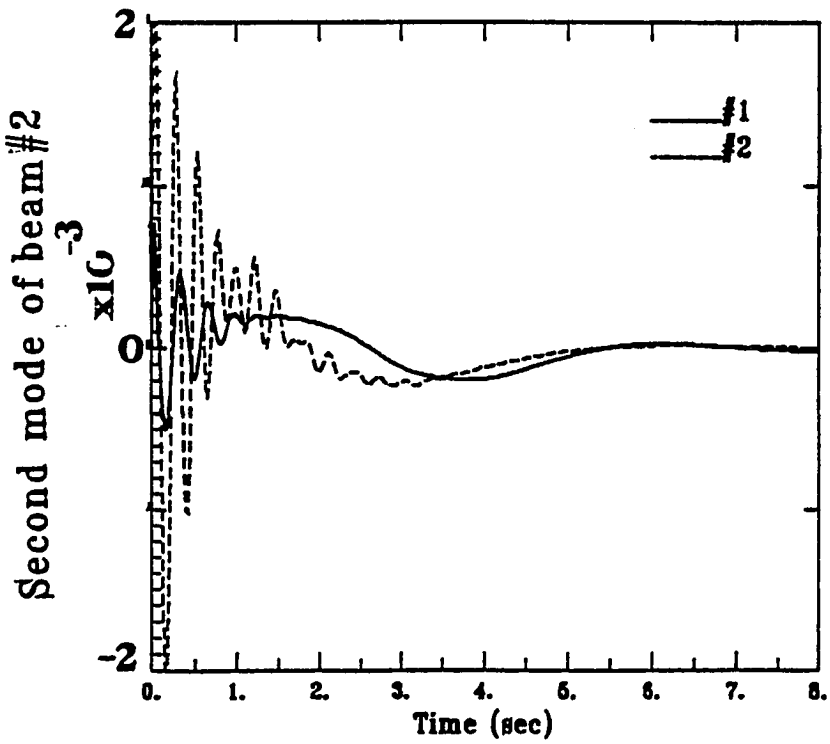

* #1: Noncircular ; #2: Circular

Figure 5.25: Second mode of beam #2 for a flexible two-beam structure

efficiently suppressed during 90-degree slewing maneuver. Figures 4.20 and 4.21 show the control torques of beam ♯1 and beam ♯2 respectively. The control torque starts with 0.7 N-M for beam ♯1 and 0.3 N-M for beam ♯2. Both control torques of noncircular gears damp out faster than with circular gears. Two modes of each beam are demonstrated in Figs. 5.22-5.25. The noncircular gears can further suppress the vibrational modes which have been damped out to some extent by output feedback control. Figure 4.22 illustrates that the noncircular gears suppress the first mode more than the circular gears. At 0.3 sec, the peak amplitude of 0.125 units with the circular gears is reduced by half to 0.063 with noncircular gears. In Fig. 5.23, the high-frequency second- mode oscillation of beam ♯1 is considerably tuned to a smooth trajectory using the noncircular gears. And the peak amplitude of each oscillation decreases greatly in the result of the noncircular gears. Hence, the noncircular gears contribute to the suppression of the second mode of beam ♯1, more than with just the output feedback control. Similarly, the suppression of beam ♯2 first mode is enhanced by the noncircular gears, as shown in Fig. 5.24. Note the elimination of the high frequency amplitude of the second mode of beam ♯2 within the first two seconds, as shown in Fig. 5.25.

The simulation results in Figs. 5.16-5.25 indicate again the feasibility of noncircular gears in the slewing maneuvers of flexible space structures. Obviously, the noncircular gears have been successful in improving the angular velocities of two flexible beams to slew more smoothly, thereby suppressing their vibrational motion of the beams, especially the high frequency modes. The structural vibration can be even suppressed in such a way that the hyperbolic parameters of noncircular gear ratios can be locally optimized to suppress more vibrational motion of two flexible beams. Also, the control gains can be regarded as the design variables in such an optimization problem for the suppression of vibration. The next section will deal with the optimal designs of noncircular gears and gains by using an optimization technique for both beam-like flexible space structures.

Table 5.4: Model parameters of two articulated flexible beams

a. Beam motors:

(1)Beam ♯1 motor:

$K_{t1} = 0.0346$	$N \bullet m/Amp$
$K_{b1} = 0.0342$	Volt-sec/rad
$R_{a1} = 4$	Ohm
$I_{m1} = 4.7 \times 10^{-6}\ kg - m^2$	
$N_{p1} = 1$	

(2)Beam ♯2 motor:

$K_{t2} = 9.3 \times 10^{-3}$	$N \bullet m/Amp$
$K_{b2} = 9.2 \times 10^{-3}$	Volt-sec/rad
$R_{a2} = 1.1$	Ohm
$I_{m2} = 2.3 \times 10^{-6}$	$kg - m^2$
$N_{p2} = 1$	

b. Steel beam:

Length	$\bar{L} = 1.0$	m
Rigidity	EI = 0.71	$N - m^2$
Density	$\rho = 0.47916$	kg/m
Thickness	h $= 0.041 \times 10^{-2}$	m

c. Parameters of noncircular gear ratio:

(1)Beam ♯1 gears:

$c_1 = \frac{\pi}{10}$

$c_2 = \frac{3\pi}{5}$

(2)Beam ♯2 gears:

$c_3 = \frac{\pi}{44}$

$c_4 = \frac{3\pi}{11}$

Table 5.5: Weighting and feedback gain matrices of two articulated flexible beams

a. Weighting matrices:

State weighting matrix:

$$Q = Diag[\ 250\ 100\ 10\ 10\ 10\ 10\ 250\ 100\ 10\ 10\ 10\ 10\ ];$$

Input weighting matrix:

$$R = [\ 500,\quad 500\ ];$$

b. Output feedback gain matrix:

$$G = \begin{pmatrix} -0.7018 & -0.0547 & 0.5633 & 2.4793 & -0.2597 & 1.3766 \\ 0.0864 & -0.4439 & 0.0345 & 4.9427 & -0.2104 & -2.9872 \\ -1.1214 & -0.2117 & 0.8029 & -0.6719 & 0.3141 & 0.0668 \\ -0.0844 & -0.5758 & 0.2477 & -0.3145 & 0.2148 & 0.0165 \end{pmatrix}$$

§ 5.7 Optimal design of noncircular gears and control gain using an optimization technique

For two kinds of beam-like flexible structures, the Generalized Reduced Gradient (GRG) method is employed to determine the optimal designs of noncircular gear ratios and control gain in terms of suppression of vibration. Generally, the GRG method is implemented to find the optimal solution to the constrained nonlinear programming problem. The constrained nonlinear programming problem can be expressed as follows.

$$Minimize: \ F(\bar{x}); \quad \bar{x} = [x_1, x_2, x_3, \cdots, x_N]^T \in R^N \tag{5.61}$$

$$Subject\ to\ \phi_k(\bar{x}) \geq 0; \quad k = 1, 2, 3, \cdots, K \tag{5.62}$$

$$\psi_\ell(\bar{x}) = 0; \quad \ell = 1, 2, 3, \cdots, L \tag{5.63}$$

where

$\bar{x}$	: a column vector of design variables,
N	: total number of design variables,
$F(\bar{x})$	: the design criteria or objective function,
$\phi_k(\bar{x})$	: K inequality constraint functions,
$\psi_\ell \bar{x}$	: L equality constraint functions.

Basically, the GRG subroutine is used to seek the optimal solution of the design variable vector $\bar{x}$ to minimize a cost function $F(\bar{x})$ in a local domain which is bounded through the given upper and lower bounds of the design variables. First, a starting point $\bar{x}^0$ of design variables must be provided for GRG to search a feasible point. The reduced gradient is then evaluated by equating a projected reduced gradient formed through Eqs. (5.61) to (5.63). The L_2 norm of the projected reduced gradient is then checked to determine if it is within some tolerance for convergence. If so, a constrained relative minimum of cost function has been obtained. If not, a line search provides a search direction to locate a

local minimum of $F(\bar{x})$. The line search is performed by initially taking a step in the direction calculated for the design variables. The design variables are adjusted by using Newton's method until the constraint functions given by Eqs. (5.62) and (5.63) are satisified. The cost function is thus minimized according to such a reduced gradient algorithm.

From the simulation results in section 4.6, the noncircular gears with hyperbolic gear ratios have improved the slewing performances of two kinds of beam-like flexible structures, especially the vibrational motion of the flexible beams. In order to further suppress vibrational motion, two kinds of optimization problems are implemented for each beam-like flexible structure. First, the mechanism design of noncircular gears is investigated to determine optimal hyperbolic parameters to suppress the magnitude of the beam vibrations. Second, an integrated approach to the optimal design of the control and mechanism is conducted via the GRG method. The hyperbolic parameters of noncircular gears along with control gains are optimally found to minimize the specified cost function. The states with severe vibration are chosen from the simulation results associated with the noncircular gears to form a constrained optimization problem. The quadratic cost function is developed to provide a criterion for the minimization of amplitudes of vibrational modes through the design variables. Furthermore, the slewing angles and angular velocity are specified at the particular values through the cost function in order to achieve a feasible point for the GRG subroutine. The second-order dynamic equations of two kinds of flexible beam-like structures, as shown in Eqs. (5.49) and (5.59), are transformed into first-order state equations. These first-order state equations thus indicate the equality constraint functions which must be satisified in terms of dynamic response. The inequality constraint functions are specified to bound the gear ratios or control torques. The upper and lower bounds of each variable are carefully assigned to obtain a bounded domain for seeking a minimum of the cost function. The designs of the noncircular gears and control gains used in section 4.6 are optimized in terms of minimizing amplitudes of vibrational modes.

Four optimization problems are listed in Tables 5.6 through 5.9 for slewing maneuvers of two kinds of beam-like flexible structures. They are

(1) Optimization problem of noncircular gears for one flexible beam [Table 5.6],

(2) Optimization problem of noncircular gears and control gain for one flexible beam [Table 5.7],

(3) Optimization problem of noncircular gears for two articulated flexible beams [Table 5.8] and

(4) Optimization problem of noncircular gears and control gain for two articulated flexible beams [Table 5.9].

Based on Eqs. (5.61) to (5.63), Table 5.6 displays the optimization problem of noncircular gears for the 90-degree slewing maneuver of a flexible one-beam structure. The state vector u and time-rate state vector $\dot{\xi}$ at 0.6 sec are selected as the design variables along with the two parameters c_1 and c_2 of noncircular gears. Obviously, there exists eighteen design variables in this optimization problem. The output feedback gain, as shown in Table 5.3, is maintained constant during this optimization process. The cost function is developed to suppress vibrational modes while simultaneously keeping the slewing angle θ and the angular velocity $\dot{\theta}$ at 0.18279 rad and 0.4529 rad/sec respectively. The equality constraint functions are provided by eight first-order state equations which must always be satisfied during optimization process. An inequality constraint function is assigned to force the gear ratio to be greater than 0.1. Two hyperbolic parameters are bounded from 0.1 to 6, and the sixteen states from -10 to 10. The starting value of cost function, i.e. $F(\bar{x}^0)$, equals 44.0442 with the optimal cost function yielding 0.0227078 as the local minimum of $F(\bar{x})$. The final solution of parameters of noncircular gears to locate the minimum of $F(\bar{x})$ yields $c_{1opt} = 0.153083$ and $c_{2opt} = 1.81478$.

The optimal design of noncircular gears is thus generated by the c_{1opt} and c_{2opt}. A 90-degree slewing simulation based on such an optimal design of noncircular gears will be performed in section 5.8.1.

The control gain can also be included in the optimization problem for the flexible one-beam structure. Table 5.7 demonstrates the optimization problem of noncircular gears and control gain for the slewing maneuver of the one-beam structure. Instead of the constant feedback gain, the control gain in the first-order state equations undergoes the optimization process along with the design of noncircular gears to locate the local minimum of cost function. Herein, eight more design variables are included due to the control gain. Therefore, this optimization problem has 26 design variables. The cost function still keeps the angle and angular velocity of the beam, as in the previous case, while minimizing the amplitudes of three modes. Two more inequality constraint functions are specified to bound the control torque between 0.5 and 1 N-M. The starting point and upper/lower bounds of the design variables are demonstrated in this table. The starting value of cost function, i.e. $F(\bar{x}^0)$, equals 42.6998 while the final cost is 0.0068555 at the minimum of $F(\bar{x})$. The optimal design of noncircular gears is obtained by $c_{1opt} = 0.14$ and $c_{2opt} = 1.81692$ which produce a hyperbolic gear ratio. The final solution of control gains that minimizes the cost function $F(\bar{x})$ is

$$G_{opt} = [-0.8942,\ -25,\ -349.8,\ -1413.7,\ -1.4153,\ -7.79999,$$
$$-0.799995,\ 1.69999] \tag{5.64}$$

which, in conjunction with optimally designed noncircular gears, could suppress the beam vibration to a higher degree. A 90-degree slewing simulation based on such an integrated optimal design of noncircular gears and control gain will be implemented in section 5.8.2 which is then compared to the results in section 5.8.1.

Four optimal parameters associated with the two noncircular gears are found by GRG algorithm to minimize the cost function. Similarly, the optimal design of noncircular gears for the flexible two-beam structure can be determined in the same way as shown in Table 5.6. Table 5.8 illustrates the optimization problem of noncircular gears for the slewing maneuver of a flexible two-beam structure. The control gain as shown in Table 5.5 is kept constant in this problem. Four parameters of two noncircular gears, i.e. c_1, c_2, c_3 and c_4, are the design variables which generate two hyperbolic gear ratios. Since the previous results have shown the severe oscillations of the two beams in 0.64 second, the state vector u and time-rate state vector $\dot{\xi}$ at that time are selected to provide an additional 24 design variables. Hence, the overall design variables are 28 for this optimization problem. The quadratic cost function is derived to suppress vibrational modes of two flexible beams while simultaneously keeping two slewing angle θ_1, θ_2 at 0.18117 rad and 0.090778 rad respectively, and two angular velocities $\dot{\theta}_1$, $\dot{\theta}_2$ at 0.19956 rad/sec and 0.20797 rad/sec respectively. Twelve first-order state equations produce the equality constraint functions. Two inequality constraint functions are given to make two gear ratios greater than 0.1. The four hyperbolic parameters are bounded by $\frac{\pi}{8} \sim \frac{6\pi}{11}$, $\frac{3\pi}{4} \sim \frac{\pi}{11}$, $\frac{\pi}{20} \sim \frac{\pi}{23}$ and $\frac{3\pi}{5} \sim \frac{12\pi}{23}$ respectively, while the 24 states are bounded by 10$\sim$-10. The starting value of cost function, i.e. $F(\bar{x}^0)$, equals 23.3353, yielding 0.224246 when the minimum of $F(\bar{x})$ is reached. The local minimum of $f(\bar{x})$ is located by the final solution of four hyperbolic parameters, yielding that the noncircular gears of the first beam are governed by $c_{1opt} = 0.285599$ and $c_{2opt} = 1.82741$, and the noncircular gears of the fore-beam $c_{3opt} = 0.136591$ and $c_{4opt} = 1.64468$. A 90-degree slewing simulation based on this optimization problem will be performed in section 5.8.3.

Similarly, the output feedback gain of this articulated two-beam structure can be treated as the design variables to further suppress vibrations of the one-beam structure. Table 5.9 provides a statement of the optimization problem of noncircular gears and control gain for the slewing maneuver of the articulated

two-beam structure. In this case, 24 more design variables are included due to the control gains. The total number of design variables becomes 52 in this optimization problem. Besides the previous inequality constraint functions in Table 5.8, four more inequality constraint functions are specified to bound the two control torques between 0.5 and 1 N-M. The starting value of cost function, i.e. $F(\bar{x}^0)$, equals 21.772, yielding 0.0157333 when the minimum of $F(\bar{x})$ is reached. The final solution to locate the minimum of $F(\bar{x})$ results in the parameters for noncircular gears of the first beam being $c_{1\,opt}$ =0.29 and $c_{2[opt}$ = 1.9, and that for the noncircular gears of the second beam as: $c_{3\,opt}$ = 0.134177 and $c_{4\,opt}$ = 1.69386. For two motors, the final solution of control gain through GRG subroutine yields

$$G_{opt} = \begin{pmatrix} -0.694 & -0.084 & -7.6 & -132.3 & -0.288 & -26.2 & -1.533 \\ 0.1332 & -0.439 & 4.70607 & -18.799 & -17.875 & -236.191 & -0.043 \end{pmatrix}$$

$$\begin{pmatrix} -0.355 & -1.999 & -1.899 & 0.3 & -0.399 \\ -0.741 & 0.01 & -0.606 & -3.4 & -0.399 \end{pmatrix} \tag{5.65}$$

A 90-degree slewing simulation based on such an integrated optimal design of noncircular gears and control gain will be performed in section 5.8.4.

Table 5.6: Optimization problem of noncircular gears for one flexible beam

Minimize:

$$F(x) = \bar{Q} \times \{\omega \times [\theta(k) - 0.18279]^2 + (1-\omega) \times \left[\dot{\theta}(k) - 0.4529\right]^2 + \sum_{i=1}^{3} [\omega \times q_i^2(k) + (1-\omega) \times \dot{q}_i^2(k)]\};$$

where the weighting numbers $\bar{Q} = 10000$ and $\omega = 0.55$.

Design variables:

$$\bar{x} = \left[c_1,\ c_2,\ \xi(k),\ \dot{\xi}(k+1)\right]^T$$

where integers k, k+1 indicate time sequences and

$$\xi(k) = \left[\theta(k), q_1(k), q_2(k), q_3(k), \dot{\theta}(k), \dot{q}_1(k), \dot{q}_2(k), \dot{q}_3(k)\right]^T;$$

$$\xi(k+1) = [\dot{\theta}(k+1), \dot{q}_1(k+1), \dot{q}_2(k+1), \dot{q}_3(k+1), \ddot{\theta}(k+1), \ddot{q}_1(k+1), \ddot{q}_2(k+1), \ddot{q}_3(k+1)]^T.$$

Subject to:

(1) Equality constraint functions:

$$\begin{cases} \psi_i(\bar{x}) = \xi(k+1) - \tilde{\xi}(k+1); & i = 1,2,3,\cdots,8 \\ \tilde{\xi}(k+1) = \tilde{A}\xi(k) + \tilde{B}u(k); \\ u(k) = G\xi(k) \end{cases}$$

where

$$\tilde{A} = \begin{pmatrix} 0 & I \\ -\bar{M}^{-1}K & -\bar{M}^{-1}\tilde{C} \end{pmatrix}; \quad \tilde{B} = \begin{pmatrix} 0 \\ \bar{M}^{-1}B \end{pmatrix}.$$

§ Continued §

(2) Inequality constraint functions:

$$\phi_1(\bar{x}) = c_2 - 0.1 \times \left[c_1 + \frac{10.40413\pi}{180}\right] \geq 0.$$

Starting point:

$$\bar{x}^0 = [\frac{\pi}{22}, \frac{6\pi}{11}, 0.18159, 0.050333, -0.00047771, -0.000077764, 0.53284,$$
$$-0.016697, -0.0044417, 0.00049086, 0.53376, -0.017172, -0.0039833,$$
$$0.00098626, 0.84918, -0.43872, 0.42355, 0.45771]^T$$

Bounds on design variables:

(1) Upper bounds:

$$\bar{x}_{max} = [6, 6, 10, 10, 10, 10, 10, 10, 10, 10, 10, 10, 10, 10, 10, 10, 10, 10]^T;$$

(2) Lower bounds:

$$\bar{x}_{min} = [0.1, 0.1, -10, -10, -10, -10, -10, -10, -10, -10, -10, -10,$$
$$-10, -10, -10, -10, -10, -10]^T.$$

Table 5.7: Optimization problem of noncircular gears and control gain for one flexible beam

Minimize:

$$F(x) = \bar{Q} \times \{\omega \times [\theta(k) - 0.18279]^2 + (1-\omega) \times \left[\dot{\theta}(k) - 0.4529\right]^2 + \sum_{i=1}^{3} [\omega \times q_i^2(k)]\};$$

where the weighting numbers $\bar{Q} = 10000$ and $\omega = 0.55$.

Design variables:

$$\bar{x} = \left[c_1,\ c_2,\ G_{(1\times 8)},\ \xi(k),\ \dot{\xi}(k+1)\right]^T$$

where integers k, k+1 indicate time sequences and

$$\xi(k) = \left[\theta(k), q_1(k), q_2(k), q_3(k), \dot{\theta}(k), \dot{q}_1(k), \dot{q}_2(k), \dot{q}_3(k)\right]^T;$$

$$\xi(k+1) = [\dot{\theta}(k+1), \dot{q}_1(k+1), \dot{q}_2(k+1), \dot{q}_3(k+1), \ddot{\theta}(k+1), \ddot{q}_1(k+1), \ddot{q}_2(k+1), \ddot{q}_3(k+1)]^T.$$

Subject to:

(1) Equality constraint functions:

$$\begin{cases} \psi_i(\bar{x}) = \xi(k+1) - \tilde{\xi}(k+1); & i = 1,2,3,\cdots,8 \\ \tilde{\xi}(k+1) = \tilde{A}\xi(k) + \tilde{B}u(k); \\ u(k) = G_{(1\times 8)}\xi(k) \end{cases}$$

where

$$\tilde{A} = \begin{pmatrix} 0 & I \\ -\bar{M}^{-1}K & -\bar{M}^{-1}\bar{C} \end{pmatrix}; \quad \tilde{B} = \begin{pmatrix} 0 \\ \bar{M}^{-1}B \end{pmatrix}.$$

§ Continued §

(2) Inequality constraint functions:

$$\begin{cases} \phi_1(\bar{x}) = c_2 - 0.1 \times [c_1 + \frac{10.40413\pi}{180}] \geq 0. \\ \phi_2(\bar{x}) = -u(k) + 1 \geq 0; \\ \phi_3(\bar{x}) = u(k) - 0.5 \geq 0. \end{cases}$$

Starting point:

$$\bar{x}^0 = [0.153083, 1.81478, -0.8944, -19.0884, -160.9831, -449.1275, -1.5449,$$
$$-4.7363, 0.2093, 0.5421, 0.18159, 0.050333, -0.00047771, -0.000077764,$$
$$0.53284, -0.016697, -0.0044417, 0.00049086, 0.53376, -0.017172, -0.0039833,$$
$$0.00098626, 0.84918, -0.43872, 0.42355, 0.45771]^T$$

Bounds on design variables:

(1) Upper bounds:

$$\bar{x}_{max} = [0.16, 1.82, -0.8942, -25, -349.2, -1413.1, -1.4,$$
$$-7.2, -0.2, 1.7, 16 \times [10]^T];$$

(2) Lower bounds:

$$\bar{x}_{min} = [0.14, 1.8, -0.8946, -25.6, -349.8, -1413.7,$$
$$-2, -7.8, -0.8, 1.1, 16 \times [-10]^T].$$

Table 5.8: Optimization problem of noncircular gears for two articulated flexible beams

Minimize:

$$F(x) = \bar{Q} \times \{\omega_1 \times [\theta_1(k) - 0.18117]^2 + (1-\omega_1) \times [\theta_2(k) - 0.090778]^2 +$$

$$\omega_2 \times \left[\dot{\theta}_1(k) - 0.19956\right]^2 + (1-\omega_2) \times \left[\dot{\theta}_2(k) - 0.20792\right]^2$$

$$+ \sum_{i=1}^{2} [\omega_1 \times q_{i1}^2(k) + (1-\omega_1) \times q_{i2}^2(k) + \omega_1 \times \dot{q}_{i1}^2(k)$$

$$+(1-\omega_1) \times \dot{q}_{i2}^2(k)\};$$

where the weighting numbers $\bar{Q} = 10000$, $\omega_1 = 0.55$ and $\omega_2 = 0.5$.

Design variables:

$$\bar{x} = \left[c_1,\ c_2,\ c_3,\ c_4,\ \xi(k),\ \dot{\xi}(k+1)\right]^T$$

where integers k, k+1 indicate time sequences and

$$\xi(k) = [\theta_1(k), \theta_2(k), q_{11}(k), q_{12}(k), q_{21}(k), q_{22}(k), \dot{\theta}_1(k), \dot{\theta}_2(k),$$

$$\dot{q}_{11}(k), \dot{q}_{12}(k), \dot{q}_{21}(k), \dot{q}_{22}]^T;$$

$$\xi(k+1) = [\dot{\theta}_1(k+1), \dot{\theta}_2(k+1), \dot{q}_{11}(k+1), \dot{q}_{12}(k+1), \dot{q}_{21}(k+1), \dot{q}_{22}(k+1),$$

$$\ddot{\theta}_1(k+1), \ddot{\theta}_2(k+1), \ddot{q}_{11}(k+1), \ddot{q}_{12}(k+1), \ddot{q}_{21}(k+1), \ddot{q}_{22}(k+1)]^T.$$

Subject to:

(1) Equality constraint functions:

$$\begin{cases} \psi_i(\bar{x}) = \xi(k+1) - \tilde{\xi}(k+1); \quad i = 1,2,3,\cdots,12 \\ \tilde{\xi}(k+1) = \tilde{A}\xi(k) + \tilde{B}u(k) + \tilde{f}; \\ u(k) = G\xi(k) \end{cases}$$

§ Continued §

where

$$\tilde{A} = \begin{pmatrix} 0 & I \\ -\bar{M}^{-1}K & -\bar{M}^{-1}\bar{C} \end{pmatrix}; \quad \tilde{B} = \begin{pmatrix} 0 \\ \bar{M}^{-1}B \end{pmatrix} \quad \tilde{f} = \begin{pmatrix} 0 \\ \bar{M}^{-1}f\left(\xi,\dot{\xi}\right) \end{pmatrix}.$$

(2) Inequality constraint functions:

$$\begin{cases} \phi_1(\bar{x}) = c_2 - 0.1 \times \left[c_1 + \frac{10.38044\pi}{180}\right] \geq 0. \\ \phi_2(\bar{x}) = c_4 - 0.1 \times \left[c_3 + \frac{5.201172\pi}{180}\right] \geq 0. \end{cases}$$

Starting point:

$$\bar{x}^0 = [\frac{\pi}{10}, \frac{3\pi}{5}, \frac{\pi}{22}, \frac{6\pi}{11}, 0.18117, 0.090778, 0.062614, -0.0012435, 0.015561,$$
$$0.00026398, 0.19956, 0.20797, -0.0062241, 0.0038742, -0.0050753,$$
$$0.0015751, 0.19952, 0.20839, -0.0063547, 0.0038599, -0.0049356,$$
$$0.0015419, -0.087725, 0.91447, -0.28073, -0.030462, 0.30025, -0.071396]^T$$

Bounds on design variables:

(1) Upper bounds:

$$\bar{x}_{max} = [\frac{\pi}{8}, \frac{3\pi}{4}, \frac{\pi}{20}, \frac{3\pi}{5}, 10, 10, 10, 10, 10, 10, 10, 10, 10, 10, 10,$$
$$10, 10, 10, 10, 10, 10, 10, 10, 10, 10, 10, 10, 10]^T;$$

(2) Lower bounds:

$$\bar{x}_{min} = [\frac{\pi}{11}, \frac{6\pi}{11}, \frac{\pi}{23}, \frac{12\pi}{23}, -10, -10, -10, -10, -10, -10, -10, -10,$$
$$-10, -10, -10, -10, -10, -10, -10, -10, -10, -10,$$
$$-10, -10, -10, -10, -10, -10]^T.$$

Table 5.9: Optimization problem of noncircular gears and control gain for two articulated flexible beams

Minimize:

$$F(x) = \bar{Q} \times \{\omega_1 \times [\theta_1(k) - 0.18117^2 + (1-\omega_1) \times [\theta_2(k) - 0.090778]^2 +$$

$$\omega_2 \times \left[\dot{\theta}_1(k) - 0.19956\right]^2 + (1-\omega_2) \times \left[\dot{\theta}_2(k) - 0.20792\right]^2$$

$$+ \sum_{i=1}^{2} [\omega_1 \times q_{i1}^2(k) + (1-\omega_1) \times q_{i2}^2(k)]\};$$

where the weighting numbers $\bar{Q} = 10000$, $\omega_1 = 0.55$ and $\omega_2 = 0.5$.

Design variables:

$$\bar{x} = \left[c_1,\ c_2,\ c_3,\ c_4,\ G_{(2\times12)},\ \xi(k),\ \dot{\xi}(k+1)\right]^T$$

where integers k, k+1 indicate time sequences and

$$\xi(k) = [\theta_1(k), \theta_2(k), q_{11}(k), q_{12}(k), q_{21}(k), q_{22}(k), \dot{\theta}_1(k), \dot{\theta}_2(k),$$

$$\dot{q}_{11}(k), \dot{q}_{12}(k), \dot{q}_{21}(k), \dot{q}_{22}]^T;$$

$$\xi(k+1) = [\dot{\theta}_1(k+1), \dot{\theta}_2(k+1), \dot{q}_{11}(k+1), \dot{q}_{12}(k+1), \dot{q}_{21}(k+1),$$

$$\dot{q}_{22}(k+1), \ddot{\theta}_1(k+1), \ddot{\theta}_2(k+1), \ddot{q}_{11}(k+1), \ddot{q}_{12}(k+1),$$

$$\ddot{q}_{21}(k+1), \ddot{q}_{22}(k+1)]^T.$$

Subject to:

(1) Equality constraint functions:

$$\begin{cases} \psi_i(\bar{x}) = \xi(k+1) - \tilde{\xi}(k+1); \quad i = 1,2,3,\cdots,12 \\ \tilde{\xi}(k+1) = \tilde{A}\xi(k) + \tilde{B}u(k) + \tilde{f}; \\ u(k) = G_{(2\times12)}\xi(k) \end{cases}$$

§ Continued §

where

$$\tilde{A} = \begin{pmatrix} 0 & I \\ -\bar{M}^{-1}K & -\bar{M}^{-1}\bar{C} \end{pmatrix}; \quad \tilde{B} = \begin{pmatrix} 0 \\ \bar{M}^{-1}B \end{pmatrix} \quad \tilde{f} = \begin{pmatrix} 0 \\ \bar{M}^{-1}f\left(\xi,\dot{\xi}\right) \end{pmatrix}.$$

(2) Inequality constraint functions:

$$\begin{cases} \phi_1(\bar{x}) = c_2 - 0.1 \times \left[c_1 + \frac{10.38044\pi}{180}\right] \geq 0. \\ \phi_2(\bar{x}) = c_4 - 0.1 \times \left[c_3 + \frac{5.201172\pi}{180}\right] \geq 0. \\ \phi_3(\bar{x}) = -u_1(k) + 1.5 \geq 0; \quad \phi_4(\bar{x}) = u_1(k) - 0.2 \geq 0 \\ \phi_5(\bar{x}) = -u_2(k) + 1.5 \geq 0; \quad \phi_6(\bar{x}) = u_2(k) - 0.2 \geq 0 \end{cases}$$

Starting point:

$$\bar{x}^0 = [\frac{\pi}{10}, \frac{3\pi}{5}, \frac{\pi}{22}, \frac{6\pi}{11}, -0.7018, 0.0864, -0.0547, -0.4439, -7.8446, 4.9652,$$
$$-132.5376, -18.6166, -0.1931, -17.8481, -26.4775, -236.0504, -1.1214,$$
$$-0.0844, -0.2117, -0.5758, -1.8674, 0.2187, -1.7980, -0.8882, 0.5880,$$
$$-3.2777, -0.2205, -0.2175, 0.18117, 0.090778, 0.062614, -0.0012435,$$
$$0.015561, 0.00026398, 0.19956, 0.20797, -0.0062241, 0.0038742, -0.0050753,$$
$$0.0015751, 0.19952, 0.20839, -0.0063547, 0.0038599, -0.0049356, 0.0015419,$$
$$-0.087725, 0.91447, -0.28073, -0.030462, 0.30025, -0.071396]^T.$$

Bounds on design variables:

(1) Upper bounds:

$$\bar{x}_{max} = [0.33, 1.9, 0.16, 1.73, -0.6943, 0.1333, -0.0840, -0.4390, -7.6, 5.1,$$
$$-132.3, -18.4, -0.08, -17.6, -26.2, -235.8, -1.5334, -0.0430, -0.3551,$$
$$-0.7408, -1.6, 0.4, -1.5, -0.6, 0.7, -3.0, -0.02, -0.01, 24 \times [10]]^T$$

(2) Lower bounds:

$$\bar{x}_{min} = [0.29, 1.86, 0.12, 1.69, -0.6947, 0.1329, -0.0844, -0.4394, -8.0, 4.7,$$
$$-132.7, -18.8, -0.3, -18.0, -26.6, -236.2, -1.5338, -0.0434, -0.3555,$$
$$-0.7412, -2.0, 0.01, -1.9, -1.0, 0.3, -3.4, -0.4, -0.4, 24 \times [-10]]^T.$$

§ 5.8 Simulations of slewing controls with optimal design of noncircular gears and control gain

The slewing simulations of two kinds of flexible beam-like structures in section 6 lead to the optimization problems of mechanism design and control in section 5.7 for suppression of beam vibration. Four optimization problems, shown in Tables 5.6 through 5.9, have been solved in the previous section. Hence, four kinds of simulations are performed by employing the optimal solutions obtained in section 5.7. The noncircular gears and control gains in section 5.6 are thus upgraded by using the in this section. Yet the integrated design of mechanism and control is investigated in Tables 5.7 and 5.9 for the slewing maneuvers of two kinds of flexible beam-like structures.

§§ 5.8.1 Simulation of a flexible one-beam structure with optimal design of noncircular gears

The simulation of a flexible one-beam structure in section 5.6.1 is carried out again through an optimal design of noncircular gears. Similarly, the control task of this flexible one-beam structure is conducted to perform 90-degree slewing maneuver as shown in Fig. 5.8. The noncircular gears are produced by using the optimal parameters of noncircular gears, i.e. c_1 and c_2, which have been achieved to suppress vibrational motion in section 5.7. The output feedback gain is equivalent to one in Table 5.3. The model parameters of this flexible structure are shown in Table. 4.2. The simulation results are demonstrated in Figs. 5.26-5.31. These results, associated with the optimal design of noncircular gears, are denoted by the solid line (♯1) and the results of the previous noncircular gears in section 5.6.1 by the dashed line (♯2). Figures 5.26 and 5.27 show 6 sec slewing angle and angular velocity of the single flexible beam respectively. Apparently, the characteristics of noncircular gears still remain to tune the slewing responses of this

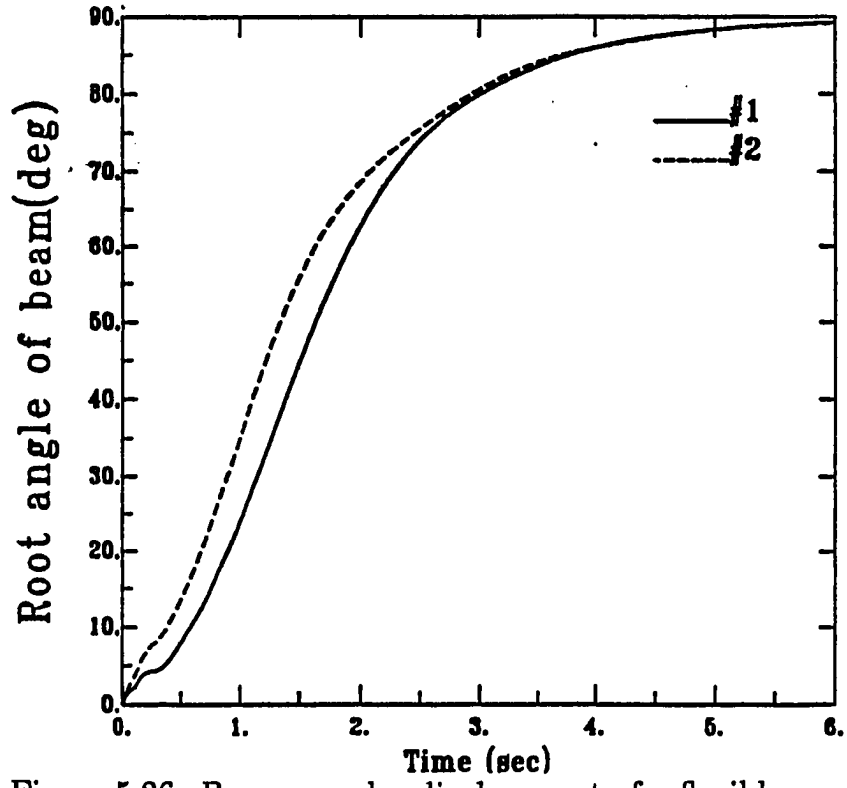

Figure 5.26: Beam angular displacement of a flexible one-beam structure for optimal design of noncircular gears

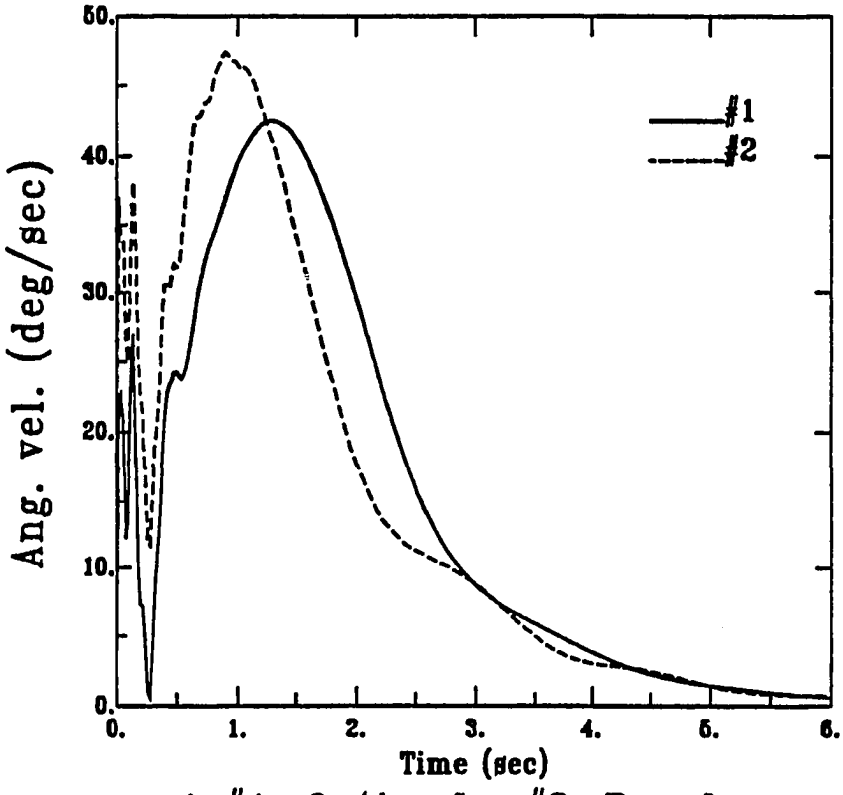

* #1: Optimal ; #2: Regular

Figure 5.27: Beam angular velocity of a flexible one-beam structure for optimal design of noncircular gears

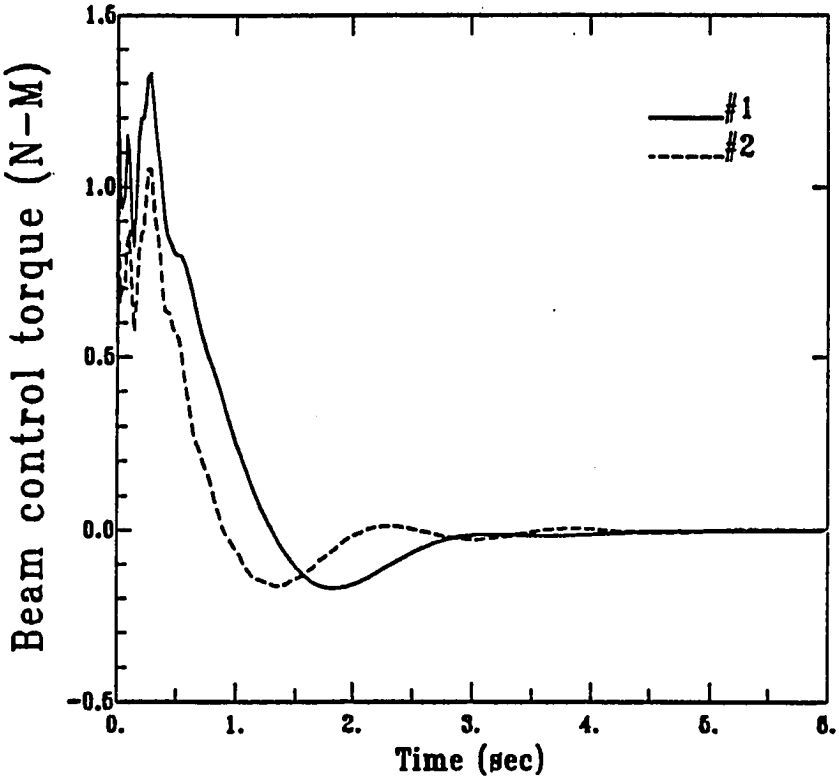

Figure 5.28: Beam control torque of a flexible one-beam structure for optimal design of noncircular gears

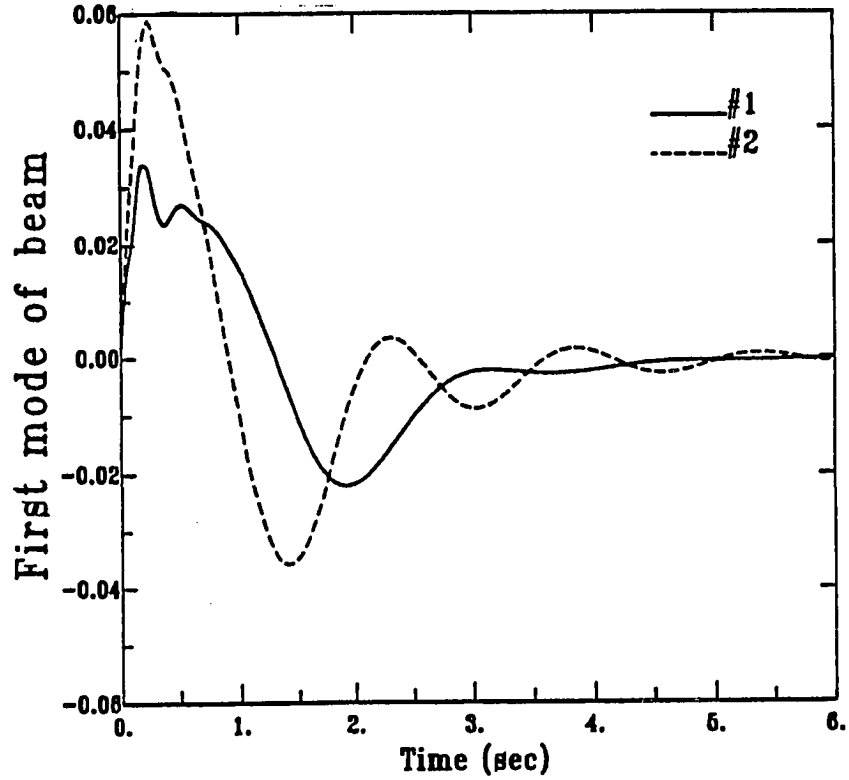

* #1: Optimal ; #2: Regular

Figure 5.29: First mode of a flexible one-beam structure for optimal design of noncircular gears

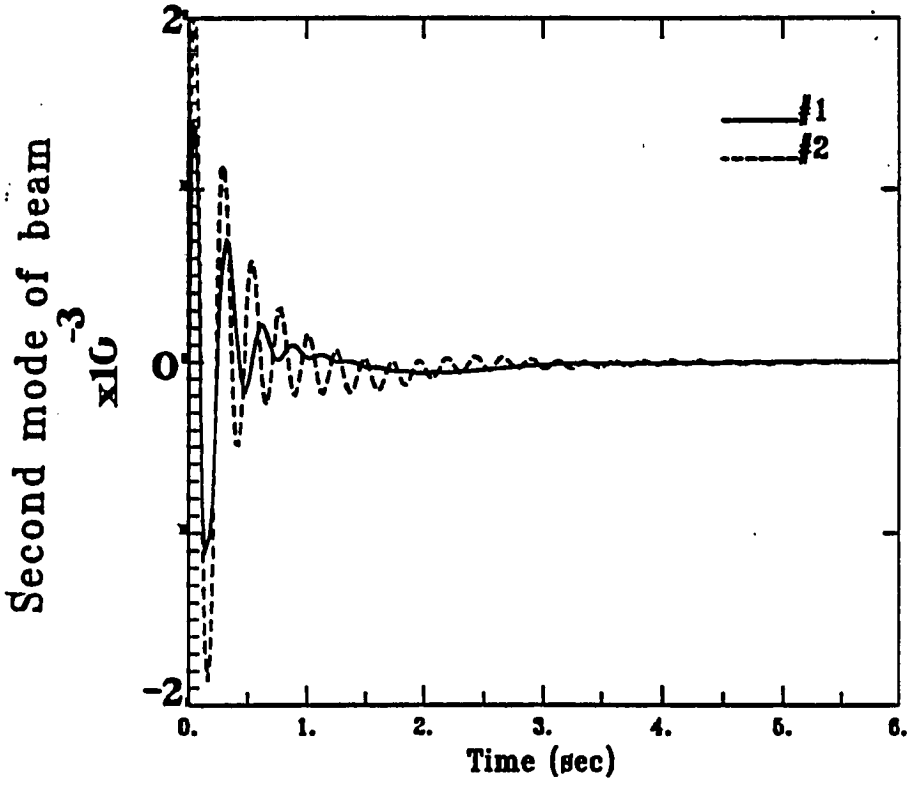

Figure 5.30: Second mode of a flexible one-beam structure for optimal design of noncircular gears

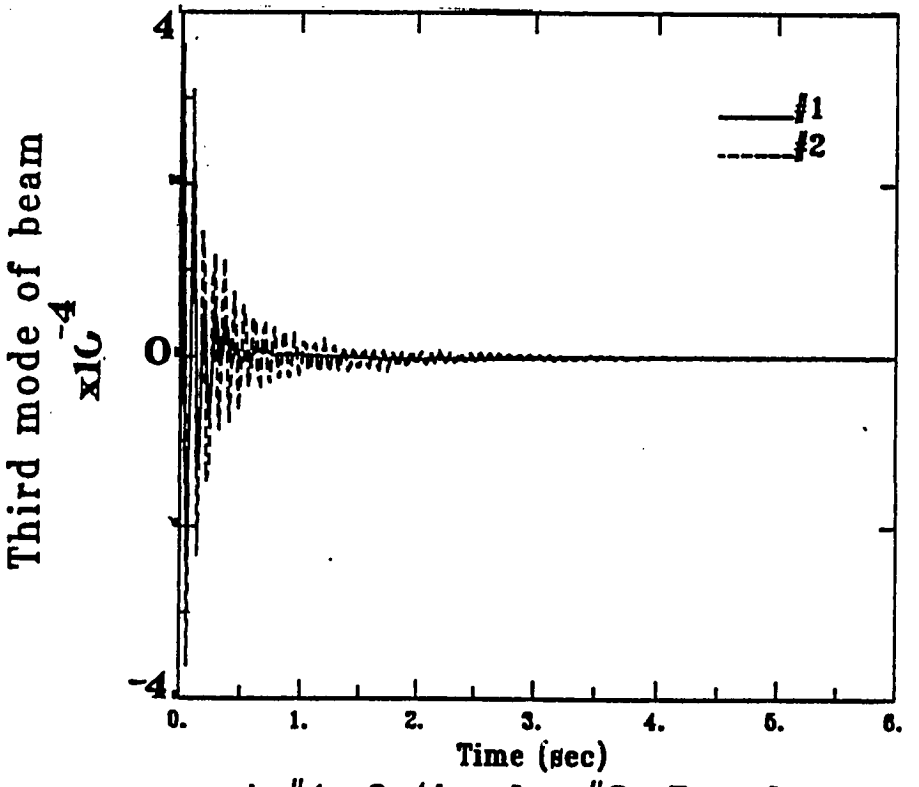

* #1: Optimal ; #2: Regular

Figure 5.31: Third mode of a flexible one-beam structure for optimal design of noncircular gears

flexible structure. The noncircular gears associated with the optimal parameters tune the angular displacement and velocity to behave more smoothly during the first 3 seconds. Figure 5.28 illustrates the histories of the two control torques which resemble each other, starting with 1 N-M and concluding with zero N-M. The noncircular gears with optimal parameters make a different outlook of the vibrational modes, as shown in Figs. 5.29-5.31. The vibrational modes are suppressed by the same output feedback gain but by different noncircular gears. Obviously, the noncircular gears with optimal parameters damp out the amplitudes of three vibrational modes after 2 sec, better than the regular noncircular gears. The peak amplitudes of the three modes are reduced by half, via the optimal design of noncircular gears. In Figs. 5.30 and 5.31, the second and third modes even damp out to vanish after 1 sec through the optimal design of noncircular gears. And the residual vibration is considerably improved which can be clearly observed in Figs. 5.29 and 5.30. Hence, the simulation results herein verify the feasibility of the optimization method to find the optimal parameters of noncircular gears for suppression of vibration in Table 5.6.

§§ 5.8.2 Simulation of a flexible one-beam structure with an integrated optimal design of noncircular gears and control gain

Besides the hyperbolic parameters of noncircular gears, the control gain of a flexible one-beam structure has been included in the design variables of optimization problem, as shown in Table 5.7. The integrated optimization of mechanism and control has provided the optimal solution of gear parameters, i.e. $c_{1\,opt}$ and $c_{2\,opt}$, and control gain in section 5.7. The 90-degree slewing simulation in section 5.8.1 is reconsidered in this section based on the cost function in Table 5.7. Note that the output feedback gain in this simulation is specified by Eq. (5.53). Figures 5.32-5.37 demonstrate two kinds of slewing simulation, including the results, due to the optimal solution of noncircular gears and control gain from section 5.6.2

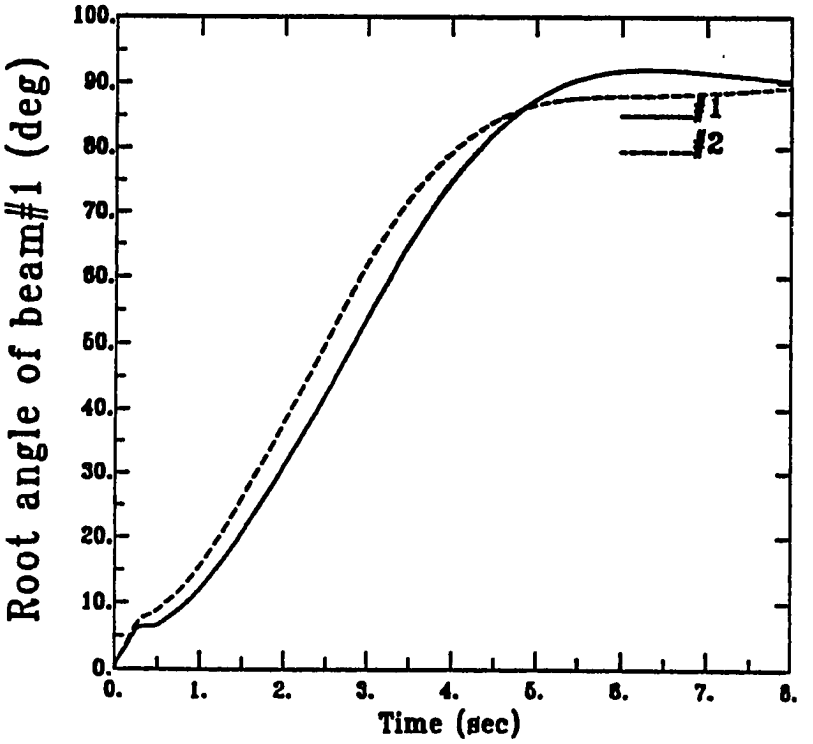

Figure 5.32: Beam #1 angular displacement of a flexible two-beam structure for optimal design of noncircular gears

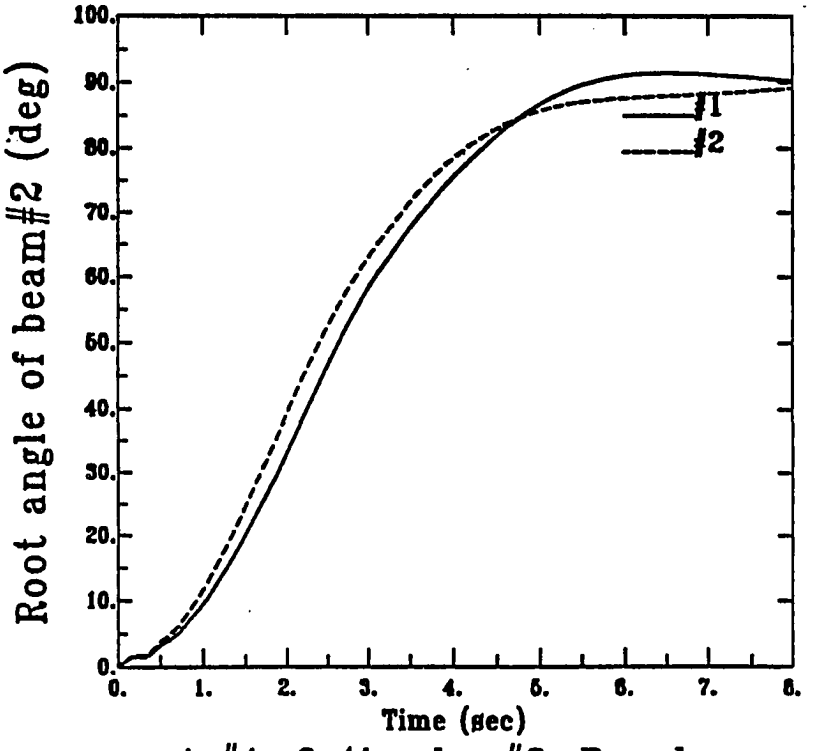

* #1: Optimal ; #2: Regular

Figure 5.33: Beam #2 angular displacement of a flexible two-beam structure for optimal design of noncircular gears

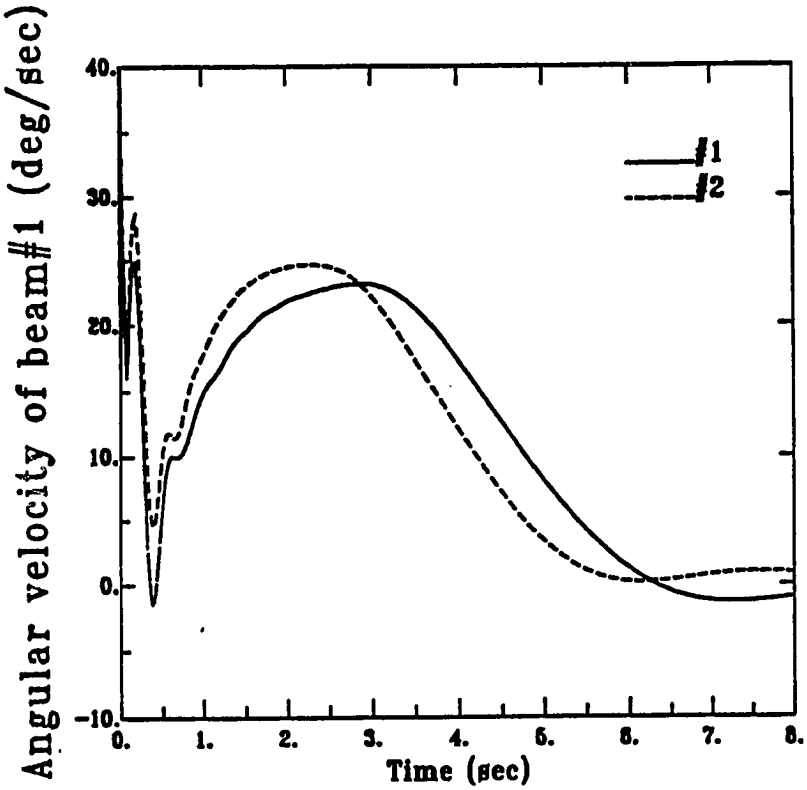

Figure 5.34: Beam #1 angular velocity of a flexible two-beam structure for optimal design of noncircular gears

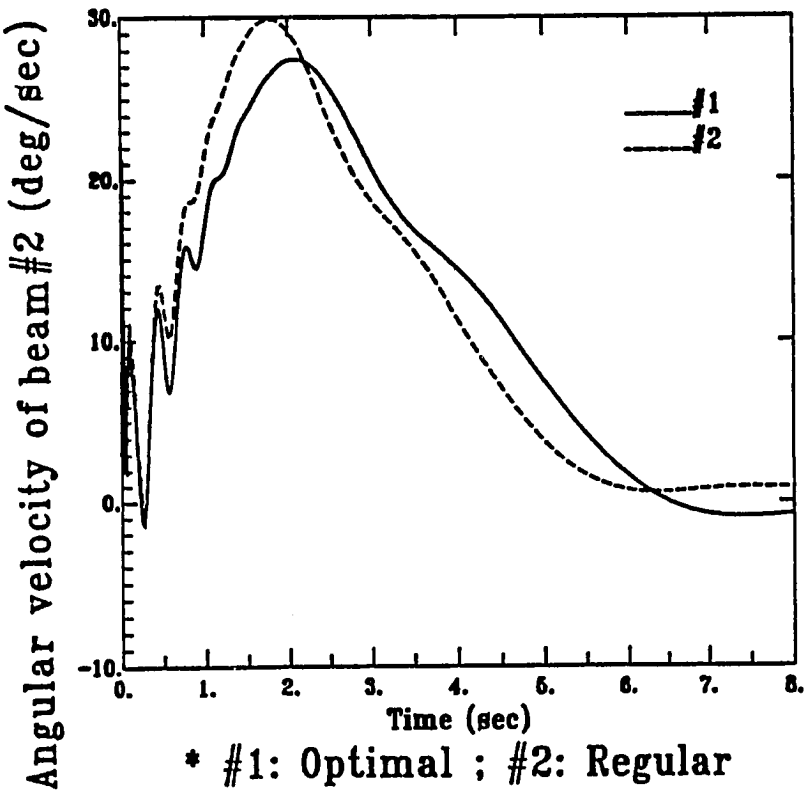

Figure 5.35: Beam #2 angular velocity of a flexible two-beam structure for optimal design of noncircular gears

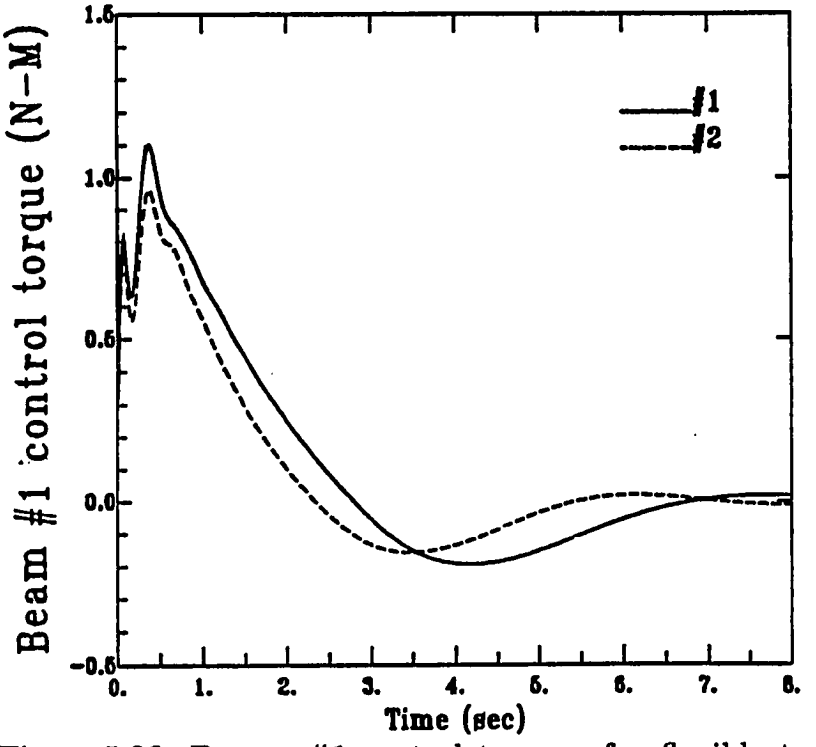

Figure 5.36: Beam #1 control torque of a flexible two-beam structure for optimal design of noncircular gears

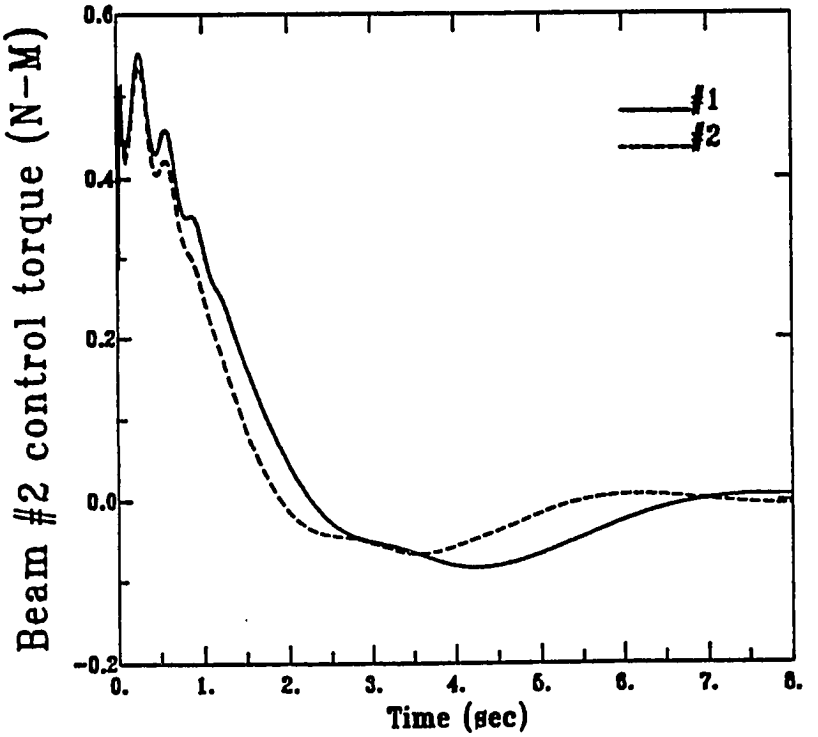

* #1: Optimal ; #2: Regular

Figure 5.37: Beam #2 control torque of a flexible two-beam structure for optimal design of noncircular gears

and the results drawn from Table 5.7. The former simulation results are indicated by the solid line (♯1) and the latter ones by the dashed line (♯2). The angular displacement and velocity are shown in Figs. 5.32 and 5.33 respectively. Figure 4.34 illustrates that the control torque associated with the optimal mechanism/control design is smaller than the one due to the optimal design of noncircular gears alone. The vibrational modes shown in Figs. 5.35-5.37 are suppressed by the integrated optimal mechanism/control approach instead of the optimal design of noncircular gears in Table 5.6. In Fig. 5.35, the amplitude of the first mode is reduced by 20oscillation is improved through the optimal mechanism/control approach. Compared with the first mode due to circular gears in Fig. 5.12, the peak amplitude is reduced by 73% through the integrated mechanism/control approach. Both oscillations (♯1) of the second and third modes in Figs. 5.36 and 5.37 are similar with the previous ones (♯2) in section 5.8.1 whose amplitudes have been tuned to be sufficiently smaller. The feedback gain for the second and third modes can be upgraded to some extent as long as their weighting coefficients of the cost function in Table 5.7 are properly adjusted. Hence, the simulation results herein confirm the effectiveness of the integrated mechanism/control design for the slewing maneuver of the flexible one-beam structure.

§§ 5.8.3 Simulation of a flexible two-beam structure with optimal design of noncircular gears

The simulation of the optimal mechanism/control design has been implemented to verify such an integrated mechanism/control method for the flexible one-beam structure discussed in section 5.8.2. Now the optimal design solution of the flexible two-beam structure shown in Table 5.8, is employed herein for the following simulation. Two noncircular gears are generated by using the optimal hyperbolic parameters, such as c_1, c_2, c_3 and c_4, in section 5.7. The model parameters are given in Table 5.4 and the output feedback gain in Table 5.5. The 90-degree slewing control task of this flexible two-beam structure is illustrated in

Fig. 5.15. The simulation results herein are compared to the ones obtained in section 5.6.3. Figures 5.38-5.47 show the simultation results. The slewing angles of two flexible beams are demonstrated in Figs. 5.38 and 5.39 and their angular velocities in Figs. 5.40 and 5.41. The range of near-zero angular acceleration in the history of beam #1 angular velocity is enlarged via the optimal design of noncircular gears. The behaviors of two angular velocities indicate that the noncircular gears with optimal parameters slow down the slewings of two flexible beams. In Figs. 5.42 and 4.43, the histories of two control torques associated with the optimal design of noncircular gears start with 0.7 N-M and 0.3 N-M for beam #1 and beam #2 respectively. The first and second modes of beam #1 in Figs. 5.44 and 5.45 are much further suppressed through the optimal design of noncircular gears. Obviously, the peak amplitudes of the first and second modes are reduced by 19% and their residual vibrations are sufficiently suppressed. Similarly, the peak amplitudes of the first and second modes associated with beam #2 are reduced by 35% in Figs. 5.46 and 5.47. The residual oscillation of the highest mode, namely the second mode of beam #2 is improved to some extent by the optimal design of noncircular gears. The simulation results in Figs. 5.38-5.47 indicate again the feasibility of optimal design of noncircular gears in the slewing maneuvers of multi-body flexible space structures.

§§ 5.8.4 Simulation of a flexible two-beam structure with an integrated optimal design of noncircular gears and control gain

Since the optimization solution in Table 5.8 has been successfully verified in the previous simulation, the similar simulation for an integrated optimal mechanism/control design in Table 5.9 is performed for further comparison. The integrated optimal design solution of the flexible two-beam structure shown in Table 5.9 is employed herein to implement the following simulation. The optimal hyperbolic parameters are specified by the values of c_{iopt} (i=1,2,3,4) in section 5.7 and

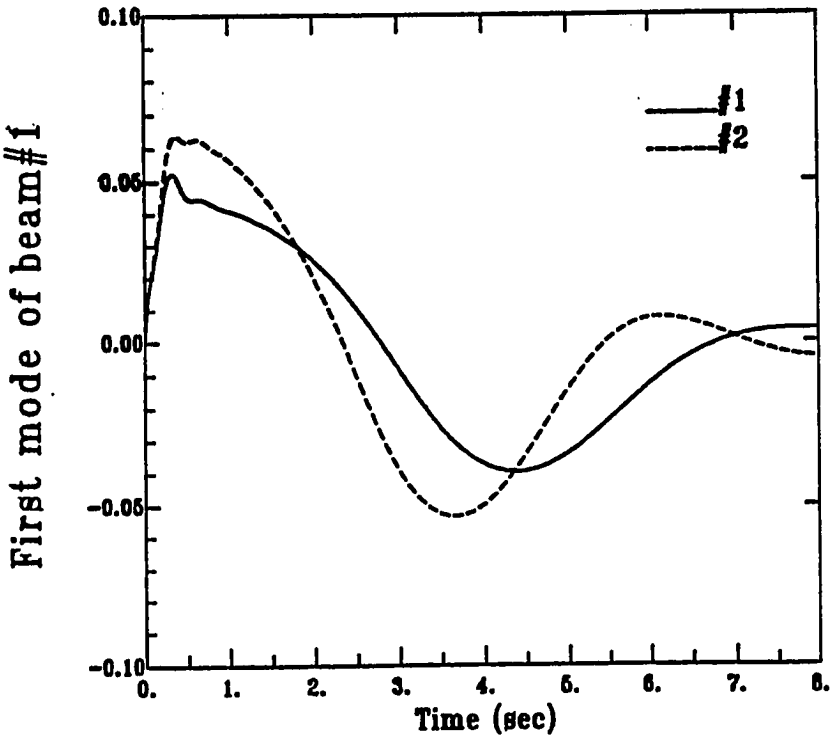

Figure 5.38: First mode of beam #1 for a flexible two-beam structure for optimal design of noncircular gears

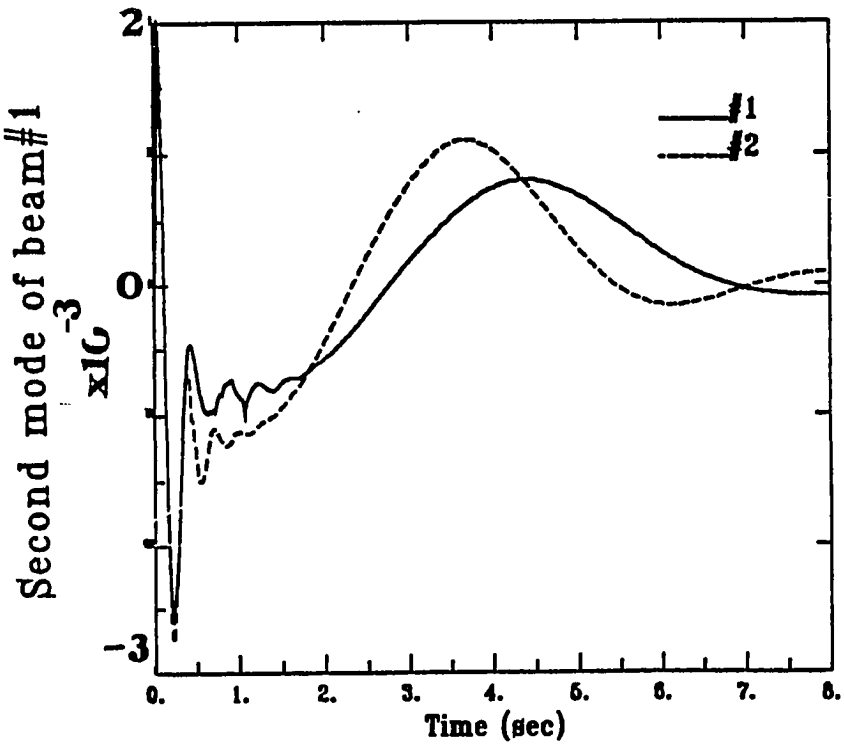

* #1: Optimal ; #2: Regular

Figure 5.39: Second mode of beam #1 for a flexible two-beam structure for optimal design of noncircular gears

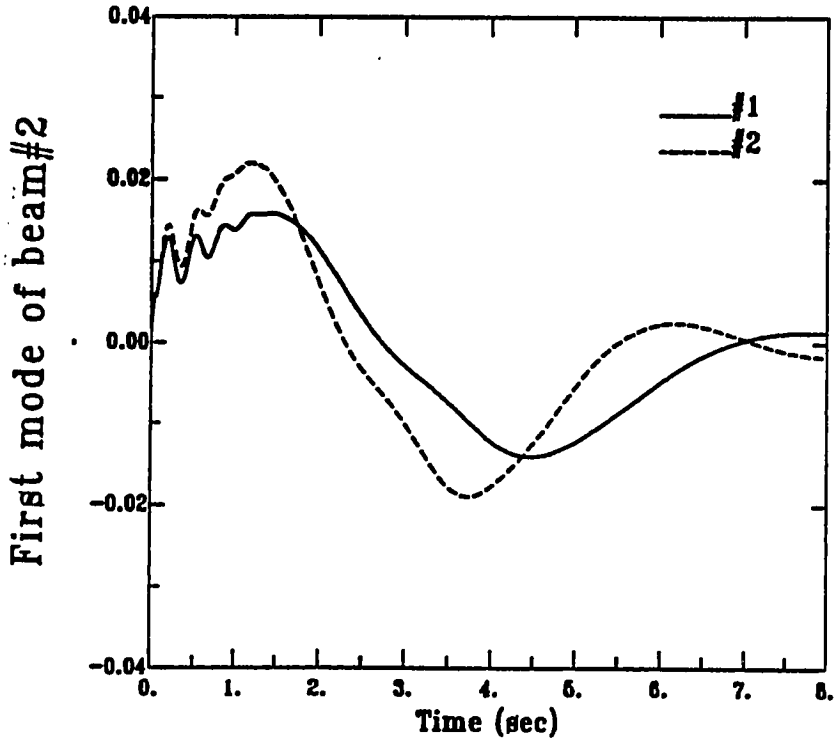

Figure 5.40: First mode of beam #2 for a flexible two-beam structure for optimal design of noncircular gears

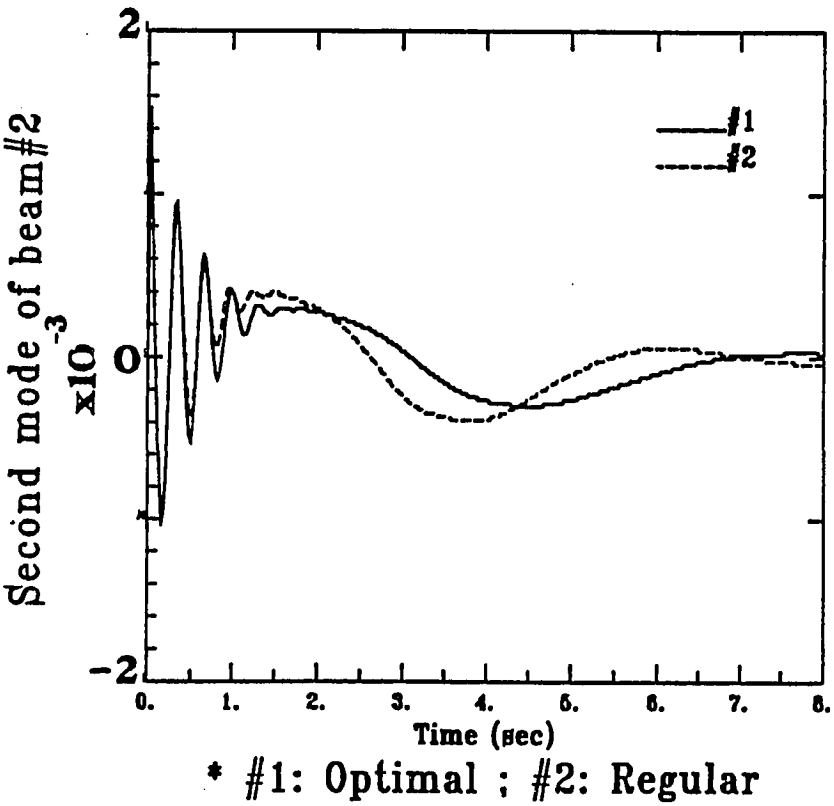

Figure 5.41: Second mode of beam #2 for a flexible two-beam structure for optimal design of noncircular gears

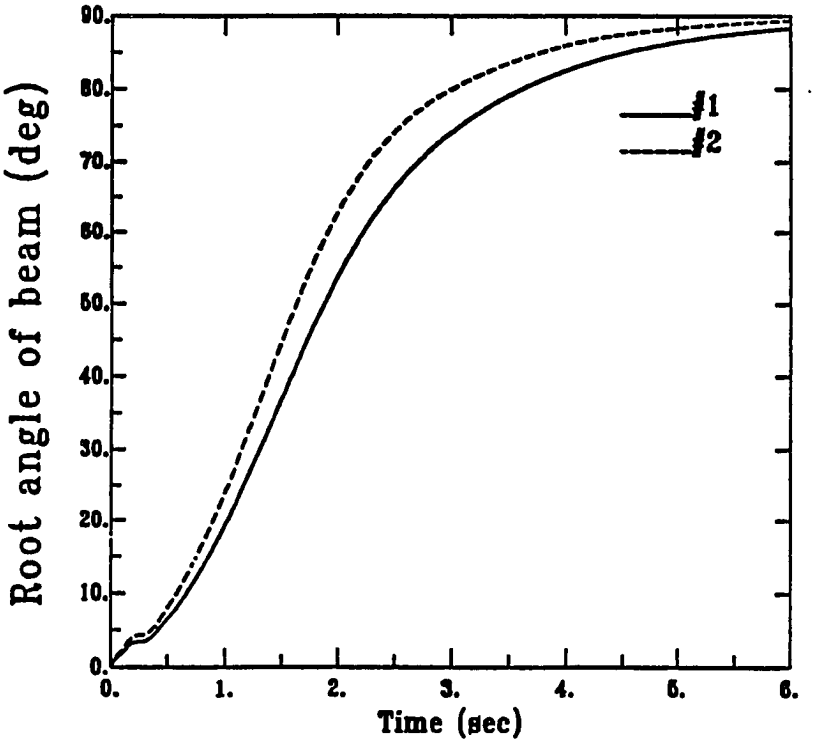

Figure 5.42: Beam angular displacement of a flexible one-beam structure for integrated mechanism/control design

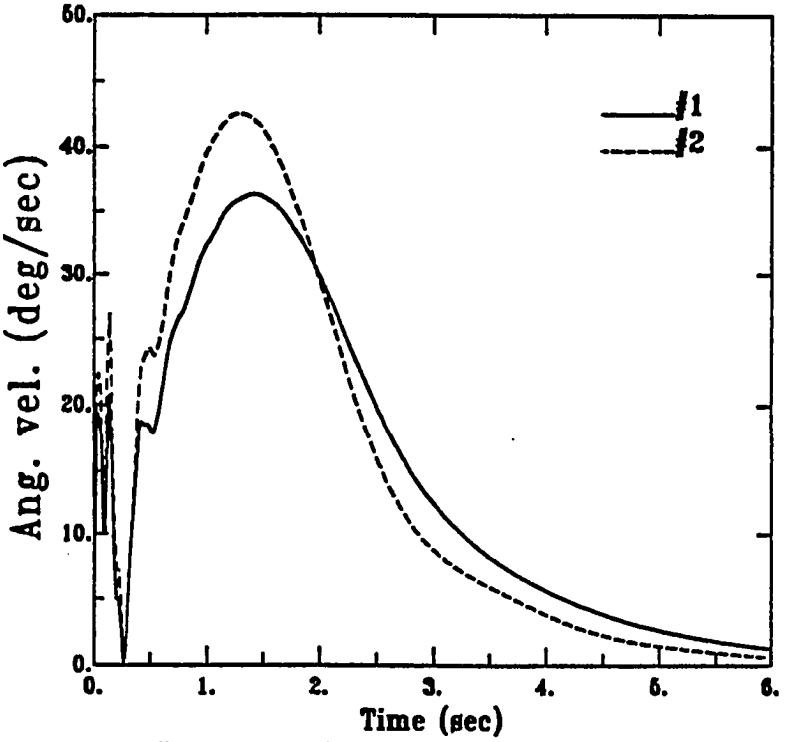

* #1: Opt.Cotr.&Nc.; #2: Opt.Nc.

Figure 5.43: Beam angular velocity of a flexible one-beam structure for integrated mechanism/control design

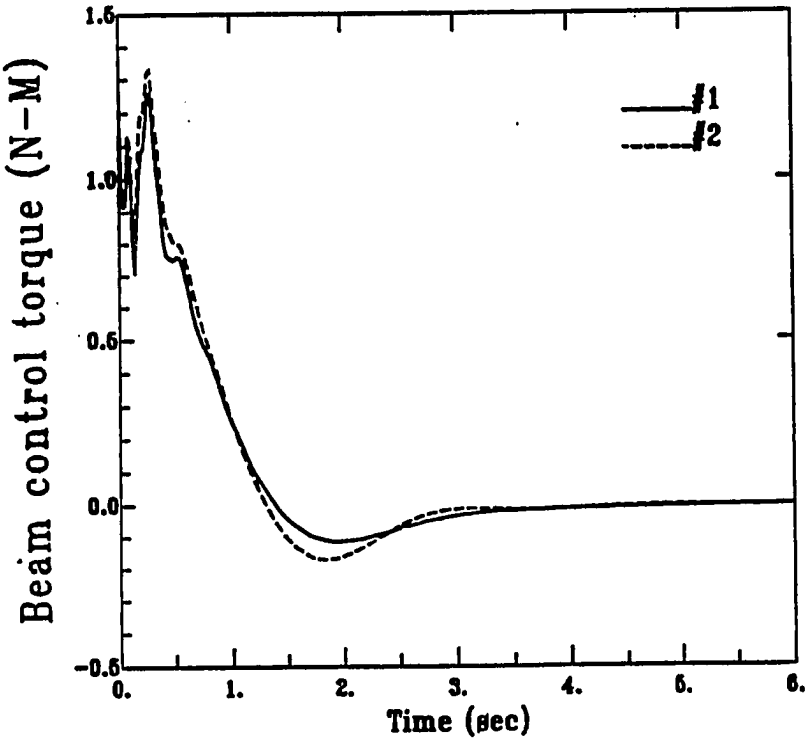

Figure 5.44: Beam control torque of a flexible one-beam structure for integrated mechanism/control design

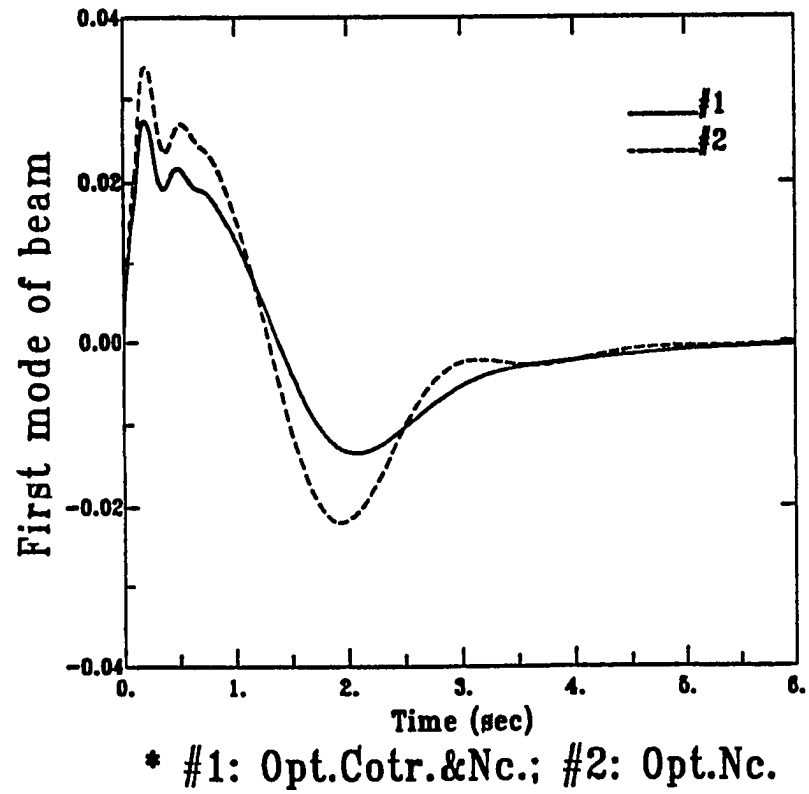

Figure 5.45: First mode of a flexible one-beam structure for integrated mechanism/control design

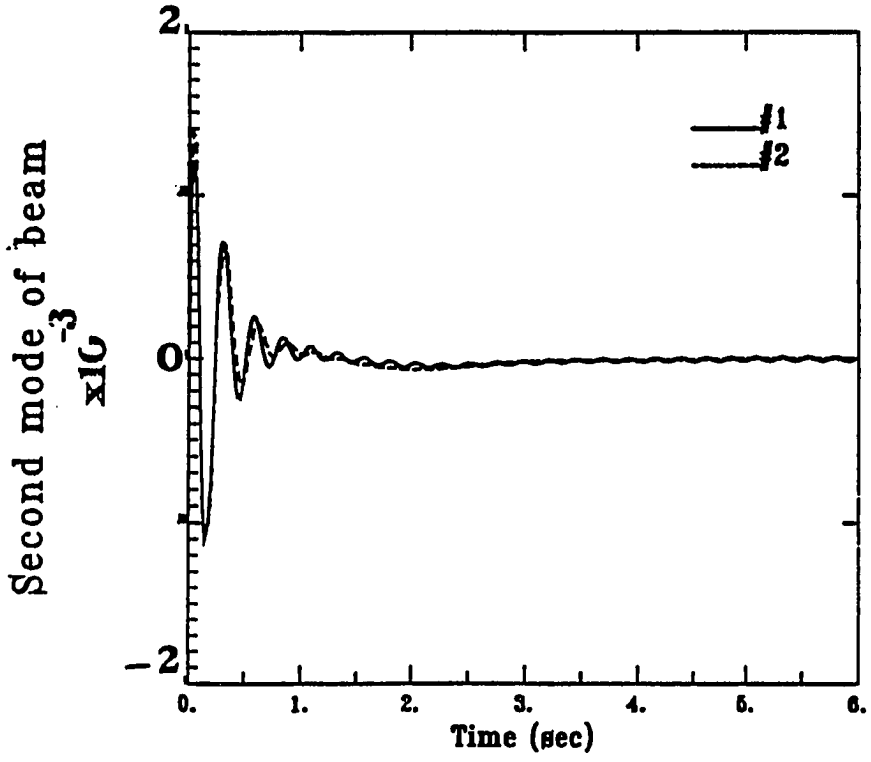

Figure 5.46: Second mode of a flexible one-beam structure for integrated mechanism/control design

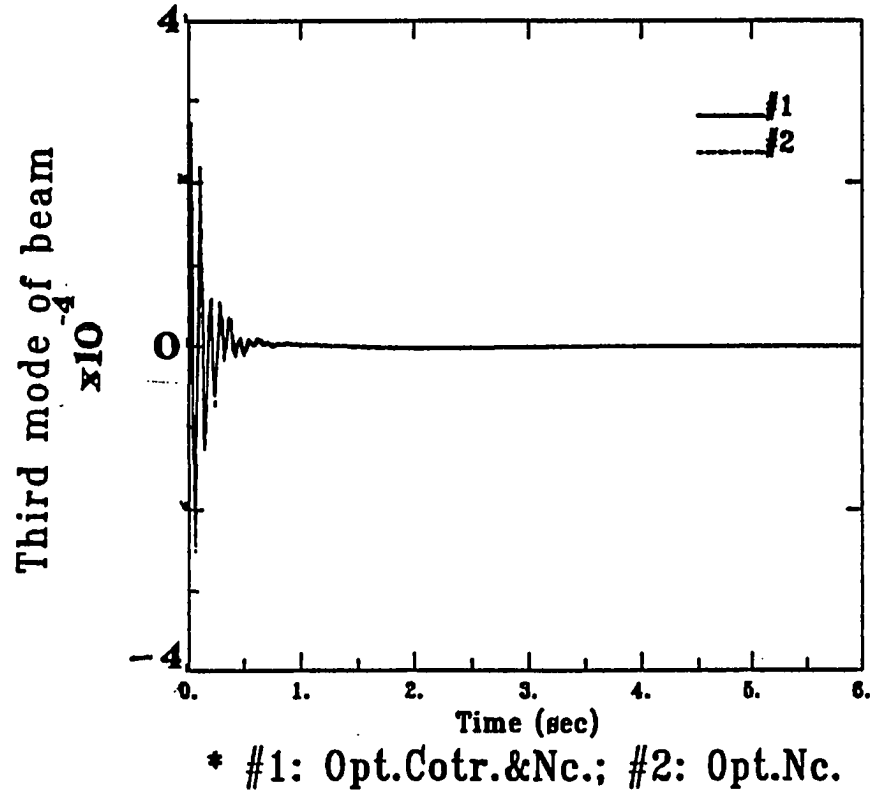

Figure 5.47: Third mode of a flexible one-beam structure for integrated mechanism/control design

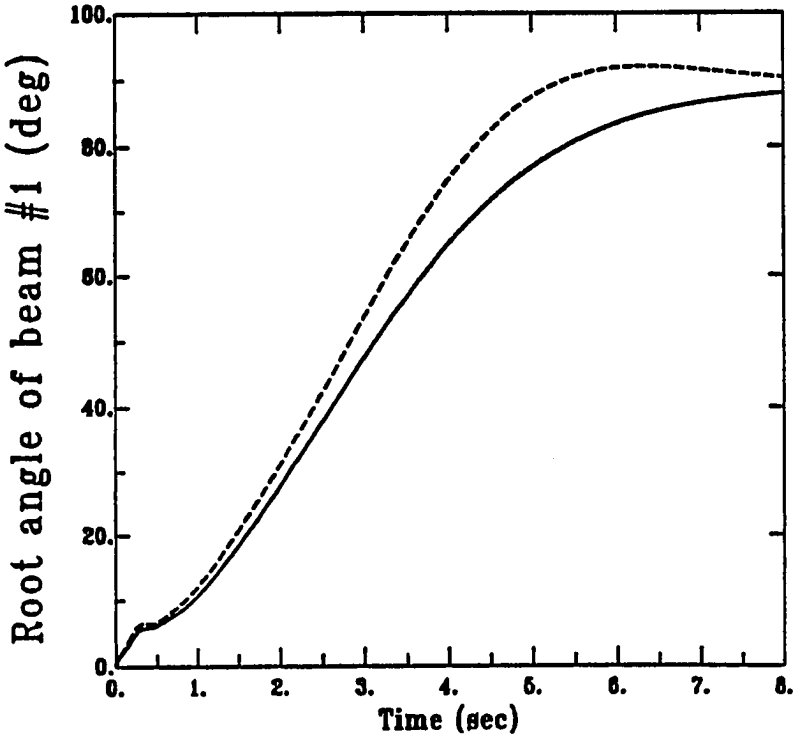

Figure 5.48: Beam #1 angular displacement of a flexible two-beam structure for integrated mechanism/control design

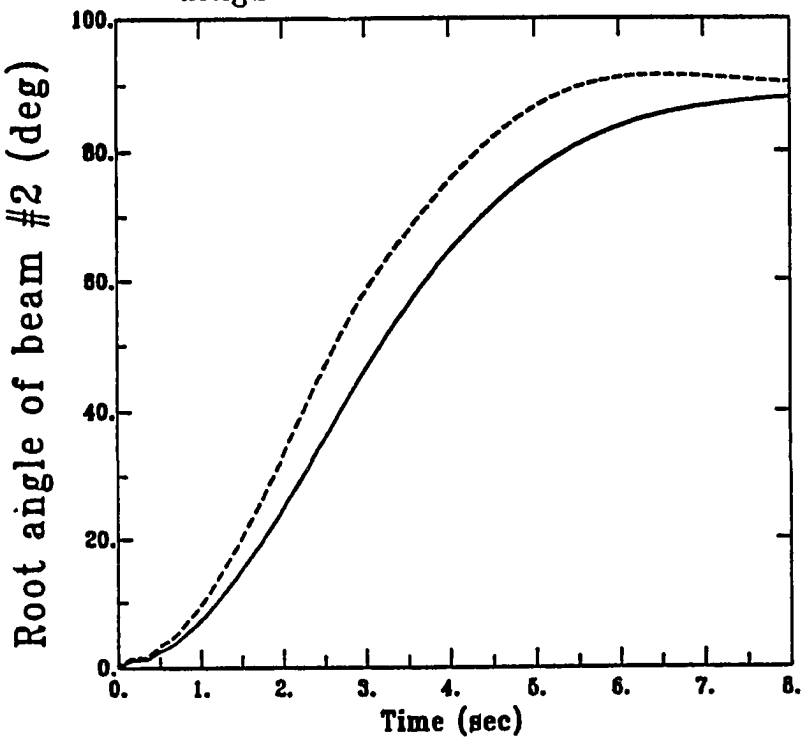

Figure 5.49: Beam #2 angular displacement of a flexible two-beam structure for integrated mechanism/control design

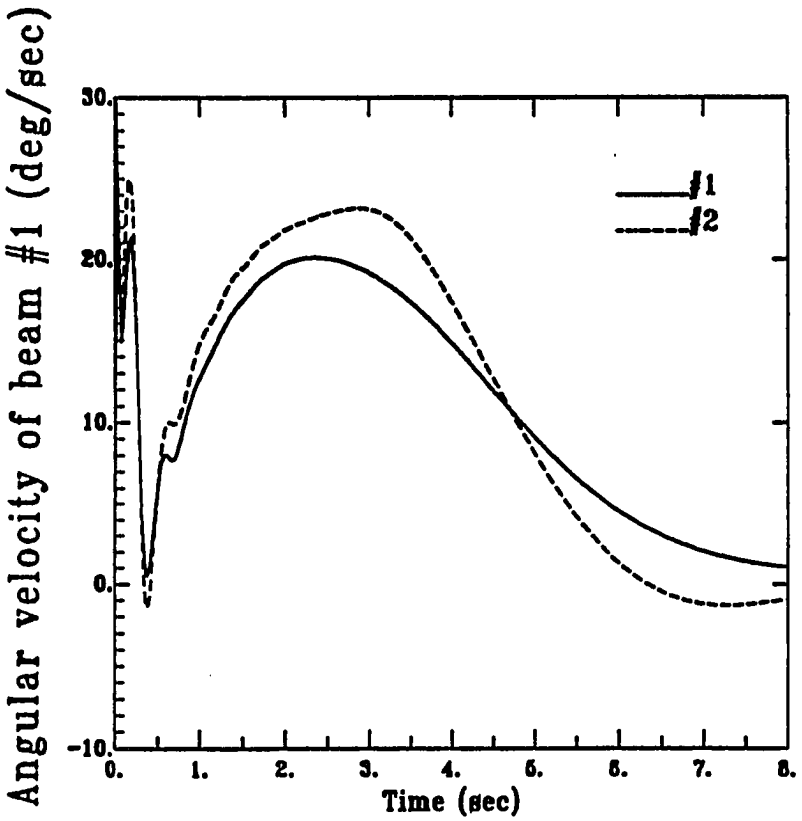

Figure 5.50: Beam #1 angular velocity of a flexible two-beam structure for integrated mechanism/control design

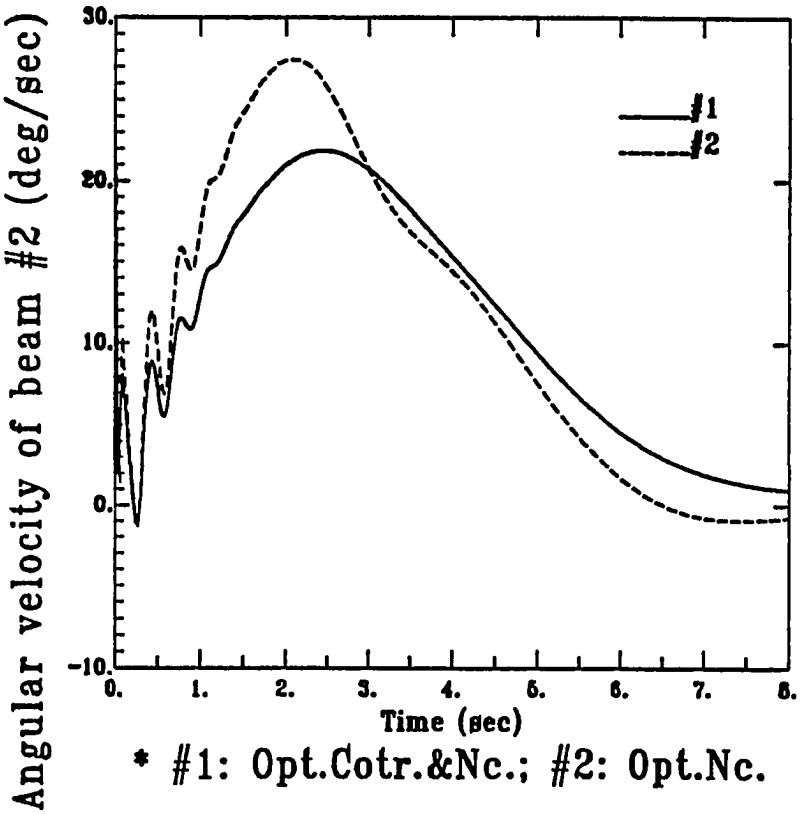

Figure 5.51: Beam #2 angular velocity of a flexible two-beam structure for integrated mechanism/control design

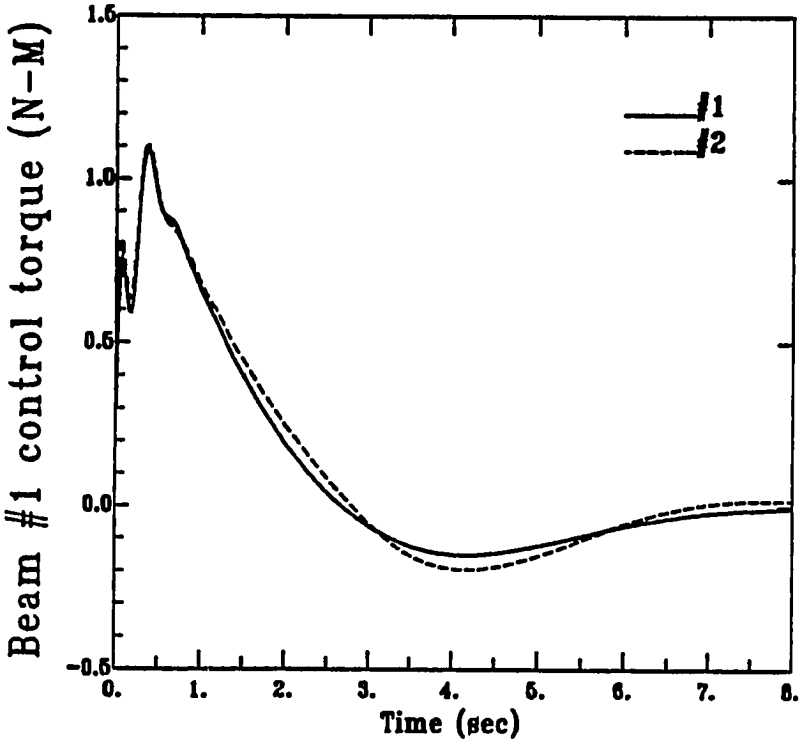

Figure 5.52: Beam #1 control torque of a flexible two-beam structure for integrated mechanism/control design

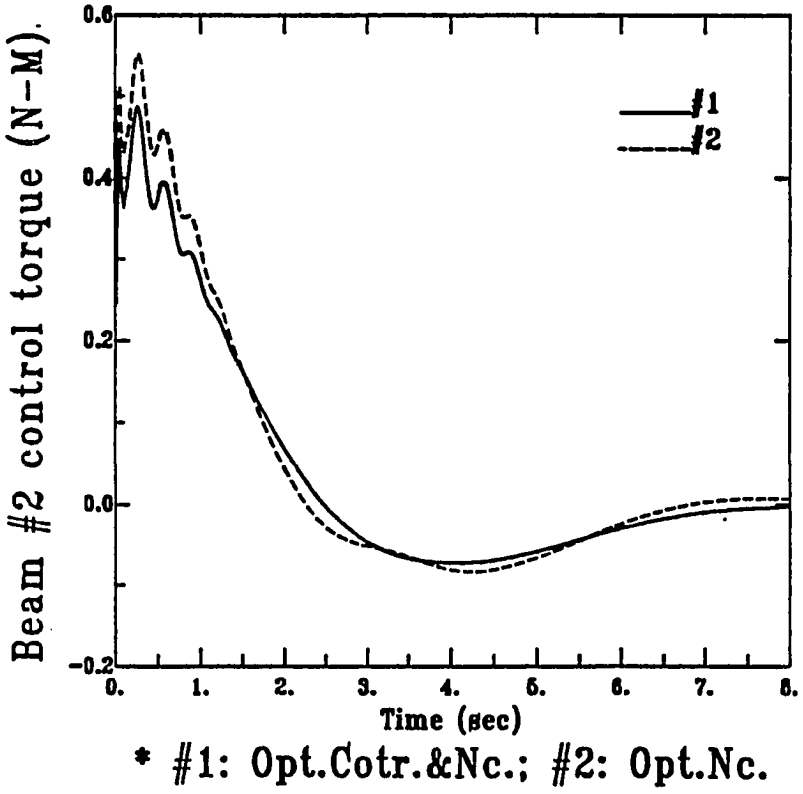

Figure 5.53: Beam #2 control torque of a flexible two-beam structure for integrated mechanism/control design

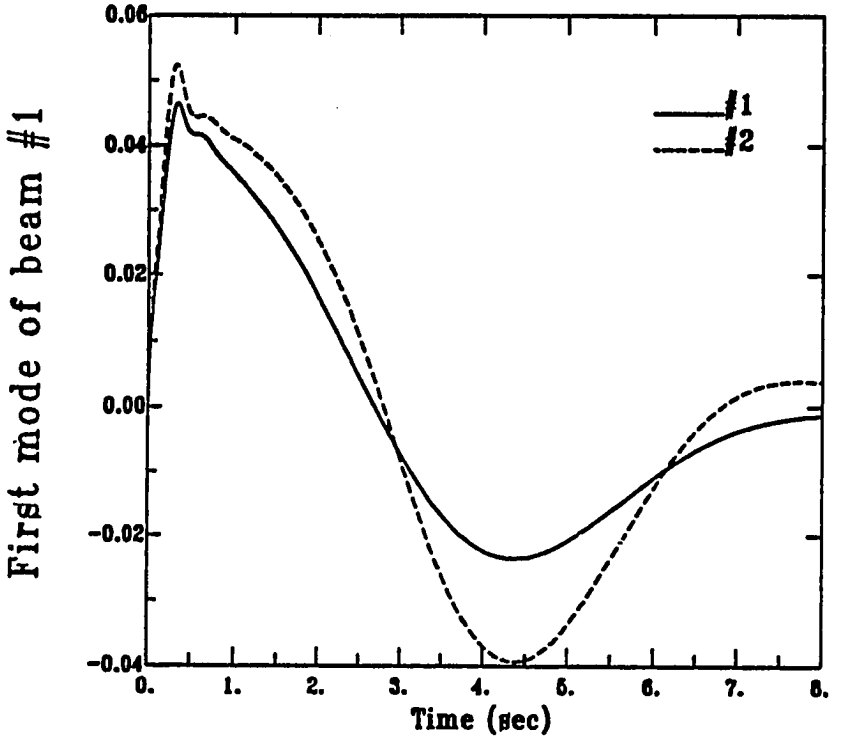

Figure 5.54: First mode of beam #1 for a flexible two-beam structure for integrated mechanism/control design

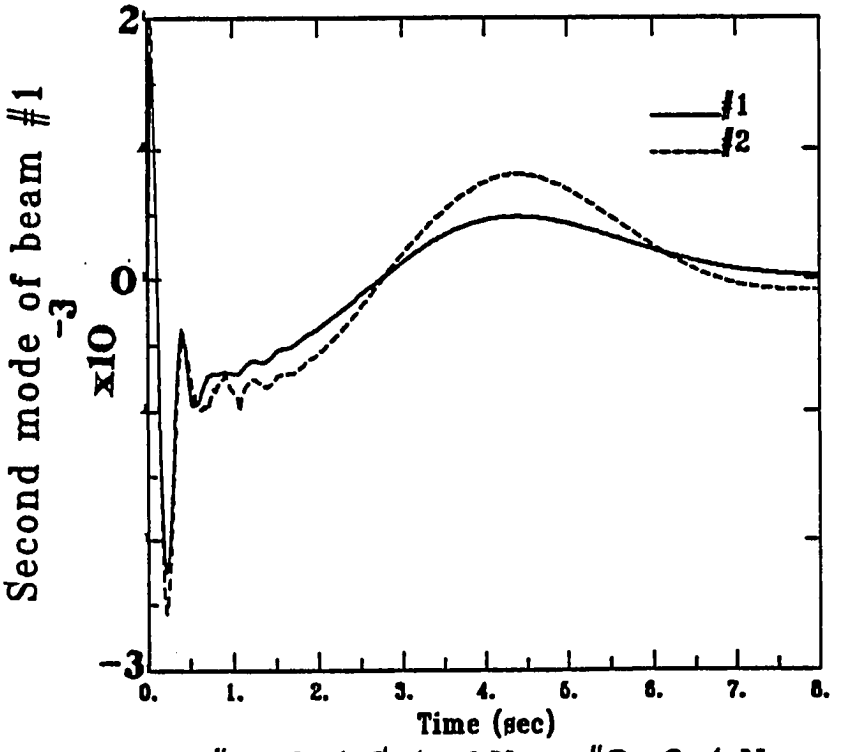

* #1: Opt.Cotr.&Nc.; #2: Opt.Nc.

Figure 5.55: Second mode of beam #1 for a flexible two-beam structure for integrated mechanism/control design

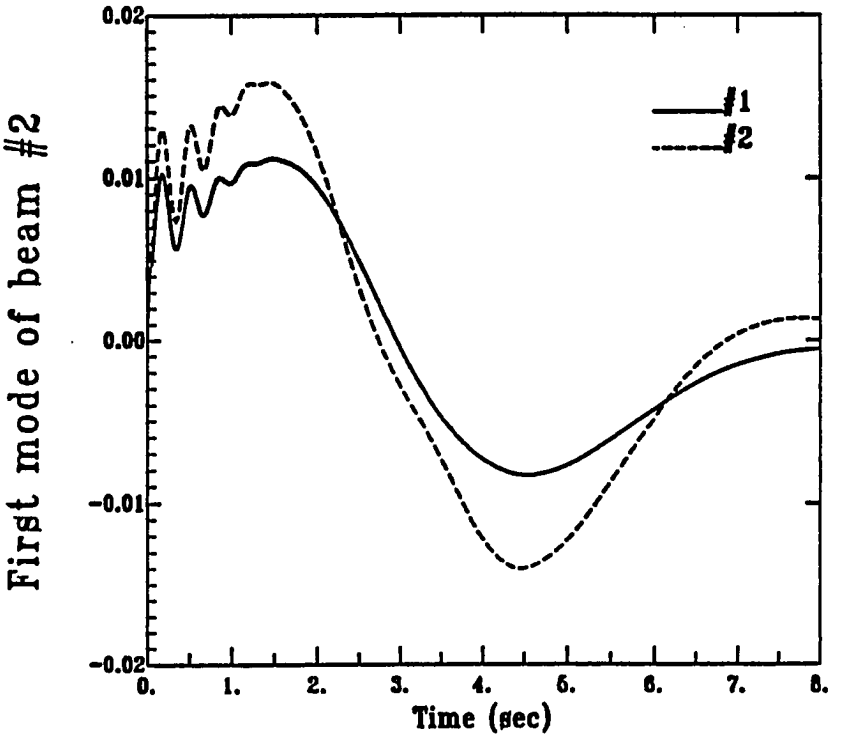

Figure 5.56: First mode of beam #2 for a flexible two-beam structure for integrated mechanism/control design

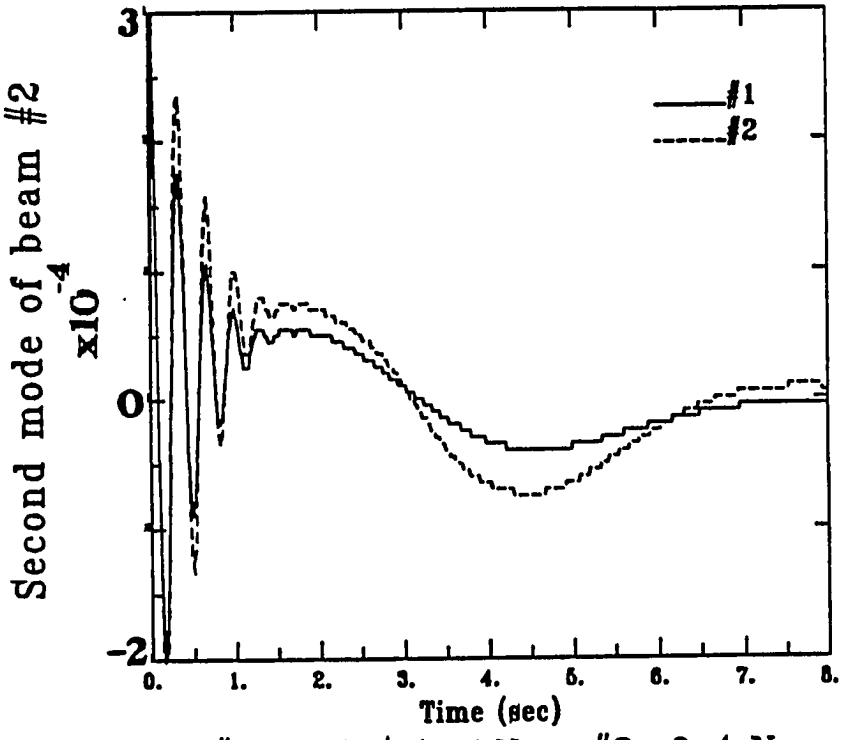

* #1: Opt.Cotr.&Nc.; #2: Opt.Nc.

Figure 5.57:. Second mode of beam #2 for a flexible two-beam structure for integrated mechanism/control design

the control gain by Eq. (5.54). The simulation results are demonstrated in Figs. 5.48-5.57. Figures 5.48 and 5.49 illustrate the slewing angles of beam ♯1 and beam ♯2 respectively. And the angular velocities of two beams are shown in Fig. 5.50 and 5.49. In Fig. 5.51, the optimal mechanism/control design considerably slows down the slewing of beam ♯2. Figures 5.52 and 5.53 show two control torques for beam ♯1 and beam ♯2 respectively. The integrated mechanism/control design reduces the amplitudes of the first and second modes associated with beam ♯1 by 21% in Figs. 5.54 and 5.55. Compared with the results associated with the circular gears in Figs. 5.22 and 5.23, the amplitude of beam ♯1 first and second modes are considerably reduced by 64%. In Figs. 5.56 and 5.57, the reduction of the amplitudes of beam ♯2 first and second modes yields 38%. And the reduction becomes 52%, compared with the results associated with the circular gears in Figs. 5.24 and 5.25. The simulation results in Figs. 5.48-5.57 thus confirm the feasibility of the integrated mechanism/control design for the multi-body slewing maneuvers of space structures.

§ 5.9 Summary and discussion

The severe flexural vibration always comes along with the rapid and large angle slewing maneuvers of the flexible space structures. In Chapter 3, the experimental results indicate the better suppression of vibration via the control technique, such as the feedback of strain gages. Besides the control method, the special mechanisms can be developed to achieve the good performance in the rapid slewing maneuvers of the flexible space structures. In this Chapter, an integrated investigation of mechanism and control is conducted for the slewing maneuvers of the large flexible space structures, whereby an optimization method is applied to determine the appropriate mechanism/control design to find the minimum cost function. A novel mechanism of noncircular gears is constructed to generate the hyperbolic gear ratio by wrapping two specially shaped cams which are properly meshed and well balanced through two pairs of thin metal bands. The

noncircular gears roll on each other along their convex profiles such that the slipping and backlash are prevented. The design of the noncircular gears is employed for the slewing maneuvers of two kinds of flexible beam-like structures, i.e. the one-beam structure and two-beam structure. The slewing response is tuned well, and the flexural vibration is suppressed while rotating the noncircular gears during the slewing control. The integrated mechanism/control design for the slewing control is implemented through the optimization technique. Based on the suppression of vibration, the optimal design solution of gear parameters and control gain is found to locate the local minimum of the assigned cost function. The 90-degree slewing simulations are thus implemented for the optimal design of noncircular gears and the integrated mechanism/control design respectively. The simulation results indicate the crucial role of the integrated mechanism/control design for the slewing maneuvers.

The comparison of simulation results with the noncircular gears and the circular gears implies that the hyperbolic gear ratio can tune the slewing and sufficiently suppress the vibrational motion. The simulation results associated with the optimal design of noncircular gears demonstrate the reduction of vibrational amplitude compared with the regular noncircular gears. Furthermore, the slewing response and flexural vibration are even improved as shown in the simulation results of the integrated mechanism/control design. Hence, this state of the art investigation paves the way for integrating the mechanism design and control method for the rapid and large angle slewing maneuvers of the flexible space structures.

Chapter 6

LYAPUNOV-BASED NONLINEAR CONTROL DESIGNS FOR FLEXIBLE SPACE STRUCTURES

Lyapunov's theory of stability of dynamic systems was published in a Russian journal in 1892, translated into French in 1907, and reprinted in America in 1947 [52]. Since then, the so-called "second method" of Lyapunov has been regarded in the Soviet Union as the principle mathematical tool for linear or nonlinear stability problems, particularly for the theory of control systems. At present, the fundamental concepts of this theory are successfully applied to:

(1) stability of linear and nonlinear systems,

(2) estimation of transient behavior,

(3) system control optimization,

(4) design of relay servos,

(5) system robustness analysis,

(6) adaptive control,

(7) robust control.

The objective of the second method of Lyapunov is to answer questions of stability of differential equations by utilizing the given form of the equations but without explicit knowledge of the solutions. The principle idea of the second method is contained in the following physical reasoning: If the rate of change of the energy of an isolated physical system is negative for every possible state, except for a single equilibrium state, then the energy will decrease until it finally assumes its minimum value of energy at the equilibrium state. In other words, a dissipative

system perturbed from its equilibrium state will always return to it, which is the intuitive concept of stability. Unlike the energy of a dynamic system, Lyapunov's function is not unique; this is precisely the reason why the second method of Lyapunov is a more powerful tool than conventional energy considerations. In this chapter, Lyapunov's second method is employed to design the nonlinear controls which ensure stability of rapid and large angle slewing maneuvers of the flexible structures during position control missions. Three nonlinear dynamic models, namely, a flexible one-beam structure, a flexible two-beam structure [38], and an inverted rigid pendulum, are selected to illustrate the Lyapunov-based design concept presented in this chapter. Numerical simulations are given comparing the system responses with and without the nonlinear control law.

§ 6.1 Concept of stability

A wide variety of principal definitions of system stability are discussed herein. In this section, the dynamic system is governed by a free (unforced) and first-order differential equation like:

$$E\frac{dq}{dt} = f(q,t) \tag{6.1}$$

where q denotes a 2n×1 state vector of $[x,\dot{x}]^T$, f(q,t) is a function of state vector and time, and E indicates a symmetric and positive-definite matrix composed of an inertia matrix. A detailed description of matrix E in Eq. (6.1) will be given in section 6.2. The stability is mainly concerned with the deviation from some fixed motion, i.e. an equilibrium state q_e of a dynamic system. In the sense of Lyapunov's second method, a precise definition of stability is:

Definition 6.1: An equilibrium state q_e of a dynamic system in Eq. (6.1) is stable if for every real number $\varepsilon > 0$ there exists a real number $\delta(\varepsilon, t_0) > 0$ such that $\|q_0 - q_e\| \leq \delta$ implies

$$\|q - q_e\| \leq \varepsilon \qquad for\ all\ \ t \geq t_0 \tag{6.2}$$

The geometric description of stability is shown in Fig. 6.1. The original state q_0 of

Eq. (6.1) is perturbed slightly from its equilibrium state q_e, and all subsequent motions remain in a corresponding small neighborhood ε of the equilibrium state q_e. Hence, the region of stability in Eq. (6.2) is locally bounded within a circle of neighborhood ε, while the system of Eq. (6.1) is slightly perturbed. The states may not rebound from the perturbed state into the equilibrium state. The motion of harmonic oscillation characterizes such a definition of stability in the sense of Lyapunov.

Instead of definition 6.1, asymptotical stability is based on a more restricted concept: namely, the states rebound into their equilibrium states after any small perturbation. The definition of asymptotical stability is expressed as follows:

Definition 6.2: An equilibrium state q_e of a free dynamic system is asymptotically stable if

(1) it is stable and

(2) every perturbed state starting sufficiently near q_e converges to q_e as $t \to \infty$. Namely, there is some real constant $r(t_0) > 0$ and to every real number $\nu > 0$ there corresponds a real number $T(\nu, q_0, t_0)$ such that $\|q_0 - q_e\| \leq r(t_0)$ implies

$$\|q - q_e\| \leq \nu \qquad for\ all\ t \geq t_0 + T \tag{6.3}$$

(see Fig. 6.2)

Generally speaking, asymptotical stability is most useful among the others in the area of control. From definition 6.2, the boundness of initial perturbation $\|q_0 - q_e\|$ is dependent of initial time t_0. Such a restriction will be further ignored for asymptotical stability in the large.

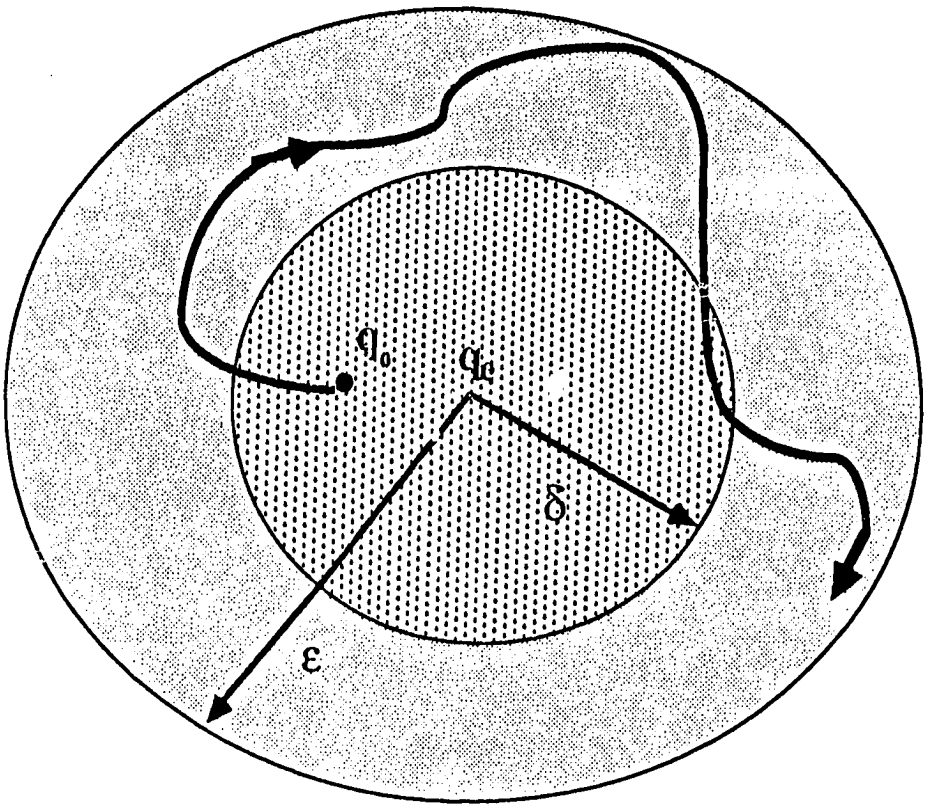

Figure 6.1: Configuration of stability

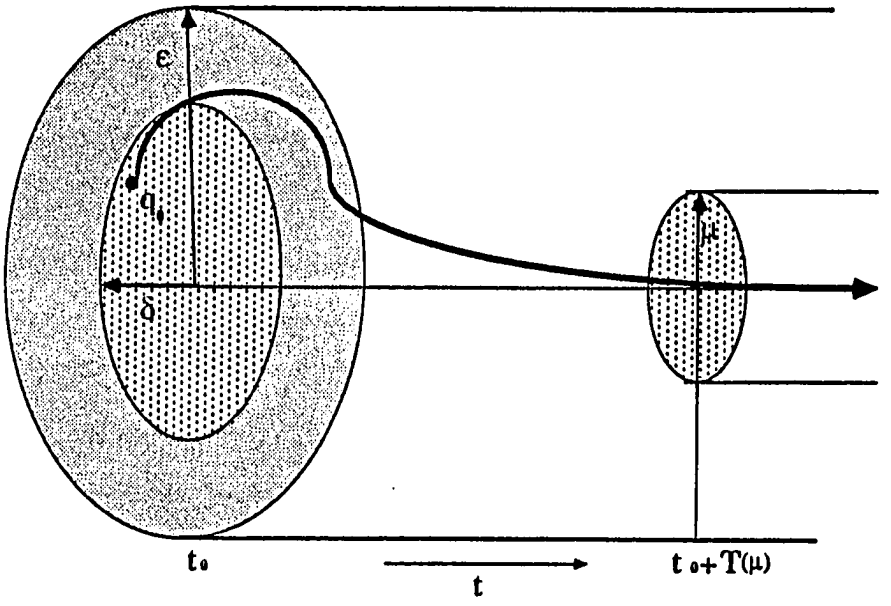

Figure 6.2: Configuration of asymptotical stability

Definition 6.3: An equilibrium state q_e of a free dynamic system is asymptotically stable in the large if

(1) it is stable and

(2) every state converges to q_e [converges to q_e uniformly in q_e for $\|q_0\| \leq r$ where r is fixed but arbitrarily large as $t \rightarrow \infty$.

In terms of Lyapunov's function, asymptotical stability in the large can be defined as:

Definition 6.4: An equilibrium state q_e of a free dynamic system is asymptotically stable in the large if a Lyapunov's function V(q,t) exists which has the following characteristics throughout the entire state space:

(1) V(q,t) is positive definite;

(2) Given any $\nu > 0$ there exists a $\delta > 0$ such that V(q,t)$> \nu$ whenever $\|q\| > \delta$ and $t \geq t_0$;

(3) $\dot{V}(q,t)$ is negative definite.

If a dynamic system is linear, the definitions 6.2-6.3 are equivalent. Asymptotical stability and asymptotical stability in the large are equivalent if they are uniform in t . Several types of stability in the sense of Lyapunov are included in Appendix D. Definition 6.4 will be applied to develop a nonlinear control design for flexible space structures in the next section.

§ 6.2 Lyapunov-based nonlinear control design

In order to achieve a closed-loop control system, the dynamic equation of the flexible structures has included the the dynamics of motors and the characteristics of sensors in the following derivation. Rapid large angle maneuvering for flexible-link structures is generally governed by

$$M(x,\dot{x},t)\,\ddot{x} + D\dot{x} + Kx = Bu + f \tag{6.4}$$

where x is an n×1 state vector, u a p×1 input vector, M(x,t) an n×n positive definite time-variant matrix, D an n×n constant damping matrix, K an n×n positive constant stiffness matrix, B an n×p constant input matrix and f an n×1 nonlinear force vector. Without loss of generality, Eq. (6.4) can be written in the matrix form as

$$E\dot{q} = Aq + \bar{B}u + \bar{f} \tag{6.5}$$

where

$$q^T = [x,\dot{x}],\ \bar{B}^T = [0,B^T],\ \bar{f}^T = [0,f^T],$$

$$E = \begin{pmatrix} I & 0 \\ 0 & M \end{pmatrix} \quad and \quad A = \begin{pmatrix} 0 & I \\ -K & -D \end{pmatrix}$$

Note that the matrix E in Eq. (6.5) is symmetric and positive-definite. Several efforts have been made in existing literature to obtain a stable feedback control via Lyapunov functions for a linear system similar to Eq. (6.5) by inverting the time-variant matrix E such that the state matrix becomes $E^{-1}A$ and is time-variant. When the matrix E is considerably large in size, computation of the time-variant E^{-1} becomes extremely cumbersome and may even be ill-conditioned. In addition, the simple structure of Eq. (6.5) with symmetric matrices M, D, and K is destroyed, thereby eliminating any of the associated computational advantages. Herein, a novel approach is developed using a Lyapunov function to derive a nonlinear stable control law without inverting the time-variant matrix E. A synopsis of which follows:

Let a Lyapunov function be defined as

$$V(q) = q^T\{E^TPE\}q \tag{6.6}$$

where P denotes an n×n symmetric and positive definite weighting matrix. Note that the matrix inside the bracket is positive definite since the matrix E is nonsingular. For asymptotical stability in the sense of Lyapunov, the following conditions shown in definition 6.6 must hold:

$$\begin{aligned} &(1)\ V(q) > 0 \ for\ \ q \neq q_e, \\ &(2)\ V(q_e) = 0 \text{ and} \\ &(3)\ \tfrac{dV(q)}{dt} < 0 \ for\ \ q \neq q_e. \end{aligned} \tag{6.7}$$

where q_e denotes the state of equilibrium. In fact, Eq. (6.7) explicitly illustrates the mathematical description of the second method of Lyapunov's theory of asymptotical stability.

The objective of defining the Lyapunov function in Eq. (6.6) is to seek a feedback control u in Eq. (6.4) that moves every initial state to an arbitrary small neighborhood of the equilibrium state. Differentiating Eq. (6.6) with respect to time and substituting Eq. (6.4) into the resulting equation yield

$$\begin{aligned} \dot{V}(q) = {} & q^T\left[E^T\dot{P}E + \left(A^T + \dot{E}^T\right)PE + E^TP\left(A + \dot{E}\right)\right]q \\ & + \left[u^T\bar{B}^T + \bar{f}^T\right]PEq + q^TE^T\left[\bar{B}u + \bar{f}\right] \end{aligned} \tag{6.8}$$

Now let

$$A + \dot{E} = \tilde{A} \quad and \quad u = u_0 + u_1 = -\left(R^{-1}\bar{B}^TPEq\right) + u_1 \tag{6.9}$$

where u_1 represents a nonlinear control which will be derived later. Substitution of Eq. (6.9) into Eq. (6.8) yields

$$\begin{aligned} \dot{V}(q) = {} & q^T\left[E^T\dot{P}E + \tilde{A}^TPE + E^TP\tilde{A} - 2E^TP\bar{B}R^{-1}\bar{B}^TPE\right]q \\ & + \left[u_1^T\bar{B}^T + \bar{f}^T\right]PEq + q^TE^TP\left[\bar{B}u_1 + \bar{f}\right] \end{aligned} \tag{6.10}$$

The question arises whether there exists a positive definite matrix P such that $\dot{V}(q) \leq 0$. Let the time-variant matrix P satisfy the following matrix Riccati equation

$$E^T\dot{P}E + \tilde{A}^TPE + E^TP\tilde{A} - 2E^TP\bar{B}R^{-1}\bar{B}^TPE = -Q \tag{6.11}$$

where Q is a positive semi-definite matrix. It is known that the matrix Riccati equation (6.11) produces a positive definite matrix P for a given positive semi-definite matrix Q and a positive definite matrix R if the system is controllable. Through the linear optimal control theory, the matrices P and Q stand for the weighting matrices for state and control input respectively such that the corresponding quadratic performance index yields

$$J = \int_0^\infty \{q^TE^TQEq + u_0^TE^TREu_0\}\, dt \tag{6.12}$$

where u_0 indicates the optimal control law defined in Eq. (6.9). In general, the matrix P is time variant, if any one of the matrices $\tilde{A}$, $\bar{B}$, and E in Eq. (6.11) is time variant. Computation of the time-variant matrix P is very time consuming, particularly for large dimensional systems. It is wise to seek a constant positive definite matrix P which satisfies Eq. (6.11) and also produces a positive definite matrix R and a positive semi-definite matrix Q for a certain specified time period of interest. If there exists such a constant matrix P, then Eq. (6.11) can be bypassed or the computation of P is only used for checking positive definiteness of the matrices R and Q. In the following section for numerical examples, it will be shown that such a matrix P exists in many cases.

In view of Eq. (6.11), Eq. (6.10) becomes

$$\dot{V}(q) = -q^TQq + 2q^TE^TP\left[\bar{B}u_1 + \bar{f}\right] \tag{6.13}$$

Now, search a minimum $\|u_1\|$ such that $\dot{V}(q) \leq 0$. Note that $-q^TQq \leq 0$ for a positive semi- definite matrix Q. To assure that $\dot{V}(q) \leq 0$, the control part u_1 in Eq. (6.13) may be chosen such that

$$q^TE^TP\left[\bar{B}u_1 + \bar{f}\right] = -q^TE^TPR_NPEq \tag{6.14}$$

where R_N is a positive semi-definite matrix. Equation (6.14) can be solved for u_1 and is given by

$$u_1 = [u_0^T R]^\dagger [q^T E^T P] (R_N P E + \bar{f}) + \{I - [u_0^T R]^\dagger [u_0^T R]\} c \qquad (6.15)$$

where the superscript $\dagger$ means the general pseudo-inverse; c is a p×1 arbitrary vector; I is an identity matrix of order p; and u_0 is given by Eq. (6.9). The matrix $\{I - [u_0^T R]^\dagger [u_0^T R]\}$ contains the column vectors which are orthogonal to the vector Ru_0 since $[u_0^T R] \{I - [u_0^T R]^\dagger [u_0^T R]\} = 0$. When the nonlinear force u_1 with minimum norm is desired, c = 0 should be used in Eq. (6.15).

Substitution of Eq. (6.14) into Eq. (6.13) yields

$$\dot{V}(q) = -q^T [Q + E^T P R_N P E] q \qquad (6.16)$$

Obviously, $\dot{V}(q) \leq 0$ holds for given positive semi-definite matrices Q and R_N. As a result, the conditions of Lyapunov stability given by Eq. (6.7) are all satisfied. In other words, the nonlinear feedback control u shown in Eq. (6.9) provides a maneuvering with Lyapunov stability, which will bring the system from an initial state to the equilibrium state. In order to minimize the nonlinear control force u_1 from Eq. (6.15), the positive semi-definite matrix R_N should be chosen such that the norm $\|R_N P E q + \bar{f}\|$ is minimum.

§ 6.3 Numerical simulations

Three control models are given, namely the flexible one-beam structure, the articulated flexible two-beam structure, and an inverted rigid pendulum, to illustrate the ideas developed in this chapter. The model of flexible one-beam structure resembles the experimental setup in chapter 4 which has performed slewing experiments of a flexible steel beam carried on a translational trolley (Fig. 1.2). One articulated flexible two-beam structure is constructed in a way that one flexible steel beam is articulated on the tip of the previous flexible beam on a trolley as

shown in Fig. 6.3. Instead of constant output feedback gains, two Lyapunov-based nonlinear controllers based on Eq. (6.15) are developed to generate the regulator-type maneuvers of two kinds of nonlinear flexible structures. Furthermore, the case of an inverted pendulum (see Fig. 6.4) is investigated to stabilize an unstable rigid system by applying the developed Lyapunov-based nonlinear controller.

§§ 6.3.1 The flexible one-beam structure

The dynamics of a flexible steel beam on a rigid and translational trolley has been described in section 4.2. The closed-loop dynamic equation is governed by Lagrange's equation of motion, consisting of dynamics of actuators and characteristics of sensors in Eq. (C.9). Due to the construction of this multi-body dynamics, the kinematic nonlinearities exist in two parts such as the cosine terms of inertia matrix in Eq. (C.4) and the Coriolis forces of the forcing term in Eq. (C.6). The first two cantilevered modes are assigned to discretize the flexural vibration of the flexible steel beam. Lagrange's equation of motion in Eq. (C.9) is rearranged in first order form as Eq. (6.4) where

$$E = \begin{pmatrix} I & 0 \\ 0 & \bar{M} \end{pmatrix} \quad and \quad E = \begin{pmatrix} 0 & I \\ -K & -\bar{D} \end{pmatrix}. \tag{6.17}$$

where $\bar{M}$, K, and $\bar{D}$ indicate the inertia, stiffness, and damping matrices which are defined in Eqs. (C.5) and (C.9). The state vector of Eq. (6.4) is defined by

$$q^T = \left[y,\ \theta,\ q_1,\ q_2,\ \dot{y},\ \dot{\theta},\ \dot{q}_1,\ \dot{q}_2 \right] \tag{6.18}$$

where y is the translational displacement of the trolley, θ the root angle of the flexible beam, and q_i (i=1,2) the general coordinates corresponding to the shape functions ψ_i (i=1,2) for discretization of the bending deflection of the flexible beam (see Fig. C.1). The control input u in Eq. (6.4) is equal to E_a in Eq. (C.9). Table 6.1 summarizes the parameters used to model the flexible one-beam structure on a trolley. Note that the symbols in Table 6.1 are associated with the dynamic equation of Eq. (C.3) shown in Appendix C. Instead of sensors in

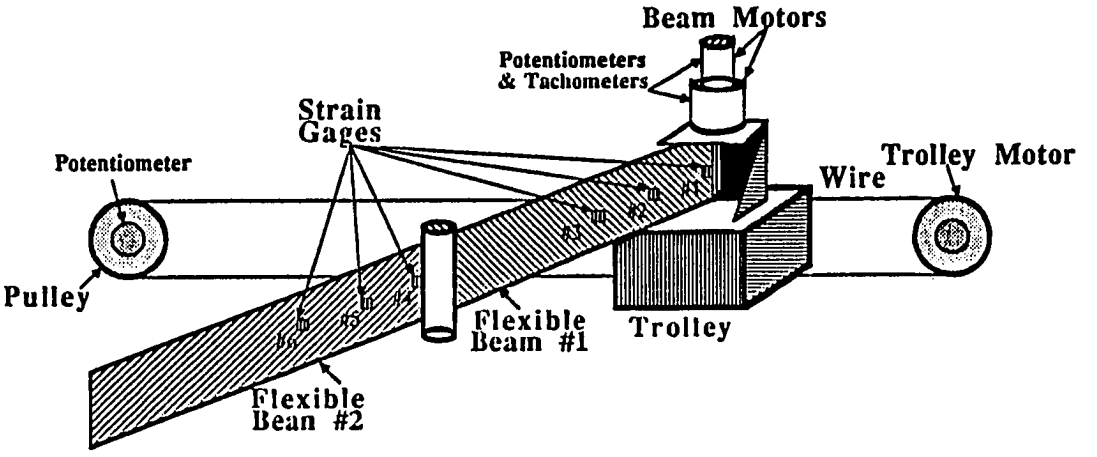

Figure 6.3: Two articulated beams on a trolley

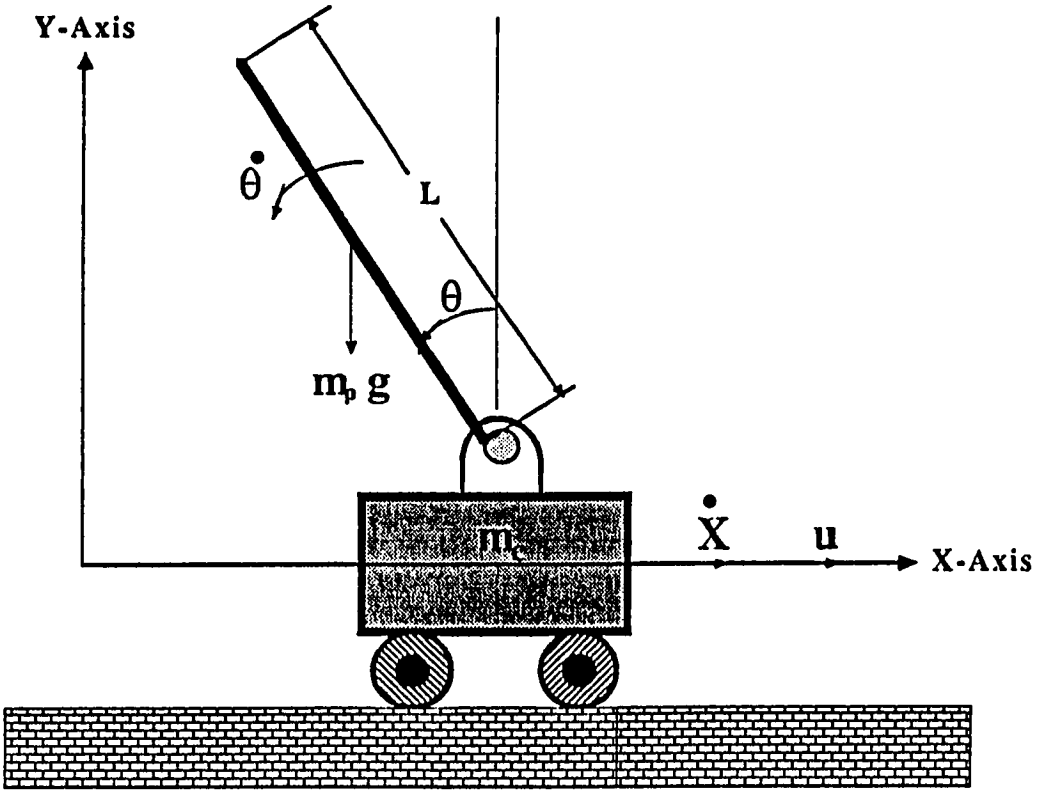

Figure 6.4: Inverted pendulum

Chapter 4, one tachometer is built into the trolley motor to measure the trolley velocity for its output feedback.

A positive definite weighting matrix P, shown in Table 6.2, will be decided to generate a quadratic Lyapunov's function (V(q,t)>0) based on Eq. (6.6). In the time rate of Lyapunov's function of Eq. (6.8), the matrix $\tilde{A}$ becomes nonlinear due to the following time derivative of the inertia matrix which appears in $\dot{E}$.

$$\dot{M} = \begin{pmatrix} m + \rho L & -\frac{\rho L^2 \sin(\theta)\dot{\theta}}{2} & \tilde{h}^T \sin(\theta)\dot{\theta} \\ -\frac{\rho L^2 \sin(\theta)\dot{\theta}}{2} & I & -\tilde{p}^T \\ \tilde{h}\sin(\theta)\dot{\theta} & -\tilde{p} & \rho L \hat{I} \end{pmatrix} \tag{6.19}$$

In Table 6.2, the input weighting matrix R(>0) of Eq. (6.12) is chosen such that the matrix $Q(\geq 0)$ satisfies the Riccati equation (6.11). To calculate the constant matrix P (see Table 6.2), three steps are involved. First, linearize the time-variant matrices $\tilde{A}$ and B to obtain a dominant constant part. Second, determine the positive definite matrix P by solving the Riccati equation (6.11) with the constant parts of the matrices $\tilde{A}$ and B and two pre-assigned positive definite matrices R and Q (see Table 6.2). Third, check the positive definiteness of $q^T Q q$ (V(q,t)>0) and negative definiteness of $2\dot{q}^T Q q$ $\left(\dot{V}(q,t) < 0\right)$ with Q determined from the Riccati equation (6.11) for the time period of interest with the original time variant matrix B, the above-computed constant matrix P and the pre-assigned matrix R.

Table 6.1: Model parameters of one flexible beam on a trolley

a. Motors:

(1)Trolley motor:

$K_{t0} = 0.0346$	$N \bullet m/Amp$
$K_{b0} = 0.0342$	Volt- sec/rad
$R_{a0} = 4$	Ohm
$I_{m0} = 4.7 \times 10^{-6}$	$kg - m^2$
$N_{g0} = 210$	

(2)Beam motor:

$K_{t1} = 9.3 \times 10^{-3}$	$N \bullet m/Amp$
$K_{b1} = 9.2 \times 10^{-3}$	Volt-sec/rad
$R_{a1} = 1.1$	Ohm
$I_{m1} = 2.3 \times 10^{-6}$	$kg - m^2$
$N_{g1} = 210$	
$m_1 = 0.92$	kg

b. Steel beam:

Length	$\bar{L} = 1.0$	m
Rigidity	EI $= 0.71$	$N - m^2$
Density	$\rho = 0.47916$	kg/m
Thickness	h $= 0.041 \times 10^{-2}$	m

c. Rigid trolley:

Mass $m_c = 0.588$ kg

Table 6.2: Weighting matrices of one flexible beam on a trolley

$$Q = Diag[\ 100\ \ 1000\ \ 0.05\ \ 0.05\ \ 1\ \ 1\ \ 1\ \ 1\ ] \times 100\ ;$$

$$R = \begin{pmatrix} 0.1627 & 0.3978 \\ 0.3978 & 9.0235 \end{pmatrix} \times 1000\ ;$$

$$P = \begin{pmatrix} 18740 & 9220 & -250 & -60 & 2900 & 1030 & -1280 & -380 \\ & 109910 & -6980 & -1160 & 7150 & 7440 & -7680 & -1310 \\ & & 5540 & 80 & 160 & -220 & 200 & -10 \\ & & & 44860 & 150 & -20 & 90 & -40 \\ & & & & 970 & 680 & -810 & -130 \\ & & \text{symmetric} & & & 630 & -720 & -100 \\ & & & & & & 870 & 100 \\ & & & & & & & 80 \end{pmatrix}$$

$\times 10^5$.

The nonlinear control force u_1, with minimum norm, is thus computed using Eq. (6.15) with $R_N = 0$ and c = 0. Figure 6.5 demonstrates the mission of the regulator-type maneuver of this flexible one-beam structure which slews about 30 deg., while the trolley is moving to -0.8 m from the original position. Herein, two cases of maneuvering simulations are performed through the Lyapunov-based control $u_0 + u_1$ and linear feedback control u_0 shown in Eq. (6.19). For the sake of comparison, the Lyapunov-based control result and the corresponding linear control result are drawn together and denoted by the solid line and dashed line respectively in the same plot. The performance of such a slewing maneuver is thus demonstrated in Figs. 6.6-6.11. The trolley moves to the terminal position in 7 sec, as shown in Fig. 6.6. Obviously, the Lyapunov-based control, i.e. $u_0 + u_1$, implements the trolley translational motion faster than linear feedback control u_0. Since the trolley transient response is associated with rigid-body motion, the influence of the nonlinear feedback control, due to higher modes, is hardly observed in its behavior. Nevertheless, the higher-mode feedback effect is visible in the trolley velocity as shown in Fig. 6.7. That is because there exists the highly coupling terms between the trolley velocity and higher modes in the nonlinear force $f\left(\xi, \dot{\xi}\right)$ of Eq. (C.6). Hence, from Figs. 6.6 and 6.7, the asymptotical stability of trolley motion is achieved through the Lyapunov-based control. For both Lyapunov-based control and linear feedback control, the beam angle takes 4 seconds to reach the desired angle, as shown in Fig. 6.8. The nonlinear control $u_0 + u_1$ speeds up the beam, slewing to about 27 deg in the first second then slows down its motion in the following three seconds. The higher modes have influence upon the beam slewing in Fig. 6.8 due to excitation of higher modes through the Lyapunov-based control $u_0 + u_1$. The slewing angle of linear control feedback demonstrates a smooth history which indicates no feedback of kinematic nonlinearity is involved. In Fig. 6.9, the beam angular velocity of Lyapunov-based control response takes about the same time, i.e. 4 sec, to settle down

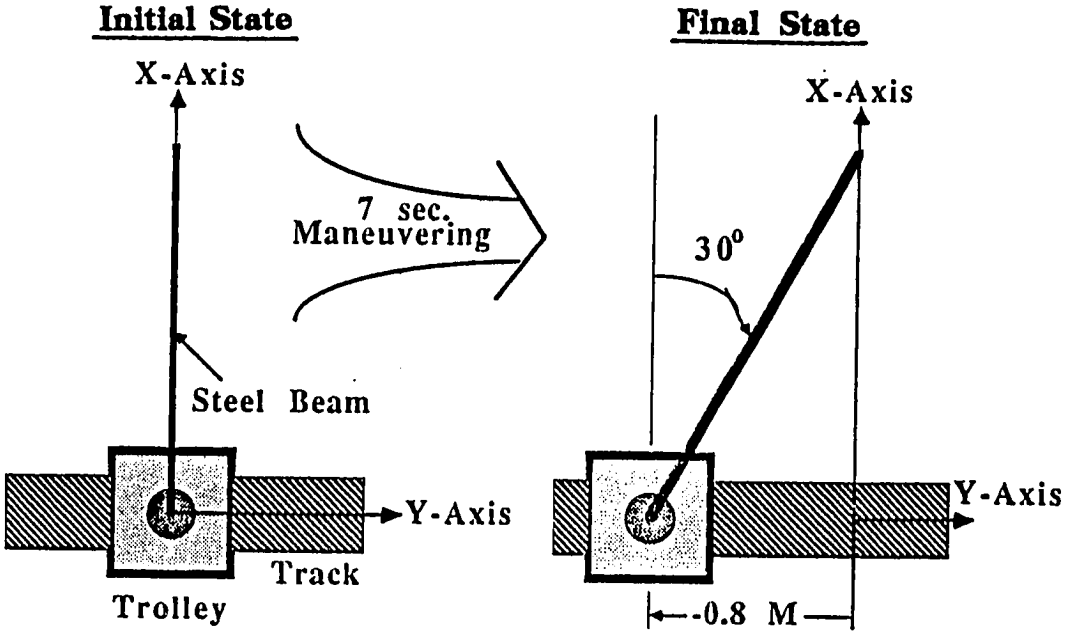

Figure 6.5: Maneuvering mission of a flexible one-beam structure

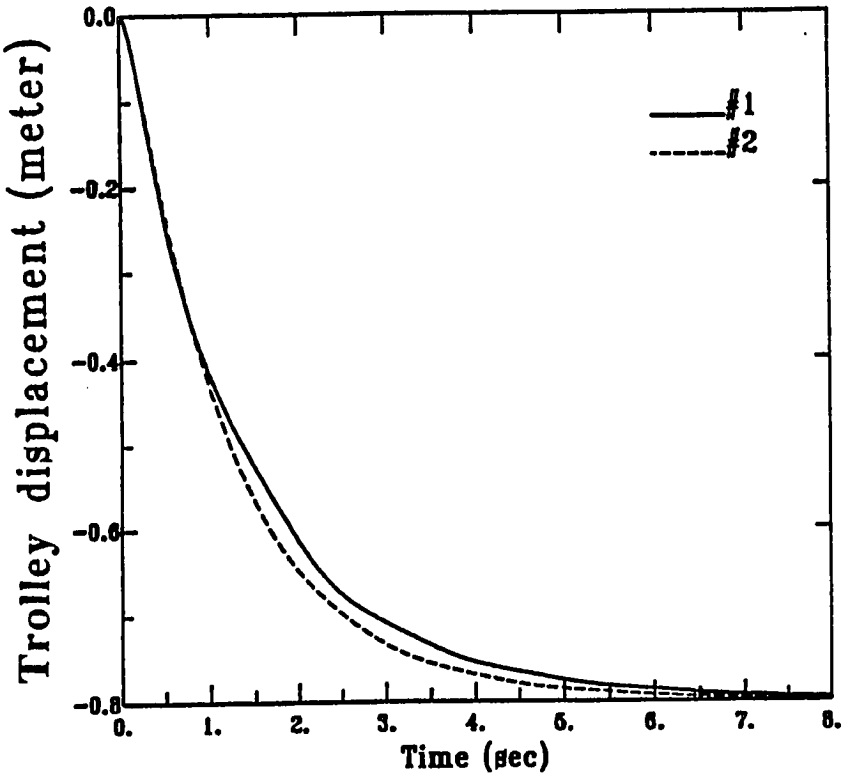

Figure 6.6: Trolley displacement of a flexible one-beam structure

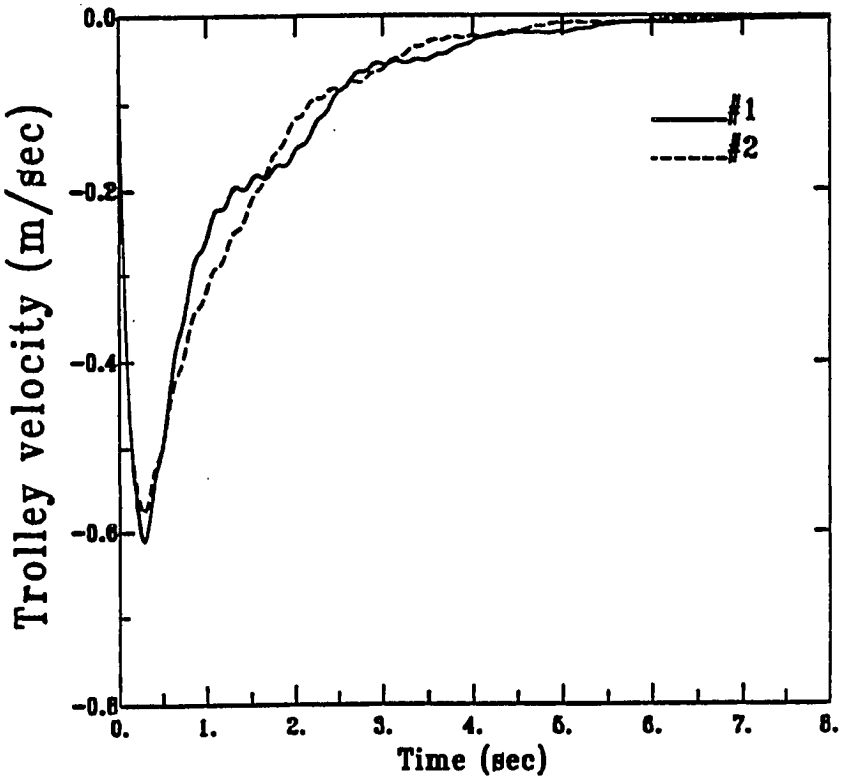

* #1: u_o+u_1; #2: u_o

Figure 6.7: Trolley velocity of a flexible one-beam structure

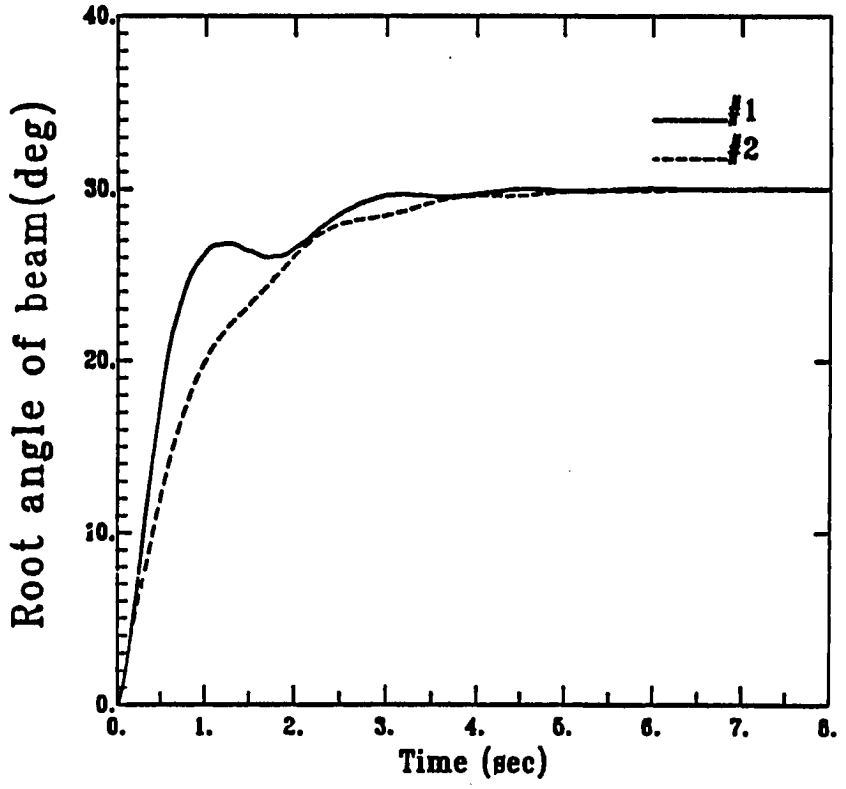

Figure 6.8: Beam angular displacement of a flexible one- beam structure

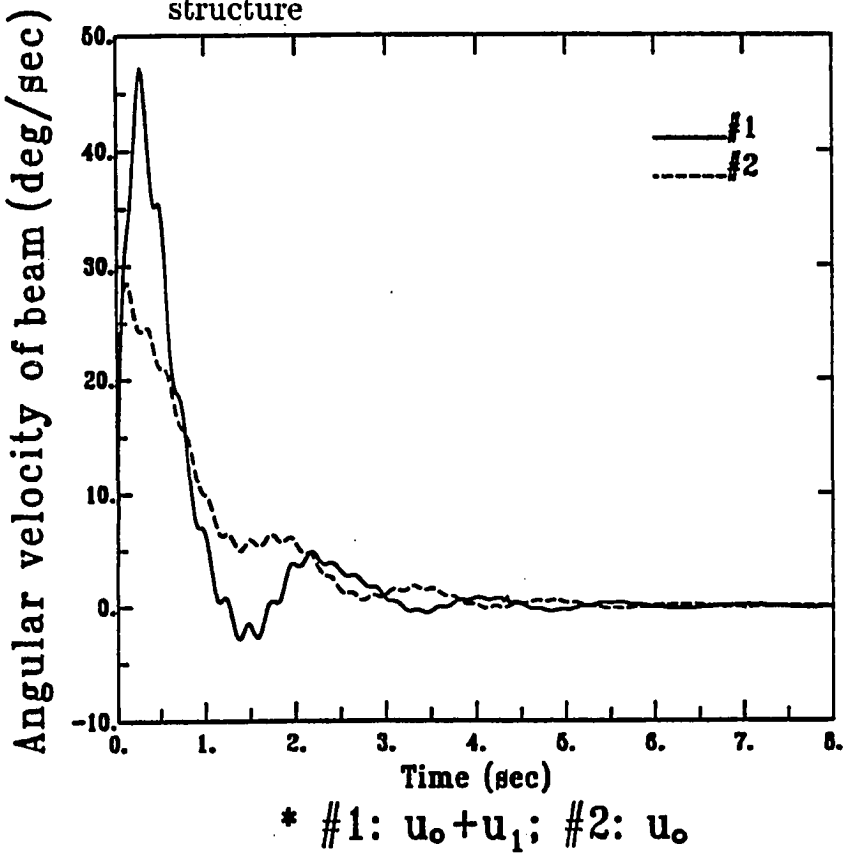

* #1: u_o+u_1; #2: u_o

Figure 6.9: Beam angular velocity of a flexible one-beam structure

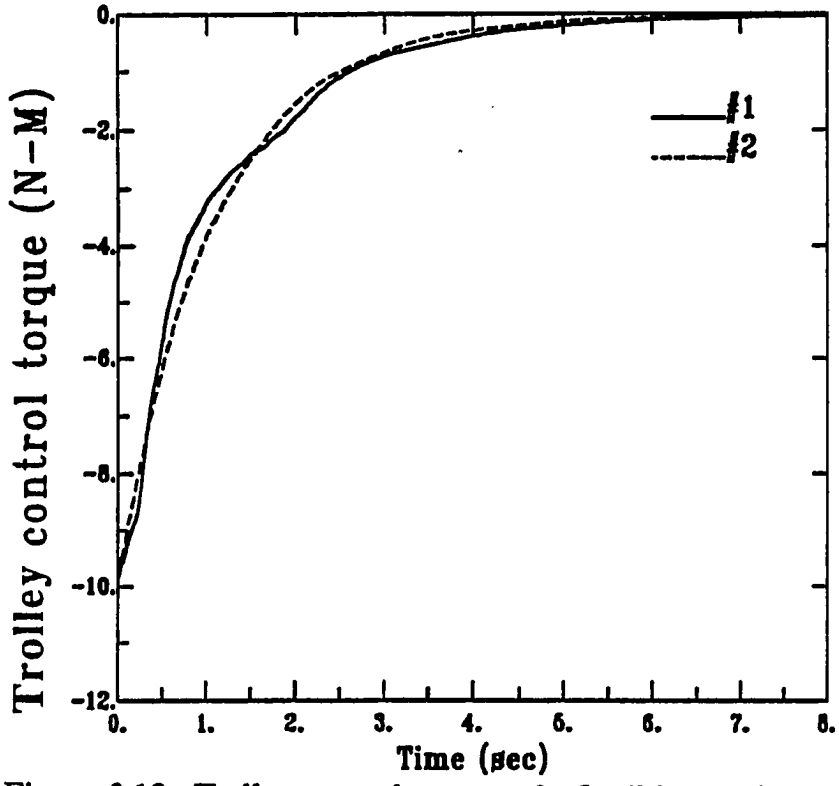

Figure 6.10: Trolley control torque of a flexible one- beam structure

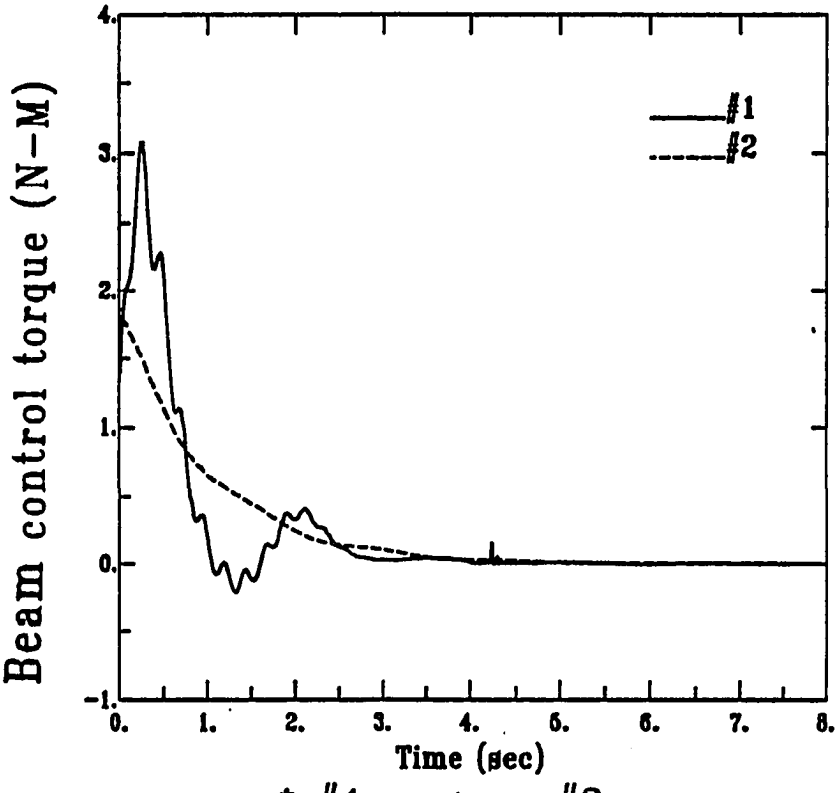

* #1: u_o+u_1; #2: u_o

Figure 6.11: Beam control torque of a flexible one-beam structure

with a very slight overshoot between 1 sec and 2.5 sec. Without a significant overshoot in the transient response of angular velocity, the linear feedback control u_0 slews the flexible beam more smoothly than $u_0 + u_1$. Two vibrational modes are observed in two time histories of angular velocities. In Fig. 6.9, the first mode dominates the feedback of the Lyapunov-based control such that $u_0 + u_1$ rotates rapidly flexible beam in the first second to produce one peak magnitude of angular velocity 47 deg/s which does not exist in the case of linear feedback control. And the second mode becomes significant during the residual vibration in the case of Lyapunov-based control which is similar with the experimental results in Chapter 4. Figure 6.10 shows that two kinds of trolley control inputs, i.e. $u_0 + u_1$ and u_0, begin with a -10 N-M and reduce to 0 N-M within 7 sec. They resemble each other because of the small influence upon the trolley motion from the feedback control u_1. Two beam control inputs, which are demonstrated in Fig. 6.11, start with 1.7 N-M and end up with 0 N-M in 4 sec. Apparently, the time history of beam Lyapunov-based control input resembles its corresponding angular velocity in Fig. 6.9. The vibrational modes react very significantly in the Lyapunov-based control input because of the complicated feedback of kinematic nonlinearity associated with higher modes in Eq. (C.6). Notice that both control inputs, $u_0 + u_1$ and u_0, start with the same magnitudes in the Figs. 6.9 and 6.10. That is because the component u_1 of Lyapunov-based control is conducted for feedback of kinematic nonlinearity so that $u_0 + u_1$ must equal to u_0 in the initial time t=0. Hence, figures 6.10 and 6.11 indicate an active and stable feedback control which is developed based on the Lyapunov's criterion of asymptotical stability. The time rate of Lyapunov's function is provided in Fig. 6.12 to insure the negative rate of the assigned quadratic function for the sake of stability. The simulation results, in Fig. 6.6-6.12, thus provide some insights into the nonlinear slewing maneuvers of large flexible space structures to the Lyapunov-based control.

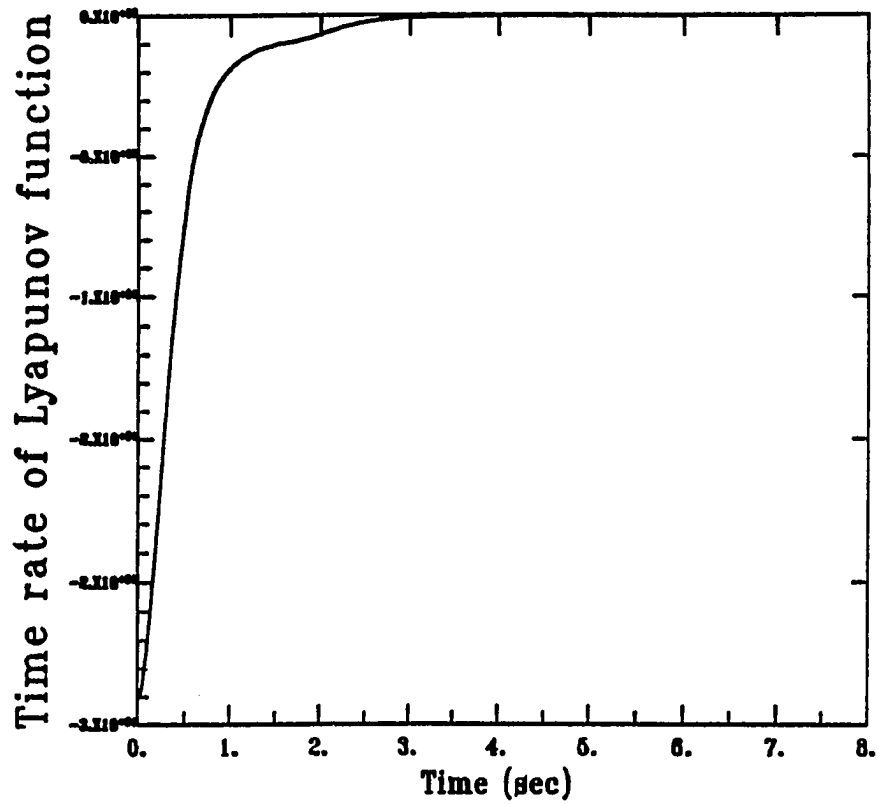

Figure 6.12: Time rate of Lyapunov's function of a flexible one-beam structure

§§ 6.3.2 The flexible two-beam structure

The previous example of the flexible one-beam structure is a typically slewing maneuver of the large flexible space structure. Normally, the huge size of flexible structures may result in several difficulties such as construction, vibration, stability and controller design. Therefore, a flexible two-beam structure is constructed to extend the maneuvering span of an original flexible one-beam structure with one more flexible beam and one more motor. One flexible beam is articulated on the tip of the previous steel beam to construct an articulated flexible structure as shown in Fig. 6.3. One more actuator is required, which is concatenated axially with the former motor on the rigid trolley. This motor thus manipulates the fore-beam through a wire-and-pulley system. Therefore, the entire system becomes a 3-body dynamics which is composed of one rigid trolley and two identical flexible steel beams. Lagrange's function and equation of motion are provided in Appendix E. The symbolic parameters and three sets of coordinates are shown in Fig. E.1. Note that the $x_2 - y_2$ coordinates are related to the $x_1 - y_1$ coordinates. Namely, the transient response of fore-beam is observed from the tip of the first flexible beam. The additional beam is also treated as a cantilever beam with the same specifications as the former one. Two cantilevered modes are assigned to discretize the flexural vibration of the fore-beam. The inertia matrix $\bar{M}$, shown in Eq. (E.7), becomes very complicated due to several cosine functions of two angles θ_1 and θ_2. And the centrifugal forces and Coriolis forces are included in the nonlinear force vector in Eq. (E.7). The stiffness matrix K and damping matrix $\bar{D}$ are defined in Eqs. (E.4) and (E.7). The state vector similar to Eq. (6.18) becomes

$$q = \left[y, \theta_1, \theta_2, q_1^T, q_2^T, \dot{y}, \dot{\theta}_1, \dot{\theta}_2, \dot{q}_1^T, \dot{q}_2^T\right]^T ;$$

$$q_1^T = [q_{11}, \cdots, q_{1n_1}] \quad and \quad q_2^T = [q_{21}, \cdots, q_{2n_2}] \tag{6.20}$$

where y is the translational displacement of the trolley and q_{1i} (i=1,2) the general coordinates corresponding to the shape functions ψ_{1i} (i=1,2) for discretization of

the bending deflection of the first flexible beam. The quantities q_{2i} and ψ_{2i} are defined similarly for the fore-beam. The model parameters of this flexible two-beam structure are specified in Table 6.3. The specifications of the fore-beam and its motor are equivalent to those for the flexible steel beam in Table 6.2. The overall length of fully expanded flexible beams is thus 2 meters long.

The same three-step procedure as mentioned in section 6.3.2 is used to compute a positive definite weighting matrix accompanied with a constant positive definite matrix R and a time-variant matrix Q, which satisfies the Riccati equation (6.11). The specified Q and R, as well as computed P matrices, are listed in Table 6.4.

In Eq. (6.15), R_N and c are assigned to be zero in order to compute the nonlinear control force u_1 with minimum norm. Figure 6.13 shows the mission of the multi-body slewing maneuver of this flexible two-beam structure. The task is to move the trolley 0.5 meters from an original position while rotating the first flexible beam -35 deg and the fore-beam 35 deg simultaneously. Two cases of maneuvering simulations are performed through the Lyapunov-based control $u_0 + u_1$ and linear feedback control u_0 shown in Eq. (6.19). This multi-body slewing maneuver is thus performed and demonstrated in Figs. 6.14- 6.22. Figure 6.14 shows that the trolley moves to the terminal position in 4 sec. The trolley almost tracks out the same trajectory within the first second for both Lyapunov-based control and linear feedback control. The smooth history of trolley displacement implies that the Lyapunov-based control does not affect the rigid-body motion very much, which has happened in the case of flexible one-beam structure. Both trolley velocities behave similarly in the first second and reach a peak magnitude 0.51 m/s in 0.3 sec as shown in Fig. 6.15. For the first flexible beam, the beam ♯1 takes 4 sec to reach the desired angle as shown in Fig. 6.16. The irregular time history of beam ♯1 angular velocity in Fig. 6.17 implies that beam ♯1 slewing is mutually interacted by the trolley motion and beam ♯2 slewing.

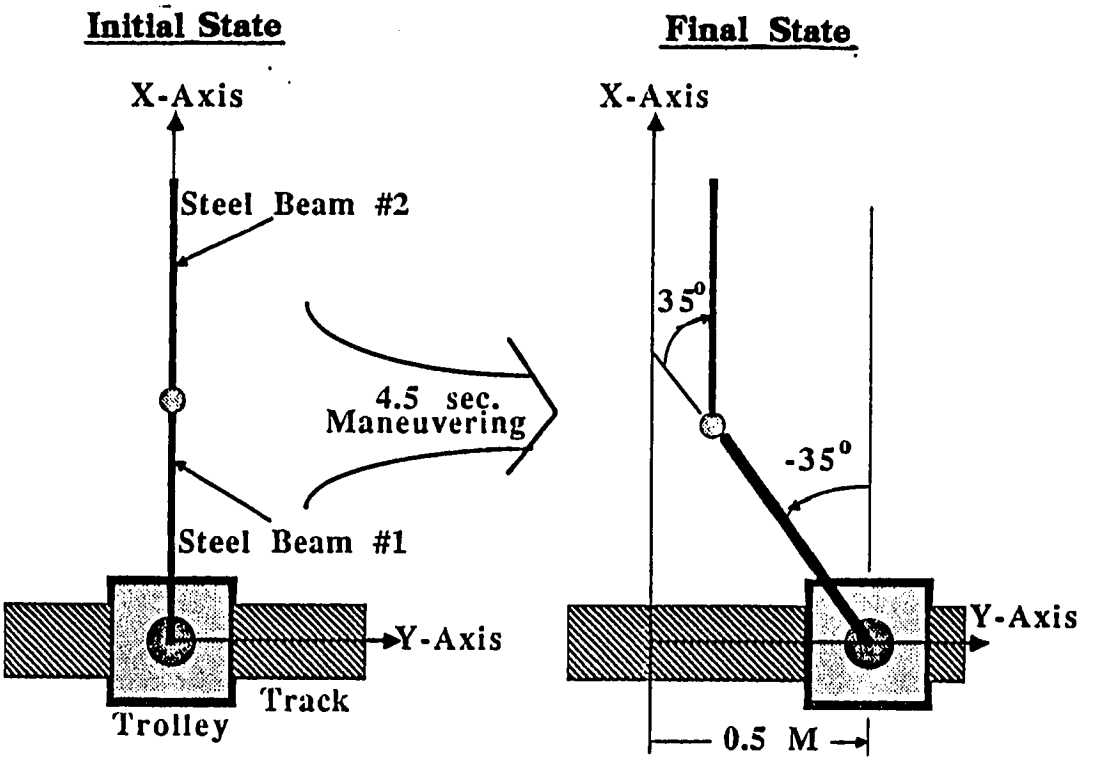

Figure 6.13: Maneuvering mission of a flexible two-beam structure

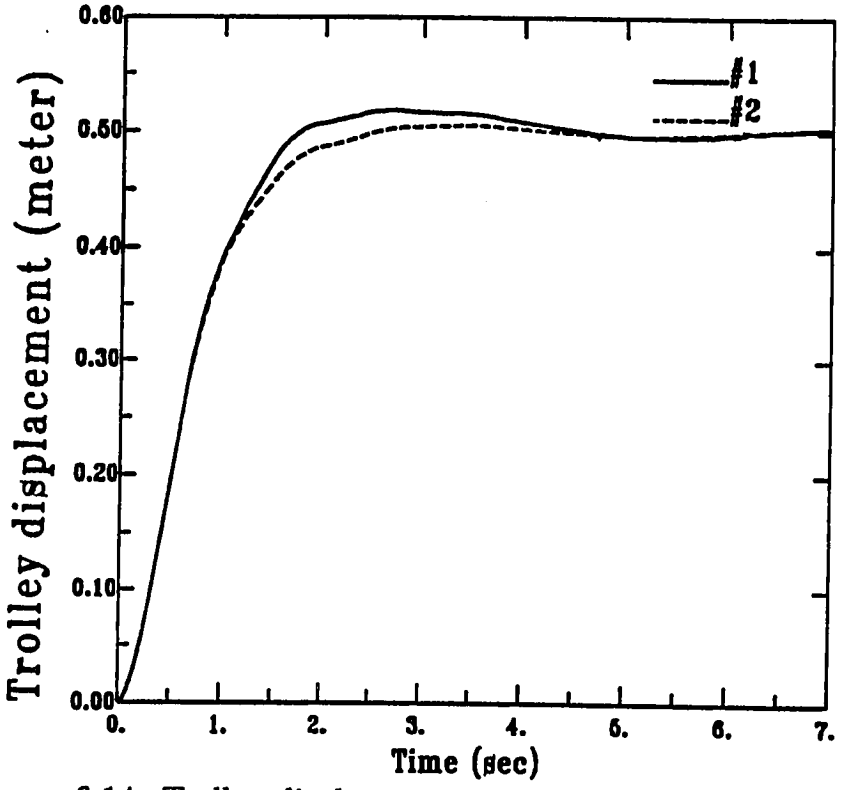

Figure 6.14: Trolley displacement of a flexible two-beam structure

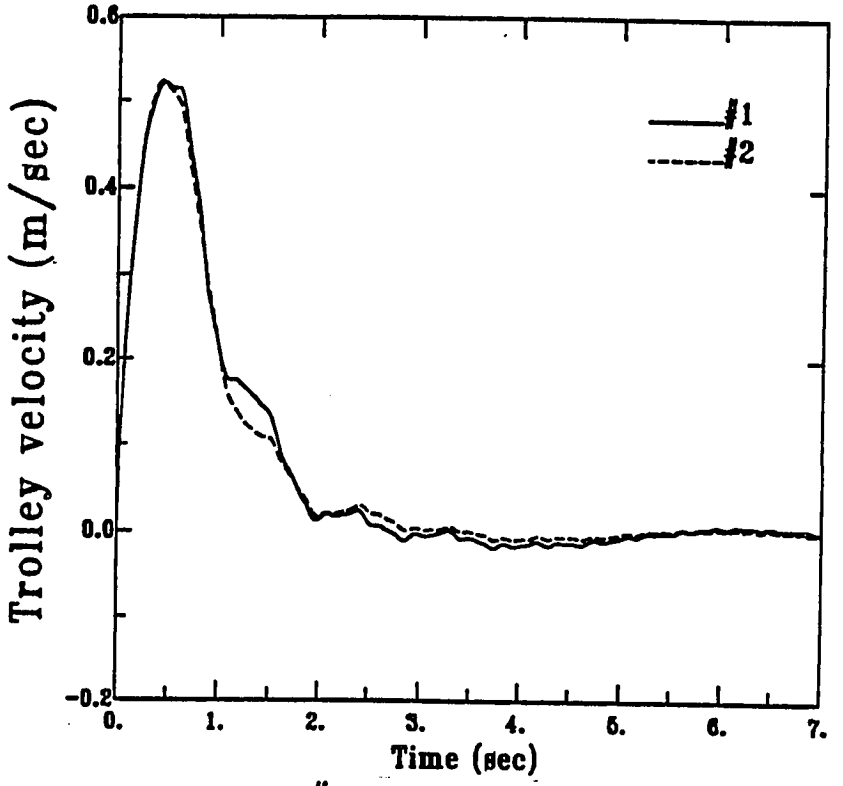

* #1: u_o+u_1; #2: u_o

Figure 6.15: Trolley velocity of a flexible two-beam structure

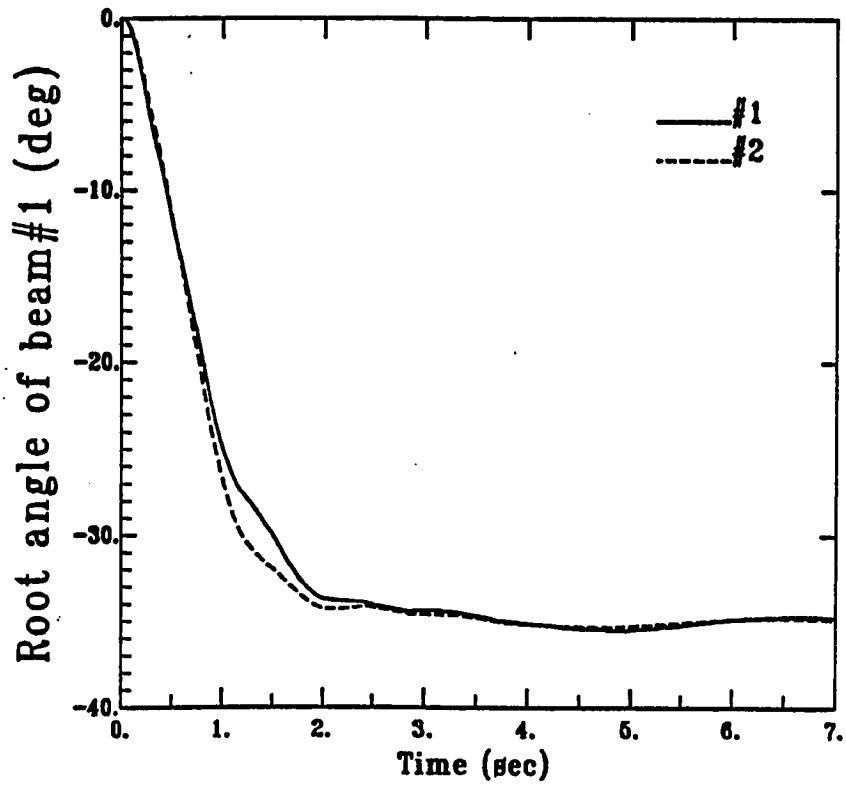

Figure 6.16: Beam #1 angular displacement of a flexible two-beam structure

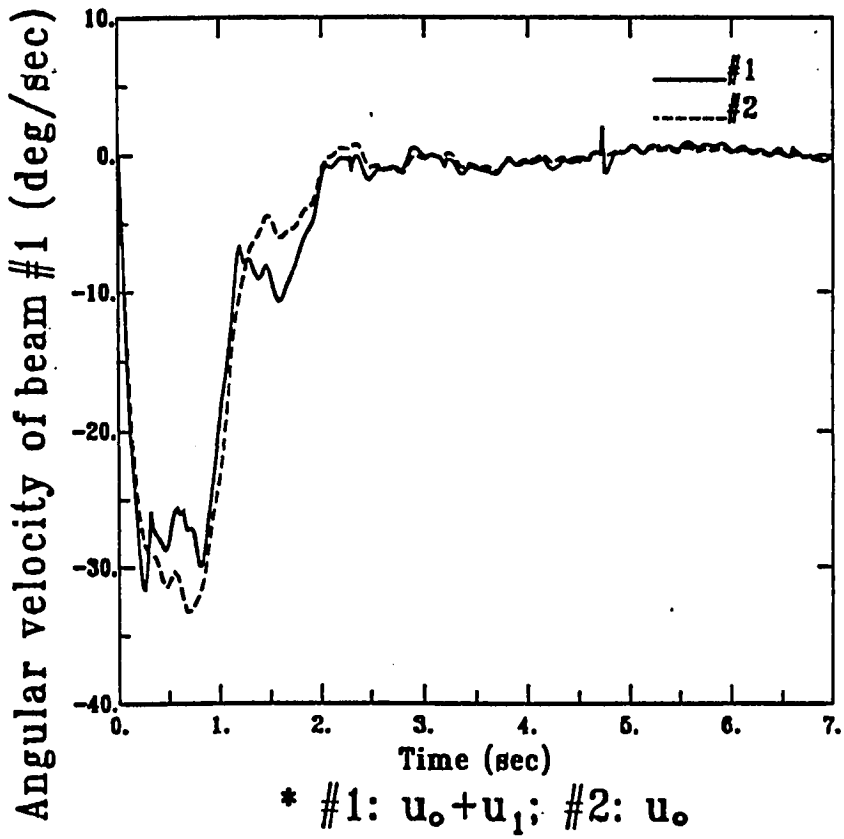

Figure 6.17: Beam #1 angular velocity of a flexible two-beam structure

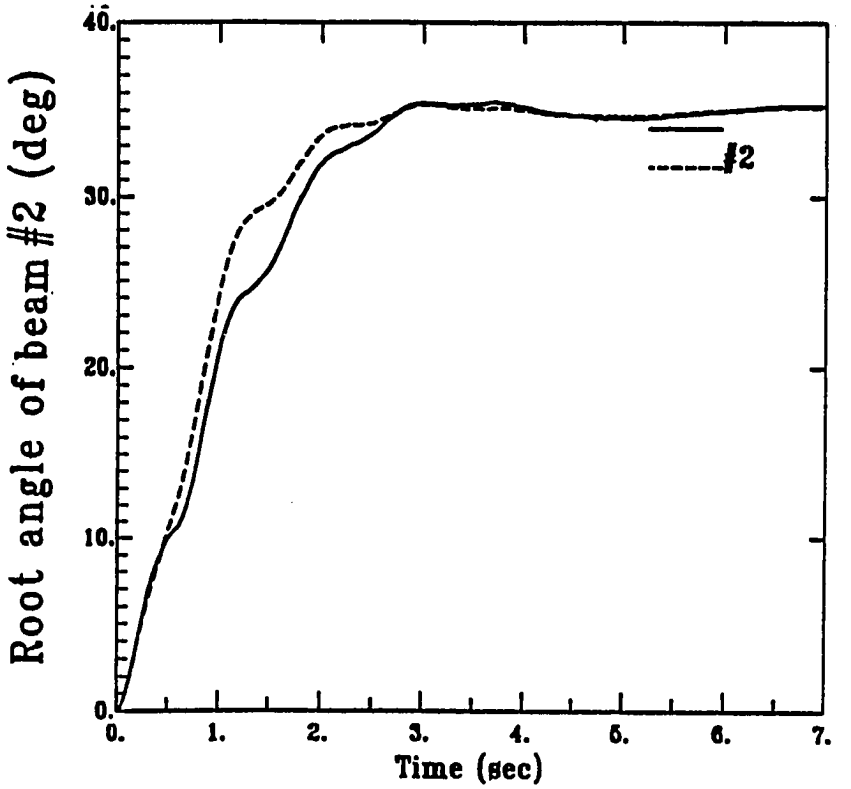

Figure 6.18: Beam #2 angular displacement of a flexible two-beam structure

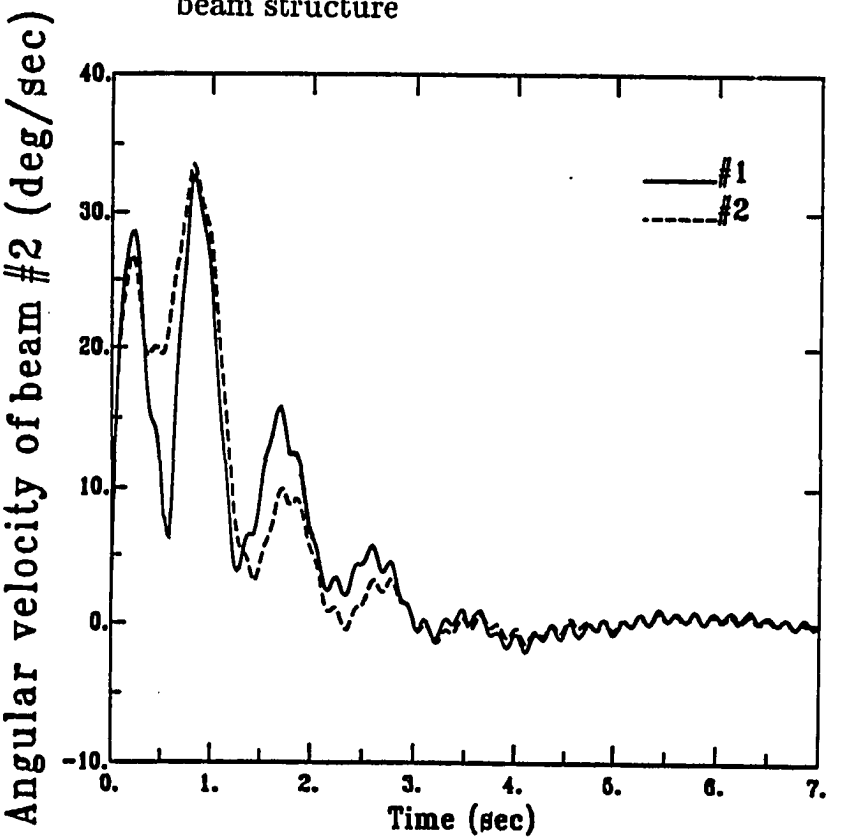

* #1: u_o+u_1; #2: u_o

Figure 6.19: Beam #2 angular velocity of a flexible two-beam structure

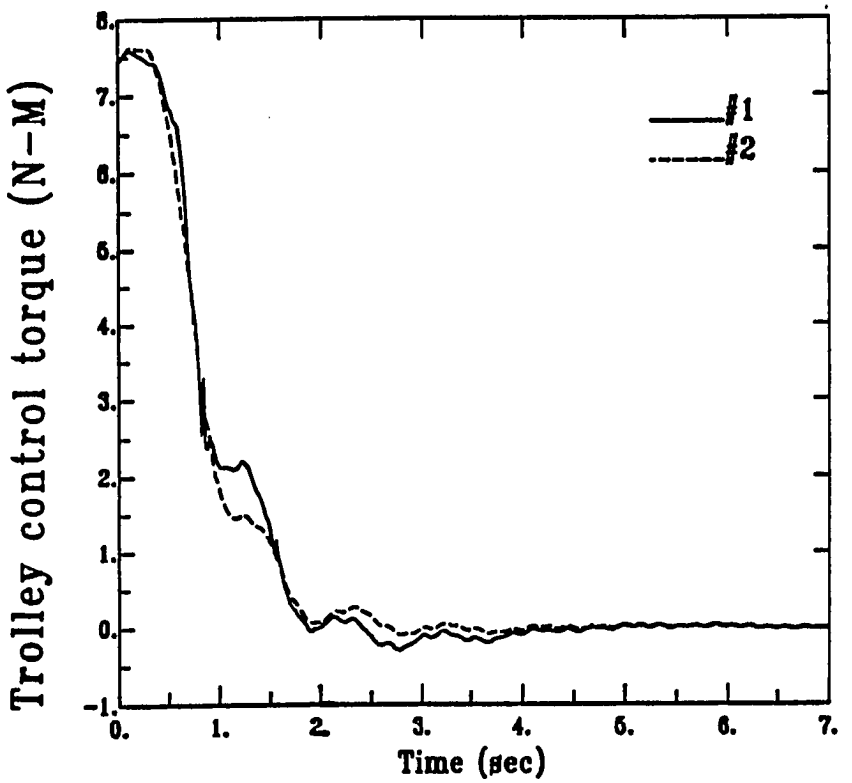

Figure 6.20: Trolley control torque of a flexible two-beam structure

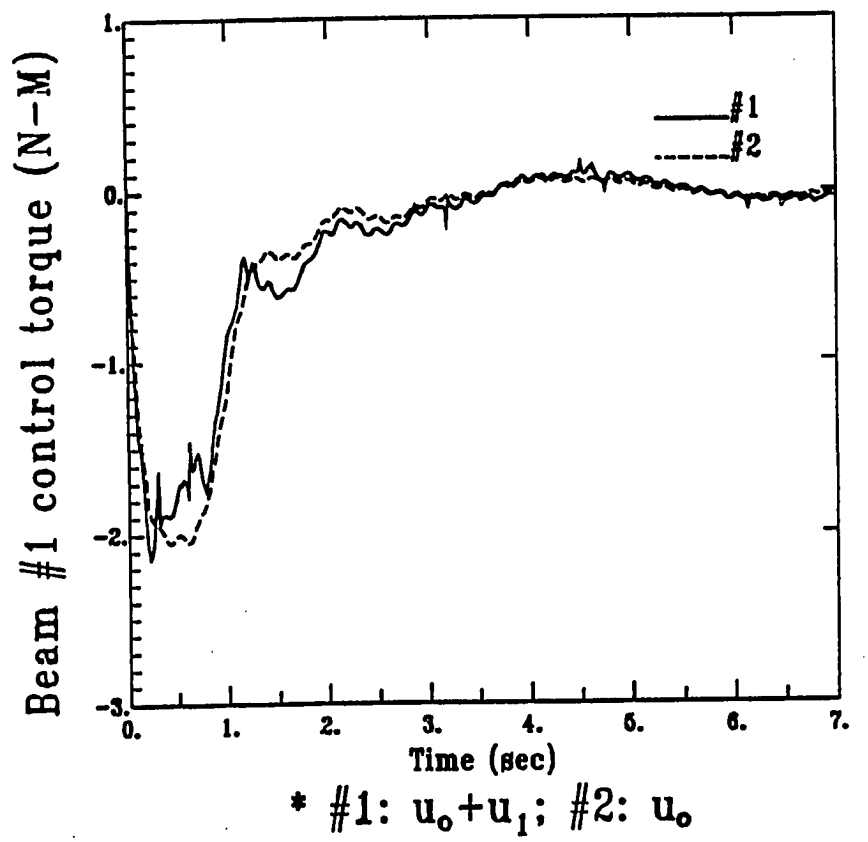

* #1: u_o+u_1; #2: u_o

Figure 6.21: Beam #1 control torque of a flexible two-beam structure

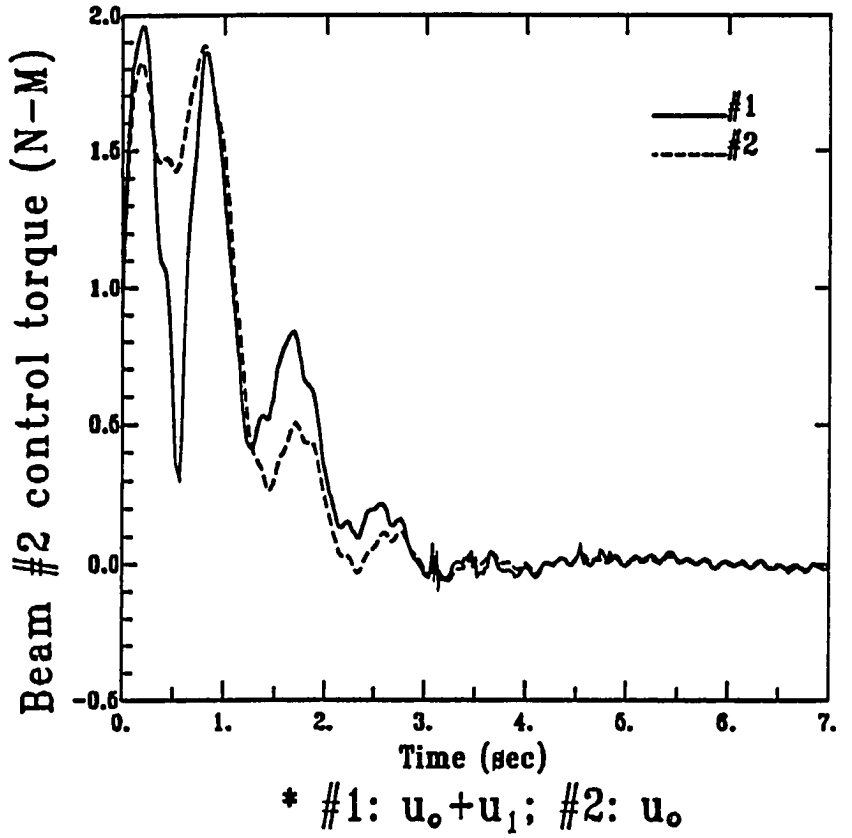

Figure 6.22: Beam #2 control torque of a flexible two-beam structure

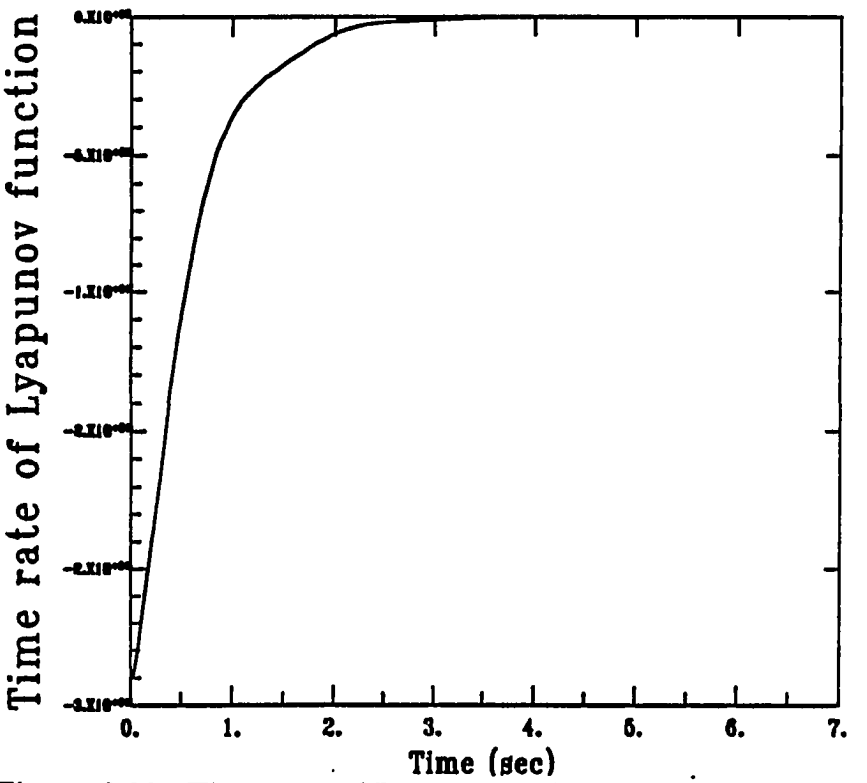

Figure 6.23: Time rate of Lyapunov's function of a flexible two-beam structure

And such a phenomenon in Fig. 6.17 is more significant in the solid curve due to excitation of higher modes of beams #1 and #2 through the Lyapunov-based control u_0+u_1. In Fig. 6.18, beam #2 takes about 4.5 sec to implement the slewing maneuver. Compared to Fig. 6.16, beam #2 gains have a greater vibrational influence than beam #1, especially the angular displacement due to Lyapunov-based control input. Figure 6.19 shows the angular velocity of beam #2. Compared to Fig. 6.17, two vibrational modes are observed in two time histories of angular velocities. The first mode dominates during the first 4 seconds, and the second mode becomes significant during the residual vibration. A big jump of angular velocity, in the solid line, at 0.5 sec implies an abrupt change of the Lyapunov-based control input to beam #2. Such a big jump can still be absorbed afterward through the control input $u_0 + u_1$. Figure 6.20 demonstrates that two kinds of trolley control inputs, i.e. $u_0 + u_1$ and u_0, begin with a 7.5 N-M and damp out to 0 N-M within 4 sec. A small ripple of the Lyapunov-based trolley input, which happens at 1 sec results in a slight change of angular velocity and displacement at the same time in Figs. 6.14 and 6.15. Both beam #1 control inputs, i.e. $u_0 + u_1$ and u_0 in Fig. 6.21, start with -0.5 N-M and continue oscillating for 7 sec to compensate the residual vibration. Obviously, the time history of beam Lyapunov-based control input resembles its corresponding angular velocity in Fig. 6.17. That implies that the Lyapunov-based control input fairly depends on the feedback of kinematic nonlinearity such as centrifugal and Coriolis forces. The beam #2 control inputs are shown in Fig. 6.22. Two control torques start with 1.0 N-M and damp out to the slight oscillation within 4.5 sec. Similarly, the behavior of Lyapunov-based beam #2 control input is similar with its angular velocity shown in Fig. 6.19. Hence, figures 6.20 and 6.22 indicate an active and stable Lyapunov-based control design for the slewing maneuver of a flexible two-beam structure. The negative time rate of the assigned Lyapunov's function is demonstrated in Fig. 6.23 to insure the asymptotical stability. Besides the previous simulation results in Figs. 6.6-6.12, the simulation results in this section enhance the feasibility of Lyapunov-based control design for the slewing maneuvers of large flexible space structures.

Table 6.3: Model parameters of two articulated flexible beams on a trolley

a. Motors:

(1)Trolley motor:

$K_{t0} = 0.0346$	$N \bullet m/Amp$
$K_{b0} = 0.0342$	Volt- sec/rad
$R_{a0} = 4$	Ohm
$I_{m0} = 4.7 \times 10^{-6}$	$kg - m^2$
$N_{g0} = 210$	

(2)Beam motor:

$K_{ti} = 9.3 \times 10^{-3}$	$N \bullet m/Amp$
$K_{bi} = 9.2 \times 10^{-3}$	Volt-sec/rad
$R_{ai} = 1.1$	Ohm
$I_{mi} = 2.3 \times 10^{-6}$	$kg - m^2$
$N_{gi} = 210$	
$m_1 = 0.92$	kg
(i = 1, 2)	

b. Steel beam:

Length	$\bar{L} = 1.0$	m
Rigidity	EI = 0.71	$N - m^2$
Density	$\rho = 0.47916$	kg/m
Thickness	h $= 0.041 \times 10^{-2}$	m

c. Rigid trolley:

Mass $m_c = 0.588$ kg

Table 6.4: Weighting matrices of two articulated flexible beams on a trolley

$$Q = Diag[\,100\ \ 1000\ \ 1000\ \ 0.05\ \ 0.05\ \ 0.05\ \ 0.05\ \ 1\ \ 1$$
$$1\ \ 1\ \ 1\ \ 1\ \ 1\,] \times 100\,;$$
$$R = Diag\,[\,1000\ \ \ 1000\ \ \ 1000]\,;$$
$$P = \begin{pmatrix} P_{11} & P_{12} \\ P_{12}^T & P_{22} \end{pmatrix};$$

where

$$P_{11} = \begin{pmatrix} 18740 & 9220 & 9220 & -250 & -60 & -250 & -60 \\ & 109910 & 0 & -6980 & -1160 & 0 & 0 \\ & & 109910 & 0 & 0 & -6980 & -1160 \\ & & & 5540 & 80 & 0 & 0 \\ & & \textbf{Symmetric} & & 44860 & 0 & 0 \\ & & & & & 5540 & 80 \\ & & & & & & 44860 \end{pmatrix}$$

$$P_{12} = \begin{pmatrix} 2900 & 1030 & 1030 & -1280 & -380 & -1280 & -380 \\ 7150 & 7440 & 0 & -7680 & -1310 & 0 & 0 \\ 7150 & 0 & 7440 & 0 & 0 & -7680 & -1310 \\ 160 & -220 & 0 & 200 & -10 & 0 & 0 \\ 150 & -20 & 0 & 90 & -40 & 0 & 0 \\ 160 & 0 & -220 & 0 & 0 & 200 & -10 \\ 150 & 0 & -20 & 0 & 0 & 90 & -40 \end{pmatrix}$$

$$P_{22} = \begin{pmatrix} 970 & 680 & 680 & -810 & -130 & -810 & -130 \\ & 630 & 0 & -720 & -100 & 0 & 0 \\ & & 630 & 0 & 0 & -720 & -100 \\ & & & 870 & 100 & 0 & 0 \\ & & \textbf{Symmetric} & & 80 & 0 & 0 \\ & & & & & 870 & 100 \\ & & & & & & 80 \end{pmatrix}$$

§§ 6.3.3 The Inverted pendulum

Figure 6.4 shows an inverted rigid pendulum driven by a frictionless translational trolley. With a nonzero initial angle of the pendulum, a controller is designed to move the trolley back and forth while keeping the pendulum standing straight up on the trolley. The kinetic energy and potential energy of the system are

$$2T = m_c\dot{x}^2 + I_p\dot{\theta}^2 + m_p\left(L^2\dot{\theta}^2 + \dot{x}^2 - L\dot{\theta}\dot{x}\cos(\theta)\right) \tag{6.21}$$

$$2V = m_p g L\cos(\theta) \tag{6.22}$$

where x denotes the displacement of the trolley moving along x-axis, r the angle of the pendulum relative to y-axis, m_c the mass of the trolley, m_p the total mass of the uniform pendulum with length L, g the gravity constant and $I_p = \frac{m_p L^2}{12}$ the inertia of the rectangular pendulum. Then, from the Lagrange function T-V applies Lagrange's equations of motion to yield following the dynamic equations of motion

$$(m_c + m_p)\ddot{x} - \frac{m_p L\cos(\theta)}{2}\ddot{\theta} + \frac{m_p L\sin(\theta)}{2}\dot{\theta}^2 = u \tag{6.23}$$

$$-\frac{m_p L\cos(\theta)}{2}\ddot{x} + \frac{m_p L^2}{3}\ddot{\theta} - \frac{m_p g L\sin(\theta)}{2} = 0 \tag{6.24}$$

where u represents the control force horizontally applied on the trolley. For convenience, Eqs. (23)-(24) can be rearranged into the first-order state equation in matrix form as follows

$$\dot{q} = Aq + Bu + f \tag{6.25}$$

where

$$A = \begin{pmatrix} 0 & 0 & 1 & 0 \\ 0 & 0 & 0 & 1 \\ 0 & a & 0 & 0 \\ 0 & b & 0 & 0 \end{pmatrix};$$

$$B = \begin{pmatrix} 0 \\ 0 \\ \frac{1}{3m} \\ \frac{\cos(\theta)}{2mL} \end{pmatrix}; \quad f = \begin{pmatrix} 0 \\ 0 \\ f_3 \\ f_4 \end{pmatrix};$$

$$m = \frac{(m_c + m_p)}{3} - \frac{m_p \cos^2(\theta)}{4};$$

$$a = \frac{3m_p g}{(4m_c + m_p)}; \quad b = \frac{6(m_c + m_p)\, g}{L(4m_c + m_p)};$$

$$f_3 = -\frac{m_p L \sin(\theta)}{6m}\dot{\theta}^2 + \frac{m_p g \sin(\theta)\cos(\theta)}{4m} - \frac{3m_p g}{(4m_c + m_p)};$$

$$f_4 = -\frac{m_p L \sin(\theta)\cos(\theta)}{4mL}\dot{\theta}^2 + \frac{(m_c + m_p)\, g \sin(\theta)}{2mL}$$

$$\frac{-6(m_c + m_p)\, g\theta}{L(4m_c + m_p)}$$

and q represents the state vector $\left[x\ \theta\ \dot{x}\ \dot{\theta}\right]^T$. Equation (6.25) is thus identical to Eq. (6.5) when E is an identity matrix.

Table 6.5 shows the model parameters of the inverted pendulum. The positive definite weighting matrices P and R, shown in Eqs. (6.6) and (6.9), are chosen so that the matrix Q satisfies the Riccati equation (6.11) and also is a positive semi-definite matrix. The same three-step procedure as mentioned in section 6.3.1 is employed again to evaluate a constant positive definite matrix P, accompanied with a constant positive definite matrix R, and a time-variant matrix Q. The weighting matrix R_N and vector c are specified to be zero in Eq. (6.15). Let the initial angle of the pendulum be 30 deg from the vertical axis. The closed-loop system responses of the inverted pendulum are shown in Figs. 6.24-6.28. The system responses include trolley displacement and velocity, pendulum angular displacement and velocity, and the control force required for the trolley. In order to satisfy the stability criterion shown in Eq. (6.16), Fig. 6.29 demonstrates that the time rate of the Lyapunov function during the control process is negative. If the initial angle of the pendulum is larger than 36 degrees, the time rate of the Lyapunov function will be positive at a given time. In other words, the asymptotical stability of the inverted pendulum cannot be maintained through Lyapunov-based control input unless its initial angle is less than 36 degrees. This is because the gravitational force in Eq. (6.25) generates too much nonlinearity so that the Lyapunov-based control cannot counteract. From Figs. 6.24-6.28, it takes

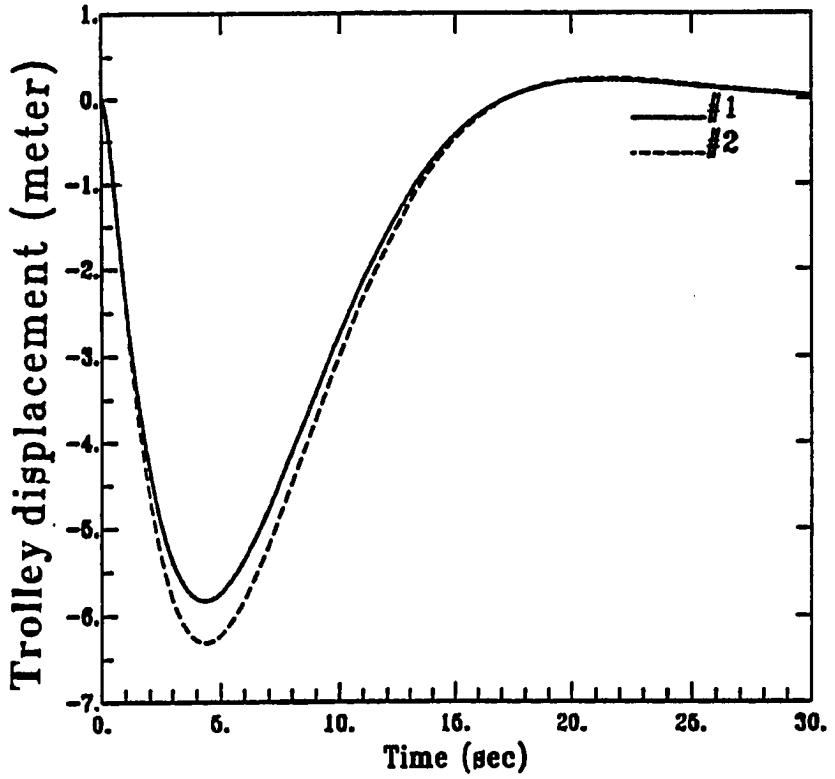

Figure 6.24: Trolley displacement of an inverted pendulum

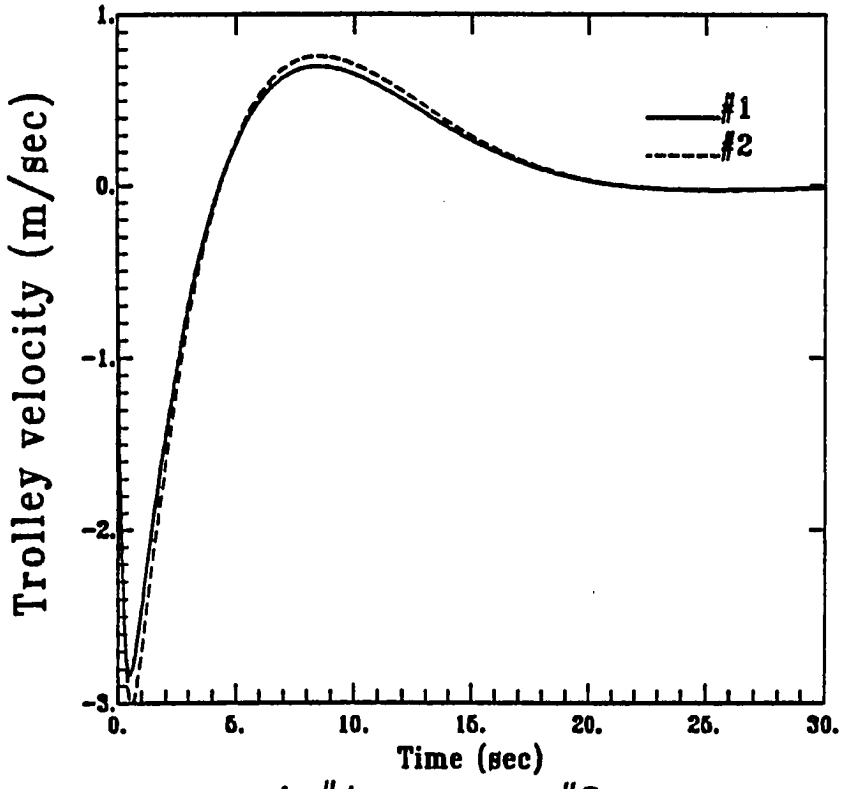

* #1: u_o+u_1; #2: u_o

Figure 6.25: Trolley velocity of an inverted pendulum

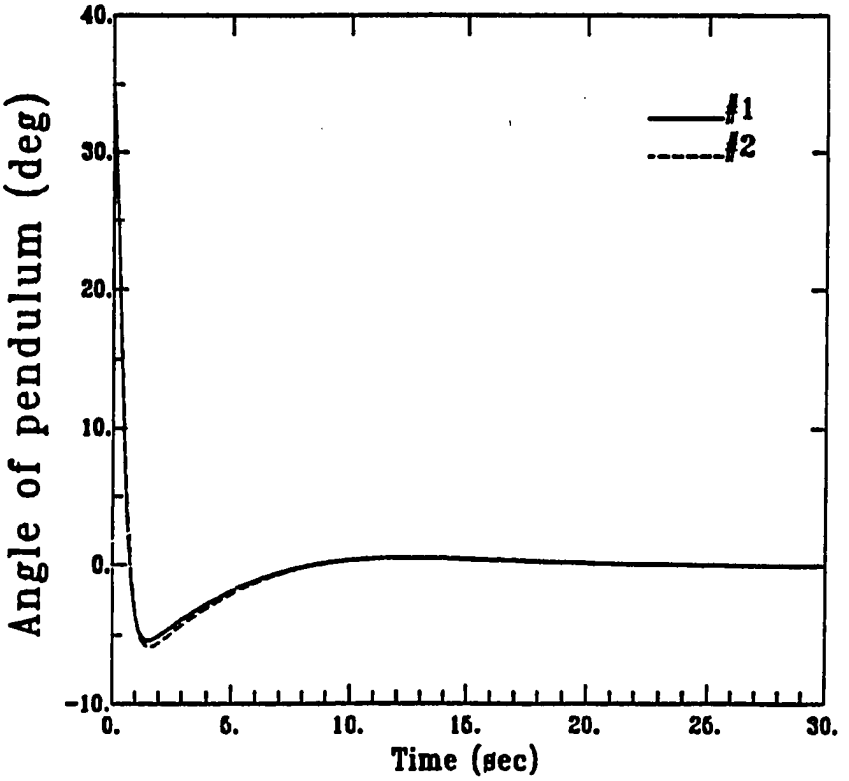

Figure 6.26: Pendulum angular displacement of an inverted pendulum

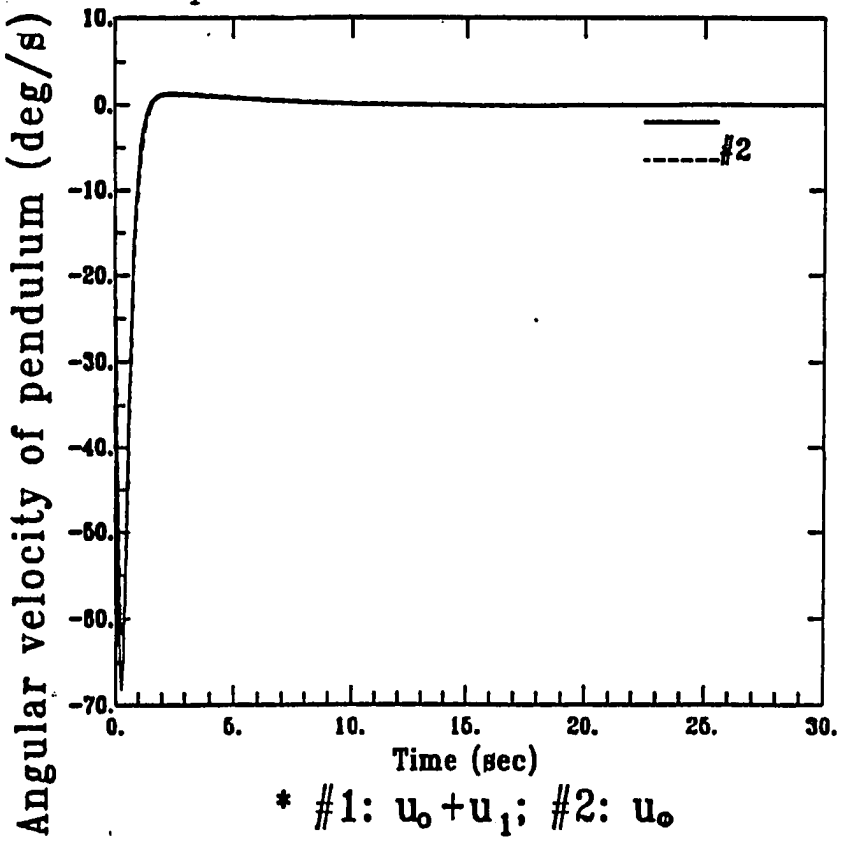

Figure 6.27: Pendulum angular velocity of an inverted pendulum

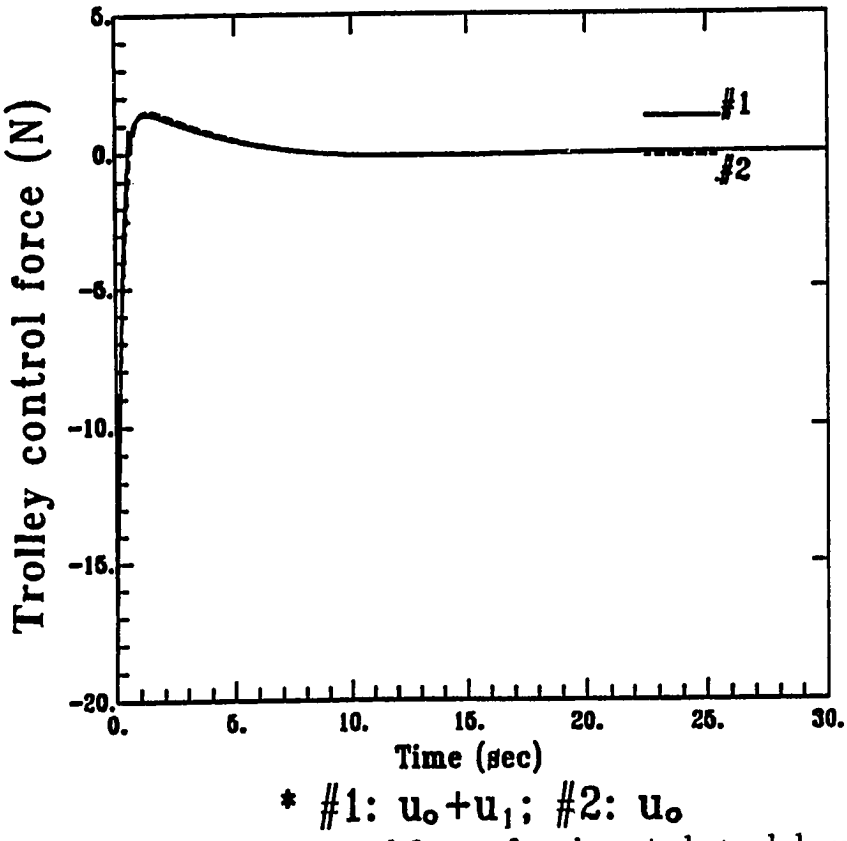

Figure 6.28: Trolley control force of an inverted pendulum

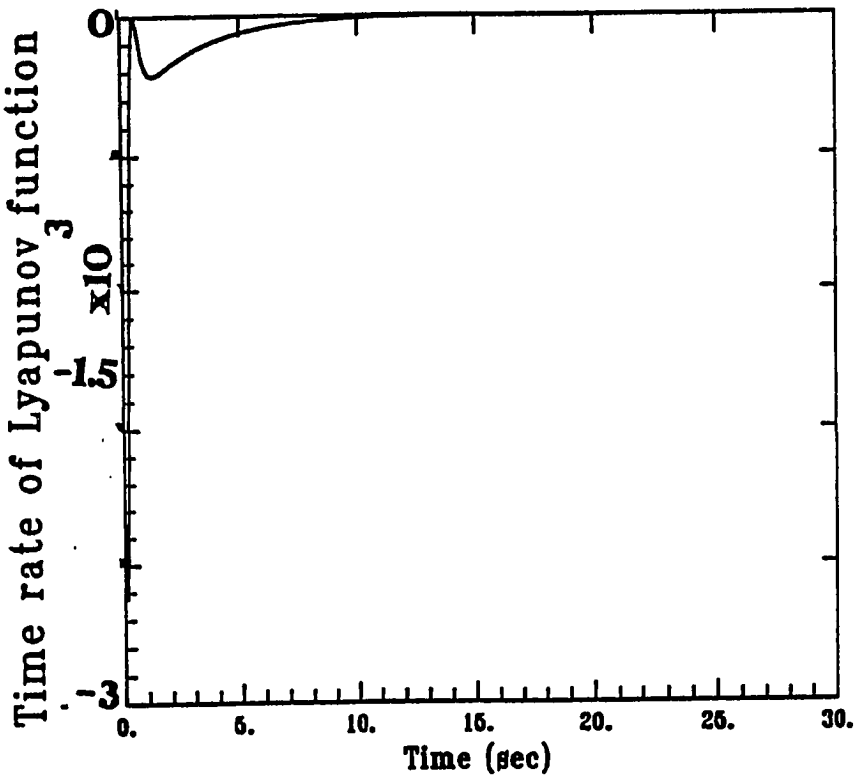

Figure 6.29: Time rate of Lyapunov's function of an inverted pendulum

about the same time to implement the assigned tasks for both control schemes. However, the first peak of the trolley displacement and the pendulum angle is improved by including the nonlinear control force u_1. The required control torques for both control algorithms are comparable.

Table 6.5: Model parameters and weighting matrices for inverted pendulum

a. Model parameters: 0.02truein

$m_c = 1$ kg

$m_p = 0.4$ kg

L $= 1$ m

g $= 9.8$ $\frac{m}{sec^2}$

b. Weighting matrices:

$$Q = \begin{pmatrix} 0.0001 & 0.0004 & -0.0001 & 0.0001 \\ & 2.4162 & -0.0018 & 0.5563 \\ & \textbf{symmetric} & -0.0006 & -0.0003 \\ & & & 0.1287 \end{pmatrix} \times 10000 \; ;$$

$$R = 100 \; ;$$

$$P = \begin{pmatrix} 0.0006 & -0.0070 & 0.0017 & -0.0018 \\ & 1.0445 & -0.0393 & 0.2465 \\ & \textbf{symmetric} & 0.0090 & -0.0103 \\ & & & 0.0584 \end{pmatrix} \times 10000$$

§ 6.4 Discussion and summary

A hybrid controller design has been developed, including a linear control law for the linear part of the system and a nonlinear control law to compensate for the nonlinear dynamic behavior. The method is based on the sufficient conditions of Lyapunov's second method for system stability. The approach starts with selecting a quadratic Lyapunov function with a weighting matrix, which is derived from the Riccati equation of optimal control theory for the linearized system equations. With the weighting matrix, the nonlinear control part is derived by making the derivative of Lyapunov's function to be negative. The nonlinear control part thus derived is directly related to the states and the nonlinear portion of the system dynamic equation. The overall controller design provides a stable closed-loop system in the Lyapunov sense even when the nonlinear behavior in the system is significant. Three numerical simulations are given to demonstrate the feasibility of these approaches.

If there is an efficient way to solve the time-variant Riccati equation (6.11) recursively, the approach developed in this chapter will be very attractive for real time implementation for control of nonlinear systems with kinematic nonlinearities. However, such an efficient way does not exist, particularly for large dynamic systems. Therefore, a systematic way is required to compute a constant positive definite matrix P such that the corresponding Riccati equation holds and produces a positive definite matrix Q and a positive definite matrix R. The open issue exists regarding the existence of a constant positive definite matrix P such that Q is a positive definite matrix which could be time-variant. This is a challenging issue to resolve. As long as a positive definite matrix P is found such that Q is positive definite, a stable closed-loop system in the Lyapunov sense is then obtained. Note that the feedback control design through the Lyapunov approach may be very conservative, since the Lyapunov stability criterion provides only the sufficient conditions for system stability.

The numerical evaluation of Eq. (6.15) should be carefully studied. Past experiences show that the nonlinear control force u_1 can be erroneously large if it is not properly computed. Sensitivity analysis of the nonlinear control force, with respect to the state vector q, may be required. Further studies are needed to solve the Lyapunov-based control designs directly from the second-order model [50] without converting to the first order model.

Reference 75 shows an investigation which is conducted to integrate the singular perturbation technique [76-79] and the Lyapunov-based nonlinear control algorithm to compensate the kinematic nonlinearity for the large flexible space structures. The singular perturbation method simplifies the controller design by designing two separate control inputs in two reduced-order subsystems, such as slow-model subsystem and fast-model subsystem. Such an integrated approach yields a nonlinear feedback controller which provides a stable closed-loop system in two separate time scales.

Intensive efforts have been made in this chapter for system stability of nonlinear dynamic systems with active feedback controllers. System stability must be studied in the front end of the robustness issue for practical problems. Robustness does not have any meaning if the system is not stable in the first place. The method developed in this chapter is believed to provide a useful tool for control engineers to address the robustness issue for control of nonlinear systems, particularly when linear models are used for controller designs.

Chapter 7

CONCLUDING REMARKS

This dissertation has covered four different yet inter-related topics for the ground-based experiments in the control of large flexible space structures. Chapter 3 has presented a mechanism device for a suspension system to provide a zero-gravity environment for the dynamic testing of the flexible space structures. In Chapter 4, the rotational/translational maneuvering experiments and simulations of a multibody structure have been implemented to verify the importance of strain feedback for flexural vibration. Chapter 5 has dealt with an integrated mechanism/control design for the slewing maneuvers of flexible structures, whereby a novel application of noncircular gears is developed in conjunction with control techniques for the suppression of vibrational motion. The kinematic nonlinearity, which takes place in the results of Chapter 4 and Chapter 5, has led to a Lyapunov-based nonlinear control design in Chapter 6 for the rapid and large angle maneuvers of flexible space structures. A more detailed conclusion of each chapter is expressed as follows.

§ 7.1 Conclusions for Chapter 3

Chapter 3 has dealt with a novel mechanical design of the suspension system which provides a practical research tool to assess characteristics of the low-frequency space structures proposed for operation in the weightless environment. Compared to the existing suspension devices, this suspension system is compact, simple, and easy to manipulate. The mechanism of this suspension system is

characterized by a noncircular disk with a convex profile. The suspension system is constructed to counteract the weight of test structures by using a specially shaped disk in conjunction with a torsional spring. The basic principle behind this suspension system is to maintain the static equilibrium of the test structure at any vertical position. The convex profile of the disk is determined through the kinematic inversion technique and envelope theory. The design of this disk suspension system is applicable for the different weights of the test structures without the change of the disk profile. Via the same noncircular disk, the torsional spring rate can be adjusted to achieve the static equilibrium for any test structure at rest. Two kinds of test structures have been chosen for the suspension simulations, such as a lumped-parameter element and a flexible steel beam. The simulation results have indicated that the characteristics of the flexible space structures can be precisely tested under this suspension system. The suspension system has shown its capability of performing a constant-speed motion along with the flexural vibration during the impulse response. The simulation results have provided the necessary insights to build up the experimental equipment. The experimental hardware has been set up in NASA-Langley for the experiments.

§ 7.2 Conclusions for Chapter 4

In Chapter 4, the experimental setup of a scale multi-body model has been constructed to verify an active output feedback control for the rapid rotational/translational maneuver. The dynamic system consists of one flexible steel beam which is carried on a translational and rigid trolley, whereby two motors are demanded to generate two control inputs for the flexible beam and trolley respectively. The primary functions and characteristics of control equipments are listed in several tables, including the motors of trolley and beam, potentiometer, strain gages, instrument amplifier, pulse amplifier and power supply. The EAI-2000 Analog Computer is used as an active controller which deals with the output feedback gain. A real-time closed-loop system is thus generated by connecting

the dynamic system and control equipments. The mission of position control is assigned to move the rigid trolley and rotate the flexible beam until their terminal positions are reached while simultaneously suppressing the flexural vibration. Four different control cases have been implemented, such as no strain feedback, the strain feedback to the beam motor, the strain feedback to the trolley motor, and the strain feedback to both trolley and beam motors. The comparisons are made with the experimental and simulation results on such four control cases. The undamped vibration is significantly observed in the first control case with no strain feedback. The second control case improves the beam controller such that the flexural vibration is sufficiently suppressed during the control process. The vibrational motion of the flexible beam also damps out through the translational motion of the trolley, while the strain feedback is applied to the trolley motor in the third control case. Furthermore, the fourth control case, where strain feedback is applied to both trolley and beam motors, yields the best maneuvering performance such that both the flexural vibration and the residual oscillation are considerably suppressed.

In each control case, the experimental and the simultation results verify each other very well. All the results offer good insights to conducting the investigation of the multi-body dynamics and control, especially the mixed rigid-flexible-body system, in the foreseeable future. Based on the successful experiments in this chapter, the translational trolley can be further used in the control of the large space facilities to effectively extend their workable region. The kinematic nonlinearity, which appears in the results, provides that motivation for an integrated approach to mechanism design and control design as well as a Lyapunov-based nonlinear control design in Chapter 5 and Chapter 6 respectively.

§ 7.3 Conclusions for Chapter 5

Chapter 5 has provided an integrated mechanism and control design approach to deal with the rapid and large angle slewing maneuvers of the flexible space structures. A novel application of noncircular gears is developed to produce the hyperbolic gear ratio which tunes the dynamic response and suppresses the flexural vibration of a flexible beam. The noncircular gears consist of two specially shaped cams which are properly meshed and well balanced through the thin metal bands. Such a design of noncircular gears incorporates the slewing maneuvers of two kinds of flexible beam-like structures, such as a flexible one-beam structure and a flexible two-beam structure. Their first simulations of 90-degree slewing maneuvers confirm the validation of noncircular gears in the suppression of vibration compared with the circular gears. Then, the optimal parameters of noncircular gears are determined to find the minimum of a cost function through the GRG optimization method. The simulation results show that the flexural vibration is sufficiently suppressed while the optimal design of noncircular gears is utilized in the slewing maneuvers of two flexible beam-like structures. Moreover, an integrated design of noncircular gears and control gain is achieved in a way that the control gain is also regarded as the design variable in the optimization problem. Such an integrated optimization results in an output feedback gain accompanied by the optimal parameters of noncircular gears to locally minimize the cost function. The simulations, with such an integrated mechanism/control design, yield the best slewing performances compared with the ones with the optimal design of the noncircular gears only. The methodology in this chapter thus paves a way to integrate the mechanism design and control technique for the rapid slewing maneuvers of the large flexible space structures.

§ 7.4 Conclusions for Chapter 6

As we know, Lyapunov's second method has been successfully applied to various control aspects, such as stability, estimation, control optimization, robustness, adaptive control etc. In Chapter 6, a Lyapunov-based nonlinear control design has been derived for the rapid maneuvers of flexible space structures in order to fit the asymptotical stability of Lyapunov's second method. One hybrid controller design has been developed so that the linear control law copes with the predominantly linear part of the system, while the nonlinear control law deals with the nonlinear dynamic behavior. Namely, the feedback of the nonlinear control law yields the compensation of the kinematic nonlinearity during the control process. Instead of the first-order state equations, the analytical formulation in this chapter is derived according to second-order equations due to no inversion of inertia matrix. A stability index, i.e. the quadratic Lyapunov's function, is developed that will result in a positive definite weighting matrix, derived from the Riccati equation of optimal control theory for the linearized system equations. The asymptotical stability implies the negative time derivative of Lyapunov's function during the control process. Then, the nonlinear control part is generated to ensure the minimum norm in the nonlinear part of the time rate of Lyapunov's function. Three numerical simulations have been performed to verify the validity of this nonlinear control design. Since Lyapunov's stability criterion provides only the sufficient conditions for system stability, the nonlinear feedback control design through the Lyapunov approach may be very conservative.

The investigation of stability associated with the nonlinear control will lead to some insights for the advanced robustness analysis in the nonlinear dynamic systems.

REFERENCES

1. Harvey, T.J., "A Second Generation Zero Spring Rate Support System," AIAA/AFOSR Workshop on Microgravity Simulation in Ground Validation Testing of Large Space Structures, Nov. 1-2 1989, Denver, Colorado.

2. Kienholz, D.A., "A Pneumatic/Electric Suspension Device for Very Low Frequency Dynamic testing," AIAA/AFOSR Workshop on Microgravity Simulation in Ground Validation Testing of Large Space Structures, Nov. 1-2 1989, Denver, Colorado.

3. Lynn, P., "Zero Gravity Suspension Systems," AIAA/AFOSR Workshop on Microgravity Simulation in Ground Validation Testing of Large Space Structures, Nov. 1-2 1989, Denver, Colorado.

4. Quartararo, R. and Hasselman, T.K., "Development of a Microgravity Suspension System," AIAA/AFOSR Workshop on Microgravity Simulation in Ground Validation Testing of Large Space Structures, Nov. 1-2 1989, Denver, Colorado.

5. Gronet, M.J., Brewster, R.G. and Crawley E.F., "Assembly and Suspension Issues for the DSMT Pathfinder Scale Model," AIAA/AFOSR Workshop on Microgravity Simulation in Ground Validation Testing of Large Space Structures, Nov. 1-2 1989, Denver, Colorado.

6. Colley, V.M., "Large Motion Suspension Devices for Flexible Structures," AIAA/AFOSR Workshop on Microgravity Simulation in Ground Validation Testing of Large Space Structures, Nov. 1-2 1989, Denver, Colorado.

7. Janiszewski, M.A., "Structural Testing Using the KC- 135 In-flight Microgravity Simulation facility," AIAA/AFOSR Workshop on Microgravity Simulation in Ground Validation Testing of Large Space Structures, Nov. 1-2 1989, Denver, Colorado.

8. Chen, F.Y., **Mechanics and Design of Cam Mechanisms**, Pergamon Press, New York, 1982.

9. Gabriele, G.A., "Application of the Reduced Gradient Method to Optimal Engineering Design," M.S. Thesis, School of Mechanical Engineering, Purdue University, December 1975.

10. Powell, M.J.D., "An Efficient Method of Finding the Minimum of a Function of Several Variables without Calculating Derivatives," Computer Journal, Vol. 7, pp. 155-162.

11. Colville, A.R., "A Comparative Study of Nonlinear Programming Codes," IBM New York Scientific Center Report No. 320-2949, June 1968.

12. Fletcher, R. and Reeves, C.M., "Function Minimization by Conjugate Gradients," Computer Journal, Vol. 7, 1964, pp. 149-154.

13. Pinson, L.D., "Large Space Structures Ground and Flight Progess," Paper No. IAF-84-388, 35th International Astronautical Federation Congress, Lausanne, Switzerland, Oct. 7-13, 1984.

14. Hanks, B.R. and Pinson, L.D., "Large Space Structures Raise Testing Challenges," Astronautics and Aeronautics, Oct. 1983.

15. Venneri, S.L., Hanks, B.R. and Pinson, L.D., "Future Trends in Spacecraft Design and Qualification," Proceedings of AGARD Conference on Mechanical Qualification of Large Flexible Spacecraft Structures, No.397, Sept. 8-13, 1985.

16. Pinson, L.D., "Recent Advances in Structural Dynamics and Control of Large Space Structures," Paper No. IAF-87-51, 38th International Astronautics Federation congress, Brighton, UK, Oct. 9-17, 1987.

17. Jaung, J.N., "Progress on Structural Dynamics and Control of Large Space Structures," Journal of Society of Instrument and Control Engineers, Vol. 26, No. 10, 1987, pp.905- 907.

18. Juang, J.N. and Turner, J.D., "Research in Slewing and Tracking Control," NASA/DOD Control/Structures Interaction Technology, NASA CP-2447, Part 2, 1986, pp.869-880.

19. Juang, J.N., Longman, R.W. and Junkins, J.L., "Methods Research Using Eigensystem Analysis," Second NASA/DOD Control/Structures Interaction Technology Conference, Colorado Springs, Colorado, Nov.17-19, 1987.

20. Jaung, J.N., Horta L.G. and Robertshaw, H.H., "A Slewing Control Experiment for Flexible Structures," Journal of Guidance, Control, and Dynamics, Vol. 9, Sept.-Oct. 1986, pp. 599-607.

21. Juang, J.N. and Horta, L.G., "Effects of Atmosphere on Slewing Control of a Flexible Structure," Journal of Guidance, Control, and Dynamics, Vol. 10, No. 4, July-Aug. 1987, pp.387-392.

22. Sparks, D.W., Horner G.C., Juang, J.N. and Klose, G, "A Survey of Experiments and Experimental Facilities for Active Control of Flexible Structures," Third NASA/DOD/CSI Technology Conference, San Diego, CA, Jan. 30-Feb. 2, 1989.

23. Peyrebrune, H.E., "Application and Design of Noncircular Gears," Transactions of the First Conference on Mechanisms, Purdue University, 1953, pp.21-24.

24. "Design Guide...when you need noncircular gears," Product Engineering Special Report, pp. 158-165.

25. Benford, B.F., "Customized Motions from Economical 'Almost Standard' Eccentric Gears," Machine Design, Sept. 26, 1968, pp. 151-154.

26. Cunningham, F.W., "Noncircular Gears," Transactions of the Fifth Conference on Mechanism, Purdue University, 1958, pp.96-103.

27. Bloomfield, B., "Noncircular Gears," Gear Design and Application, McGraw-Hill Book Co., 1967, pp.158-165.

28. Rappaport, S., "Elliptical Gears for Cyclic Speed Variations," Gear Design and Applications, McGraw Hill Book Co., 1967, pp. 166-168.

29. Miano, S.V., "Twin Eccentric Gears," Gear Design and Applications, McGraw Hill Book Co., 1967, pp. 169-173.

30. Book, W. J., "Feedback Control of Two Beam, Two Joint Systems with Distributed Flexibility," Trans. of ASME, Journal of Dynamic Systems, Measurement, and Control, Dec. 1975, pp.424- 431.

31. Book, W. J., "Analysis of Massless Elastic Chains with Servo-Controlled Joints," Trans. of the ASME, Journal of Dynamic Systems, Measurement, and Control, Sept. 1979, Vol.101, pp.187-192.

32. Rakhsha, F. and Goldenberg, A. A., "Dynamic Modelling of a Single-link Flexible Robot," IEEE Trans. on Automatic Control, 1985, pp.984-989.

33. Hastings, G. G. and Book, W. J., "Verification of a Linear Dynamic Model for Flexible Robotic Manipulators," IEEE Trans. on Automatic Control, 1986, pp.1024-1029.

34. Bejczy, A. K., "Robot Arm Dynamics and Control," Tech. Memo 33-669, Jet Propulsion Laboratory, Feb. 1974.

35. Hunt, L.R., Su, R., and Meyer, G., "Global Transformations of Nonlinear Systems," IEEE Transaction on Automatic Control, Vol. AC-28, No. 1, Jan. 1983.

36. Dwyer, T. A. W., III and Batten, A. L., "Exact Multiaxial Spacecraft Attitude Maneuvers with Torque Saturation," Proc. IEEE International Conf. on Robotics and Automation, ST. Louis, Mo, March 1985, pp.978-983.

37. Ghaemmaghami, P. and Juang, J.-N., "A Controller Design for Multi-body Large Angle Maneuvers," Proc. of International Symposium on the Mathematics of Networks and Systems, Phoenix, Arizona, June 15-19, 1987.

38. Huang, J.-K., Yang, L.-F. and Juang, J.-N., "Large Planar Maneuvers for Articulated Flexible Manipulators," Proceedings of the Guidance, Navigation and Control Conference, AIAA Paper No. 88-4119, August 1988.

39. Yang, L.F. and Huang, J.-K. "Two-Time-Scale Controller Designs for Large Flexible Structures," SPIE's Conference on Controls for Optical Systems, Orlando, Florida, April 16-20, 1990.

40. Freund, E. and Syrbe, M., "Control of Industrial Robots by Means of Microprocessors," Lecture Notes in Control and Information Sciences, 1977, Vol.2, pp.167-185.

41. Tarn, T. J., Bejczy, A. K., Isidori, A. and Chen, Y., "Nonlinear Feedback in Robot Arm Control," Proc. of the 23rd IEEE Conference on Decision and Control, Las Vegas, Nevada, Dec.12-14, 1984, pp.736-751.

42. Juang, J.-N., Lim, K. B. and Junkins, J. L., "Robust Eigensystem Assignment," AIAA Journal of Guidance, Control and Dynamics, to appear.

43. Lee, G.C.S., "Robust Arm Kinematics, Dynamics, and Control," Journal of Computers, IEEE, December 1982.

44. Wang, P.K.C., "A Robust Nonlinear Attitude Control Law for a Satellite with Flexible Appendages," Proc. 24th IEEE Conf. on Decision and Control, Ft. Lauderdale, FL., December 1985, pp. 1654-1659.

45. Varga, R.S., **Matrix Iterative Analysis**, Prentice-Hall, Inc., Englewood Cliffs, N.J., 1962.

46. Safonov, M.G., **Stability and Robustness of Multivariable Feedback Systems**, The MIT Press, Cambridge, Massachusetts, 1980.

47. Fujii, H. and Ishijima, S., "The Mission Function Control for Deployment and Retrieval of Subsatellite," Proceedings of the Guidance, Navigation and Control Conference, AIAA Paper No. 87-2326, August 1987.

48. Kalman, R.E. and Bertram, J.E., "Control System Analysis and Design Via the 'Second Method' of Lyapunov," Journal of Basic Engineering, pp 371-393, June 1960.

49. Kwakernaak, H. and Sivan, R., **Linear Optimal Control Systems**, John Wiley & Sons, Inc., New York, N.Y., 1972.

50. Oshman, Y., Inman, D. J. and Laub, A. J., "Square Root State Estimation for Second-order Large Space Structures Models," To appear in the J. of Guidance, Control and Dynamics, 1988.

51. Junkins, J.L., Rahman, Z., Bang, H. and Hecht, N., "Near-Minimum-Time Maneuvers of Flexible Vehicles: A Lyapunov Design Method," presented to 7th VPI&SU Symposium on Dynamics and Control of Large Structures, Virginia Polytechnic Institute and State University, Blacksburg, Virginia, May 8-10 1989.

52. Liapunov, A.M., **Stability of Motion**, Mathmatics in Science and Engineering, Volume 30, Academic Press, Inc., New York, N.Y., 1966.

53. Storey and Barnett, **Matrix Methods in Stability Theory**, Barnes & Noble, Inc., New York, N.Y., 1873.

54. Salle, La and Lefschetz, S., **Stability by Lyapunov's Direct Method with Applications**, Mathematics in Science and Engineering, Volume 4, Academic Press, Inc., New York, N.Y., 1961.

55. Harris, C.J. and Valenca, J.M.E., **The Stability of Input-Output Dynamic Systems**, Academic Press Inc. Ltd., New York, New York, 1983.

56. Razumikhin, B.S., "On the Application of Lyapunov's Methods to Stability Problems," Prikl. Mat. Mekh., Vol 22, 1958, pp.338-349.

57. Junkins, J.L. and Turner, J.D., **Optimal Spacecraft Rotational Maneuvers**, Elsevier, 1986.

58. Massera, J.L., "Contributions to Stability Theory," Ann. Math., Vol. 64, 1956, pp.182-206.

59. Malkin, I.G., "Theory of Stability of Motion," (book), AEC Translation 3352, Dept. of Commerce, USA, 1958.

60. Perron, O., "The Stability Problem in Differential Equations," (in Germany), Math. Zeitsch, Vol. 32, 1930, pp. 465-473.

61. Zadeh, L.A., "On the Stability of Linear Time-Varying Systems," J. Appl. Phys., Vol. 22, 1952, pp.402-405.

62. Antosiewicz, H.A. and Davis, P., "Some Implications of Lyapunov's conditions of Stability," J. Rat. Math. and Mech., Vol. 3, 1954, pp.447-457.

63. Bellman, R.E., "Kronecker Products and the Second Method of Lyapunov," Math. Nachrichten, 1959.

64. Kalman, R.E., "On Physical and Mathematical Mechanisms of Instability in Nonlinear Automatic Control systems," Trans. ASME, Vol. 79, 1957, pp.553-556.

65. Timoshenko, S.P. and Goodier, J.N., **Theory of Elasticity**, Third Edition, McGraw-Hill Book Company, New York, N.Y., 1970.

66. Bishop, R.E.D. and Johnson, D.C., **The Mechanics of Vibration**, Cambridge University Press, London, England, 1960.

67. Meirovitch, L., **Analytical Methods in Vibrations**, Third Printing, MacMillan Company, New York, N.Y., 1971.

68. Schultz, D.G. and Melsa, J.L., **State Functions and Linear Control Systems**, McGraw-Hill Company, New York, N.Y., 1967.

69. Greenwood, D.T., **Principles of Dynamics**, Prentice-Hall, Inc., Englewood Cliffs, New Jersey.

70. Shampine, L.F. and Gordon M.K., **Computer Solution of Ordinary Differential Equations: The Initial Value Problem.**

71. Yang, L.F., Chew, M., and Juang, J.N., "Ground-Based Testing of the Dynamics of Flexible Space Structures Using Band Mechanisms", will be presented at 1990 ASME Mechanisms Conference, Chicago, Illinois, September 16-19, 1990.

72. Juang, J.N., Yang, L.F., Huang, J.K. and Macauley, R., "Rapid Rotational/Translational Maneuvering Experiments of a Flexible Steel Beam," 1989 American Control Conference, Pittsburgh, Pennsylvania, June 21-23, 1989.

73. Huang, J.K., Yang, L.F. and Juang, J.N., "Large Planar Maneuvers for Articulators Flexible Manipulators", Proceedings of the Guidance, Navigation and Control Conference, AIAA Paper No. 88-4119, August 1988.

74. Juang, J.N., Yang, L.F. and Huang, J.K., "Lyapunov-based Control Designs for Flexible-Link Manipulators", AIAA/ASME/ASCE/AHS 30th Structures, Structural Dynamics and Materials Conference, Mobile, Alabama, April 5-7, 1989.

75. Yang, L.F. and Huang, J.K., "Two-Time-Scale Controller Designs for Large Flexible Structures," will be presented at SPIE's Conference on Controls for Optical Systems, Orlando, Florida, April 16-20, 1990.

76. Kokotovic, P.V. and Yackel, R.A., "Singular Perturbation of Linear Regulators: Basic Theorems," IEEE Trans. Automat. Contr., Vol. AC-17, pp. 29-37, Feb. 1972.

77. Chow, J.H. and Kokotovic, P.V., "Eigenvalue Placement in Two-Time-Scale Systems," Proc. IFAC Symp. Large-Scale Systems, 1976, pp. 321-326.

78. Siciliano, B., Calise, A.J. and Jonnalagadda, V.R.P., "Optimal Output Fast Feedback in Two-Time Scale Control of Flexible Arms," Proc. 25th IEEE Conf. on Decision and Control, Athens, Greece, pp. 1400-1404, 1986.

79. Kokotovic, P.V., Khalil, H.K. and O'Reilly, J., **Singular Perturbation Methods in Control: Analysis and Design**, Academic Press Inc., Orlando, Florida, 1986.

APPENDIX A

ENVELOPE OF A ONE-PARAMETER FAMILY OF CURVES

In the area of mechanism, the envelope theory is an analytical method which has been used to determine a wide variety of cam profiles including

(1) Radial cams with roller followers,

(2) Translating cams with offset roller followers,

(3) Swinging cams with roller followers,

(4) Radial cams with flat-faced followers,

(5) Cams with swinging centric flat-faced followers and

(6) Cams with swinging eccentric flat-faced followers.

In the development of a suspension disk, the disk profile is developed by observing a trajectory performed through an envelope of a family of the centric swinging strings depending on an angular parameter. The process to decide disk profile coordinates will be discussed in the next section. Figure A.1 shows the layout of graphical method associated with the envelope theory [8]. Assume that $S\{\gamma_c\}$ is a family of smooth curves on a surface, depending on a parameter c. A smooth curve γ is called an envelope of the family S if

(1) For every point of the curve γ , it is possible to give a curve γ_c of the family that is tangent to the curve γ at this point.

(2) For every curve γ_c of the family, it is possible to give a point on the curve γ at which the curve γ_c is tangent to γ .

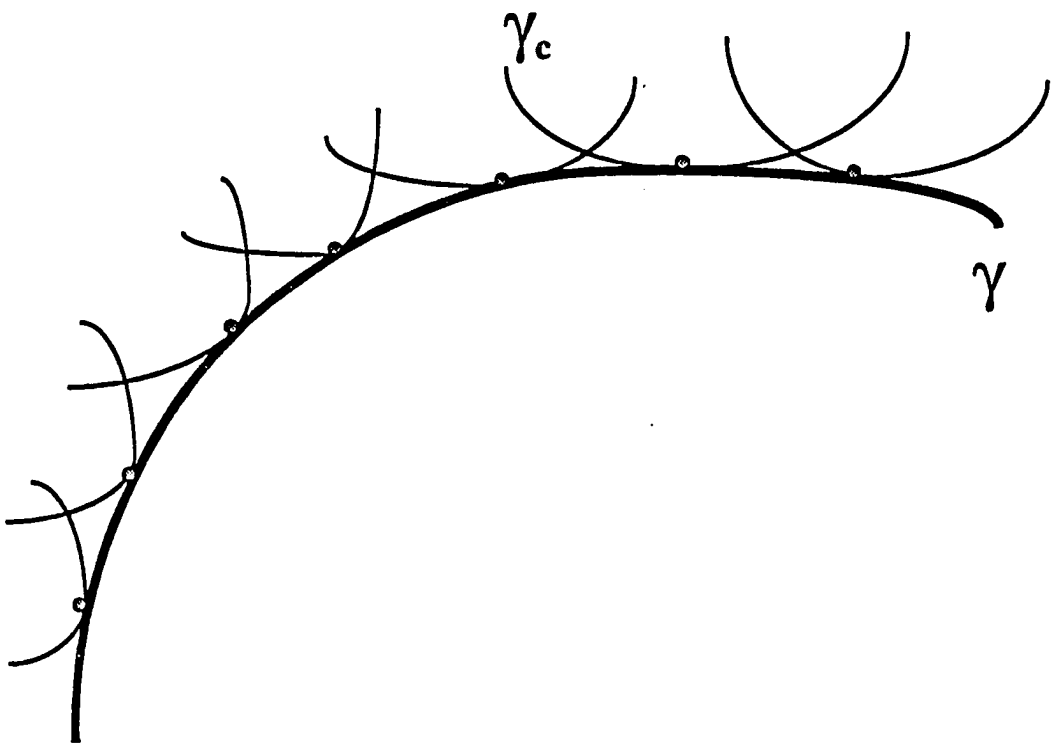

Figure A.1: Envelope of a one-parameter family of curves

(3) No curve of the family has a segment in common with the curve γ .

Theorem A.1: Suppose the curves γ_c of a family S are given by the equation $F(x,y,c)=0$, where F is continuous and continuously differentiable for all its arguments in a neighborhood of the point (x_0,y_0,c_0) . At the point (x_0,y_0,c_0) let the following relations hold:

$$F(x_0,y_0,c_0)=0, \tag{A.1}$$

$$\frac{\partial F(x_0,y_0,c_0)}{\partial c}=0, \tag{A.2}$$

$$\begin{pmatrix} \frac{\partial F}{x} & \frac{\partial F}{y} \\ \frac{\partial^2 F}{\partial c \partial x} & \frac{\partial^2 F}{\partial c \partial x} \end{pmatrix} \neq 0, \tag{A.3}$$

$$\frac{\partial^2 F}{\partial^2 c}=0 \tag{A.4}$$

Then in a certain neighborhood u of the point (x_0,y_0) , and for c from a definite neighborhood V of the point c_0 , there exists an envelope of the family $F(x,y,c)=0$. In general, the equation of the envelope can be obtained by

$$F(x,y,c)=0, \tag{A.5}$$

$$\frac{\partial F(x,y,c)}{\partial c}=0 \tag{A.6}$$

which expresses x and y as a function of the parameter c. Expressing the parameter c as a function of the variables x , y and substituting for c into Eq. (A.4) yield

$$F\big(x,y,c(x,y)\big)=0 \tag{A.7}$$

APPENDIX B

LAGRANGE'S FUNCTIONS FOR FOUR KINDS OF FLEXIBLE STRUCTURES

For the one flexible beam on a rigid translational trolley shown in Fig. 1.1, the kinetic energy T and the potential energy V for small bending amplitude can be expressed as

$$2T = m\dot{y}^2 + \int_0^L \rho \left[\dot{\vec{y}} + \dot{\vec{\theta}}_1 \times \vec{x}_1 - \dot{\vec{y}}_1\right] \bullet \left[\dot{\vec{y}} + \dot{\vec{\theta}}_1 \times \vec{x}_1 - \dot{\vec{y}}_1\right] dx_1, \qquad (B.1)$$

$$2V = \int_0^L EI\{\frac{\partial y_1}{\partial x_1 \partial x_1}\}^2 dx_1 \qquad (B.2)$$

where $\vec{x}_1$ is a vector tangent to the longitudinal axis of the base of flexible beam. The symbols and coordinate systems are displayed in Fig. B.1.

Moreover, the distributed coordinates are expanded in an orthogonal basis of assumed mode shapes as

$$y_1(x_1,t) = \psi_1^T(x_1)\, q_1(t),$$

$$\psi_1^T = [\psi_{11},\cdots,\psi_{1n_1}] \qquad and \quad q_1^T = [q_{11},\cdots,q_{1n_1}] \qquad (B.3)$$

where $\psi_1(x_1)$ is a vector of assumed mode shapes relative to a spatial coordinates derived from the fixed-free cantilever beam's boundary condition problem, $q_1(t)$ are generalized coordinates [65,66,67], and n_1 is an appropriate number of assumed modes.

Inserting Eq. (B.3) into Eqs. (B.1) and (B.2) yields

$$2T = m\dot{y}^2 + I_1\dot{\theta}_1^2 + \rho L\dot{y}^2 + \sum_{i=1}^{n_1}\sum_{j=1}^{n_1} m_{1ij}\dot{q}_{1i}\dot{q}_{1j} + \rho L^2 c\theta_1 \dot{\theta}_1 \dot{y}$$

$$- 2\sum_{i=1}^{n_1} P_{1i}\dot{q}_{1i}\dot{\theta}_1 \; - \; 2c\theta_1 \sum_{i=1}^{n_1} h_{1i}\dot{q}_{1i}\dot{y}, \tag{B.4}$$

$$2V \; = \; \sum_{i=1}^{n_1}\sum_{j=1}^{n_1} \kappa_{1ij} q_{1i} q_{1j} \tag{B.5}$$

where

$$I_1 \; = \; \int_0^L \rho x_1^2 \, dx_1,$$

$$m_{1ij} \; = \; \int_0^L \rho \psi_{1i}(x_1)\, \psi_{1j}(x_1) \; dx_1,$$

$$P_{1i} \; = \; \int_0^L \rho x_1 \psi_{1i}(x_1) \; dx_1,$$

$$h_{1i} \; = \; \int_0^L \rho \psi_{1i}(x_1) \; dx_1,$$

$$\kappa_{1ij} \; = \; \int_0^L EI \frac{\partial \psi_{1i}}{\partial x_1 \partial x_1} \frac{\partial \psi_{1j}}{\partial x_1 \partial x_1} \, dx_1 \quad for \; i,j \; = \; 1,2,\cdots,n_1.$$

To simplify the state variables in the above equations, denote $\xi_0 = y$, $\xi_1 = \theta_1$, $\xi_{i+1} = q_{1i}$, for $i = 1,2,\cdots, n_1$, $Q_0 = \tau_0$, $Q_1 = \tau_1$, $Q_{i+1} = 0$, for $i = 1,2,\cdots,n_1$. Via the Lagrange's equation of motion [69], we obtain

$$\frac{d}{dt}\left[\frac{\partial T}{\partial \dot{\xi}_i}\right] - \frac{\partial T}{\partial \xi_i} + \frac{\partial V}{\partial \xi_i} \; = \; Q_i \tag{B.6}$$

for $i = 0,1,\cdots,n_1$. This leads to the equations of motion as shown in Eq. (B.9).

Obviously, the dynamics of one flexible beam shown in Fig. 5.2 is a special case of the previous dynamic system without the rigid trolley. The system parameters and coordinates are similar with a previous system shown in Fig. 5.2 by ignoring the trolley. Similar with Eqs. (B.1) and (B.2), the kinetic energy T and the potential energy V become

$$2T \; = \; \int_0^L \rho \left[\, \dot{\bar{\theta}}_1 \times \bar{x}_1 \,\right] \bullet \left[\dot{\bar{\theta}}_1 \times \bar{x}_1 \,\right] \, dx_1, \tag{B.9}$$

$$2V \; = \; \int_0^L EI\{\frac{\partial y_1}{\partial x_1 \partial x_1}\}^2 \, dx_1 \tag{B.10}$$

where $\bar{x}_1$ is a vector tangent to the longitudinal axis of the base of flexible beam. With the definition of Eq. (B.3), equations (B.9) and (B.10) can be rewritten as

$$2T = I_1\dot{\theta}_1^2 + \sum_{i=1}^{n_1}\sum_{j=1}^{n_1} m_{1ij}\dot{q}_{1i}\dot{q}_{1j} - 2\sum_{i=1}^{n_1} P_{1i}\dot{q}_{1i}\dot{\theta}_1, \qquad (B.11)$$

$$2V = \sum_{i=1}^{n_1}\sum_{j=1}^{n_1} \kappa_{1ij}q_{1i}q_{1j} \qquad (B.12)$$

where I_1, m_{1ij}, P_{1i} and κ_{1ij} have been defined in Eqs. (B.4) and (B.5). Then, the Lagrange's equation of motion for one flexible beam shown in Fig. 5.2 can be derived by inserting Eqs. (B.11) and (B.12) into Eq. (B.6).

Similarly, for the articulated two-beam flexible structure on a rigid trolley shown in Fig. 5.3, the kinetic energy and the potential energy can be derived as

$$\begin{aligned} 2T = m\dot{y}^2 &+ \int_0^L \rho\left[\dot{\bar{y}} + \dot{\bar{\theta}}_1 \times \bar{x}_1 - \dot{\bar{y}}_1\right] \bullet \left[\dot{\bar{y}} + \dot{\bar{\theta}}_1 \times \bar{x}_1 - \dot{\bar{y}}_1\right] dx_1 + \\ &\int_0^L \rho\left[\dot{\bar{y}} + \dot{\bar{\theta}}_1 \times \bar{L}_2 + \dot{\bar{\theta}}_2 \times \bar{L}_2 - \dot{\bar{y}}_1(L) - \dot{\bar{y}}_2\right] \bullet \\ &\left[\dot{\bar{y}} + \dot{\bar{\theta}}_1 \times \bar{L}_2 + \dot{\bar{\theta}}_2 \times \bar{L}_2 - \dot{\bar{y}}_1(L) - \dot{\bar{y}}_2\right] dx_2, \end{aligned} \qquad (B.13)$$

$$2V = \int_0^L EI\{\frac{\partial y_1}{\partial x_1 \partial x_1}\}^2 dx_1 + \int_0^L EI\{\frac{\partial y_2}{\partial x_2 \partial x_2}\}^2 dx_2 \qquad (B.14)$$

The symbols and coordinate systems are demonstrated in Fig. D.1. Expanding Eqs. (B.13) and (B.14) provides

$$\begin{aligned} 2T = m\dot{y}^2 &+ 4I_1\dot{\theta}_1^2 + I_2\dot{\theta}_2^2 + 2\rho L\dot{y}^2 + \sum_{i=1}^{n_1}\sum_{j=1}^{n_1} m_{1ij}\dot{q}_{1i}\dot{q}_{1j} \\ &+ \sum_{i=1}^{n_2}\sum_{j=1}^{n_2} m_{2ij}\dot{q}_{2i}\dot{q}_{2j} - 2\sum_{i=1}^{n_1} P_{1i}\dot{q}_{1i}\dot{\theta}_1 - 2\sum_{i=1}^{n_2} P_{2i}\dot{q}_{2i}\dot{\theta}_2 \\ &+ 3\rho L^2 c\theta_1\dot{\theta}_1\dot{y} - 2c\theta_1\sum_{i=1}^{n_1} h_{1i}\dot{q}_{1i}\dot{y} - 2c(\theta_1 + \theta_2)\sum_{i=1}^{n_2} h_{2i}\dot{q}_{2i}\dot{y} \\ &+ \rho L\sum_{i=1}^{n_1}\sum_{j=1}^{n_1} \psi_{1i}(L)\psi_{1j}(L)\dot{q}_{1i1j} + \rho L^2 c(\dot{\theta}_1 + \theta_2)\dot{y}\dot{\theta}_2 \end{aligned}$$

$$- 2\rho Lc\theta_1 \sum_{i=1}^{n_1} \psi_{1i}(L)\dot{q}_{1i}\dot{y} + \rho L^3 c\theta_2 \dot{\theta}_1\dot{\theta}_2$$

$$- 2\rho L^2 \sum_{i=1}^{n_1} \psi_{1i}(L)\dot{q}_{1i}\dot{\theta}_1 - 2Lc\theta_2 \sum_{i=1}^{n_2} h_{2i}\dot{q}_{2i}\dot{\theta}_1$$

$$- \rho L^2 c\theta_2 \sum_{i=1}^{n_1} \psi_{1i}(L)\dot{q}_{1i}\dot{\theta}_2 + 2c\theta_2 \sum_{i=1}^{n_1}\sum_{j=1}^{n_2} \psi_{1i}(L)h_{2j}\dot{q}_{1i}\dot{q}_{2j}, \qquad (B.15)$$

$$2V = \sum_{i=1}^{n_1}\sum_{j=1}^{n_1} \kappa_{1ij}q_{1i}q_{1j} + \sum_{i=1}^{n_2}\sum_{j=1}^{n_2} \kappa_{2ij}q_{2i}q_{2j} \qquad (B.16)$$

where

$$I_1 = \int_0^L \rho x_1^2 \, dx_1,$$

$$I_2 = \int_0^L \rho x_2^2 \, dx_2,$$

$$m_{1ij} = \int_0^L \rho\psi_{1i}(x_1)\psi_{1j}(x_1) \, dx_1,$$

$$m_{2ij} = \int_0^L \rho\psi_{2i}(x_2)\psi_{2j}(x_2) \, dx_2,$$

$$P_{1i} = \int_0^L \rho x_1\psi_{1i}(x_1) \, dx_1,$$

$$P_{2i} = \int_0^L \rho x_2\psi_{2i}(x_2) \, dx_2,$$

$$h_{1i} = \int_0^L \rho\psi_{1i}(x_1) \, dx_1,$$

$$h_{2i} = \int_0^L \rho\psi_{2i}(x_1) \, dx_2,$$

$$\kappa_{1ij} = \int_0^L EI \frac{\partial\psi_{1i}}{\partial x_1\partial x_1}\frac{\partial\psi_{1j}}{\partial x_1\partial x_1} \, dx_1 \quad for \; i,j = 1,2,\cdots,n_1.$$

$$\kappa_{2ij} = \int_0^L EI \frac{\partial\psi_{2i}}{\partial x_2\partial x_2}\frac{\partial\psi_{2j}}{\partial x_2\partial x_1} \, dx_2 \quad for \; i,j = 1,2,\cdots,n_2.$$

where n_1 and n_2 are the numbers of the shape functions for the first arm and the forearm respectively. Substitution of Eqs. (B.15) and (B.16) into Eq. (B.6)

provides the Lagrange's equation of motion for two articulated flexible beams on a rigid and translational trolley.

The dynamics of an articulated flexible two-beam structure carried on a trolley in Fig. 5.3 can be simplified into the system of two flexible beams as shown in Fig. 5.3. Based on the parameters and coordinates as shown in Fig. 5.3, the kinetic energy and the potential energy of such an articulated flexible beam can be expressed as

$$2T = \int_0^L \rho \left[\dot{\vec{\theta}}_1 \times \bar{x}_1\right] \bullet \left[\dot{\vec{\theta}}_1 \times \bar{x}_1\right] dx_1 + \int_0^L \rho \left[\dot{\vec{\theta}}_1 \times \bar{L} + \dot{\vec{\theta}}_2 \times \bar{x}_2 - \bar{y}_1(\dot{L}) - \dot{\vec{y}}_2\right]$$

$$\bullet \left[\dot{\vec{\theta}}_1 \times \bar{L} + \dot{\vec{\theta}}_2 \times \bar{x}_2 - \bar{y}_1(\dot{L}) - \dot{\vec{y}}_2\right] dx_2, \qquad (B.17)$$

$$2V = \int_0^L EI\{\frac{\partial y_1}{\partial x_1 \partial x_1}\}^2 dx_1 + \int_0^L EI\{\frac{\partial y_2}{\partial x_2 \partial x_2}\}^2 dx_2 \qquad (B.18)$$

Expanding Eqs. (B.17) and (B.18) provides

$$2T = 4I_1\dot{\theta}_1^2 + I_2\dot{\theta}_2^2 + \sum_{i=1}^{n_1}\sum_{j=1}^{n_1} m_{1ij}\dot{q}_{1i}\dot{q}_{1j}$$

$$+ \sum_{i=1}^{n_2}\sum_{j=1}^{n_2} m_{2ij}\dot{q}_{2i}\dot{q}_{2j} - 2\sum_{i=1}^{n_1} P_{1i}\dot{q}_{1i}\dot{\theta}_1 - 2\sum_{i=1}^{n_2} P_{2i}\dot{q}_{2i}\dot{\theta}_2$$

$$+ 3\rho L^2 c\theta_1\dot{\theta}_1\dot{y} - 2c\theta_1\sum_{i=1}^{n_1} h_{1i}\dot{q}_{1i}\dot{y} - 2c(\theta_1 + \theta_2)\sum_{i=1}^{n_2} h_{2i}\dot{q}_{2i}\dot{y}$$

$$+ \rho L\sum_{i=1}^{n_1}\sum_{j=1}^{n_1} \psi_{1i}(L)\psi_{1j}(L)\dot{q}_{1i}\dot{q}_{1j} + \rho L^3 c\theta_2\dot{\theta}_1\dot{\theta}_2$$

$$- 2\rho L^2\sum_{i=1}^{n_1} \psi_{1i}(L)\dot{q}_{1i}\dot{\theta}_1 - 2Lc\theta_2\sum_{i=1}^{n_2} h_{2i}\dot{q}_{2i}\dot{\theta}_1$$

$$- \rho L^2 c\theta_2\sum_{i=1}^{n_1} \psi_{1i}(L)\dot{q}_{1i}\dot{\theta}_2 + 2c\theta_2\sum_{i=1}^{n_1}\sum_{j=1}^{n_2} \psi_{1i}(L)h_{2j}\dot{q}_{1i}\dot{q}_{2j}, \qquad (B.19)$$

$$2V = \sum_{i=1}^{n_1}\sum_{j=1}^{n_1} \kappa_{1ij}q_{1i}q_{1j} + \sum_{i=1}^{n_2}\sum_{j=1}^{n_2} \kappa_{2ij}q_{2i}q_{2j} \qquad (B.20)$$

where I_1, I_2, m_{1ij}, m_{2ij}, P_{1i}, P_{2i}, h_{1i}, h_{2i}, κ_{1ij} and, κ_{2ij} have been defined in Eqs. (B.15) and (B.16). Finally, substitution of Eqs. (B.19) and (B.20) into Eq. (B.6) provides Lagrange's equation of motion for two articulated flexible beams. Note that the closed-loop dynamic equations of one flexible beam and two articulated flexible beams will be modified by applying the mechanism of noncircular gears developed in Chapter 5.

APPENDIX C

DYNAMIC EQUATION OF ONE FLEXIBLE BEAM ON A TROLLEY

Figure 1.2 shows a planar flexible beam clamped on an axial shaft of a motor by a hinge. The motor is mounted on a translational trolley which is driven along a linear track by another motor. The flexible beam is modeled as a cantilever beam with the fixed end at the motor and the free end at the tip $x_1 = L$ (see Fig. B.1). Only the bending vibration is allowed during the motion of the arm. The x-y axes are the fixed inertial coordinate, whereas the $x_1 - y_1$ axes represent the moving relative coordinate. Lagrange's equations of motion, in conjuction with the modal expansion to discretize the deflection of the flexible-link manipulator, are applied to derive the dynamic equations of motion. Let the state vector be defined by

$$\xi = [\, y,\ \theta,\ q^T \,]^T \quad ; \quad q^T = [\, q_1,\ q_2, \cdots,\ q_n] \tag{C.1}$$

where y is the translational displacement of the trolley, r the root angle of the flexible beam, and $q_i\ (i = 1, 2, \cdots, n)$ the general coordinates corresponding to the shape functions $\psi_i\ (i = 1, 2, \cdots, n)$ for discretization of the bending deflection of the flexible beam. The control torques introduced by the two motors can be expressed by the vector

$$\tau = [\, \tau_0,\ \tau_1,\ 0, \cdots,\ 0]^T \tag{C.2}$$

where τ_0 and τ_1 represent the applied torques for the trolley and the flexible beam respectively.

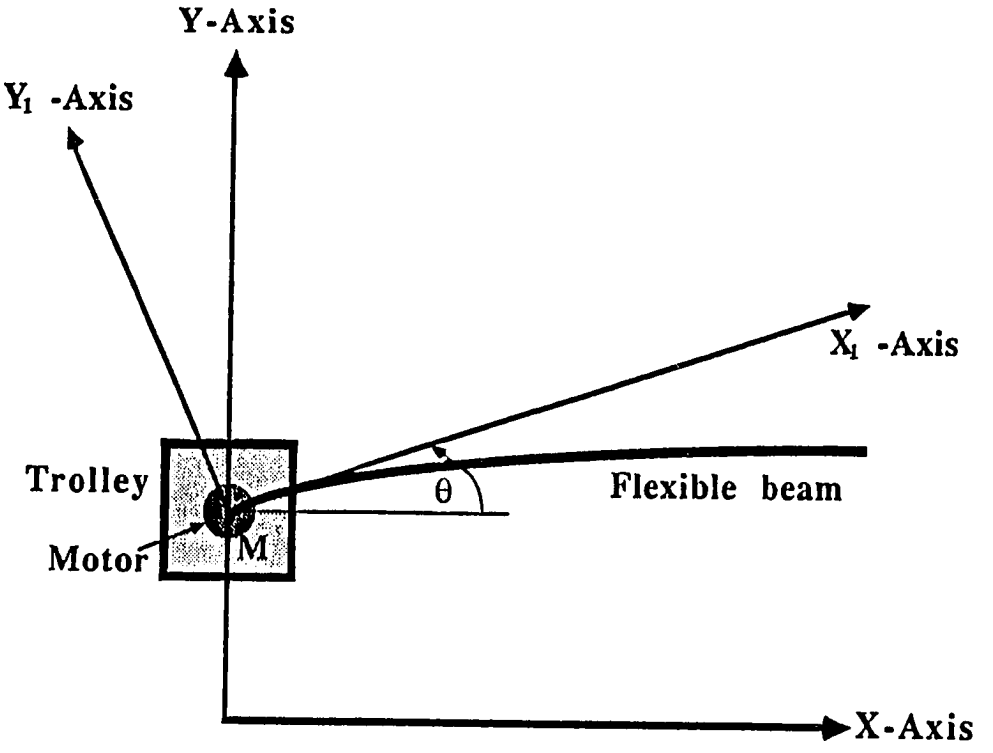

Figure C.1: Coordinates of one flexible beam on a trolley

The equations of motion including actuator dynamics can then be written by

$$M\ddot{\xi} + K\xi = f\left(\xi, \dot{\xi}\right) + \tau \qquad (C.3)$$

Denote ρ the mass density of the arm per unit length, L the length of the flexible beam, m the total mass of the trolley and the motor on the trolley, and I the total moment of inertia. The inertia matrix is expressed by

$$M = \begin{pmatrix} m + \rho L & & \\ \frac{\rho L^2 c\theta}{2} & I & \textbf{symmetric} \\ -\tilde{h}c\theta & -\tilde{p} & \rho L\hat{I} \end{pmatrix} \qquad (C.4)$$

where $\hat{I}$ is an $n \times n$ identity matrix, and $c\theta = \cos(\theta)$. The constant vectors $\tilde{h}$ and $\tilde{p}$ are defined in reference [37,38]. The constant stiffness matrix is

$$K = Diag\left[\, 0,\ 0,\ \rho L\omega^2 \,\right] \quad ;\ \omega = Diag\left[\, \omega_1, \cdots, \omega_n \,\right] \qquad (C.5)$$

where $\omega_i\ (i = 1, 2, \cdots, n)$ are the frequencies associated with the shape functions $\psi_i(x_1)$, which are used to discretize the deflection of the flexible beam. The nonlinear force yields

$$f\left(\xi, \dot{\xi}\right) = \begin{pmatrix} s\theta\left[\frac{\rho L^2 \dot{\theta}^2}{2} - \tilde{h}^T \dot{q}\dot{\theta}\right] \\ s\theta\tilde{h}^T\dot{q}\dot{y} \\ -s\theta\tilde{h}\dot{\theta}\dot{y} \end{pmatrix} \qquad (C.6)$$

where $s\theta = \sin(\theta)$.

The actuator dynamics and sensor characteristics play major roles in the controller design. The two actuators for the feedback control are dc electric motors. The electric motor can be regarded as a standard armature circuit. Denote the armature resistance by R_a, the back-EMF (Electro-Motive-Force) constant by K_b, the motor torque constant by K_t, the gear train viscous drag coefficient by C_v, the motor inertia by I_m, and the overall gear ratio by N_g. Then the torque t produced by the actuator provides

$$\tau = \left[\frac{N_g K_t}{R_a}\right] e_a - \left[\frac{K_t K_b}{R_a} + C_v\right] N_g^2 \dot{\theta} - I_m N_g^2 \ddot{\theta} \qquad (C.7)$$

where e_a is the voltage applied into the armature and θ is the output shaft angle. For the flexible beam, θ in Eq. (C.7) represents the root angle. For the translational trolley, it is equivalent to the linear displacement y divided by the transmission pulley radius r. The passive damping of the whole system results from the second term in Eq. (C.7).

Referring to the sensors, the rotational angles are measured by the 10-turn rotary potentiometers, whereas the angular velocities are calibrated by tachometers. Strain gages are used to sense the bending moments along the flexible beam. Denote c_p the conversion factor between the output shaft angle θ and the output voltage e_p of the potentiometer, c_t the conversion factor between the output angular velocity and the output voltage e_t, c_s the conversion factor between the strain and the strain output voltage e_0. Suppose two strain gages are placed along the flexible beam respectively at x_a and x_b. An output measurement equation can be written in the following matrix form

$$\begin{aligned} \hat{e} &= [\, e_{t0},\ e_{t1},\ e_{p0},\ e_{p1},\ e_0(x_a),\ e_0(x_b)\,]^T = C_f \left[\, \dot{y},\ \dot{\theta},\ \xi^T \,\right]^T \\ &= Diag\left[\, \frac{c_{T0}}{r},\ c_{t1},\ \frac{c_{p0}}{r},\ c_{p1},\ C_e \,\right] \left[\, \dot{y},\ \dot{\theta},\ y,\ \theta q^T \right]^T \end{aligned} \tag{C.8}$$

where each element of the matrix C_e is a product of the conversion factor c_s. The reader is directed to reference [37,38] for more detailed information. Note that the sub-subscripts 0 and 1 indicate the associated quantities corresponding to the trolley and the flexible beam respectively. Equation (C.8) relates the output voltage $\hat{e}$ to the state variables y, θ, and ξ through the coefficients of the matrix C_f.

Substituting Eq. (C.7) into Eq. (C.3) provides

$$\bar{M}\ddot{\xi} + \bar{C}\dot{\xi} + K\xi = BE_a(t) + f\left(\xi, \dot{\xi}\right) \tag{C.9}$$

in which,

$$\bar{M} = M + Diag\left[\, \frac{I_{m0}N_{g0}^2}{r},\ I_{m1}N_{g1}^2,\ 0,\ 0 \,\right],$$

$$\bar{C} = Diag\left[\left(\frac{K_{t0}K_{b0}}{R_{a0}} + C_{v0}\right)\frac{N_{g0}^2}{r},\ \left(\frac{K_{t1}K_{b1}}{R_{a1}} + C_{v1}\right)N_{g1}^2,\ 0,\ 0 \right]$$

$$B = \begin{pmatrix} \frac{N_{g0}K_{t0}r}{R_{a0}} & 0 \\ 0 & \frac{N_{g1}K_{t1}r}{R_{a1}} \\ 0 & 0 \\ 0 & 0 \end{pmatrix}$$

and $E_a(t) = [\, e_{a0},\ e_{a1} \,]^T$ with e_{a0} and e_{a1} being the applied voltages for the motors of the trolley and the flexible beam respectively.

APPENDIX D

TYPES OF LYAPUNOV-BASED STABILITY

In this appendix, Lyapunov's second method is expressed in conjunction with five sufficient conditions in Theorem D.1. In corollaries D.1 and D.2, various types of system stability are treated in several ways such that Lyapunov's function is restricted through the desired sufficient conditions. One quadratic type of Lyapunov's function is assigned in corollary D.3 to perform a so-called Lyapunov's matrix equation, which has been applied for control designs to satisfy the criterion of asymptotical stability in Chapter 6. Corollary D.4 demonstrates a modified Lyapunov's matrix equation with a given limit value for real parts of system eigenvalues for asymptotical stability. Instead of linear systems, a nonlinear dynamics with a special function of state is shown in corollary D.5 to satisfy the Lyapunov's matrix equation.

Theorem D.1: [48] Consider a free (unforced) dynamic system in first-order state form such as

$$E\frac{dq}{dt} = f(q,t) \qquad (D.1)$$

where q is a state vector of $[\, x, \dot{x}\,]^T$, f(q,t) is a nonlinear function of state vector and time, and E indicates a symmetric and positive-definite matrix composed of the inertia matrix (see Chapter 6). Suppose there exists a scalar function V(q,t) with continuous first partial derivatives with respect to q and t such that V(0,t)=0 and

(1) V(q,t) is positive definite; i.e., there exists a continuous, nondecreasing

scalar function a such that $\alpha(0)=0$ and, for all t and all $q \neq 0$

$$0 < \alpha(\|q\|) \leq V(q,t); \tag{D.2}$$

(2) There exists a continuous scalar function q such that $\tau(0)=0$ and the derivative $\dot{V}$ of V along the motion at t, q satisfies, for all t and $q \neq 0$,

$$\dot{V}(q,t) = \frac{\partial V}{\partial t} + (\mathbf{grad}\ V)^T f(q,t) \leq -\gamma(\|q\|) < 0 \tag{D.3}$$

(3) There exists a continuous, nondecreasing scalar function such that $\beta(0)=0$ and, for all t,

$$V(q,t) \leq \beta(\|q\|); \tag{D.4}$$

(4) $\alpha(\|q\|) \to \infty \quad with \quad \|q\| \to \infty$

(D.5)

Then the equilibrium state $q_e=0$ is uniformly asymptotically stable in the large; V(q,t) is called a Lyapunov function of the system (D.1). In the following corollaries, several weaker types of system stability are characterized in terms of the restrictions of Eqs. (D.2)-(D.5).

Corollary D.1: [48] The following conditions are sufficient for the various weaker types of stability:

(a) Uniform asymptotic stability: [Eqs. (D.2)-(D.4)].

(b) Equiasymptotic stability in the large: [Eqs. (D.2)-(D.3), (D.5)].

(c) Equiasymptotic stability: [Eqs. (D.2)-(D.3)].

(d) Uniform stability: [Eqs. (D.2)-(D.4) and $\dot{V}(q,t) \leq 0$ for all [q,t].

(e) Stability: [Eqs. (D.2)-(D.3) and $\dot{V}(q,t) \leq 0$ for all q,t].

Corollary D.2: For a continuous-time autonomous dynamic system

$$E\frac{dq}{dt} = f(q) \qquad (D.6)$$

where the initial condition is f(0)=0. Equiasymptotic stability in the large is assured by the existence of scalar function V(q) with a continuous first partial derivative with respect to q, such that V(0)=0 and

(1) $V(q) > 0$ for all $q \neq 0$, (D.7)

(2) $\dot{V}(q) < 0$ for all $q \neq 0$, (D.8)

(3) $V(q) \rightarrow \infty$ with $\|q\| \rightarrow \infty$. (D.9)

Lyapunov's function can be assigned to be a quadratic equation of state q with a positive-definite matrix P. Differentiation of Lyapunov's function, with respect to time, yields a so-called Lyapunov's matrix equation which provides a negative-definite and symmetric matrix Q as long as the system is asymptotically stable. Corollary D.3 shows such a Lyapunov's matrix equation for a linear dynamic system.

Corollary D.3: [48] The equilibrium state $q_e = 0$ of a continuous-time, linear, free, and stationary dynamic system

$$E\frac{dq}{dt} = Aq \qquad (D.10)$$

is asymptotically stable if and only if given any symmetric, positive-definite matrix Q there exists a symmetric, positive- definite matrix P which is the unique solution of the set of $\frac{n(n+1)}{2}$ linear equations

$$A^TPE + E^TPA = -Q \qquad (D.11)$$

and $q^T\{E^TPE\}q$ is a Lyapunov's function for Eq. (D.10).

Stability of the linear dynamic system can be evaluated by using the eigenvalue analysis. The locations of eigenvalues associated with system matrix A can

judge whether the system is stable or not. The stable eigenvalues must always lie in the left-hand side of pole plot; i.e., real parts of eigenvalues are negative in the stable system. Based on eigenvalue analysis, corollary D.3 has been modified by Kalman [48] for some purposes:

Corollary D.4: The real parts of the eigenvalues of a linear matrix A are less than s if and only if given any symmetric, positive-definite matrix Q there exists a symmetric, positive-definite matrix P which is the unique solution of the set of $\frac{n(n+1)}{2}$ linear equations

$$-2\sigma PE + A^T PE + E^T PA = -q \qquad (D.12)$$

Furthermore, Barnett and Storey [53] have extended corollary D.3 for nonlinear dynamic system such as

$$E\frac{dq}{dt} = Aq + g(q) \quad and \quad g(0) = 0 \qquad (D.13)$$

Basically, equation (D.10) is the first approximation (or linear part) of Eq. (D.13) and is said to be achieved from Eq. (D.10) by linearization. The asymptotical stability of dynamics in Eq. (D.13) can be achieved as long as the nonlinear term g(q) is formed to be a special state function shown in the following corollary.

Corollary D.5: [53] The origin of dynamic system (D.13) is asymptotically stable with Lyapunov's function $V = q^T\{E^T PE\}q$ having $\dot{V} = -q^T Rq$ for all functions of the form $g(p) = E^{-1}P^{-1}\left[\frac{Q}{2} - \frac{R}{2} + S\right]q$, where P, Q are constant positive definite matrices, satisfying $A^T PE + E^T PA = -Q$, R(q) is an arbitrary symmetric positive definite matrix and S(q) an arbitrary skew-symmetric matrix.

APPENDIX E

DYNAMIC EQUATION OF TWO ARTICULATED FLEXIBLE BEAMS ON A TROLLEY

One flexible beam is articulated on the tip of the previous beam to construct an articualted flexible structure as shown in Fig. 6.2. This additional beam is also treated as a fixed-free cantilever beam. This system has three (one translational and two rotational) degrees of freedom attributed to rigid body motion. One more actuator is required, which is concatenated axially with the former one on the rigid trolley. The fore-beam is manipulated by this additional motor through a wire. In Fig. E.1, the mass M includes the mass of the new motor for the fore-beam. θ_1 denotes the root angle of the first flexible beam and θ_2 the root angle of the fore-beam measured relative to the previous local coordinates, i.e., $x_1 - y_1$ axes.

The state vector similar to Eq. (E.1) becomes

$$\xi = [\, y,\ \theta_1,\ \theta_2,\ q_1^T,\ q_2^T \,]^T$$

$$q_1^T = [\, q_{11},\ q_{12}, \cdots,\ q_{1n1}]$$

and

$$q_2^T = [\, q_{21},\ q_{22}, \cdots,\ q_{2n2}] \qquad (E.1)$$

where y is the translational displacement of the trolley and q_{1i} $(i = 1, 2, \cdots, n_1)$ the general coordinates corresponding to the shape functions ψ_{1i} $(i = 1, 2, \cdots, n_1)$ for discretization of the bending deflection of the first flexible beam. The quantities q_{2i} and ψ_{2i} are defined similarly for

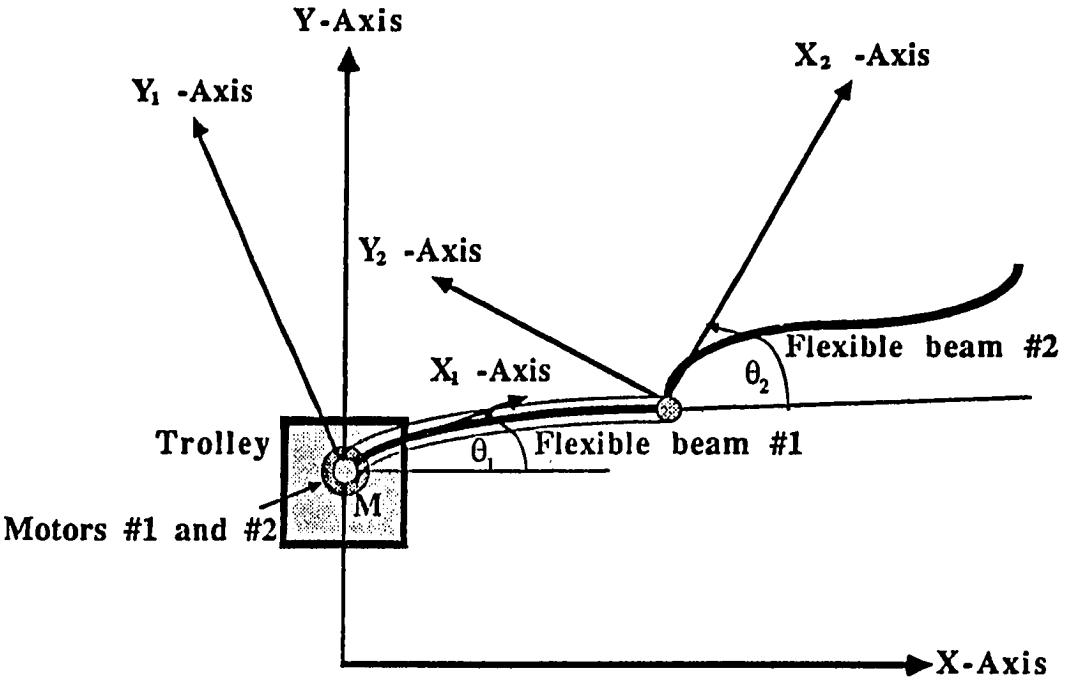

Figure E.1: Coordinates of two articulated flexible beams on a trolley

the fore-beam. The input vector for the articulated flexible beams is

$$\tau = [\, \tau_0,\ \tau_1,\ \tau_2,\ 0, \cdots,\ 0\,]^T \qquad (E.2)$$

where τ_0 represents the applied torque for the trolley, and τ_1 and τ_2 for the two flexible beams.

Application of Lagrange's equations of motion in terms of state variables yields a set of equations in matrix form as Eq. (E.3). The symmetry inertia matrix becomes

$$M = \begin{pmatrix} m+2\rho L & \frac{3\rho L^2}{2}c\theta_1 & \frac{\rho L^2}{2}c(\theta_1+\theta_2) - \rho L\psi_1^T(L)c\theta_1 \\ \frac{3\rho L^2}{2}c\theta_1 & 4I_1 & \frac{\rho L^3}{2}c\theta_2 \\ \frac{\rho L^2}{2}c(\theta_1+\theta_2) & \frac{\rho L^3}{2}c\theta_2 & I_2 \\ -h_1 c\theta_1 & -\rho L^2\psi_1(L) - \rho L\psi_1(L)c\theta_1 & \frac{-\rho L^2}{2}\psi_1(L)c\theta_2 - P_1 \\ -h_2 c(\theta_1+\theta_2) & -Lh_2 c\theta_2 & -P_2 \end{pmatrix}$$

$$\begin{pmatrix} -h_1^T c\theta_1 & -h_2^T c(\theta_1+\theta_2) \\ -\rho L^2\psi_1^T(L) - P_1^T & -Lh_2^T c\theta_2 \\ \frac{-\rho L^2}{2}\psi_1^T(L)c\theta_2 & -P_2^T \\ \rho L\psi_1(L)\psi_1^T(L) + \rho L\hat{I}_1 & h_2^T\psi_1(L)c\theta_2 \\ h_2\psi_1^T(L)c\theta_2 & \rho L\hat{I}_2 \end{pmatrix} \qquad (E.3)$$

where $c\theta_1 = \cos(\theta_1)$, $c\theta_2 = \cos(\theta_2)$, $c(\theta_1+\theta_2) = \cos(\theta_1+\theta_2)$. Here $\hat{I}_1$ and $\hat{I}_2$ are $n_1 \times n_1$ and $n_2 \times n_2$ identity matrices respectively with n_1 and n_2 being the numbers of the mode shapes respectively for discretization of bending deflections of the two beam-like flexible beams. Moreover, the stiffness matrix becomes

$$K = Diag\,[\, 0,\ 0,\ 0,\ \rho L\omega_1^2,\ \rho L\omega_2^2\,]$$

$$\omega_1 = Diag\,[\, \omega_{11}, \cdots, \omega_{1n_1}\,] \quad and \quad \omega_2 = Diag\,[\, \omega_{21}, \cdots, \omega_{2n_2}\,] \qquad (E.4)$$

and the nonlinear force vector is

$$f\left(\xi, \dot{\xi}\right) = [\, f_0,\ f_1, f_2,\ f_3,\ f_4\,]^T \qquad (E.5)$$

where

$$f_0 = \frac{3\rho L^2 s\theta_1}{2}\dot{\theta}_1^2 - s\theta_1\left(h_1^T\dot{q}_1\right)\dot{\theta}_1 - s(\theta_1+\theta_2)\left(h_2^T\dot{q}_2\right)\left(\dot{\theta}_1+\dot{\theta}_2\right)$$

$$+ \frac{\rho L^2}{2} s(\theta_1+\theta_2)\dot{\theta}_2\left(\dot{\theta}_1+\dot{\theta}_2\right) - \rho L s\theta_1 \left(\psi_1^T(L)\dot{q}_1\right)\dot{\theta}_1$$

$$f_1 = s\theta_1\left(h_1^T\dot{q}_1\right)\dot{y} + s(\theta_1+\theta_2)\left(h_2^T\dot{q}_2\right)\dot{y} - \frac{\rho L^2}{2} s(\theta_1+\theta_2)\dot{y}\dot{\theta}_2$$

$$+ \rho L s\theta_1\left(\psi_1^T(L)\dot{q}_1\right)\dot{y} + \frac{\rho L^3}{2} s\theta_2\dot{\theta}_2^2 - L s\theta_2\left(h_2^T\dot{q}_2\right)\dot{\theta}_2$$

$$f_2 = s(\theta_1+\theta_2)\left(h_2^T\dot{q}_2\right)\dot{y} - s\theta_2\left(\psi_1^T(L)\dot{q}_1\right)\left(h_2^T\dot{q}_2\right) + L s\theta_2\left(h_2^T\dot{q}_2\right)\dot{\theta}_1$$

$$+ \frac{\rho L^2}{2} s(\theta_1+\theta_2)\dot{y}\dot{\theta}_1$$

$$f_3 = -s\theta_1 h_1\dot{y}\dot{\theta}_1 - \rho L s\theta_1\psi_1(L)\dot{y}\dot{\theta}_1 - \frac{\rho L^2}{2}\psi_1(L)s\theta_2\dot{\theta}_2^2 + s\theta_2\psi_1(L)\left(h_2^T\dot{q}_2\right)\dot{\theta}_2$$

$$f_4 = -h_2 s(\theta_1+\theta_2)\dot{y}\left(\dot{\theta}_1+\dot{\theta}_2\right) - L s\theta_2 h_2\dot{\theta}_1\dot{\theta}_2 + h_2 s\theta_2\left(\psi_1^T(L)\dot{q}_1\right)\dot{\theta}_2$$

where $s\theta_1 = \sin(\theta_1)$, $s\theta_2 = \sin(\theta_2)$, $s(\theta_1+\theta_2) = \sin(\theta_1+\theta_2)$.

Then, the output measurement equation is

$$\hat{e} = \left[\, e_{t0}, e_{t1}, e_{t2}, e_{p0}, e_{p1}, e_{p2}, e_{01}(x_a), e_{01}(x_b), e_{02}(x_a), e_{02}(x_b) \,\right]^T$$

$$= C_f\left[\, \dot{y},\ \dot{\theta}_1,\ \dot{\theta}_2,\ \xi^T \,\right]^T \qquad (E.6)$$

where

$$C_f = Diag\left[\, \frac{c_{T0}}{r}, c_{t1}, c_{t1}, \frac{c_{p0}}{r}, c_{p1}, c_{p1}, C_{e_1}, C_{e_2} \,\right]$$

$$C_{ei} = c_s h\begin{pmatrix} \frac{\partial^2\psi_{i1}}{\partial x_1\partial x_1}(x_1), \cdots, \frac{\partial^2\psi_{in_1}}{\partial x_1\partial x_1}(x_1) \\ \frac{\partial^2\psi_{i1}}{\partial x_2\partial x_2}(x_2), \cdots, \frac{\partial^2\psi_{in_2}}{\partial x_2\partial x_2}(x_2) \end{pmatrix} \quad for\ i = 1,2.$$

The dynamic equations can thus be developed yielding

$$\bar{M} = M + Diag\left[\, \frac{I_{m0}N_{g0}^2}{r},\ I_{m1}N_{g1}^2,\ I_{m2}N_{g2}^2,\ 0,\ 0,\ 0,\ 0 \,\right] \qquad (E.7)$$

$$\bar{D} = Diag\left[\, \left(\frac{K_{t0}K_{b0}}{R_{a0}} + C_{v0}\right)\frac{N_{g0}^2}{r},\ \left(\frac{K_{t1}K_{b1}}{R_{a1}} + C_{v1}\right)N_{g1}^2,\ \left(\frac{K_{t2}K_{b2}}{R_{a2}} + C_{v2}\right)N_{g2}^2 \right.$$

$$\left., 0, 0, 0, 0\right]$$

$$B = \begin{pmatrix} \frac{N_{g0}K_{t0}r}{R_{a0}} & 0 & 0 \\ 0 & \frac{N_{g1}K_{t1}r}{R_{a1}} & 0 \\ 0 & 0 & \frac{N_{g2}K_{t2}r}{R_{a2}} \\ 0 & 0 & 0 \\ 0 & 0 & 0 \\ 0 & 0 & 0 \\ 0 & 0 & 0 \end{pmatrix}$$

and $E_a(t) = [\, e_{a0},\, e_{a1},\, e_{a2} \,]^T$.